Therapeutic targeting of PRMT5 and mutant ACVR1 in paediatric glioma

Elizabeth J Brown

Nuffield Department of Medicine

St. Edmund Hall

University of Oxford

Michaelmas Term 2021

Thesis submitted for the degree of Doctor of Philosophy in Clinical Medicine

Therapeutic targeting of PRMT5 and mutant ACVR1 in paediatric glioma

Elizabeth J Brown, St. Edmund Hall.

Thesis submitted for the degree of Doctor of Philosophy in Clinical Medicine, Nuffield Department of Medicine. Michaelmas term 2021.

Abstract

Diffuse Intrinsic Pontine Glioma (DIPG) is a universally fatal paediatric brainstem tumour with a median overall survival of 9-11 months. The unique genetic, anatomical and developmental identity of the tumour means that there are currently no effective chemotherapies or targeted therapies. This thesis aimed to identify and characterise novel targets for the treatment of DIPG. Potential therapeutic opportunities arise from the frequent mutations found in histone H3 (H3K27M) and kinase *ACVR1* found in DIPG tumours. A screen of epigenetic protein inhibitors revealed that the viability of the patient-derived DIPG cell line HSJD-DIPG-007 was highly sensitive to arginine methyltransferase (PRMT) inhibitors, particularly in *ACVR1* mutant lines. The PRMT5 inhibitor LLY-283 was identified as the most promising lead for its potent inhibition of DIPG viability and the recognised role of PRMT5 in the regulation of the cell cycle and stemness. RNA-sequencing and phenotypic analyses revealed that LLY-283 did not induce cell death, but reduced stemness and invasiveness, altered metabolism and restored H3K27me3 levels in DIPG cells. Through collaboration with Ángel Montero Carcaboso, LLY-283 was tested in an orthotopic murine xenograft model of DIPG. LLY-283 reduced infiltration of DIPG cells into the murine forebrain, but did not prolong survival, perhaps reflecting inadequate drug exposure. In parallel, the CRISPR/Cas9 system was used to correct the causative G328V *ACVR1* mutation in DIPG cells. The resultant isogenic DIPG cells demonstrated slowed proliferation after correction of *ACVR1* mutations, rather than a complete growth arrest as observed with published shRNA mediated *ACVR1* knockdown. Surprisingly, the isogenic cell lines also showed comparable sensitivity (GI_{50}) to PRMT5 and ACVR1 inhibition, suggesting other genetic differences contribute to the variation in treatment sensitivity between DIPG cell lines. My findings highlight the value of isogenic DIPG cell lines for interrogating the effects of individual tumorigenic mutations. It remains incredibly challenging to develop new strategies to treat DIPG. This thesis supports the future design of combination treatments for DIPG and provides new experimental tools to aid their development.

Declaration

I declare that there are no parts of this thesis or its research herein that have been reproduced or accepted for another award or degree at any other university or learning institution.

This thesis contains no other person's work except where indicated in text (summarised below)

Summary of contributions

In section 4.2 cDNA library preparation, RNA sequencing, genome alignment and tabulation of read counts were performed by the University of Oxford Nuffield Department of Orthopaedics, Rheumatology and Musculoskeletal Sciences (NDORMS) Next Generation Sequencing (NGS) Facility (Martin Philpott, Adam Cribbs, Chao Jiang). The parallel transcriptomic analysis presented in section 4.2.4 (Figure 4.8a, b) was performed by Trajecture (Guy Hill).

For sections 3.2.4 and 3.2.5 (Figure 3.5, Figure 3.6, Figure 3.7 and Figure 3.8) radiation treatment was performed by James Thompson (Oxford Institute for Radiation Oncology). In section 4.2.9 (Figure 4.15) *in vivo* experiments and ddPCR were designed and performed by Leire Balaguer Lluna and Ángel Montero Carcaboso (Hospital Sant Joan de Déu, Barcelona). Survival, weight and ddPCR analysis were performed by Leire Balaguer Lluna. In sections 4.2.10, 4.2.11 and 4.2.12 (Figures 4.16, 4.17 and 4.18) fixing and embedding of mouse brains was performed by Leire Balaguer Lluna. For sections 4.2.10, 4.2.11 and 4.2.12 (Figure 4.17, Figure 4.18 and Figure 4.19) embedded mouse brains were sectioned and stained in the University of Oxford Oncology Department's Translational Histopathology Laboratory (THL) (Leticia Campo and Molly Browne).

Impact of COVID-19 pandemic

National lockdowns led to the closure of both the Botnar and Old Road Campus Research Building labs for 4 months from April 2020 – July 2020. During this time no experimental work could be completed. The closure interrupted optimisation of the CRISPR/Cas9 system and follow up of signatures found within the RNA-sequencing data, namely experiments in sections 4.2.5, 4.2.3 (RT-qPCR) and 5.2.1. Following lockdown experiments continued in the Botnar laboratories only, which limited access to reagents and deliveries and meant, for example, that immunoblotting had to be performed by a different protocol (sections 2.1.4 vs 2.1.5). After the return to onsite work, the limited time remaining motivated the refocusing of the project away from exploratory *in vitro* work in Chapter 4, towards finishing Chapter 5. The national lockdown also delayed parallel analysis by Trajecture to the point that findings from this analysis could not be included in subsequent experimental characterisation.

Acknowledgements

Firstly, I must extend my sincerest gratitude to my supervisors Professor Alex Bullock and Dr Gillian Farnie, who gave me the opportunity to complete a DPhil and who guided me through it with passion, wisdom and vast knowledge. I am also deeply grateful to Professor Udo Oppermann and his group for kindly hosting me within his lab and Dr Sally Cowley for her guidance on how to successfully implement CRISPR/Cas9.

During my time in Oxford, I also had the great pleasure of working with the GFSU, the cellular assays group, the Oppermann group and the whole of the SGC/CMD past and present who were as kind as they were smart. In particular, Dr Eleanor Williams, Alice Hunt, Dr Mel Sweeney, Dr Ling Felce, Vicki Gamble, Charlotte Manning, Eva Dalietou, Dr Nadia Halidi, Dr Cassandra Adams, Dr Filiz Senbabaoglu, Shubhashish Mukhopadhyay and most of all, Dr Jong Fu Wong, who helped me every single day, both as a brilliant scientist and a fantastic friend. Thank-you Dr Ling Felce for setting a near perfect example; I'll do my best to remember what I learnt from watching you be brilliant. Thank-you also to Dr Agnese Baronina, Dr Zhuoyao Chen, Dr Laiyin Nie, Adam Evans, Dr Ed Bower and Matthew Croker who were no help scientifically but all great fun to tell terrible jokes to.

I would like to extend my thanks to my collaborators: The Udo Oppermann group, especially Dr Martin Philpott, Dr Adam Cribbs, Graham Wells and Dr Chao Jiang; Dr Ángel Montero Carcaboso and Leire Balaguer Lluna and Hospital Sant Joan de Déu; The members of the THL, Leticia Campo and Molly Browne; To Dr Guy Hill and Trajecture for giving me access to the pipeline. Thank-you each for accommodating my experiments and explaining the finer details with utmost patience. Special thanks to Professor Chris Jones for generously providing the DIPG cell lines, and to Zahid Quyoom Bonday and Ely Lilly for providing the compound LLY-283. I must also acknowledge The Simcox family for generously funding this project and to St. Edmund Hall for hosting me within the university.

Finally, I would love to send my infinite gratitude to my family and friends who have always supported and believed in me. To my Mum – who bought me too many books; to my Dad – who invented puzzles just for me to solve; and my whole family for their smarty pants genes; to the late Bacon Brown for being stinky and soft while he could; to Lisa McMinn – for being the best big sis I never expected to get; to Ioana Grigoras for knowing how to deal with everything I don't; and to the No Mercy GC for being incredibly distracting.

Abbreviations

ACVR1	Activin receptor type-1
AF488	Alexa Fluor 488
ALK2	Activin receptor-like kinase-2
AMP	Amplification
APOE	Apolipoprotein A
BART	Binding Analysis for Regulation of Transcription
BBB	Blood brain barrier
BMP	Bone morphogenetic protein
BRD	Bromodomain
CAR	Chimeric antigen receptor
CCL2	C-C motif chemokine ligand 2
CDK	Cyclin dependent kinase
CDKN2A	Cyclin dependent kinase inhibitor 2A
CED	Convection enhanced delivery
CI	Confidence intervals
ChIP-seq	Chromatin immunoprecipitation sequencing
CNS	Central nervous system
CRISPR	Clustered regularly interspaced short palindromic repeat
CTG	CellTiter-Glo
DE	Differentially expressed
DEHYDR	Dehydrogenase
diH_2O	De-ionised water
DIPG	Diffuse intrinsic pontine glioma
DNMT	DNA methyltransferases
DRD2	Dopamine receptor D2
ECM	Extracellular matrix
EGFP	Enhanced green fluorescent protein
ELDA	Extreme limiting dilution assay
EPHB2	Ephrin type-B receptor 2
EZH2	Enhancer of zeste homolog 2
FDR	False discovery rate
FFPE	Formalin fixed, paraffin embedded
FGFR4	Fibroblast growth factor receptor 4
FN1	Fibronectin 1
FOP	Fibrodysplasia ossificans progressiva
FSC	Forward scatter
FSCN-1	Fascin-1
GDF-15	Growth/differentiation factor 15
GO	Gene ontology
HAT	Histone acetyltransferase
HDAC	Histone deacetylase
HDR	Homology directed repair
HSJD	Hospital Sant Joan de Déu
IDT	Integrated DNA Technologies
IGFBP	Insulin growth factor binding protein
IL	Interleukin
Indel	Insertion/deletion mutation
iPSC	Induced pluripotent stem cell
KCJN10	Potassium inwardly rectifying channel subfamily J member 10
KDM	Lysine demethylase
Kme	Methyl-lysine
l2fc	Log_2(fold change)
LSS	Lanosterol synthase
MATN2	Matrilin 2

MCP-1	Monocyte chemoattractant protein 1
MDK	Midkine
MIS	Missense mutation
MMP2	Matrix metalloprotease 2
MT	Methyltransferase
NCBI	National Centre for Biotechnology Information
NDORMS	Nuffield Department of Orthopaedics, Rheumatology and Musculoskeletal Sciences
NF- κB	Nuclear factor κB
NGFR	Nuclear growth factor receptor
NGS	Next generation sequencing
NSC	Neural stem cell
nt	Nucleotides
NHEJ	Non-homologous end joining
p.adj	Adjusted p value
PAM	Protospacer adjacent motif
PC	Principal component
PCA	Principal component analysis
PDGF-B	Platelet derived growth factor beta
PDGFRA	Platelet derived growth factor receptor alpha
PDX	Patient derived xenograft
PI	Propidium iodide
PI3KCA	Phosphatidylinositol-4,5-bisphosphate 3-binase catalytic subunit alpha
POSTN	Periostin
PRC	Polycomb repressive complex
PRMT	Protein arginine methyltransferase
PTEN	Phosphatase and tensin homolog
PTX3	Pentraxin 3
RNP	Ribonucleoprotein
RT	Radiotherapy
RT-qPCR	Real time quantitative PCR
SAHA	Suberanilohydroxamic acid
SAM	S-adenosyl methionine
SD	Standard deviation
SEM	Standard error of the mean
SGC	Structural Genomics Consortium
sgRNA	Single guide RNA
SHP	Small heterodimer partner
SMAD	Small mothers against decapentaplegic
SMN	Spinal motor neuron
SREBP	Sterol regulatory element binding transcription factor
SSC	Side scatter
ssDNA	Single stranded DNA
Stat3	Signal transducer and activator of transcription 3
TNFR2	Tumour necrosis factor receptor 2
TRUNC	Truncation
TSM-B	Tumoursphere medium (basal)
TSM-C	Tumoursphere medium (complete)
ULA	Ultra-low-attachment
VEGF	Vascular endothelial growth factor
YEATS	Yaf9, ENL, AF9, Taf14, Sas5 domain

Table of contents

List of figures

List of tables

Chapter 1. Introduction

1.1. Clinical outlook of Diffuse Intrinsic Pontine Glioma

Brain tumours are the leading cause of cancer related deaths in children (Cancer Research UK, 2021) (**Figure 1.1**). Of these, diffuse intrinsic pontine glioma (DIPG) has the highest mortality rate so, despite accounting for only 10% of central nervous system (CNS) tumours (20-30 cases per year in the UK), it is the leading cause of death (The Brain Tumour Charity, 2022; Freeman and Farmer, 1998; Jansen *et al.*, 2012; Grasso *et al.*, 2015; Qi *et al.*, 2019). Considering that the median age at diagnosis is 6-7 years and median overall survival is only 9-11 months, this represents tens of thousands of years of life lost annually in the US alone (Cooney *et al.*, 2017; Vitanza and Monje, 2019).

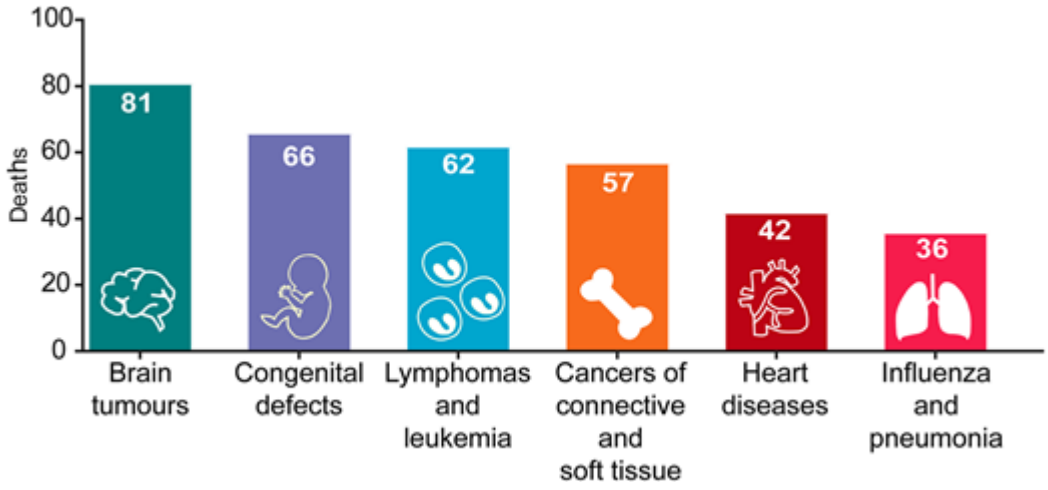

Figure 1.1 - Leading causes of childhood death in England and Wales

Common causes of death among children from ages 4-19 in England and Wales in 2017 [data from the Office for National Statistics]. Figure reproduced from (Wong *et al.*, 2019)

At diagnosis DIPG tumours present as a diffuse tumour infiltrating greater than 50-66% of the pons (Robison and Kieran, 2014), which likely arises from an Olig2+ population of neural stem cells found in the human ventral pons at 6-7 years of age (Monje *et al.* 2011). Compression or dysfunction of the surrounding tissues (such as the cerebellum) leads to presentation typically with a triad of: dysconjugate gaze, pyramidal tract dysfunction (weakness and

hyperreflexia) and impaired gait or speech (Johung and Monje, 2016; Kluiver *et al.*, 2020). Over the progression of the disease cells infiltrate the midbrain, medulla, cerebellum or thalamus (in over 50% of cases) and the frontal cortex in 25% of cases, with occasional metastasis to the spinal cord (Caretti, Bugiani, *et al.*, 2014; Kluiver *et al.*, 2020; Lu, Brown and Daniels, 2020). The sites to which DIPG spreads suggests direct invasion along the subventricular zone or seeding from cerebrospinal fluid (Caretti, Bugiani, *et al.*, 2014; Kluiver *et al.*, 2020). Treatment and study focus mainly on progression within the brainstem, however extrapontine spread is less common in long term survivors (Hoffman *et al.*, 2018), and predicts shorter survival in patients after radiotherapy (RT) (Jansen *et al.*, 2015). The highly aggressive nature of DIPG, reflected in its rapid progression and infiltrative growth, and its delicate anatomical location render it currently untreatable as discussed below.

1.2. Treatment of DIPG

This diffuse growth, along with the vital non-redundant role of the brainstem, mean that surgical resection of DIPG remains impossible (Mentlein, Hattermann and Held-Feindt, 2012; Srikanthan *et al.*, 2021). Steroids are used to stabilise neurological symptoms, but courses are kept short because of toxicity and because they may close the blood brain barrier (Fauquette *et al.*, 2012). Fractionated focal RT remains the current standard of care, as it provides transient symptomatic improvement and increases overall survival by 3 months, although progression remains inevitable (Lassman and Arjona, 1967; Langmoen *et al.*, 1991). Many fractionation strategies have been compared, with the finding that hypo- but not hyper-fractionated RT provides a similar survival benefit with reduced medical burden (Zaghloul *et al.*, 2014; Gallitto *et al.*, 2019) and reirradiation after progression provides a modest survival benefit (Lassaletta *et al.*, 2018; Vitanza and Monje, 2019). Given the infiltration of DIPG beyond the pons, some have suggested additional irradiation outside of the pons could be necessary, especially once control

of local disease can be achieved (Donahue *et al.*, 1998; Gururangan *et al.*, 2006; Caretti, Bugiani, *et al.*, 2014).

Since the introduction of radiotherapy in the late sixties (Lassman and Arjona, 1967) more than 200 clinical trials have failed to generate a clinical improvement (Robison and Kieran, 2014). The development of therapeutic molecules for paediatric brain tumours is incredibly challenging. Any safety data collected from adult patients cannot necessarily be extrapolated to children, meaning phase I clinical trials must be repeated (Conroy *et al.*, 2000). Treatment toxicity in children can also have more severe long-term consequences than in adults because paediatric tissues are still developing (Conroy *et al.*, 2000).

The entry of most compounds and pathogens into the brain is also prevented or slowed by the blood:brain barrier (BBB) – the monolayer of cells separating CNS tissue from the blood or CSF that are joined by stringent tight junctions and express specialised transport proteins (Banks, 2009; Dong, 2018). Most therapeutic compounds for brain diseases fail because they cannot penetrate the brain (Aldape *et al.*, 2019; Sasaki *et al.*, 2020). As the pons regulates vital processes such as breathing and heartrate it has an even more stringent BBB that further reduces compound penetration relative to the rest of the brain (Warren, 2018; Zeiadeh, Najjar and Karaman, 2018). Most medicines cross the BBB by transmembrane diffusion and therefore a low molecular weight, high lipid solubility and low number of hydrogen bond donors (≤1) facilitate the movement of compounds across the BBB (Banks, 2009). Optimisation of these parameters cannot always be achieved alongside on-target efficacy, thus several methods to bypass the BBB are under development. For example, delivery to the brain via the nasal cavity, where the BBB is relatively leaky (Bruinsmann *et al.*, 2019), or convection enhanced delivery (CED), which circumvents the BBB by delivering a compound directly into the brain under positive pressure (Sasaki *et al.*, 2020). BBB bypass can significantly improve the outcome of treatment in animal models where systemic administration was insufficient (Sasaki *et al.*, 2020).

Conventional cytotoxic, myeloablative or radiosensitising agents such as platins, motefaxin-gadolinium, topotecan, high-dose etoposide, thiotepa or carnustine do not prolong survival and can be associated with significant toxicity (Dunkel *et al.*, 1998; Walter *et al.*, 1998; Mandell *et al.*, 1999; Bouffet *et al.*, 2000; Bernier-Chastagner *et al.*, 2005; Bradley *et al.*, 2013). Attempts to treat DIPG based on knowledge about adult tumours have failed: Temozolomide and tamoxifen were both tested because of previous clinical efficacy in adult high grade glioma, but they did not similarly provide benefit in 'equivalent' childhood tumours (Michalski *et al.*, 2010; Cohen *et al.*, 2011); Inhibition of EGFR and VEGFR signalling were tested because in adult glioma amplification of EGFR is frequent and tumours are well vascularised, but neither improved the outcome for DIPG patients (Pollack, Sapkota and Cartee, 2011; Kreisl *et al.*, 2012). Thus, there has been no improvement in overall survival in 30 years (Gallitto *et al.*, 2019) and DIPG represents a disease with great unmet clinical need.

The molecular characterisation of DIPG (discussed in sections 1.3-1.5) has facilitated the design of a new generation of potential therapeutic strategies for DIPG tumours. The frequent alterations in receptor tyrosine kinases (RTKs) motivated pre-clinical testing of the RTK inhibitor dasatinib and the MEK inhibitor trametinib and reduced infiltration of DIPG cells into *ex vivo* brain slices (Izquierdo *et al.*, 2022). The direct targeting of epigenetic changes found in DIPG is discussed in section 1.4, but inhibitors selected to counteract the metabolic changes introduced by H3K27M mutations, such as glutamine antagonists, prolonged the survival of mice xenografted with DIPG cells (Chung *et al.,* 2020). The amplification of the cyclin dependent kinases (CDK)4/6 in DIPG tumours informed the current testing of the CDK4/6 inhibitor ribociclib with a phase I/II clinical trial (ClinicalTrials.gov identifier NCT02607124) (DeWire *et al.*, 2020). The dopamine receptor (DR)D2/3 inhibitor ONC201 is being trialled because of DRD2 overexpression in H3K27M glioma and mediated tumour regression in a subset of patients (Chi *et al.*, 2019; Hall *et al.,* 2019). Administration of chimeric antigen receptor (CAR) T cells directed

against disialoganglioside GD2, which is highly expressed in DIPG cells, produced clinical and radiographic improvement in 3/4 participants (Majzner *et al.,* 2022). These small phase I/II clinical trials highlight the necessity and promise of therapies that are rationally designed based on the molecular character of DIPG.

1.3. Genetics of DIPG

Historically the molecular understanding of DIPG was limited by a paucity of tumour material to study. Given the delicate anatomical location of DIPG, diagnosis was typically based on symptoms and appearance on MRI (Gallitto *et al.*, 2019), with biopsies in only 25-33% of cases at diagnosis (Freeman and Farmer, 1998). For lack of a better option childhood tumours were grouped with their adult counterparts for treatment although, as described above, this was not a successful strategy (Jones *et al.*, 2017). This began to change around the introduction of safe stereotactic biopsy procedures (Roujeau *et al.*, 2007; Gupta *et al.*, 2018).

Strikingly, 80% of DIPG patients have monoallelic p.Lys27Met (K27M) mutations in histones H3.3 (*H3F3A*) or H3.1 (*HIST1H3B/C*) which confer a significantly worse prognosis than H3K27 wild-type paediatric high grade gliomas (Schwartzentruber *et al.*, 2012; Wu *et al.*, 2012; Fontebasso *et al.*, 2014; Mackay *et al.*, 2017). 30-50% of these patients have a further truncating mutation in *ATRX*, a member of the complex which mediates incorporation of H3.3 into chromatin (Khuong-Quang *et al.*, 2012; Schwartzentruber *et al.*, 2012; Wu *et al.*, 2014; Mackay *et al.*, 2017). These K27M mutations uniquely occur in paediatric midline (thalamus, pons or spinal cord) tumours, unlike H3.3 G34R/V or *IDH1* mutations found in adolescent or young adult tumours (respectively) of the cerebral hemispheres (Schwartzentruber *et al.*, 2012; Sturm *et al.*, 2012). The discovery of H3K27M mutations led the World Health Organisation to create the new tumour classification of ‘diffuse midline glioma, H3 K27M-mutant’ which thus encompasses 80% of all DIPG tumours (Louis *et al.*, 2016).

Lineage analysis suggests that these histone mutations are the first step in DIPG's development, but are invariably closely followed by obligate partner mutations in either the *TP53*/cell-cycle pathway, the receptor serine/threonine kinase *ACVR1* or the receptor tyrosine kinase (RTK)-PI3K-AKT signalling pathway (**Figure 1.2**) (Nikbakht *et al.*, 2016). The most common of these alterations are in *TP53* or genes that regulate the cell cycle or DNA damage: A total of 70% of patients have non-overlapping mutations in *TP53* (42%), *PPM1D* (23%), *ATM* or amplification of cyclins D1/2/3 or cyclin dependent kinases (CDK)4/6 (Schwartzentruber *et al.*, 2012; Sturm *et al.*, 2012; Buczkowicz *et al.*, 2014; Taylor *et al.*, 2014). The next most common alterations are *ACVR1* mutations, as discussed below. DIPG patients also frequently have non-overlapping alterations in the receptor tyrosine kinase (RTK)-PI3K-AKT pathway including amplification of receptors (such as *PDGFRA* or *MET*), and mutations, deletions or truncations of downstream proteins (such as *PIK3CA*, *PTEN* or *AKT1*) (Paugh *et al.*, 2011; Wu *et al.*, 2014). The specific part of the pathway which is altered further depends on which histone is mutated or the location of the tumour (Sturm *et al.*, 2012; Buczkowicz *et al.*, 2014; Fontebasso *et al.*, 2014; Mackay *et al.*, 2017). Around a third of patients, without H3K27M mutations, may instead high-level amplification of *MYCN* (due to chromothripsis) or very few mutations but overexpression of the WNT pathway (Buczkowicz *et al.*, 2014; Saratsis *et al.*, 2014).

After histones and *TP53*, the most common mutations are heterozygous missense mutations in the receptor serine/threonine kinase Activin A Receptor Type 1 (ACVR1)[1] found in 20-30% of cases (Buczkowicz *et al.*, 2014; Fontebasso *et al.*, 2014; Taylor *et al.*, 2014; Wu *et al.*, 2014). These are highly specific to DIPG – only present elsewhere in 2% of endometrial tumours and as a germline mutation in 95% of cases of the rare disorder fibrodysplasia ossificans progressiva (FOP) (Kaplan *et al.*, 2009; Zhao and Pritchard, 2016; Valer *et al.*, 2019). Alternatively, a minority of patients have amplification of the downstream *ID2/3* genes or

[1] Also known as activin receptor-like kinase 2 (ALK2)

mutations in the ligand *BMP3* (Mackay *et al.*, 2017). Discussed below in more detail, these missense mutations are limited to codons 328, 258 and 356 in the kinase domain and codon 206 in the GS domain and confer increased activity (**Figure 1.2b**) (Taylor *et al.*, 2014). *ACVR1* mutations (or gain of chromosome 2 which carries *ACVR1*) co-segregate with H3.1, *PIK3CA* or *PIK3R1* and wild-type *TP53* (Fontebasso *et al.*, 2014; Taylor *et al.*, 2014; Wu *et al.*, 2014; Mackay *et al.*, 2017).

Some of these mutations have known clinical implications: NRTK1-NRTK3 fusions are more frequent in patients diagnosed under the age of 12 months that a significantly improved 2 year survival rate (Mackay *et al.*, 2017). Similarly, H3.1/2 and *ACVR1* mutations, which frequently co-occur, are more specific to tumours of the pons than H3.3 mutations and are associated with a younger age of diagnosis and better prognosis (Mackay et al., 2017; Taylor *et al.*, 2014; Wu *et al.*, 2014). Furthermore, *ACVR1* mutation is more common in female DIPG patients suggesting a link between *ACVR1* mutation and a pathological developmental process (Taylor *et al.*, 2014; Wong *et al.*, 2019).

The unique set of genetic alterations found in DIPG patients confirmed the biological differences between adult and childhood, brainstem and cortical tumours that could be inferred from previous failed treatment attempts.

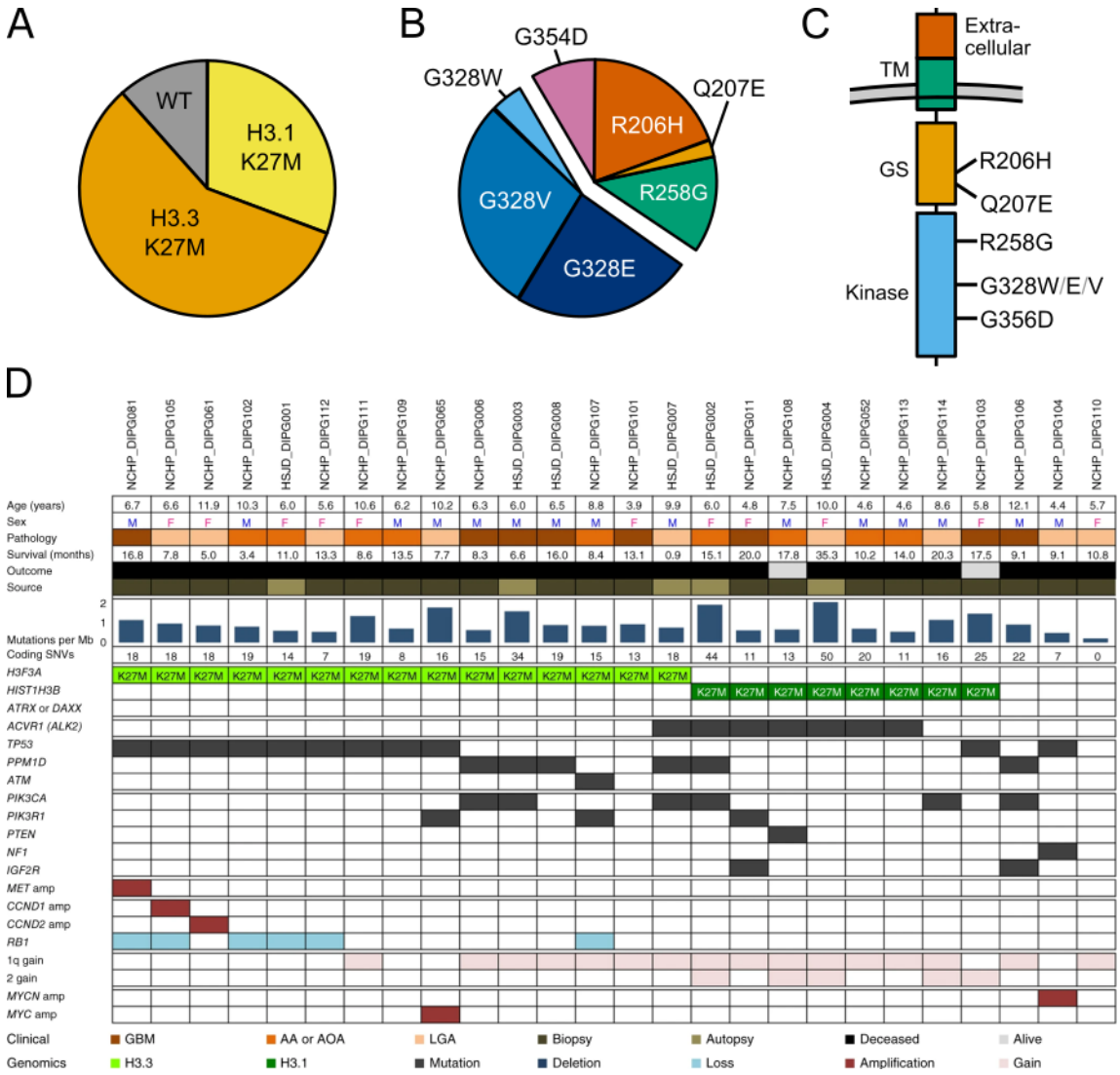

Figure 1.2 - Frequency of mutations in DIPG patients

(A) *Frequency of histone H3F3A (H3.3) or HIST1H3B (H3.1) K27M mutations in DIPG patients.* ***(B)*** *Relative frequency of each recorded ACVR1 mutation in DIPG and* ***(C)*** *their location within the protein. TM = transmembrane domain; GS = glycine-serine rich domain.* ***(D)*** *Reproduced with permission from* (Taylor *et al.*, 2014)*. The spectrum of mutations found in 26 DIPG patients.*

1.4. Altered histone signalling in H3K27M mutant DIPG cells

The ubiquity throughout cases of a single histone mutation highlights the importance of epigenetics in the development of DIPG. In the normal cell, polycomb repressive complex 2 (PRC2) and its catalytic subunit enhancer of zeste homolog 2 (EZH2) maintain developmental heterochromatin and gene silencing by di- or tri-methylating the K27 residue of H3 (H3K27me2/3) (Margueron and Reinberg, 2011). H3K27me3 itself allosterically activates PRC2 activity via the EED subunit, mediating spread of H3K27me3 along the genome (Margueron *et al.*, 2009). PRC1 is then recruited by binding of its CBX subunit to H3K27me3 allowing ubiquitination of histone H2A lysine 119 and further repression of Polycomb targets (Cao *et al.,* 2002). Regulated repression of Polycomb target genes is vital for the correct expression of developmental genes (Cao *et al.,* 2002).

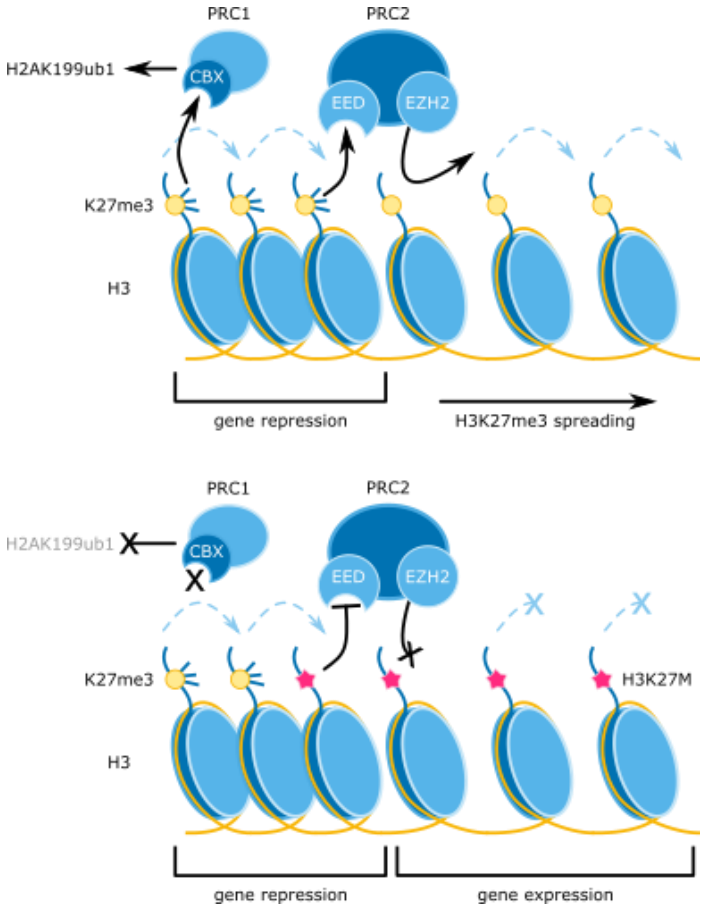

***Figure 1.3 – H3K27M mediated inhibition of H3K27me3 deposition by PRC2 leads to aberrant* gene expression in DIPG**

Within the DIPG cell H3K27M mutations disrupt these processes. K27M histones are competitive inhibitors of EZH2, leading to sequestration of the inactive complex on chromatin or impeding normal H3K27me3 spreading (Chan *et al.*, 2013; Lewis *et al.*, 2013; Justin *et al.*, 2016; Harutyunyan *et al.*, 2019; Jain *et al.*, 2020). Despite representing only 18% (H3.3) or 4% (H3.1) of the total histone pool (Lewis *et al.*, 2013), K27M histones cause global histone H3

hypomethylation and hyperacetylation (Bender *et al.*, 2013; Chan *et al.*, 2013; Piunti *et al.*, 2017). Conversely, the greater number of PRC2 binding sites at strong Polycomb targets leads to retention of H3 hypermethylation (Mohammad *et al.*, 2017). As these strong Polycomb targets include tumour suppressor genes such as *P16INK4a* or *CDK6* H3K27M supports tumorigenesis by promoting proliferation (Mohammad *et al.*, 2017). Consequently the epigenome of H3K27M cells is distinct from that of H3 wild-type neural stem cells (NSCs), H3.3 G34R/V and *IDH1* mutant cells (Schwartzentruber *et al.*, 2012; Sturm *et al.*, 2012) and has been likened to that of foetal developmental states and oligodendrocyte precursor cells (Sturm *et al.*, 2012; Filbin *et al.*, 2018). Any of these changes could introduce unique vulnerabilities to the inhibition of epigenetic regulatory proteins, and thus create an opportunity to develop novel targeted therapies.

With this in mind, many studies have focused on therapeutically altering PRC2 or related epigenetic pathways within DIPG cells. Some suggest that if PRC2/EZH2 activity is already impaired in H3K27M cells, then DIPG cells would be sensitive to further EZH2 inhibition (Mohammad *et al.*, 2017; Zhang *et al.*, 2017). Others instead try inhibition PRC1, hypothesising that with impaired PRC2 activity, DIPG cells would be more dependent on PRC1 activity (Filbin *et al.*, 2018). A number of broader epigenetic interventions with pre-clinical efficacy in a wide range of tumours have been tried in DIPG: Bromodomain inhibition is being explored as a means to inhibit N-Myc (Taylor *et al.*, 2015), and because bromodomain proteins co-localise with H3K27M-K27ac (Zhang *et al.*, 2017). Histone de-acetylase inhibitors are effective in a number of pre-clinical paediatric CNS tumour models, including DIPG (Grasso *et al.*, 2015; Perla *et al.*, 2020) and could work in DIPG by allowing poly-acetylation of the H3 N-terminal tail reversing the inhibition of PRC2 by the K27M mutation (Hennika *et al.*, 2017). However, both bromodomain and HDAC inhibition have failed pre-clinically or clinically due to either poor blood brain barrier

penetration or significant toxicity (Rodgers *et al.*, 2016; Hennika *et al.*, 2017; Mita and Mita, 2020). Thus, the need for novel targets or therapeutics remains.

1.5. Altered BMP signalling in *ACVR1* mutant DIPG cells

ACVR1 is a receptor serine/threonine kinase and a type I member of the bone morphogenetic protein (BMP) receptor family. These *ACVR1* mutations are interesting both because of their uniqueness to DIPG and because of its eminent druggability (Knapp and Sundström, 2014; Ensan *et al.*, 2020). The normal signalling of ACVR1, as illustrated in **Figure 1.4** and reviewed in (Mueller and Nickel, 2012), is as follows: In the inactive state ACVR1 is autoinhibited by its intracellular glycine-serine rich (GS) domain – a state which is further stabilised by binding of FKBP12 to the GS domain (Huse *et al.*, 1999). Upon binding of either BMP-2, -4, -6 or -7, two ACVR1 receptors hetero-tetramerise with two of the constitutively active type II receptors (BMPRII) to facilitate downstream signalling (Agnew *et al.*, 2021). Formation of the hetero-tetramer allows BMPRII to phosphorylate the GS domain of ACVR1, triggering dissociation of FKBP12 and activation of ACVR1 (Wrana *et al.*, 1994; Huse *et al.*, 2001). ACVR1 then phosphorylates the small mothers against decapentaplegic (SMAD)1/5/8 transcription factors, allowing their oligomerisation with SMAD4 and translocation into the nucleus where they activate

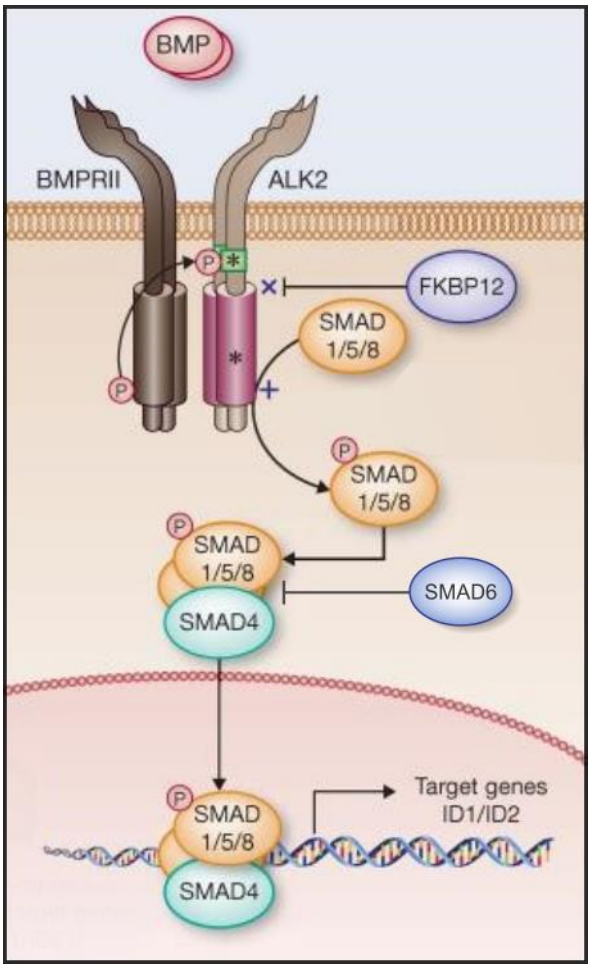

Figure 1.4 - Normal ACVR1/ALK2 signalling

Adapted with permission from (Taylor et al., 2014)

transcription of genes such as *ID1*, *2* or *3* (Hollnagel *et al.*, 1999; Katagiri *et al.*, 2002). Signalling is further regulated by the inhibitory I-SMADs, SMAD6 and SMAD7 (Hata *et al.*, 1998; Miyazawa and Miyazono, 2017).

Although ACVR1 mutations had not previously been reported in cancer, their ubiquity in FOP meant there was already a wealth of information about the molecular impact of the mutations. The reported missense mutations in the kinase and GS domains of ACVR1 destabilise its inactive state and impair binding of FKBP12 (Shen *et al.*, 2009; Song *et al.*, 2010). This increases BMP signalling via ACVR1 by the following mechanisms:

1. A low level of constitutive activation or 'leaky signalling' even in the absence of the ligand binding domain (Billings *et al.*, 2008; Fukuda *et al.*, 2009; Shen *et al.*, 2009; Song *et al.*, 2010; Haupt, Xu and Shore, 2018).
2. Enhanced responsiveness to normal ligands (Billings *et al.*, 2008; Song *et al.*, 2010).
3. 'Neofunction' or aberrant activation by the additional ligand activin A (Hino *et al.*, 2015) which normally activates ALK4/7 or forms a non-signalling complex with wild-type ACVR1 that prevents downstream signalling (Hatsell *et al.*, 2015; Olsen *et al.*, 2015).

Increased BMP signalling thus causes increased expression of downstream *ID1/2/3* and differential expression of immune genes (Fontebasso *et al.*, 2014; Wu *et al.*, 2014), especially when combined with H3 mutations (Buczkowicz *et al.*, 2014). There is building evidence that the specific mutation present differentially alters BMP signalling: G328V mutations cause higher kinase activity and downstream gene expression than R206H/G356D mutations (Haupt, Xu and Shore, 2018; Carvalho *et al.*, 2019; Cao *et al.*, 2020) and G328V mutations are more likely to co-segregate with H3.1 mutations than R206H (Carvalho *et al.*, 2019).

1.6. Pre-clinical models of DIPG

Greater availability of patient derived DIPG material has facilitated pre-clinical study of DIPG with both patient-derived and genetically modified *in vitro* and *in vivo* models:

The development of rapid post mortem protocols (Monje *et al.*, 2011; Caretti *et al.*, 2013) allowed the identification of histone H3K27M and *TP53* mutations (Khuong-Quang *et al.*, 2012; Schwartzentruber *et al.*, 2012). The subsequent introduction of safe stereotactic biopsy (Roujeau *et al.*, 2007) was crucial for identification of *ACVR1* mutations (Buczkowicz *et al.*, 2014; Fontebasso *et al.*, 2014; Taylor *et al.*, 2014; Wu *et al.*, 2014). Serial *in vitro* passage of patient derived cells faithfully recapitulates the mutations found in patient tumours, although it cannot account for the influence of the tumour microenvironment, and must be cultured in appropriate conditions to avoid deviation from the gene expression found in primary tissue (Filbin *et al.*, 2018). They are often the first model used to evaluate novel therapeutic targets (Mueller *et al.*, 2014; Grasso *et al.*, 2015; Truffaux *et al.*, 2015; Carvalho *et al.*, 2019, 2021) and allow study of cell intrinsic signalling characteristic of DIPG (i.e. that of mutant *ACVR1* or H3K27M), especially when genetic editing is used to generate isogenic cell lines (Harutyunyan *et al.*, 2019; Agnew *et al.*, 2021).

Patient derived cells can also be xenografted into immunodeficient mice allowing the influence of the tumour microenvironment to be incorporated into the testing of hypotheses. Early patient derived xenograft (PDX) models of brainstem glioma relied on implantation of adult glioma cells into the mouse brainstem, but as discussed above this model did not faithfully represent DIPG and was unable to predict effective therapeutic strategies (Misuraca, Cordero and Becher, 2015). Implantation of DIPG derived cells produced a more representative model – tumours histopathologically resemble DIPG, infiltrate anatomical structures outside of the pons and have gene expression similar to patient tumours (Monje *et al.*, 2011; Caretti, Sewing, *et al.*, 2014; Filbin *et al.*, 2018). The similarity of these tumours to a set of neural precursor cells found

in the subventricular zone of healthy children suggests that this could be the cell of origin of DIPG tumours (Monje *et al.*, 2011). However, the phenotype of xenografted tumours can vary drastically depending on the processing or passage of DIPG cells prior to implantation (Caretti, Sewing, *et al.*, 2014). This, in addition to a take rate of only 50% and the continuing relative rarity of patient material means most PDX models implant cells otherwise maintained *in vitro.* Such PDX models are frequently used in conjunction with *in vitro* patient derived cells to pre-clinically evaluate novel therapeutic strategies (Monje *et al.*, 2011; Mueller *et al.*, 2014; Grasso *et al.*, 2015; Carvalho *et al.*, 2019, 2021; Katagi *et al.*, 2019; Meel *et al.*, 2020; Sasaki *et al.*, 2020). Occasionally, subcutaneous xenografts are used as a compromise to evaluate a therapeutic target *in vivo* independently of whether a given inhibitor can cross the BBB (Barnett *et al.*, 2021).

Since the molecular characterisation of DIPG, a number of genetically engineered *in vitro* and *in vivo* models have been developed. By their nature, these models tend to provide information about what genetic events are required for tumour initiation. Early genetically engineered mouse models (GEMMs) used the RCAS/t-va gene delivery system to induce *PDGFB* overexpression in the Nestin+ pons cells of neonatal p16/Ink4a-ARF knockout (KO) mice (Becher *et al.*, 2010). This induced 'brainstem glioma' that histologically resembled DIPG but was not limited to the pons (Becher *et al.*, 2010). This model showed that CDK4/6 inhibition could prolong survival, which was later recapitulated with patient derived cells (Barton *et al.*, 2013; Asby *et al.*, 2018). The incorporation of H3K27M or *ACVR1* mutations in Nestin+ cells confirmed that H3K27M or *ACVR1* mutations alone were insufficient for tumour initiation, but that instead p53 KO, PDGF-B amplification and H3K27M or *ACVR1* mutations co-operate to induce brainstem glioma (Nikbakht *et al.*, 2016; Cordero *et al.*, 2017; Hoeman *et al.*, 2019). Similarly, genetic editing of NSCs has shown that H3.3K27M can malignantly transform brainstem but not cortex

NSCs (Bressan *et al.*, 2021). Thus, GEMMs confirm that DIPG initiation depends on multiple genetic alterations in a highly specific cell type.

1.7. Aims of the project

The two primary aims of this project were as follows:

1. To identify and pre-clinically characterise a novel therapeutic target for DIPG
2. To assess the role of *ACVR1* mutations in maintenance of DIPG cells

The primary hypotheses of the project were that:

1. Histone mutations altered the epigenome of DIPG such that therapeutic vulnerabilities were introduced (tested in Chapters 3 and 4)
2. *ACVR1* mutations contribute to DIPG tumour maintenance (tested in Chapter 5)

Given the delayed molecular understanding of DIPG, its aggressive nature and difficult anatomical location, DIPG remains a disease with severe unmet clinical need. Experiments focused on *ACVR1* mutant DIPG cells because, despite being a common and eminently druggable mutation, *ACVR1* remains a relatively under-studied target. The project completed these aims using patient derived cell lines grown *in vitro* as they faithfully reproduce the mutations found in primary tumours and have the most faithful gene expression profile after PDX models (Filbin *et al.*, 2018).

Chapter 3 presents an unbiased screen of inhibitors of epigenetic regulatory proteins, from which a novel target, PRMT5, was identified as necessary for DIPG viability.

Chapter 4 covers characterisation of PRMT5 inhibition *in vitro* and the initial test of the PRMT5 inhibitor LLY-283 in a PDX model of DIPG.

Chapter 5 outlines the correction of the *ACVR1* mutation c.983G>T (p.G328V) to the wild-type sequence in patient derived cells and characterising the subsequent phenotypic changes.

Together the results presented in this thesis characterise PRMT5 as a putative therapeutic target in DIPG worthy of further study. The project also emphasises the value of targeting ACVR1 for therapy and provides isogenic cell lines as an experimental tool for future research.

Chapter 2. Materials and Methods

2.1. Buffers and solutions

2.1.1. DNA lysis buffer

10 mM Tris HCl (pH 8.0), 10 mM EDTA (pH 8.0), 150 mM NaCl, 0.2% SDS made up in diH_2O.

2.1.2. Protein lysis buffer

Triton X-100 (1% v/v), NaCl (150 mM), Tris HCl (pH 7.5, 20 mM), NaF (25 mM), Na β-glycerolphosphate (25 mM), sodium pyrophosphate (4 mM), sodium orthovanadate (2 mM), cOmplete™ EDTA-free protease inhibitor cocktail (Roche, 1 tablet/10 mL) made up to 10 mL with diH_2O.

2.1.3. 6X Laemmli sample buffer

375 mM Tris (pH 6.8), 416 mM SDS (12% w/v), 60% glycerol (v/v), 0.9 mM bromophenol blue (0.6 mg/mL), 300 mM dithiothreitol (DTT).

2.1.4. Transfer buffer

Methanol (20% v/v), Tris base (25 mM), Glycine (200 mM) made up in diH2O.

2.1.5. Acidic stripping buffer

Glycine (200 mM), SDS (35 mM), 1% Tween-20 made up in diH2O.

2.1.6. 5x SDS loading buffer

Reproduced from ('5X SDS-loading buffer', 2006). 300 mM Tris-HCl (pH 8.0), 10% SDS, 20 mM EDTA, 25% -mercaptoethanol, 0.1% bromophenol blue, 50% glycerol.

2.2. Molecular biology and protein methods

2.2.1. DNA purification

Cells were lysed in 200 µL DNA Lysis Buffer supplemented with 8 U/mL proteinase K (P8107, New England Biolabs), and incubated at 55 °C overnight with periodic vortexing. To precipitate protein, 67 µL saturated NaCl was added to the lysate and it was shaken for 15 min, at room temperature. Supernatant was transferred to a fresh tube containing 400 µL ice cold ethanol, mixed by vortexing, then DNA was pelleted by centrifugation (full speed, 10 min, room temperature). The pellet was washed with room temperature 70% ethanol, then DNA was resuspended in nuclease free water.

2.2.2. PCR (Q5) amplification of genomic DNA

25 µL PCR reactions were made up at room temperature according to manufacturer's protocol to include: 10 µM each of the forward and reverse primers (**Table 2.4**), template DNA (concentration varying according to experiment), 12.5 µL Q5® Hot Start High-Fidelity 2X Master Mix (M0494, NEB) and nuclease free water to 25 µL. Reactions were vortexed, then centrifuged briefly to ensure mixing of components. Reactions were amplified in a Veriti thermal cycler (Applied Biosystems) with the following cycle parameters:

Step	**Temperature (°C)**	**Time**	
Melt	98	30 s	
Melt	98	10 s	Repeat for 35 cycles
Anneal	64*	15 s	
Extend	72	30 s	
Run off extension	72	3 min	

* Varied according to primer T_m

The annealing temperature of 64 °C was used for amplification of exon 6 of ACVR1 with primers listed in **Table 2.4**.

2.2.3. Immunoblotting (method 1)

Developed from standard protocols such as (Harlow and Lane, 2006; Litovchick, 2018).

Used for: **Figure 3.1**, methods section 2.4.1. See section 2.1 for buffer recipes.

Protein was lysed using protein lysis buffer for 20 min at 4 °C. Protein concentration was measured with the DC Protein Assay (5000111, Bio-Rad) and protein concentration normalised by dilution into 6X Laemmli buffer. Protein was loaded into a NuPAGE 4-12% Bis-Tris Midi gel (WG1403BOX, Novex), alongside the Precision Plus Dual Stained Protein Ladder (1610374, Bio-Rad) and resolved at 120 V for 60-90 min. Protein was transferred to 0.2 µm PVDF (Roche), in Transfer buffer for 60 min at 100 V (max amperes) for 60 min. Membrane was blocked for 60 min in primary blocking buffer (below), then incubated with primary antibody diluted in PBS (with 3% BSA, 0.1% Na azide, 0.1% Tween-20) to the concentrations listed in **Table 2.1** (below). Membranes were washed 3 × 5 min in PBS-T, then incubated in secondary antibodies (**Table 2.2**) diluted in PBS (with 3% skimmed milk powder, 0.1% Tween-20). Blots were washed again, incubated in Pierce™ ECL Western Blotting substrate (32209, Thermo Fisher Scientific, UK) for 1 min, then imaged with ImageQuant™ Las-4000 (GE Healthcare, UK).

Blots were then stripped with Acidic Stripping Buffer (2.1.5) for 1 h at room temperature, washed in de-ionised water (diH_2O) until foaming ceased, then in PBS-T, and the process was repeated from the blocking step for the second primary antibody.

2.2.4. Immunoblotting (method 2)

Used for: Figure 3.12, results section 3.2.6, methods section 2.4.4; Figure 4.11, results section 4.2.6, methods section 2.5.5; Figure 5.10, results section 5.2.8, methods section 2.6.7. See section 2.1 for buffer recipes.

Cellular protein was harvested in RIPA buffer, with cOmplete protease inhibitor cocktail (Roche, 11697498001), DNA digested with 0.5 U/µL benzonase (E1014, Sigma) 20 min 4 °C.

Protein was clarified by centrifugation (17 kg, 3 min), protein concentration measured by DC protein assay (5000111, Bio-Rad), and normalised by dilution into Protein Loading Buffer (LICOR, 928-40004, LICOR) supplemented with 10% beta-mercaptoethanol. Protein was denatured by boiling at 95 °C for 5 min. Protein was loaded into a NuPAGE 4-12% Bis-Tris Midi gel (WG1403BOX, Novex), alongside the Precision Plus Dual Stained Protein Ladder (1610374, Bio-Rad) and resolved at 120 V for 60-90 min. Protein was transferred to 0.2 µm PVDF (Roche), in Tris-Glycine Transfer Buffer (LC3675, Novex) with 10% methanol, for 1 h at 100 V. Membrane was blocked for 60 min in TBS (with 5% bovine serum albumin, 0.1% Tween-20), then incubated with primary antibody diluted in TBS (with 5% BSA, 0.1% Tween-20) to the concentrations listed in **Table 2.1** (below). Membranes were washed 3x 5 min in TBS-T, then incubated in secondary antibodies (**Table 2.2**) diluted in PBS (with 3% skimmed milk powder, 0.1% Tween-20). Blots were washed again, incubated in Pierce™ ECL Western Blotting substrate (32209, Thermo Fisher Scientific) for 1 min, then imaged digitally with an Alliance 4.7 (UVITEC) and quantified in ImageStudio Lite® (v5.2).

Blots were then stripped with Restore Plus Western Blot Stripping Buffer (46430, Life Technologies) for 1 h at room temperature, washed in diH_2O until foaming ceased, then 3 × 5 min in PBS-T, and the protocol was repeated from the blocking step for the second primary antibody.

Table 2.1 - Primary antibodies used for immunoblotting

Target	Company, catalogue number	Dilution	Figure reference
pSMAD1/5/9	CST, 13820	1:1000	3.1
pSMAD1/5	CST, 9516	1:1000	3.1, 5.10
SMAD1	CST, 9743	1:1000	3.1, 5.10
Tubulin	Sigma, T5201	1:2000	3.1
GAPDH	CST, 97160	1:2000	3.12, 4.11, 5.10
SDMA	CST, 13222	1:1000	3.12
S_m B/B'/N	Santa Cruz, sc-130670	1:200	3.12
H3K27me3	Abcam, ab6002	1:500	4.10
Histone H3	CST, 4499	1:3000	4.10

Table 2.2 - Secondary antibodies used for immunoblotting

Target	Company, catalogue number	Dilution	Figure reference
Anti-rabbit	Sigma, A6667	1:2000	3.1
Anti-mouse	Genetex, GTX213111-01	1:2000	3.1
Anti-rabbit	Dako, P0448	1:5000	3.12, 4.11, 5.10
Anti-mouse	Dako, P0260	1:5000	3.12, 4.11, 5.10

2.2.5. Software and equipment

Transcriptomic (section 2.5.2) and limiting dilution analysis (section 2.3.5) was performed with R (v4.1.1) in RStudio (2021.09.0 build 351).

Graphs were generated either with GraphPad Prism (v9.1.2) or within RStudio with pheatmap (v1.0.12) or ggplot2 (v3.3.5).

Where indicated immunoblots were quantified using ImageStudio Lite (v5.2).

2.3. Cell culture maintenance and assays

2.3.1. Patient derived cell lines

Patient derived DIPG cell lines were kindly provided by Chris Jones (ICR, London). They were isolated from biopsy or autopsy tissue from patients. The 'HSJD' series were derived from the Hospital Sant Joan de Deu, as previously described (Taylor *et al.*, 2014), and the 'SU' series were derived from Stanford University, as previously described (Monje *et al.*, 2011; Caretti, Sewing, *et al.*, 2014; Lin and Monje, 2017). Mutations were identified by Angel Montero-Carcaboso, Chris Jones or as previously published (Taylor *et al.*, 2014; Mackay *et al.*, 2017).

Table 2.3 - Summary of cell lines used

MIS = missense mutation; TRUNC = truncation; AMP = amplification

Cell line	Diagnosis	Source	Histone status	ACVR1 status	PDGFR status	p53 status	Other mutations
HSJD-DIPG-007	DIPG	Autopsy	H3F3A K27M	R206H	WT	WT	PI3KCA MIS[2]
SU-DIPG-XXI [3]	DIPG	Autopsy	HIST1H3B K27M	G328W	-	-	-
SU-DIPG-IV	DIPG	Autopsy	HIST1H3B K27M	G328V	WT	MIS	MDM4 AMP[4]
HSJD-DIPG-011	DIPG	Biopsy	H3F3A K27M	WT	WT	WT	-
HSJD-GBM-002	Left frontal GBM	Biopsy	H3F3A G34R	WT	MIS	TRUNC	-
SU-DIPG-VI	DIPG	Autopsy	H3F3A K27M	WT	WT	MIS	-

2.3.2. Confirmation of *ACVR1* mutational status

Genomic DNA was isolated and purified from $5x10^6$ cells of each cell line using a QIAamp DNA mini kit (Qiagen) according to manufacturer's protocol.

Amplification primers (**Table 2.4**) were designed to be complementary to the genomic regions 50-200 bp from the end of exons 4, 5, 6 and 7 of ACVR1 (ENSEMBL ID ENSG00000115170), in which DIPG associated mutations are found (Han, Jain and Resnick, 2018), using the National Centre for Biotechnology (NCBI) Primer design tool using the default settings (accessible at: https://www.ncbi.nlm.nih.gov/tools/primer-blast/).

DNA was purified using a QIAquick PCR Purification kit (28104, Qiagen), diluted to 10 ng/µL and sent to SourceBioscience (Oxford) for Sanger sequencing alongside the forward primers listed in **Table 2.4**. All ACVR1 mutations were present (or absent) as expected (**Table 2.3**), and no other variations from the deposited sequence were found.

[2] (Mackay *et al.*, 2017)
[3] Full exon sequencing not performed
[4] (Qin *et al.*, 2017)

Table 2.4 - Table of primers used to amplify mutant exons of ACVR1

Primer	Sequence
ACVR1_exon4_f001	GCTGCCCTTCATGTGAGTTA
ACVR1_exon4_r001	GCAGATTTTCCAAGTTCCATCT
ACVR1_exon5_f001	CTCCAGTAAGCAATGGAGGG
ACVR1_exon5_r001	CACTCTCGAATTCACATTCACC
ACVR1_exon6_f001	CTCCTCTTAGGGCAATTGGT
ACVR1_exon6_r001	GAGATGCAACTCACCTAACC
ACVR1_exon7_f001	TGTATTGCAACAGTGACCCT
ACVR1_exon7_r001	TTCAATAGTCCCTTCAGCCC

Reaction components:

Component	Final concentration
Herculase II reaction buffer (5x)	1x
dNTP mix	250 µM
Genomic DNA	30 ng/µL
Primer pair	10 µM each primer
Herculase II fusion DNA polymerase	0.5 µL
RNase free H_2O	To 50 µL

Reaction conditions:

Step	Temperature (°C)	Time	
Melt	95	3 min	
Melt	95	15 s	Repeat for 35 cycles
Anneal	55	15 s	
Extend	72	30 s	
Run off extension	72	3 min	

2.3.3. Cell line maintenance

DIPG cells were maintained as neurospheres in standard tissue culture flasks in the previously described medium (referred to as TSM-C, **Table 2.5**) (Monje *et al.*, 2011; Mohammad *et al.*, 2017). The complete medium (TSM-C) was discarded if not used within 3 days. A basal medium (TSM-B) was used during short experimental steps.

Table 2.5 - Components of basal Tumour Stem Medium (TSM-B)

Component	Quantity	Source
Neurobasal-A medium	50% (v/v)	Gibco, 10888022
Dulbecco's Modified Eagle Medium/F-12	50% (v/v)	Gibco, 11320074
To which is added:		
HEPES	1 M	Gibco, 15630056
Sodium pyruvate	100 mM	Gibco, 11360039
MEM non-essential amino acids	10 mM	Gibco, 11140035
GlutaMAX-I	2 mM	Gibco, 35050038
Antibiotic-antimycotic	1:100 (v/v)	Gibco, 15240062
Components added to make complete Tumour Stem Medium (TSM-C):		
B-27 Supplement Minus Vitamin A (50X)	1:50 (v/v)	Thermofisher, 12587010
Recombinant human EGF	20 ng/mL	Peprotech, AF-100-15
Recombinant human FGF-basic	20 ng/mL	Peprotech, AF-100-18B
H-PDGF-AA	10 ng/mL	Peprotech, 100-13A
H-PDGF-BB	10 ng/mL	Peprotech, 100-14B
Heparin solution	2 µg/mL	Sigma, H3149-10KU

Spheres were dissociated for maintenance passage or experimental seeding by suspension in TrypLE™ Select (Gibco, 12563-029) for 5 min, followed by manual pipetting. Trypsin was quenched with TSM-B, the suspension passed through a 40 µm filter, trypsin removed by pelleting cells (400 g, 4 min) and cells re-suspended in TSM-C. Cells were passaged a maximum of 20 times before a fresh set of cells was thawed from storage in liquid nitrogen.

2.3.4. Cryopreservation

Cells were dissociated and counted as previously described (section 2.3.3) then 500,000-2,000,000 cells were resuspended in Synth-a-Freeze (A1254201, Gibco, US) and stored in standard cryovials. Cryovials were immediately transferred to a Mr. Frosty™ (Thermo Scientific, US) filled with ice cold isopropanol, and then into a -80 °C freezer. Once frozen, cryovials were transferred to liquid nitrogen for long term storage.

2.3.5. Limiting dilution assay

5,000 (vehicle) or 27,500 (+ LLY-283) HSJD-DIPG-007 cells were seeded as loose spheres in 6 well plates. The following day a vehicle control or the LLY-283 GI_{70} were added in 200 µL (1:10

dilution). After a 7-day treatment period cells were dissociated as described in section 2.3.3. To ensure a single cell suspension, cells were passed through a 0.2 µm strainer. Live cells were counted in a haemocytometer with the addition of 10% trypan blue. Cells were diluted and seeded at a density of 9 cells per well in 6 technical replicates, then serially diluted by 1.5x across the plate, into seeding densities of 6, 4, 2.7, 1.8, 1.2, 0.79, 0.53, 0.35 and 0.23 cells per well, each with 6 technical repeats. After 7 days of growth, clones were visualised by addition of Calcein AM (C1359, Sigma-Aldrich, USA) to a final concentration of 2 µM (diluted in PBS), incubated for 30 min at 37°C, then imaged with the Nexcelom Celigo image cytometer. Clones were called using Nexcelom analysis software with the 'Colony 1' algorithm, and the minimum colony size limited to 2,000 μm^2.

The fraction of wells which had clones at each concentration for each cell line in each independent repeat were input to the 'elda' function (R, statmod package, v1.4.36) and a Poisson distribution describing the proportion of clonogenic cells (with 95% CI) in each independent repeat was estimated. Mean clonogenic cell fractions were compared between groups by unpaired t-test.

For Chapter 5 (section 5.2.11), the limiting dilution assay was performed with SU-DIPG-IV, EGFP control E2E2 and WT ACVR1 1G6 cells as described above with the following changes: Clones were visualised after 5 days, because the spreading of this adherent cell line made smaller clones easier to detect. The minimum colony size was limited to 25,000 μm^2, again because of the difference in morphology from HSJD-DIPG-007. For each cell line, the fraction of wells with clones at each seeding concentration was combined and one Poisson distribution calculated per cell line. The statistical significance of the difference between cell lines was inferred from 95% CIs generated by the 'elda' function.

2.4. Epigenetic probe screen

2.4.1. Comparison of growth substrates

Plates were coated with indicated proteins (**Table 2.6**) for 2 h at 37 °C, rinsed in PBS, and stored in PBS at 4 °C. 2.5% (v/v) Matrigel (354234, Corning) was added to the medium just after cells were seeded.

Table 2.6 - Tested DIPG growth substrates

Coating	Source	Concentration
Laminin	Sigma, L2020	1:100 in diH_2O
Poly-L-ornithine	Sigma, P4957	Undiluted
Poly-L-lysine	Sigma, P4707	Undiluted

Cells were cultured for 24 h, before 150 ng/mL of BMP6 or Activin A was added. After 1h intracellular signalling was quenched with ice cold PBS and cells were lysed in Protein Lysis Buffer for 15 min.

Cell debris was pelleted via centrifugation (18,000 g, 3 min) and protein concentration determined by BCA assay. Protein solutions were diluted to equal concentration in 5X SDS Loading Buffer and Protein Lysis Buffer and boiled for 10 min (95 °C). Proteins were processed for immunoblot according to the protocol outlined in section 2.2.3. The antibodies and buffers used are listed in **Table 2.1**.

2.4.2. Epigenetic probe screen

Compounds (**Table 2.15, Table 2.16**) were diluted to 10 mM in DMSO (D5879, Sigma-Aldrich) and stored at -80 °C in aliquot plates to avoid excessive freeze-thaw cycles. Cells were seeded at the densities described below (**Table 2.7**) and compounds added to a final concentration of 1 µM (0.01% DMSO vehicle control). Cells were irradiated by James Thompson (Oxford Institute for Radiation Oncology), University of Oxford) with 4 Gy from a ^{137}Cs source on the third day of culture.

End point measures were taken as follows:

The CellTiter-Glo (CTG) assay produces light in proportion to the amount of ATP in the cell lysate, which quantifies viability, because live cells maintain a stable concentration of ATP. The CTG assay was performed according to manufacturer's instructions, briefly: half of the culture medium was removed and replaced with room temperature CTG reagent. After a 30 min incubation at room temperature, luminescence was recorded directly (96-well assay), or lysate was transferred to a white 384-well plate before luminescence was recorded (384-well assay) using a ClarioSTAR plate reader (BMG Labtech Ltd.).

Table 2.7 - Seeding densities for epigenetic probe screen

Cell line	2D/adherent, 96-well assay seeding density (cells/well)	3D/spheroid, 384-well assay seeding density (cells/well)	3D/spheroid, 384-well, GI(50) assay seeding density (cells/well)
HSJD-DIPG-007	1500	40	40
HSJD-DIPG-011	6000	200	2000
HSJD-GBM-02	-	-	2000
SU-DIPG-IV	-	-	175[5]
SU-DIPG-VI	-	-	2000
SU-DIPG-XXI	-	-	2000

For figures in Chapter 3, luminescence values were normalised to the vehicle control on the same plate, to account for expected variation between independent additions of the CTG assay and aid data visualisation. Graphs were generated in GraphPad Prism and the significance of changes in viability determined by multiple t-tests, using a Two-stage linear step-up procedure, with Q = 1% (Benjamini, Krieger and Yekutieli, 2006).

2.4.3. GI_{50} curve generation

Four technical repeats were seeded at the indicated densities (**Table 2.7**) in 50% final medium volume. The following day, compounds were diluted in TSM-C and added 1:1 with the

[5] This cell line could not grow as spheroids and was instead grown as a monolayer in black walled, flat bottomed 384-well plates. For the CellTiter-Glo assay the lysate was not transferred to a white plate.

existing medium to the concentrations indicated. Vehicle controls were 0.1% (v/v) DMSO in TSM-C, which is the concentration of DMSO in each treated well.

After 7 days of culture in the presence of the compound the CTG assay was performed as previously described. GI_{50} values were interpolated from sigmoidal curves generated in GraphPad Prism using the four-parameter '[Inhibitor] vs. response' which fits the data to the equation:

$$Y = Y_{min} + \frac{(Y_{max} - Y_{min})}{(1 + \left(\frac{IC_{50}}{X}\right)^{HillSlope})}$$

This does not assume a Hill Slope of -1 and instead fits the slope from the data. Y_{min} and IC_{50} were constrained to > 0. Where described in the figure legend, Y_{max} was constrained to 1.

2.4.4. Validation of demethylation *in vitro*

HSJD-DIPG-007 cells were seeded as outlined below (**Table 2.8**) in 3.6 mL TSM-C in 6 cm^2 plates. The following day (day 0) cells were treated with the GI_{40} or GI_{70} of LLY-283 or a 0.245% DMSO vehicle control in 400 µL TSM-C. At the indicated time point cellular protein was harvested and 10 µg used for immunoblotting as outlined in 2.2.4. For each repeat a single blot was probed for SDMA, S_m B/B'/N and GAPDH (in that order, antibody details in **Table 2.1**). Bands were quantified using ImageStudio Lite (v5.2) and their intensity normalised to the vehicle control at each time point. Values from three independent repeats were averaged.

Table 2.8 - Seeding densities for validation of in vitro demethylation

Time point (days)	Cells seeded (vehicle)	Cells seeded (GI_{40})	Cells seeded (GI_{70})
0	225,000	225,000	225,000
3	90,000	155,000	335,000
5	22,500	45,000	90,000
7	11,000	22,500	45,000

2.4.5. Assay of cell death *in vitro*

175 SU-DIPG-IV cells were seeded per well in 4 technical replicates in flat-bottomed 384 well plates. The following day serial dilutions of LLY-283, GSK591, M4K2009 or M4K2163 and 10 µg/mL PI (final concentration 1 µg/mL) were added in 0.1 volumes of TSM-C. After 7 days of growth with compounds, fluorescence intensity due to PI staining of dead cells was recorded with a ClarioSTAR plate reader (2 mm spiral scan). PI intensity was normalised to the vehicle control for each compound before graphing in GraphPad Prism. Points are the mean of three independent repeats, bars are SD.

2.5. RNA-sequencing and *in vitro* assays

2.5.1. Cell culture set up for RNA-sequencing following PRMT5 inhibition

HSJD-DIPG-007 cells were seeded into 2 mL TSM-C in 6 well plates (densities summarised in **Table 2.9**) in technical triplicate. The seeding densities were optimised to avoid overgrowth in untreated samples or longer time points. Seeding densities and number of replicates are summarised below (**Table 2.9**). Growth medium for day 7 and day 10 samples was replaced with fresh medium (again supplemented with the LLY-283 GI_{40}) after 5 days. After the relevant treatment period total cellular RNA was harvested and purified with the RNeasy Micro kit, with an on-column DNase digest (74004 and 79254, Qiagen) according to manufacturer instructions.

Table 2.9 - Seeding densities for RNA-sequencing of HSJD-DIPG-007 cells

Time point (days)	Cells seeded (vehicle)	Cells seeded (treated)	Repeats sequenced
0	90,000	90,000	3
1	72,000	72,000	1
2	72,000	72,000	1
3	36,000	72,000	1
5	9,000	18,000	3
7	4,500	9,000	2
10	2,250	4,500	1

RNA concentration was measured by UV spectroscopy with a NP80 NanoPhotometer (Implen) and normalised to 2 ng/µL in 105 µL RNase free water. All samples had an RNA integrity number (RIN) of > 9.9 as measured by electrophoresis in a Tapestation 4150 (Agilent).

RNA samples were passed to the NDORMS Next Generation Sequencing Facility (Martin Philpott, Adam Cribbs, Chao Jiang) for RNA library preparation with the NEBNext Ultra II direction RNA prep kit (E7760, NEB) as follows:

Poly adenylated RNA was enriched using the NEBNext polyA mRNA magnetic isolation module (E7490, NEB). Fragmentation of poly(A) enriched RNA was performed at 94 °C for 15 min in a thermal cycler. First and second strand synthesis were carried out to generate cDNA which was then purified by addition of 1.8 volumes of solid-phase reversible (SPRI) beads, 5 min incubation at room temperature, 2 washes in 80% (v/v) ethanol, followed by air-drying for 5-10 min. cDNA was eluted in 50 µL 0.1X TE buffer. The NEBNext adaptor was diluted 1:30 in nuclease-free water, adaptor ligation performed, and the product purified again with SPRI beads. The PCR step was performed with a reduced number of cycles (13) to minimise PCR duplicates. The sequencing library was again purified with SPRI beads, and its concentration and quality assessed with a high sensitivity D1000 ScreenTape and TapeStation 4150 (Agilent) according to manufacturer's protocol. Sequencing libraries were pooled at equimolar concentration, purified with SPRI beads and final concentration again measured with the TapeStation 4150.

The pooled library was paired-end sequenced (150 bp reads) on a NextSeq 500 (Illumina, USA) according to manufacturer's instructions. Raw sequence information was collected as FASTQ files and trimmed reads were pseudoaligned to the human genome (hg38) with kallisto (Bray *et al.*, 2016). Read counts tables were returned for transcriptomic analysis.

2.5.2. Transcriptomic analysis

The script for the analysis outlined here was deposited in GitHub at https://github.com/ej-brown/Thesis_RNAseq

Read counts tables were read into RStudio (v1.3.1093). Two DESeq2 (v1.32.0) datasets were generated: one in which day 5 samples were annotated with only the treatment group ('day 5 only') and one where all samples were annotated with time and treatment ('time course'). Genes with < 10 total reads across all samples were excluded from both datasets.

Samples distances for plotting of principal components were calculated from a variance stabilising transformed (VST) dataset with the stats package (v.4.1.1). PC analysis revealed day 10 samples did not separate by treatment so day 10 samples were excluded from subsequent analysis.

Differential transcript expression was assessed using DESeq2 with a Benjamini-Hochberg adjusted *p* (p.adj) value < 0.05 (Benjamini and Hochberg, 1995). For the 'day 5 only' dataset a Wald test was used for hypothesis testing, whereas for the 'time course' dataset a likelihood ratio test (LRT) was used for hypothesis testing. Log fold change is expressed as LLY-283 treated (numerator) versus vehicle treated (denominator) samples.

Gene lists for gene ontology (GO) enrichment analysis were generated with or without filtering according to p.adj and l2fc as indicated in section 4.2.3. GO enrichment was calculated using the enrichGO function from the clusterProfiler package (v4.0.5) (Wu *et al.*, 2021), using the org.Hs.eg.db genome annotation package (v3.13.0), limited to "biological process" annotations, with p and q value cutoffs as described in section 4.2.3. Lists of enriched gene ontology terms were shortened by combining similar terms using the simplify function with a cut-off value of 0.7.

To predict factors regulating the DE genes identified (day 5 only), a list of gene symbols was input to the Binding Analysis for Regulation of Transcription (BART) webtool (accessed from http://bartweb.org/).

Read counts tables were passed to Trajecture who returned a list of markers, and visualisation such as that shown in **Figure 4.9a-b**. Trajecture markers were visualised using the ConsensusPathDB-human induced network model webtool (accessed from http://cpdb.molgen.mpg.de/) using default settings with the following changes: low-confidence protein-protein interactions were excluded, a cut-off for intermediate ('inferred') nodes at z-score = 40.

2.5.3. RT-qPCR validation

HSJD-DIPG-007 cells were seeded and treated with a vehicle control, LLY-283 GI_{40} or GI(70) as described in section 2.4.4. After 0, 3, 5 or 7 days total cellular RNA was harvested with the RNeasy Mini Kit (74104, Qiagen, Germany). RNA concentration was measured with a NP80 NanoPhotometer (Implen). cDNA was synthesised from 250 ng RNA by reverse transcription using a SuperScript™ IV First-Strand Synthesis System (18091050, Invitrogen). RT-qPCR reactions consisted of the following: 200 nM each of the forward and reverse primers (listed in **Table 2.10**), 2 ng cDNA, 5 µL KAPA SYBR® FAST qPCR Master Mix (KK4617, KAPA Biosystems, USA) all made up to 10 µL in nuclease free water. Four technical repeats of each sample were included. RT-qPCR was performed in a Viia7 Real-Time PCR System (Roche, Switzerland) with the following cycle parameters:

Step	**Temperature (°C)**	**Time**	
Enzyme activation	95	3 min	
Denaturation	95	2 s	Repeat for 40 cycles
Annealing/extension/ data acquisition	60	20 s	
Followed by melt curve generation			

Primers (**Table 2.10**) are from one of two sources:

1. Where available, primer pairs generating amplicons of 80-120 bp were selected from the Harvard PrimerBank (Spandidos *et al.*, 2010).
2. Designed using the NCBI Primer-BLAST tool (Ye *et al.*, 2012) to generate an amplicon of 80-125 bp that, where possible, spans an exon-exon junction.

Table 2.10 - Sequences of qPCR primers

Purchased from Eurofins as unmodified DNA oligos (HPSF purification)

Target	Forward sequence	Reverse sequence	Source
TBP	GAGCTGTGATGTGAAGTTTCC	TCTGGGTTTGATCATTCTGTAG	Primer-BLAST
ACAT2	CCCAGCCAATGCTTCAGGAAT	AAGCCCACGTTTATCAGCTTC	PrimerBank
HMGSC1	CTCTTGGGATGGACGGTATGC	GCTCCAACTCCACCTGTAGG	PrimerBank
ABCG1	ATTCAGGGACCTTTCCTATTCGG	CTCACCACTATTGAACTTCCCG	PrimerBank
DLL1	GACGAACACTACTACGGAGAGG	AGCCAGGGTTGCACACTTT	PrimerBank
TNFRSF1B	CACATGCCGGCTCAGAGAAT	CTCACAGGAGTCACACACGG	Primer-BLAST
MDK	AATGCTCAGTGCCAGGAGAC	GGCTTGGCGTCTAGTCCTTT	Primer-BLAST
MATN2	GTGTCAACACCCATGACTATGC	CATCAGGACCAATGTCCAAGAA	PrimerBank
APOE	GGACGTCCTTCCCCAGGA	CTGTCTCCACCGCTTGCTC	PrimerBank
NGFR	CCTACGGCTACTACCAGGATG	CACACGGTGTTCTGCTTGT	PrimerBank
EPHB2	GTGTGCAACGTGTTTGAGTCA	ACGCACCGAAAACTTCATCTC	PrimerBank

Transcript expression was normalized to the loading control (TBP) by the delta cycle threshold method (dCt), then to the time = 0 of each independent repeat (as ddCt). Changes in expression were visualised with GraphPad Prism, and groups were statistically compared by two-way ANOVA, with Dunnett's multiple comparison test between the vehicle and either the LLY-283 GI_{40} or GI_{70} treatments.

2.5.4. Cholesterol rescue

175 SU-DIPG-IV cells were seeded per well of flat bottomed, black walled 384 well plate. The following day Ro 48-8071 (Cayman Chemical) was added to a final concentration of 56.2 nM (that is, the GI_{80} value calculated by (Phillips *et al.*, 2019)) versus a DMSO vehicle control and/or 0.1, 1 or 10 µM water-soluble cholesterol-methyl-β-cyclodextrin (Sigma-Aldrich, C4951) versus a 0.2% water (v/v) control. At the indicated time points growth medium was removed and replaced with the CTG viability assay.

40 HSJD-DIPG-007 cells were seeded per well of a U-bottomed 384 well ultra-low-attachment (ULA) plates (Nexcelom, USA). The following day compounds were added as follows: The LLY-283 GI_{40}, GI_{70} or DMSO vehicle control were added in 20 µL (1:4 dilution). Concurrently, 40 µM cholesterol or a 0.2% water control were added in 20 µL (1:4 dilution to a final concentration of 10 µM cholesterol). After 0, 3, 5 and 7 days the CTG assay reagent was added and incubated according to manufacturer's instructions. Cell lysate was then transferred to a white 384 well plate to measure luminescence.

In both experiments luminescence was measured using a ClarioSTAR (BMG Labtech, UK) then normalised to that of the vehicle only control spheres from day 0 (LLY-283 experiment) or day 3 (Ro 48-8071 experiment).

2.5.5. H3K27me3 immunoblot

15 µg of protein generated as outlined in section 2.4.4 was processed as described in section 2.2.4 using the antibodies listed in **Table 2.1** and **Table 2.2**. Blots of two independent repeats were run, of which one is shown in **Figure 4.11**. Membranes were probed, stripped and re-probed in the following order: H3K27me3, total H3, GAPDH.

2.5.6. Invasion assay (HSJD-DIPG-007 cells with LLY-283 treatment)

This assay was developed based on that previously published by (Vinci, Box and Eccles, 2015), but optimisation was performed for this system:

In the first optimisation experiment, 40 or 200 HSJD-DIPG-007 cells were seeded into a U-bottomed ULA 384-well plate in technical triplicate. After 3 days to allow spheroid formation, Matrigel was added to a final concentration of 50% (v/v). The Matrigel was supplemented with K00991 to final concentrations of 10, 5, 1, 0.5, 0.1, 0.05 or 0.01 µM, or with a DMSO vehicle control and PI to a final concentration of 1 µg/mL to mark cell death. Invasion was imaged by brightfield at 4 h, 19 h and then daily for 4 days with the Celigo. Propidium iodide was also

imaged with the red channel (excitation 531-40 nm, emission 629-53 nm), but the Matrigel caused a high background of fluorescence, therefore PI was excluded from future experiments. The invading HSJD-DIPG-007 cells were called with the 'Tumorsphere Migration' algorithm. From this analysis confluence (% of field of view) values were used for the time course in **Figure 4.12b** and the area calculated (μm^2) for **Figure 4.12c**.

As for the previous experiment, 200 cells were then seeded into a U-bottomed ULA 384-well plate and 3 days later the indicated % of Matrigel was added. M4K1139 was either diluted and added with the Matrigel (50 and 37.5%) or added in an additional 10 µL TSM-C. Spheroids were imaged and called as previously. 'Area of invasion' was calculated as: area after 3 days in Matrigel (μm^2) – area of the same sphere immediately before Matrigel addition (μm^2).

As 3-7 days are required to see a phenotypic response to LLY-283, a pilot experiment was performed to adapt the assay to allow a treatment window of a total of 6 days. Thus, 190,000 (vehicle), 285,000 (GI_{50}) or 410,000 (GI_{70}) HSJD-DIPG-007 cells were seeded as loose spheroids and the next day the growth medium was supplemented with the LLY-283 GI_{50} or GI_{70}, or a 0.05% DMSO vehicle control. The concentration of LLY-283 or vehicle was maintained in each of the following steps. After 2 days, cells were split and single spheroids seeded in U-bottomed ULA 384-well plates from 1000 HSJD-DIPG-007 cells each. Seeding density was increased from previous optimisation experiments to ensure spheres were 250 µm in diameter when Matrigel was added. The following day the spheres were embedded in Matrigel (final concentration of 4.65 mg/mL). Spheres were imaged by brightfield with a Celigo (Nexcelom, USA) before addition of Matrigel and 3 days later (a 6-day total treatment period).

The fully optimised experiment followed this protocol with the following changes: Only 95,000 (vehicle), 142,000 (GI_{50}), or 205,000 (GI_{70}) HSJD-DIPG-007 cells were seeded for initial treatment. Single spheroid seeding density was adjusted to 1000 (vehicle) or 1500 cells (treated) to account for the reduced viability of treated cells and ensure all spheroids were 250 µm in

diameter when Matrigel was added. Additional spheres were seeded so that for each sphere embedded in Matrigel there was a matched control sphere to which no Matrigel was added. These matched controls were used to estimate how much spheres would increase in diameter over 3 days even when not invading outwards. Spheres were imaged by brightfield with a Celigo (Nexcelom, USA) before addition of Matrigel and 3 days post Matrigel addition (a 6-day total treatment period). The overhead cross-sectional area of each sphere was scored with the Nexcelom analysis software. Invasion was scored with the 'Tumorsphere 1' algorithm at 4 µm resolution as this best captured the complex invasion front, whereas control spheres were scored at 9 µm resolution as this best measured the sphere whilst disregarding debris due to cell death. Invasion was quantified as: cross-sectional area of Matrigel embedded sphere / average cross-sectional area of 4 matched non-embedded spheres.

2.5.7. Treatment of xenografted mice with LLY-283

All *in vivo* experiments were performed by Ángel Montero Carcaboso's group in Hospital Sant Joan de Déu (Barcelona, Spain) in accordance with institutional and European guidelines (EU Directive 2010/63/EU) and were approved by the local animal care and use committee (Comite Etico de Experimentacion Animal at Universidad de Barcelona, protocol 135/11).

500,000 HSJD-DIPG-007 cells were stereotactically implanted into the fourth ventricle of athymic nude mice (vehicle treatment n = 15, LLY-283 50 mg/kg n = 15). Mice were treated +/- 50 mg/kg LLY-283 daily by oral gavage for 3-days-on-4-days-off, for 4 weeks as previously described (Sachamitr *et al.*, 2021). The remaining mice (n=10 for each group) were used to assess survival with the endpoint criteria being 20% weight loss due to disease.

After being sacrificed, mouse brains were formalin fixed and paraffin embedded (FFPE). Briefly, the tissue was fixed in 4% buffered formol (24-48 h). Tissue was dehydrated prior to paraffin embedding by soaking in ascending concentrations (70%, 96%, 100%) of ethanol, 100% isopropanol.

Tumour burden was assessed by digital drop PCR (ddPCR) with reporter primers specific to either the mutant or wild-type alleles (**Table 2.11**). DNA was extracted from FFPE brain tissue with the QIAmp DNA FFPE Tissue kit (Qiagen). ddPCR reactions included 2X ddPCR Supermix (no dUTP) (BIO-RAD, UK), TaqMan Liquid Biopsy dPCR Assay (40X), and 5 µL DNA made up to 25 µL with nuclease free water. The ddPCR reactions and Droplet Generation Oil for Probes (BIO-RAD) were added to a DG8 Cartridge for a QX100TM/QX200 Droplet Generator (BIO-RAD). Droplets generated were transferred to a ddPCR™ 96-Well Plate (BIO-RAD) and sealed at 170 °C. The amplification was performed in a Veriti 96 Well Thermal Cycle (Applied Biosystems). Amplification cycles were as follows: enzyme activation at 95 °C for 10 min; 40 cycles of 94°C (30 seconds) and denaturation at 60 °C (1 min), followed by enzyme deactivation at 98 °C for 10 min. The reactions finished when the thermal cycler reached 12 °C. Droplets generated were read a QX200 Droplet reader™ (BIO-RAD). The data obtained was analysed using Quantasoft Analysis Pro programme. The mass of DNA was calculated as (number of mutant allele positive droplets + number of WT allele positive droplets) * 0.003 ng.

Table 2.11 - ddPCR primer sequences

Name	Sequence
Forward primer	GAATTACCGACACACTCCAACAGT
Reverse primer	CTCTGGTCTTCCTTTTCTGGTACAA
WT reporter (VIC)	AGTGGCTCGCCAGATT
Mutant reporter (FAM)	CAGTGGCTCACCAGATT

2.5.8. Immunohistochemical staining

Paraffin embedded section were processed for immunohistochemical staining with the BOND-MAX autostainer (Leica, Germany) with the following settings: antigen retrieval at 100 °C for 20 min with Epitope Retrieval Solution 1 (AR9961, Leica); primary antibody or IgG control incubation for 1 h then detection using the BOND™ Polymer Refine Detection System (DS9800, Leica) according to manufacturer's instruction.

Table 2.12 - Primary antibodies and isotype controls used for immunohistochemistry

Target / control	Isotype control	Company, catalogue number	Dilution	Figure reference
SDMA	Rabbit IgG	CST, 13820	1:200	4.16
H4R3me2s	Rabbit IgG	EpiGentek, a-3718	1:150	4.16
GFAP	Rabbit IgG	Agilent, Z033429-2	1:500	4.17
MASH1	Mouse IgG1	BD Pharmingen, 55604	1:100	4.17
OLIG2	Mouse IgG2a	Millipore, MABN50	1:1000	4.17
Human nuclear antigen	Mouse IgG1	Sigma-Aldrich, MAB4383	1:200	4.18
Rabbit IgG	-	ReliaTech, IgG-010	1:150	4.16, 4.17
Mouse IgG1	-	CST, 5415	1:500	4.16, 4.18
Mouse IgG2a	-	CST, 61656	1:1250	4.17

2.5.9. IHC image analysis

Images were analysed using FIJI/ImageJ (v1.53c). Briefly, the trainable Weka Segmentation plugin (v3.2.34) (Arganda-Carreras *et al.*, 2017) was trained to segment images into nuclei and background using a representative image of both a stained vehicle and treated section. An individual model was trained for each primary antibody. One field of view from each biological repeat was segmented using the trained algorithm and the H DAB intensity (deconvoluted from the RGB image) of each nucleus was recorded. For MASH1 and OLIG2 nuclear intensity was subsequently used to categorise nuclei as positive or negative based on the intensity of a small selection of nuclei (MASH1) or the population as a whole (OLIG2). As GFAP was not a nuclear stain, the stain intensity in one field of view was quantified without segmentation. Macro and Weka segmentation models can be accessed at https://github.com/ej-brown/Thesis_IHC.

2.6. CRISPR/Cas9 optimisation and cell line characterisation

2.6.1. sgRNA design

The CRISPOR (Concordet and Haeussler, 2018) and Broad Institute GPP/CRISPick (Doench *et al.*, 2014; Sanson *et al.*, 2018) single guide (sg)RNA design tools were supplied with the genomic sequence 100 bp on either side of the c.983G>T mutation. 15 sgRNA target sequences

were predicted by each tool. The top 3 predicted sequences within 30 nucleotides (nt) of c.988G>T from each algorithm (**Table 2.13**) were purchased from Sigma as synthetic sgRNA molecules designed for SpCas9, with stabilising 2'-O-methyl and phosphorothioate linkages (3 nmol, HPLC purified).

Table 2.13 - sgRNA sequences

Name	Algorithm	Orientation	Sequence (without PAM)
CL2	CRISPOR	antisense	CTTTAAATCTCGATGGGCAA
CL3 (BL2)	CRISPOR	antisense	ATGTGCAAGACCACTAGCTA
CL5	CRISPOR	antisense	AAATCTCGATGGGCAATGGC
BL1	GPP/CRISPick	antisense	GGCAATGGCTGGTTTCACTT
BL4	GPP/CRISPick	antisense	GGGCAATGGCTGGTTTCACT
BL5	GPP/CRISPick	antisense	TTTGCTCTTTAAATCTCGAT
EGFP	(Shalem *et al.*, 2014)	n/a	GAAGTTCGAGGGCGACACCC

2.6.2. Electroporation of ribonucleoprotein complexes into SU-DIPG-IV cells

Two days before electroporation SU-DIPG-IV were seeded in TSM-C in T75 flasks such that the confluency was 25-60% on the day of electroporation.

To generate mock ribonucleoprotein (RNP) complexes for optimisation experiments, 44 µM anti-EGFP sgRNA and 10 µM AlexaFluor488 antibodies (A21202, Invitrogen) in TE buffer (10 mM Tris, 0.1 mM EDTA, pH 8.0). sgRNA and antibodies were combined in equal parts (final concentrations of 18 pmol sgRNA and 0.5 µM antibody) and allowed to complex (10-20 min, room temperature).

Electroporation was performed according to the pre-programmed Neon 24-well electroporation protocol, using a Neon™ Transfection System 10 µL Kit (MPK1025, Invitrogen, USA). Before electroporation cells were split as previously described and resuspended in TSM-C without antibiotics. For each of the 26 electroporation reactions, 400,000 cells were spun down, washed in PBS and resuspended in buffer R.

400,000 cells were used for each of the 26 electroporation reactions. Cells were spun down, washed in PBS, and resuspended in buffer R. 9 µL of cells, 1 µL of RNP complexes and 2 µL of electroporation enhancer (1075915, IDT, USA) were combined, of which 10 µL was used for each electroporation reaction. Electroporation was then performed according to manufacturer protocol and electroporated cells plated into a 24-well plate (with 500 µL pre-warmed antibiotic free TSM-C per well).

24h later growth medium was removed from the plate and cells were dissociated by trypsinisation. Cell suspensions were transferred to flow cytometry tubes, spun down (500 g, 4 min), supernatant removed, and cells resuspended in 300 µL 4 °C PBS. Flow cytometry was performed using a BD LSRFortessa; forward scatter (FSC), side scatter (SSC), AlexaFluor-488 and PE amplitudes were recorded. Analysis was performed using FlowJo (v10.7).

2.6.3. Optimisation of sgRNA genome cutting

500,000 SU-DIPG-IV cells were electroporated as in the optimisation experiment with the selected ideal settings (1x 20 ms pulse at 1700 V).

RNP complexes were synthesised by combining 18 pmol Alt-R® S.p. HiFi Cas9 Nuclease V3 (henceforth Cas9) (IDT, USA) and 22 pmol of each sgRNA (**Table 2.13**), as previously described (section 2.6.2). Each electroporation reaction consisted of 1 µL RNP complexes, 2 µL IDT electroporation enhancer (i.e. carrier DNA) (10.8 µM) and 9 µL suspended cells, from which 10 µL was aspirated into the Neon Tip and electroporated. A reaction in which no electroporation was performed was included using leftover CL2/Cas9 and BL5/Cas9 RNP complexes. Following electroporation cells were seeded in T25 flasks and the mixed populations allowed to grow until confluent, when cells were harvested for cryopreservation and DNA collection.

DNA was purified as described in section 2.2.1 and amplified as described in section 2.2.2 using exon 6 primers from **Table 2.4**. DNA was Sanger sequenced by SourceBioscience and the

frequency of indel mutations quantified using the TIDE algorithm online tool (Brinkman *et al.*, 2014).

2.6.4. Design of ssDNA repair template

The repair template was designed by providing the Horizon Discovery Edit-R HDR Donor Designer (*https://horizondiscovery.com/en/ordering-and-calculation-tools/edit-r-hdr-donor-designer-oligo*, no date) with the genomic target and sgRNA sequence. The template already included the wild-type c.983G and was edited to include the silent c.993G>T mutation. The final single-stranded (ss)DNA oligo 5' –C*A*TTTGCACATAGAGATATTTGGGACCCAAGG GAAACCAGCTATTGCCCATCGAGATTTAAAGAGCAAA AA*T* – 3' was ordered from Horizon Discovery Ltd, with stabilising phosphorothioate linkages between the final two bases on each end (marked with *).

2.6.5. Final CRISPR/Cas9

RNP complexes were synthesised by combining 18 pmol Cas9 and 22 pmol EGFP or CL5 sgRNAs, as described above (section 2.6.3). Electroporation was performed as previously optimised (section 2.6.2) with the following changes: the IDT electroporation enhancer was replaced with the ssDNA repair template (21 pmol). Following electroporation, cells from each electroporation were seeded into 2 separate flasks +/- 30 µM HDR enhancer (IDT, 1081073).

For single cell cloning, cells were seeded at a concentration of 0.5 cells/well in 100 µL TSM-C in 96 well plates and fed once a week by replacing half of the growth medium. When a well reached >60% confluency, it was split (as previously described in section (2.3.3, p35) and reseeded into a 6 well plate. When this culture reached confluence, it was again dissociated. Half of the cells were cryopreserved (described in section 2.3.4), and DNA was harvested and sequenced from the rest, as described in section 2.2.1 and 2.2.2.

2.6.6. Sequencing of CRISPR cell lines

Off-target sites were predicted alongside sgRNAs by the CRISPOR algorithm.

Table 2.14 - Primers for on and off-target sequencing of CRISPR cell lines

Name	Sequence
ACVR1_exon6_f001	CTCCTCTTAGGGCAATTGGT
ACVR1_exon6_r001	GAGATGCAACTCACCTAACC
BMPR1APS1_f001	CCTGTTGTCATAGGTCCGTT
BMPR1APS1_r001	GACGGATCACTCGGTACCAT
BMPR1A_f001	GTAACACATTCACGACTTGGTGT
BMPR1A_r001	AGAACCACTCACCTGTTGAA
BMPR1APS2_f001	CTGGGGTCCGGACTTATGA
BMPR1APS2_r001	CGTATGACGGATCACTCGGT
ACVR1C_f001	GAACTGCTGGTGTGGGGTAA
ACVR1C_r001	ATTTCTTGGGCCCAGTGGTT
ZNF534_f001	AGTGAGAAGCTGTAACATGGAGT
ZNF534_r001	TGCTGCCTACTGTTGATCTCC

DNA was purified from SU-DIPG-IV, EGFP control (clone E2E2) and edited ACVR1 WT (clone 1G6) cells as described in section 2.2.1. 750 ng genomic DNA was amplified as described in section 2.2.2, using an annealing temperature of 62 °C for all primers (**Table 2.14**), and a 30 s extension period. The PCR reactions were purified using the QIAquick PCR purification kit (QIAGEN, 28104), according to manufacturer's instructions (including addition of 3M sodium acetate (pH 5) to correct the reaction pH). 50 ng DNA and sequencing primers (i.e. the forward primers in **Table 2.14**) were sent to SourceBioscience for Sanger sequencing.

2.6.7. Validation of ligand induced signalling in CRISPR cell lines

750,000 SU-DIPG-IV, EGFP control E2E2 and edited ACVR1 WT 1G6 cells were seeded into 6 well plates. 24 h later 50 ng/mL BMP-7 (120-03P, Peprotech, UK) or Activin A (120-14, Peprotech, UK) were added to cells. Signalling was halted after 1 h by washing the cells in ice cold PBS, then protein was harvested with ice cold protein lysis buffer (section 2.2.3) supplemented with 0.5 U/µL benzonase (Sigma, E1014). After a 20 min at 4 °C protein was

clarified by centrifugation (17,000 g, 3 min), and protein concentration measured by DC protein assay (5000111, Bio-Rad).

10 µg protein was visualised according to the immunoblot protocol outlined in section 2.2.4, with the following changes: Protein was transferred from NuPAGE gel to PVDF membrane at 400 mA (variable voltage) for 1 h. Primary antibodies are listed in **Table 2.1** (Figure 5.10) and secondary antibodies are listed in section section 2.2.4.

2.6.8. Comparison of growth rates of CRISPR cell lines

To select the EGFP control clone: 23,750 SU-DIPG-IV, clone E1D12, clone E2E2 and clone E2A11 cells were seeded in technical triplicate in a 24-well plate. Cells were brightfield imaged daily with the Nexcelom Celigo image cytometer and confluence calculated with the 'Confluence 1' setting. Curves were calculated by non-linear regression, assuming logistic growth and Y_{max} = 100 in GraphPad Prism (v9.1.2).

To compare the growth rates of the parental, EGFP control and edited cell lines: 1500 SU-DIPG-IV, EGFP control E2E2, edited ACVR1 WT 1G6 cells were seeded per well, for four technical repeats each, in a 96 well plate. Cells were brightfield imaged daily with the Nexcelom Celigo image cytometer and confluence calculated with the 'Confluence 1' setting. Curves were calculated from the mean of three independent repeats by non-linear regression in GraphPad Prism. The data was fit to a curve with the equation:

$$Y = Y_{max} * \frac{Y_0}{(Y_{min} - Y_0) * e^{-k*X} + Y_0}$$

With Y_{max} = 100, and Y_0 to an equivalent value in all cell lines.

2.6.9. Comparison of drug sensitivity in CRISPR cell lines

175 (SU-DIPG-IV), 150 (EGFP control E2E2) or 400 (edited WT ACVR1 1G6) cells were seeded per well in 4 technical replicates in flat-bottomed, 384 well plates. The following day

serial dilutions of LLY-283, GSK591, M4K2009 or M4K2163 were added in 0.1 volumes of TSM-C. After 7 days of growth with the compounds, viability was measured by CTG assay. GI_{50} values were interpolated from curves generated in GraphPad Prism as described in section 2.4.3 with no Y_{max} constraint.

2.6.10. Cytokine array of CRISPR cell line conditioned medium

200,000 SU-DIPG-IV, EGFP control E2E2 or edited ACVR1 WT 1G6 cells were seeded T25 flasks. 3 days later 2 mL of conditioned medium was collected from each flask. Debris was removed by centrifugation at 1000 g for 10 min. Proteins in the conditioned medium of three independent repeats were visualised using a Proteome Profiler™ Human XL Cytokine Array Kit according to manufacturer's protocol (R&D Systems, USA).

Briefly, array membranes were blocked in the provided solution for 1 h at room temperature, then 500 µL of each conditioned medium sample was incubated with a membrane overnight at 4 °C. The following day the membranes were washed and incubated with the Detection Antibody Cocktail for 1h at room temperature. Membranes were again washed, then incubated with Streptavidin-HRP for 30 min at room temperature. To visualize antibody binding, Chemi Reagent Mix was added to each membrane, and the chemiluminescence imaged digitally with an Alliance 4.7 (UVITEC).

The signal intensity of spots was normalised to the reference spots included on each array, then (where indicated) to the relative intensity of the same spot on the SU-DIPG-IV medium treated array.

2.7. Compounds

Table 2.15 - Full list of probes used in the epigenetic probe set screen

Additional information on the Structural Genomics Consortium (SGC) probe set can be viewed on the SGC website (https://www.thesgc.org/chemical-probes/epigenetics)
MT = methytransferase; Kme = binds to methylated lysine; HAT = histone acetyltransferase; BRD = bromodomain; DEHDRY = dehydrogenase; KDM = lysine demethylase; WD40 also known as: beta-transducin repeat domain; YEATS = Yaf9, ENL, AF9, Taf14, Sas5 domain

Probe name	Domain	Protein Target	*in vitro* IC_{50} or Kd (nM)	PubMed ID	Negative control
(R)-PFI 2 hydrochloride	MT	SETD7	2.0 ± 0.2	25136132	(S)-PFI 2 hydrochloride
A 196	MT	SUV420H1/H2	21 ± 3		SGC2043
A 366	MT	G9a/GLP	3.3/38	24900801	
A 395	Kme	EED	34		A-395N
A 485	HAT	p300/CBP	10/3	28953875	A 486
BAY 299	BRD	BRPF2/TAF1	BRPF2: 67; TAF1 (2nd): 14		BAY-364
BAY 598	MT	SMYD2	27	27075367	BAY-369
BAY 6035*	MT	SMYD3	88±16		
BAZ2-ICR	BRD	BAZ2A/2B	130/180	25719566	
BI 9564	BRD	BRD9/7	14/239	26914985	
GSK 2801	BRD	BAZ2A/2B	257/136	25799074	GSK8573
GSK 343	MT	EZH2	4	24900432	
GSK 591 dihydrochloride	MT	PRMT5	11	26985292	SGC2096
GSK 6853	BRD	BRPF1B	8	27326325	GSK9311
GSK 864*	DEHYDR	IDH1 R132C/R132H/R132G	R132C/R132H/R132G: 9/15/17	26436839	
GSK 8814	BRD	ATAD2A/B	50	27530368	GSK 8815
GSK J4	KDM	JMJD3/UTX	GSK-J1: 60	22842901	GSK J5
GSK LSD 1 dihydrochloride	KDM	LSD1	16	26175415	
I-BRD9	BRD	BRD9	50 ± 17	25856009	
I-CBP 112	BRD	CREBBP/EP300	151/625	26552700	
JQ-1	BRD	BET family	BRD4 1st/2nd BRD: 50/90	20871596	(-)-JQ1
L Moses dihydrochloride	BRD	PCAF/GCN5	PCAF/GCN5: 126/600 (ITC)	27966810	D-Moses
LLY-283*	MT	PRMT5	22	26985292	SGC2096
MS 023 dihydrochloride	MT	PRMT type 1	PRMT1/3/4/6/8: 39/135/93/4/5	26598975	MS094
MS049 oxalate salt	MT	PRMT4/6	PRMT4/6: 44/63	27584694	MS049N
NI 57	BRD	BRPF1/2/3	31/108/408		
NVS-CECR2-1	BRD	CECR2	8		
OF 1	BRD	BRPF1/2/3	100/500/2400		

Probe name	Domain	Protein Target	*in vitro* IC_{50} or Kd (nM)	PubMed ID	Negative control
OICR 9429	WD40	WDR5	64	26167872	OICR-0547
PFI 3	BRD	SMARCA2/4	SMARCA4:89; PB1 (5th):48	26139243	BDF25488524
SGC 0946	MT	DOT1L	0.3 ± 0.1	23250418	SGC 0649
SGC 707	MT	PRMT3	31 ± 2	25728001	XY-1
SGC-CBP30	BRD	CREBBP/EP300	21/38	24946055	BDOIA513
SGC-iMLLT	YEATS	MLLT1/3			YT26870
TP 064	MT	PRMT4	< 10		TP-064N
TP 472	BRD	BRD9/7	33/340		TP 472N
UNC 0642	MT	G9a/GLP	< 2.5	24102134	
UNC 1215	Kme	L3MBTL3	40	23292653	UNC 1079
UNC 1999	MT	EZH2/H1	10/45 ± 3	23614352	

Table 2.16 – Additional probes used in the epigenetic probe screen

Probe name	Domain/ complex	Target	PubMed ID	Negative control
Clomipramine		5-HT transporter		
PRT4165	PRC1	RNF2/RING1A		
UNC3866	PRC1	CBX4/7		
Atovaquone		Antimalarial		
Metformin		Respiratory chain complex III		
SAHA	HDAC	Broad spectrum		
SPIN … 23[6]	Kme	SPIN1		SPIN … 26
EPZ 6438	PRC2	EZH2		

[6] This is a precursor to the VinSpinIn probe listed at https://www.thesgc.org/chemical-probes/VinSpinIn

Table 2.17 – LSS and ACVR1 inhibitors

Compound	Target	Source	Structure
LDN-193189	ACVR1	Paul Yu, Harvard	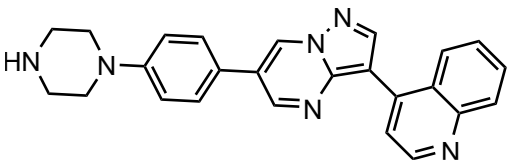
M4K1139	ACVR1	M4K Pharma	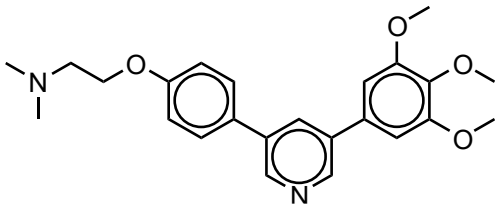
M4K2009	ACVR1	M4K Pharma	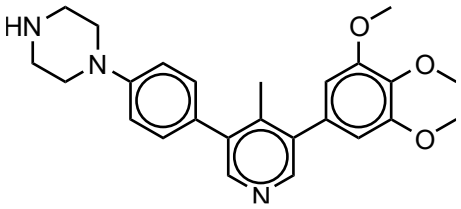
M4K2163	ACVR1	M4K Pharma	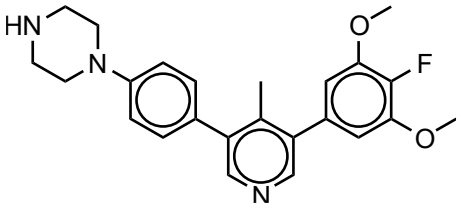
Ro 48-8071	LSS	Cayman Chemical, 161582-11-2	

Chapter 3. An epigenetic probe screen identifies PRMTs as necessary for DIPG cell viability

3.1. Background

The ubiquity of histone H3 and *ATRX* mutations in DIPG tumours, and their specificity to paediatric midline tumours, indicates the importance of epigenetics in DIPG development (Mackay *et al.*, 2017). The impairment of PRC2 activity by H3K27M histones leads to global hypomethylation and hyperacetylation, but localised retention of methylation on tumour suppressing genes (Chan *et al.*, 2013; Lewis *et al.*, 2013; Mohammad *et al.*, 2017; Piunti *et al.*, 2017; Filbin *et al.*, 2018). This sets up a unique epigenetic landscape and gene expression profile, which could introduce vulnerability to the inhibition of epigenetic proteins in DIPG cells, and create the opportunity to develop a novel targeted therapy. With this is mind, several epigenetic therapeutic targets have been pre-clinically investigated (as discussed in Chapter 1), but have so far failed to translate into clinical benefit due to poor BBB penetrance or toxicity (Rodgers *et al.*, 2016; Hennika *et al.*, 2017; Mita and Mita, 2020). Thus, the need to identify additional potential targets remains.

To achieve this, I employed the open-source epigenetic chemical probe library developed by the Structural Genomics Consortium (browsable at https://www.thesgc.org/chemical-probes/epigenetics). These chemical probes inhibit a comprehensive range of readers, writers and erasers of methylation and acetylation marks on histones H3 and H4, including arginine and lysine methyltransferases and bromodomain proteins (Scheer *et al.*, 2019; Wu *et al.*, 2019) (full panel listed in **Table 2.15**). Each probe has been developed according to best practice guidelines for experimentally useful chemical probes: they have been validated to specifically inhibit the target protein over other family members (or have a defined set of off-targets), and to have significant on-target cellular activity at 1 µM (Ackloo, Brown and Müller, 2017; Scheer *et al.*, 2019). This is in contrast to many published inhibitors or marketed drugs – a 2011 study found

that more than half of oral drugs have IC_{50} values of less than 1 μM for two or more targets (Gleeson *et al.*, 2011). Unlike most commercial screening libraries, each of the chemical probes are also paired with a close analogue that has been validated as inactive against the primary target of the probe, that can be used to identify if any recorded activity is due to off-target inhibition (Scheer *et al.*, 2019). In summary, selection of this library should allow simple experimental execution, produce readily interpretable result with reduced risk of confounding off-target activity.

In order to perform this epigenetic probe screen, I used patient-derived DIPG cell lines as the experimental model. These cell lines were isolated either by stereotactic biopsy or autopsy of DIPG patients and include cell lines with a wide range of the mutations found in the clinic (**Table 2.3**) (Caretti, Sewing, *et al.*, 2014; Taylor *et al.*, 2014; Grasso *et al.*, 2015). Patient-derived cell lines have several advantages as an experimental model: they allow a more high-throughput approach relative to mouse models; they contain characteristic combinations causative mutations from original tumours; they are the *in vitro* DIPG model with gene expression patterns most like that of primary patient tissue (Filbin *et al.*, 2018); and there are no confounding unphysiological interactions with non-human cells. Thus, this panel of patient derived DIPG cells is a reasonably representative model that nevertheless allows relatively high throughput experimental work.

For years, assays performed on monolayer cultures were the 'gold-standard'. However, many studies have observed that the drug sensitivity of cancer cells can change depending on whether the cells were grown in adherent monolayers or as 3D structures such as spheroids – for example (Howes *et al.*, 2007; Vinci *et al.*, 2012). Differences in treatment sensitivity may be due to altered signalling within the cell dependent on the presence or absence of adhesion complexes from cell-cell interactions or from oxygen, nutrient or pH gradients across the

population (Kimlin, Casagrande and Virador, 2013). For these reasons, my screening was performed with both adherent and spheroid culture to allow comparison of the results.

3.1.1. Experimental overview

In this chapter, a non-biased screen of small molecule inhibitors of epigenetic mediators was performed on the patient derived DIPG cell lines HSJD-DIPG-007 (H3.3 K27M, *ACVR1* R206H) and HSJD-DIPG-011 (H3.3 K27M, *ACVR1* WT) grown both adherently and as spheroids. From this, the activity of the protein arginine methyl transferase (PRMT) family was identified as necessary for DIPG viability. By comparing the growth inhibition curves of each PRMT family probe in 5 DIPG cell lines, both PRMT5 probes were found to potently reduce DIPG viability at the lowest doses.

3.2. Results

Before establishing a cell-based screening effort, the optimal conditions for the culture of patient-derived DIPG cells were first explored. In particular to allow the 7 day incubation needed for epigenetic probes to cause phenotypic changes (Daigle *et al.*, 2011; Vedadi *et al.*, 2011; McCabe *et al.*, 2012; Yu *et al.*, 2012) whilst avoiding death due to overgrowth of cells.

3.2.1. Selection of adherent and spheroid growth substrates

As this project was focused on *ACVR1* mutant DIPG, the experimental model needed to support the associated aberrant BMP signalling via SMAD1/5/8 in response to activin A. Growth substrates such as laminin or Matrigel, which have been previously used to induce adherent growth of DIPG cells (Grasso *et al.*, 2015; Vinci, Box and Eccles, 2015; Vinci *et al.*, 2018; Carvalho *et al.*, 2019), were tested. Supplementation with FCS was not tested as it induces differentiation and thus gene expression unlike that of patient tumours (Filbin *et al.*, 2018). Here, cells were grown for 24 hours either with no coating, a 2.5% Matrigel, a poly-L-lysine or a poly-L-lysine/laminin coating, then stimulated with either BMP-6 or activin A for 1 hour. Resultant

phosphorylation of SMAD proteins was measured by immunoblot (**Figure 3.1**). BMP signalling downstream of ACVR1 was activated in response to both ligands as expected in all growth conditions tested (**Figure 3.1**). Therefore, for future experiments requiring 3D spheroid growth no coating was applied to culture plates and where adherent growth was required, laminin coated plates were used.

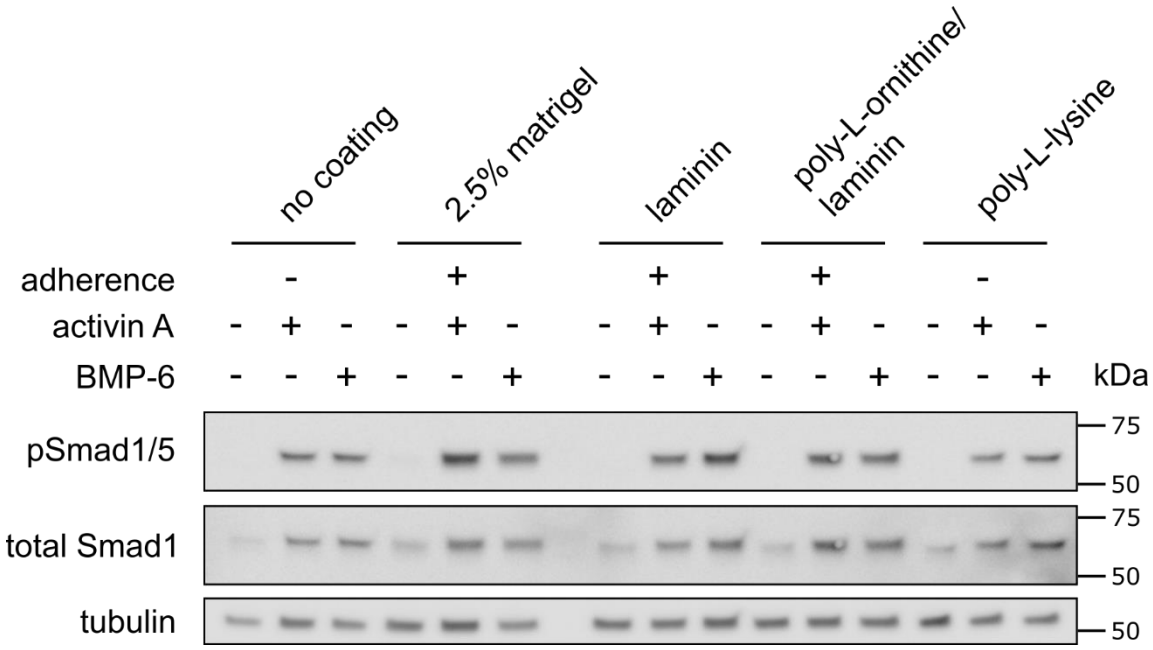

Figure 3.1 - Multiple growth substrates support BMP/SMAD signalling in ACVR1 mutant DIPG cells

HSJD-DIPG-007 cells were grown on each growth substrate for 24 h, 150 ng/mL of BMP-6 or activin A was administered, and after 1 h cells were processed for detection of SMAD proteins by immunoblot. pSMAD1/5 is induced as expected in response to BMP-6 and activin A in all conditions. SMAD1 expression appears uneven likely as a result of incomplete antibody stripping between rounds of probing, although the tubulin loading control confirms equal protein was loaded in each well.

3.2.2. Selection of seeding densities for epigenetic probe set screen

To ensure that cells were growing exponentially throughout the experiment, the seeding density was optimised for the two cell lines selected for initial screening, HSJD-DIPG-007 and HSJD-DIPG-011. HSJD- DIPG-007 was selected for screening as it is the fastest growing *ACVR1* mutant cell line (allowing a large volume of cells to be used in regular experiments) and can be used in a mouse xenograft model (Vinci *et al.*, 2018). HSJD-DIPG-011 was selected as the most closely matched *ACVR1* wild-type cell line.

To select the appropriate seeding density, HSJD-DIPG-007 cells were seeded at a range of densities into laminin coated 96 well plates and their confluence was measured over time (**Figure 3.2**). After reaching confluence the population became unhealthy and the associated cell death and detachment could be seen as a subsequent fall in confluence (**Figure 3.2a, b**). The recommended incubation period needed to see phenotypic changes due to inhibition of methyltransferases is 7 days (Daigle *et al.*, 2011; Vedadi *et al.*, 2011; McCabe *et al.*, 2012; Yu *et al.*, 2012), and so seeding densities were selected to allow for this incubation period. For such an 8-day assay, 1500 HSJD-DIPG-007 cells would be reaching confluency at the end of the experiment, having grown exponentially for the whole incubation if the probe tested had no effect (**Figure 3.2a, b**).

Each of these cell lines have unique growth behaviours so may need to be optimised with different methods. HSJD-DIPG-011 cells did not form a monolayer even with a laminin coating (**Figure 3.2c**) so automated measurements of confluency could not be used to infer culture health. HSJD-DIPG-011 cells were treated with propidium iodide (PI), a fluorescent DNA binding dye that only permeates the membranes of dead or dying cells (Riccardi and Nicoletti, 2006; Pan, Bartneck and Jahnen-Dechent, 2012), to detect necrotic cores. After 7 days, culture viability was measured using the CellTiter-Glo (CTG) assay. Both 2D and 3D CTG reagent sets were tested under the assumption that the centre of larger spheres may only be reached by reagents specialised for use with spheroids. At higher seeding densities, where larger spheres were produced, 3D CTG detected a two-fold higher signal (**Figure 3.2d**) so this reagent set was used in future with the HSJD-DIPG-011 cell line. In a laminin coated 96 well plate, cells seeded at a density of 12,000 cells/well or less could be grown for 7 days without the centre of the sphere becoming intensely stained with propidium iodide (**Figure 3.2c**). A high number of PI positive cells in the centre of the spheroid would suggest the formation of a necrotic core. A seeding density of 6,000 HSJD-DIPG-011 cells/well, grown for 7 days produced a luminescence signal

equal to that of a confluent HSJD-DIPG-007 culture (dotted line on graph in **Figure 3.2d**) so 6,000 HSJD-DIPG-011 cells/well was selected as a density that would allow detection of changes in viability in future experiments.

A similar methodology was used to select the seeding density for the single spheroid 3D assay. A range of densities of HSJD-DIPG-007 cells were seeded into round-bottomed 384-well plates. A subset of wells was treated with centrifugal force or Matrigel to test if this improved spheroid formation. The inclusion of a low percentage of Matrigel caused the HSJD-DIPG-007 cells to adhere to and migrate across the plate surface, and centrifugal compaction did not improve sphere formation (**Figure 3.3**), so these steps were excluded from the protocol. As with the adherent cultures, spheroids were grown for 6 days, to match the incubation period recommended for phenotypic assays with methyltransferase probes (Daigle *et al.*, 2011; Vedadi *et al.*, 2011; McCabe *et al.*, 2012; Yu *et al.*, 2012). The speckled PI staining on all HSJD-DIPG-007 spheroids illustrates that in all spheroids a proportion of cells die (**Figure 3.3a**). However, in spheroids greater than 500 µm in diameter a large necrotic core formed thus reducing the total volume of viable cells. This was visible as saturated PI staining in the centre of the spheroid, with only a thin layer of viable cells around the perimeter (for example Figure 3.3a, 1000 cells at day 6). Optimising to produce large spheres with minimal cell death maximised the assay window by maintaining the maximum possible number of viable cells in the absence of treatment. A seeding density of 40 cells/well was chosen from between the 20 cells/well and 100 cells/well as it was estimated that this would produce spheres 500-600 µm in diameter after 6 days (**Figure 3.3a**). This was chosen based on the qualitative appearance of PI staining in spheroids, although ideally quantification of PI staining should be performed to provide a robust measure of spheroid viability.

For the HSJD-DIPG-011 spheroid screen a seeding density of 200 cells/well was selected to match the size of HSJD-DIPG-007 spheroids at day 3 (200-300 µm in diameter). This decision

assumed a similar rate of growth in the two cell lines, however section 3.2.7 discusses the error in this assumption, and how it was corrected. Thus, with the seeding densities of HSJD-DIPG-007 and HSJD-DIPG-011 for the epigenetic probe screen selected the final screening protocol was designed.

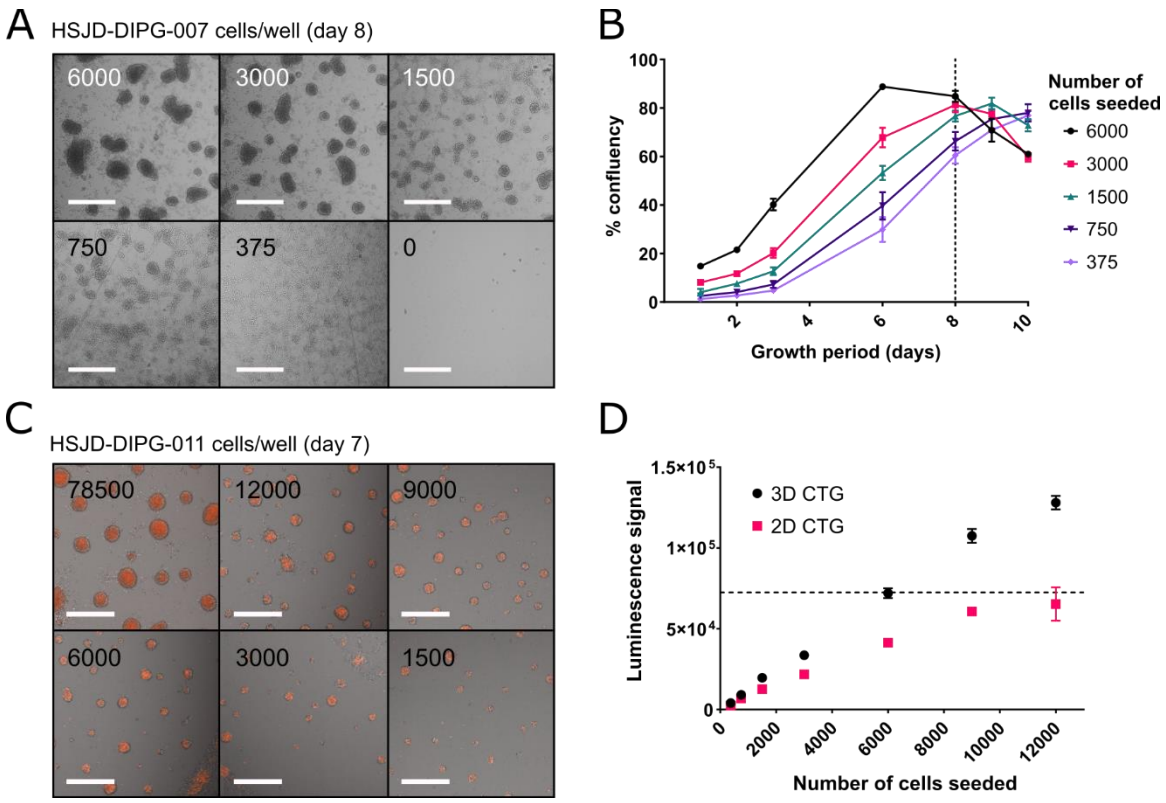

Figure 3.2 - Optimisation of cell seeding densities for adherent viability assays

(A) *Brightfield images of HSJD-DIPG-007 cultures after 8 days of growth in a 96 well plate. Values are the number of cells seeded per well. Scale bars are 500 µm.*

(B) *Graph of HSJD-DIPG-007 culture confluence over time as measured using automated image cytometry. Points are the average of 3 technical repeats.*

(C) *Merged brightfield and flourescence (propidium iodide, marking areas of cell death) images of HSDJ-DIPG-011 cells after 7 days of growth. Values are number of cells seeded per well. Scale bars are 500 µm.*

(D) *Graph of the luminescence signal produced by the CellTiter-Glo reagent (measure of viability) after 7 days of HSJD-DIPG-011 growth in a 96 well plate. Dashed line indicates the typical signal from a confluent well of HSJD-DIPG-007 cells. Points are the average of 3 technical repeats.*

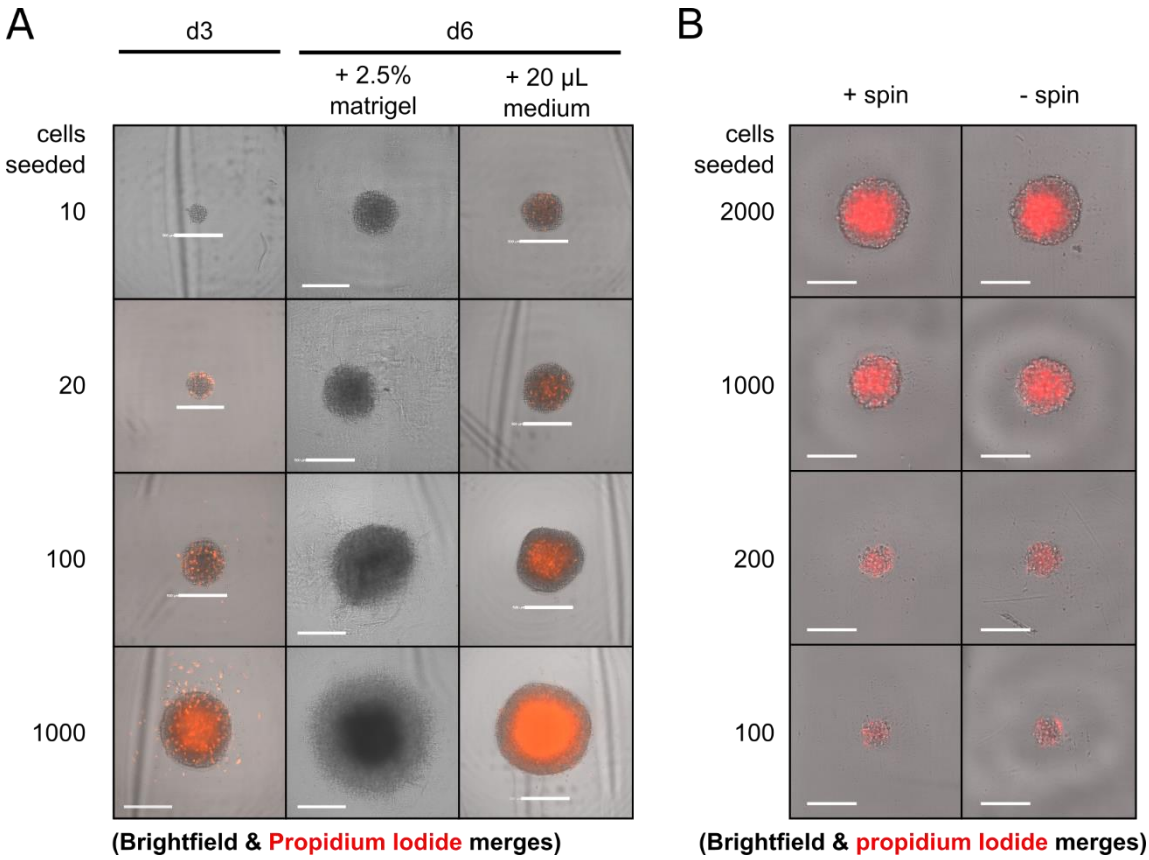

Figure 3.3 - Optimisation of spheroid generation

(A) *Merged brightfield and fluorescence (PI, as a cell death marker; Not included in 2.5% Matrigel treatment) images of HSJD-DIPG-007 spheroids afters 3 days of growth. Scale bars are 500 µm.*

(B) *Merged brightfield and fluorescence (PI) images of HSJD-DIPG-011 spheroids after 3 days of growth. Scale bars are 200 µm.*

3.2.3. Final design of epigenetic probe screen

The viability of a cell culture depends on the balance between proliferation and cell death in the population (Ucker and Levine, 2018), therefore viability was selected as the end point measure as this would identify probes that impair proliferation or that induce cell death. To detect the potential therapeutic impact of *ACVR1* mutations, each probe was tested against HSJD-DIPG-007 (*ACVR1* R206H, H3.3 K27M) and HSJD-DIPG-011 (*ACVR1* WT, H3.3 K27M) cells. Comparing the drug sensitivity of these cell lines could inform the selection of patients for future clinical trials and provide mechanistic insight into why ACVR1 mutations promote DIPG or FOP.

In addition, the clinical context in which a therapy would be administered was incorporated into the screen. Any new therapy for DIPG is first clinically tested either after or alongside focal radiotherapy (Cohen, Jabado and Grill, 2017). To mimic this, and to identify any probes that were differentially effective in combination with radiation, half of the screen plates were treated with 4 Gy of gamma radiation. This single dose was selected from literature as a typical *in vitro* radiation treatment for glioma or DIPG cells (Narayan *et al.*, 2018; Pal *et al.*, 2018; Deland *et al.*, 2021) which is comparable to one or two of the daily doses patients would receive in the clinic (Zaghloul *et al.*, 2014; Cohen, Jabado and Grill, 2017). Radiation was administered 3 days after the addition of the chemical probes as by that point each chemical probe was likely to have altered the chromatin in a way which could lead to a differential response to radiotherapy (Daigle *et al.*, 2011; Vedadi *et al.*, 2011; McCabe *et al.*, 2012; Yu *et al.*, 2012).

To test this initial workflow (illustrated in **Figure 3.4a**), 15 probes from an old iteration of the SGC probe set were tested in a pilot experiment with one independent repeat, and three (adherent) or four (spheroid) technical repeats. The pilot included JQ-1, a probe already known to reduce DIPG cell viability (Piunti *et al.*, 2017), as a positive control. Indeed JQ-1 reduced viability by 71%, 95% and 41% in the adherent (- radiation), adherent (+ 4 Gy) and spheroid

(- radiation) tests respectively. Additionally, 4 probes reduced viability more than 50% in at least one condition. The most effective, the SMYD2 probe LLY-507, reduced viability by 100% in both adherent tests and by 58% in the spheroid test. The 4 Gy radiation treatment reduced the viability of the vehicle control by 50%, a value which still allowed detection of viability reduction by JQ-1 and LLY-507. Given the success of this pilot experiment, the complete set of probes was next selected.

Although the SGC epigenetic probe set can query a wide range of targets, additional small molecule inhibitors (listed in Table 2.3) were included to test specific hypotheses or to act as a benchmark for other pre-clinical targets. The broad range histone deacetylase inhibitor SAHA (also known as Vorinostat) was included as a positive control, in addition to JQ-1, because of its ability to arrest proliferation in paediatric CNS tumour xenograft models (Milde *et al.*, 2011). Similarly probes inhibiting PRC2 (EPZ 6438 inhibiting EZH2) and PRC1 (PRT4165 and UNC3866) were included in addition to the EZH2 inhibitors already in the probe set (GSK 343 and UNC1999) because of the published efficacy of PRC1 and PRC2 inhibitors (Mohammad *et al.*, 2017; Zhang *et al.*, 2017; Filbin *et al.*, 2018). Similarly, the SMYD2 inhibitor LLY-507 was included because of the effect demonstrated in the pilot, despite having been retired as an SGC chemical probe. This probe was retired because of extensive off-target activity (Structural Genomics Consortium, https://www.thesgc.org/chemical-probes/LLY-507). Its inclusion enabled direct comparison to the more specific SMYD2 inhibitor BAY598 and the SMYD3 inhibitor BAY6035.

Several clinically approved compounds were included to test whether they could be repurposed for the treatment of DIPG. Drug repurposing is increasingly sought after because it allows accelerated approval of a therapy and is especially useful in rare diseases such as DIPG that are not commercially attractive for the development of new therapies (Lotfi Shahreza, Ghadiri and Green, 2020). The tricyclic antidepressant Clomipramine was included because of its ability to induce the apoptosis of glioma cells (Levkovitz *et al.*, 2005). Metformin, the first line

treatment for type II diabetes, was included because of the prolonged survival of high grade glioma patients taking metformin (Seliger *et al.*, 2019). The anti-malarial Atovaquone was identified as a radiosensitiser of multiple cancer types (Ashton *et al.*, 2016), and was included to test its potential as a radiosensitiser of DIPG cells. The inclusion of the outlined pre-clinical and clinically approved allowed previously articulated hypotheses to be tested alongside and compared to the results of the non-biased screen.

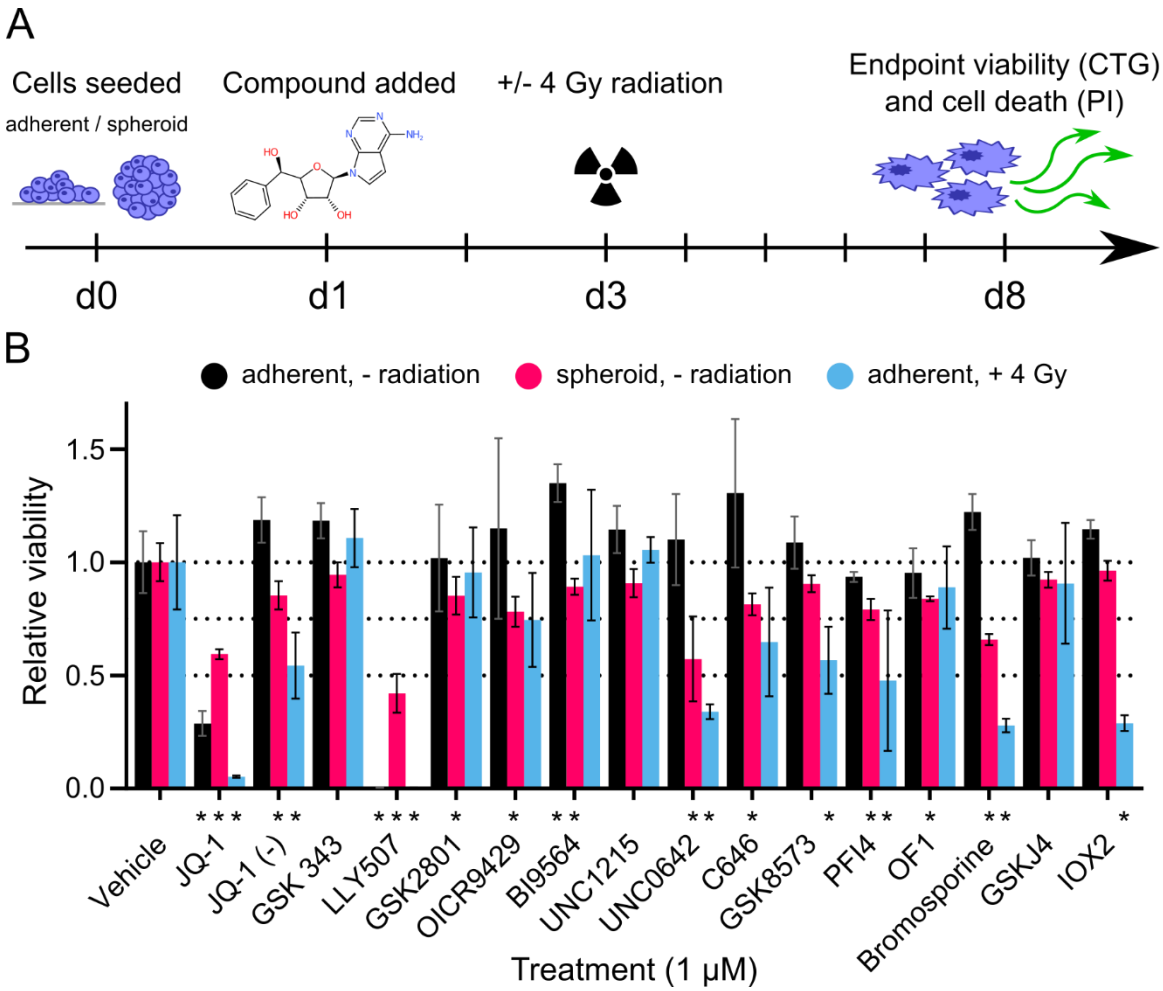

Figure 3.4 – Workflow for epigenetic probe set screens and results of pilot experiment

*A) DIPG cell lines were seeded at the densities listed in Table 2.7 into low attachment U-bottomed plates to generate spheroids or onto laminin coated flat-bottomed plate to induce adherent growth. The following day each epigenetic probe was added to a final concentration of 1 µM onto three (adherent) or four (spheroid) technical repeat wells. Two days later half of the repeats were treated with 4 Gy of gamma radiation. After 7 days of growth in the presence of each epigenetic probe end point viability was recorded with the CTG assay. B) A bar chart showing the relative viability of cells grown adherently or as spheroids for 7 days in the presence of 1 µM of the indicated probe (normalised to the vehicle control of each growth condition). The data represent the mean of 3 (adherent) or 4 (spheroid) technical repeats, with error bars displaying the standard deviation. Treatments labelled with * were significantly different from the matched vehicle control (multiple unpaired t-tests, FDR = 1%).*

3.2.4. The *ACVR1* R206H HSJD-DIPG-007 cell line is susceptible to PRMT inhibition

The results of all four screens are presented in **Figure 3.5** and **Figure 3.6**, but the results of the screen of HSJD-DIPG-007 cells grown adherently, without radiation will be considered first here. 16 probes significantly reduced the viability of HSJD-DIPG-007 (multiple two-tailed t-tests, using a two-stage linear step-up procedure, Q = 1%). Of these, 10 reduced viability by more than 25% and 5 reduced viability by more than 50% relative to a vehicle control (**Figure 3.5**, **Table 3.1**). These hits included the two positive controls, JQ-1 and SAHA, which reduced viability by 88% (SD 3%) and 95% (SD 2%) respectively (**Figure 3.5**), and as in the pilot experiment UNC0642, LLY-507 and Bromosporine significantly reduced viability (**Figure 3.4**, **Figure 3.5**). However, although LLY-507 reduced viability a mean of 67%, the SD was large (40%) and the other SMYD2 probe (BAY-598) did not significantly reduce viability. Therefore, the target inhibition that causes this effect is unclear, and not suitable for follow up.

A number of interesting targets appear as hits within this set of data: A485, a p300/CBP inhibitor, reduced viability by 36% (SD 12%) and has been shown to reduce H3K27 acetylation in prostate cancer cells (Lasko *et al.*, 2017). This could oppose the hyperacetylation found H3K27M cells, thus reducing overexpression of oncogenes (Piunti *et al.*, 2017). A366, a G9a/GLP complex inhibitor, reduced viability by 29% (SD 0.6%) and could do so by reducing p53 methylation thus promoting apoptosis (Huang *et al.*, 2010), or induce autophagy and differentiation in glioblastoma cells (Ciechomska *et al.*, 2016). Most notably, of the 10 most effective probes, 4 targeted the protein arginine methyltransferase (PRMT) family. The 2 most effective probes both inhibited PRMT5, which symmetrically methylates many proteins including histones and cystosolic proteins that regulate a multitude of cellular processes (Zheng *et al.*, 2013; Chu *et al.*, 2015; Jin *et al.*, 2016; Hamard *et al.*, 2018; Scaglione *et al.*, 2018; Sachamitr *et al.*, 2021).

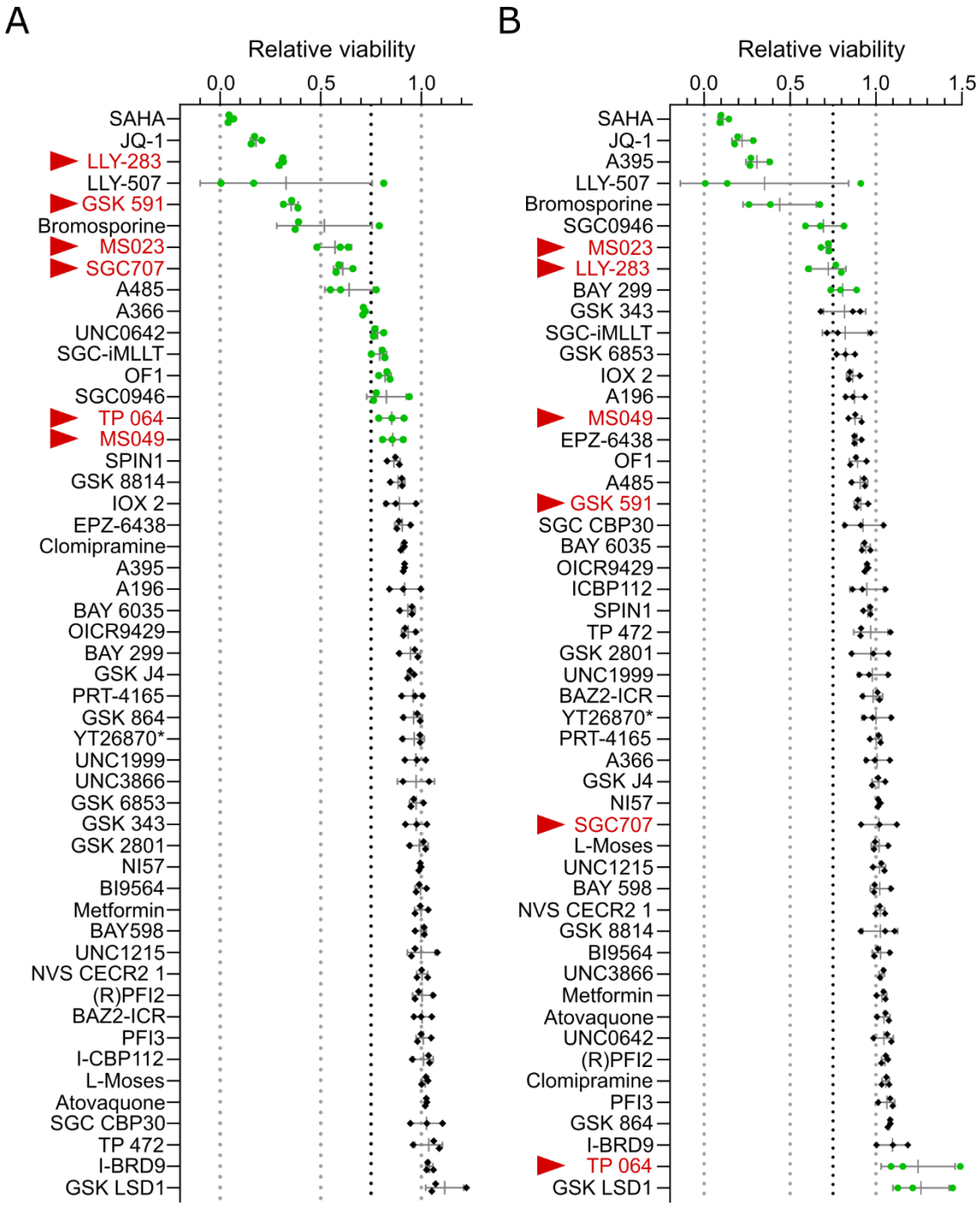

Figure 3.5 – Treatment of adherent HSJD-DIPG-007 cells with the full epigenetic probe set reveals that PRMT inhibition decreases cell viability

Graphs of HSJD-DIPG-007 adherent cell culture viability (relative to DMSO vehicle controls, measured with the CellTiter-Glo assay) after 7 days in the presence of the indicated epigenetic probes (1 µM) with no radiation treatment **(A)** or with 4 Gy gamma radiation administered on day 3 of treatment **(B)**. Each point is the average of three technical repeats from one independent repeat. Bars are mean ± SD. Treatments that significantly changed the viability of the HSJD-DIPG-007 culture are highlighted as green, circular points (multiple two-tailed t-tests, using a Two-stage linear step-up procedure, Q = 1%). PRMT family probes are highlighted with a red triangle.*

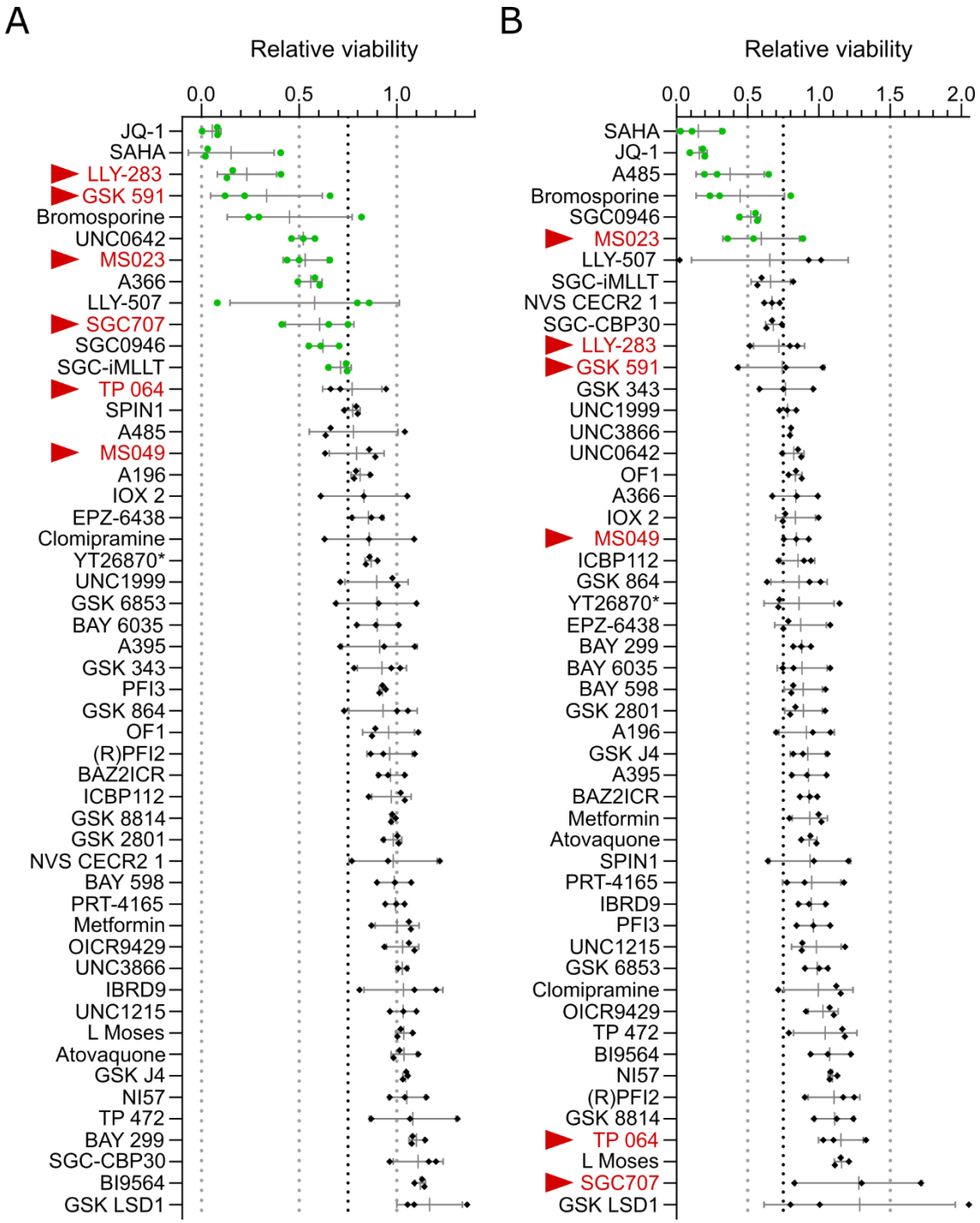

Figure 3.6 – Treatment of spheroid HSJD-DIPG-007 cells with full epigenetic probe set again reveals PRMT inhibition decreases cell viability

The viability of HSJD-DIPG-007 single spheroids (relative to DMSO vehicle controls, measured with the CTG assay) after a 7 day treatment with the indicated epigenetic probe (1 µM) with no radiation treatment **(A)** or with 4 Gy gamma radiation administered on day 3 of treatment **(B)**. Each data point is the average of 4 technical repeats from one independent repeat. Bars are mean ± SD. Probes that significantly changed HSJD-DIPG-007 viability are depicted as green circles (multiple two-tailed t-tests, using a Two-stage linear step-up procedure, Q = 1%). PRMT inhibitors are highlighted with a red triangle. *YT26870 was added at 0.5 µM.*

Table 3.1 - Hits identified in the epigenetic probe screen with adherently grown HSJD-DIPG-007 cells

Hits were identified by multiple t-test using a False Discovery Rate (FDR) approach with a q value cut-off of 1%. Probes reducing viability (relative to the vehicle control) > 25% or > 50% are highlighted in yellow and orange respectively. Probes inhibiting PRMTs are additionally highlighted in green.

Probe	Class	Target	Relative viability reduction	SD	q value
MS049	Methyltransferase	PRMT4/6	0.14	0.05	0.00875
TP 064	Methyltransferase	PRMT4	0.15	0.06	0.00659
SGC0946	Methyltransferase	DOT1L	0.17	0.10	0.00118
OF1	Bromodomain	BRPF1/2/3	0.18	0.03	0.00080
SGC-iMLLT	YEATS domain	MLLT1/3	0.21	0.04	0.00009
UNC0642	Methyltransferase	G9a/GLP	0.22	0.03	0.00004
A366	Methyltransferase	G9a/GLP	0.29	0.01	<0.000001
A485	Histone acetyltransferase	p300/CBP	0.36	0.12	<0.000001
SGC707	Methyltransferase	PRMT3	0.39	0.04	<0.000001
MS023	Methyltransferase	PRMT type I	0.43	0.08	<0.000001
Bromosporine	Bromodomain	Broad spectrum	0.48	0.24	<0.000001
GSK 591	Methyltransferase	PRMT5	0.65	0.04	<0.000001
LLY-507	Methyltransferase	SMYD2 (non-specific)	0.67	0.43	<0.000001
LLY-283	Methyltransferase	PRMT5	0.69	0.01	<0.000001
JQ-1	Bromodomain	BET family	0.82	0.03	<0.000001
SAHA	Histone deacetylase	Broad spectrum	0.95	0.01	<0.000001

The results in the HSJD-DIPG-011 cell line were too variable to find any significantly effective probes (multiple two-tailed t-tests, using a two-stage linear step-up procedure, Q = 1) so will not be discussed in depth (**Appendix Figure 0.1**). This high variance could be because the slower growth rate of HSJD-DIPG-011 was not correctly accounted for when optimising its seeding density. Having smaller spheres at the assay end point would have reduced the assay window and increased the signal to noise ratio such that hits could no longer be statistically detected. Although it did not reach statistical significance, GSK591 was the most effective at decreasing HSJD-DIPG-011 viability, with a reduction of 64% (Q = 0.04) (Appendix **Figure 0.1**, **Table 0.1**). Rather than repeating the entire screen, this cell line was simply included in the subsequent validation of the PRMT family probes (section 3.2.6), which also showed that HSJD-DIPG-011 is more resistant to all probes tested.

3.2.5. Comparison of results between screen conditions identifies probes less effective in combination with radiation

Once known, the hits were compared between different experimental conditions to identify any trends in the data.

The screen performed on adherent cells, without a radiation treatment produced the most statistically significant discoveries, with 16 probes identified as significantly different from the vehicle control, and changes in viability as small as 14% were detected (**Figure 3.5a**, **Figure 3.7**, **Table 3.1**). The addition of radiation reduced the number of significant discoveries to 11, although changes as low as 19% could still be detected (**Figure 3.5b**, **Figure 3.7**). The spheroid assay had 12 significant discoveries without the radiation treatment, which fell to 6 discoveries with the radiation treatment (**Figure 3.6**, **Figure 3.7**). Neither spheroid assay detected viability reduction less than 25%, but this is not an issue because smaller changes are unlikely to be biologically relevant.

Looking beyond just the most effective probes the whole dataset was compared between experimental conditions. Changes in viability in cells grown as spheroids significantly correlated with those grown adherently with a Pearson R^2 value of 0.87 (no radiation) and 0.54 (+ 4 Gy) (Pearson correlation, $p < 0.0001$). Without radiation treatment, there were no probes identified as differentially effective between adherent and spheroid assays (**Figure 3.8a**). This is unsurprising given that the morphology of the cells remained largely the same when laminin was included (**Figure 3.2**). With radiation treatment, only two probes (A485 and A395) behaved significantly differently between adherent and spheroid screens (discussed below) ($p < 0.0001$, multiple t-tests, two-stage linear step-up procedure, Q = 1%). The concordance between the adherent and spheroid data suggests that validation of PRMT probes can be performed using a spheroid assay only without gaining false positive or negative results.

In contrast, the 4 Gy gamma radiation treatment at 3 days of growth did have some notable impacts on the results of the screen. Raw luminescence values, without normalisation, suggest that the radiation treatment reduced final viability 82 ± 4% across both adherent and spheroid growth conditions and HSJD-DIPG-007 and HSJD-DIPG-011 cell lines (**Appendix Figure 0.2**). This was far higher than the 50% reduction similarly observed in the pilot screen and resulted in a far smaller signal to noise ratio that hindered hit identification. The viability recorded for each probe +/- radiation treatment significantly correlated with those not treated with radiation in both adherent (Pearson correlation, $R^2 = 0.53$) and spheroid screens (Pearson correlation, $R^2 = 0.45$). Perhaps because of the reduced signal to noise ratio, 5/10 hits from the adherent screen and 4/6 PRMT family probes, were significantly less effective with the addition of radiation treatment, with a similar trend in the spheroid data (**Figure 3.8c, d**). Note that because these viability values are relative to the vehicle control, PRMT5 inhibition still decreases viability more in combination with a radiation treatment than without it by an estimated further 18% (adherent) or 10% (spheroid) (**Appendix Figure 0.2**). Only A395 (inhibitor of EED, part of

the PRC2 complex) reduced viability significantly more in combination with radiation treatment (**Figure 3.8c**). In contrast to previous reports that GSK-J4 radiosensitises DIPG cells by inhibiting JMJD3, which demethylates H3K27 in opposition to PRC2 (Katagi *et al.*, 2019), this effect was not observed here. Further experiments investigating GSK-J4 or PRMT family probes in combination with radiation therapy were not pursued as radiosensitisation was not the focus of this thesis, and the xenograft model use in Chapter 4 does not include radiation treatment.

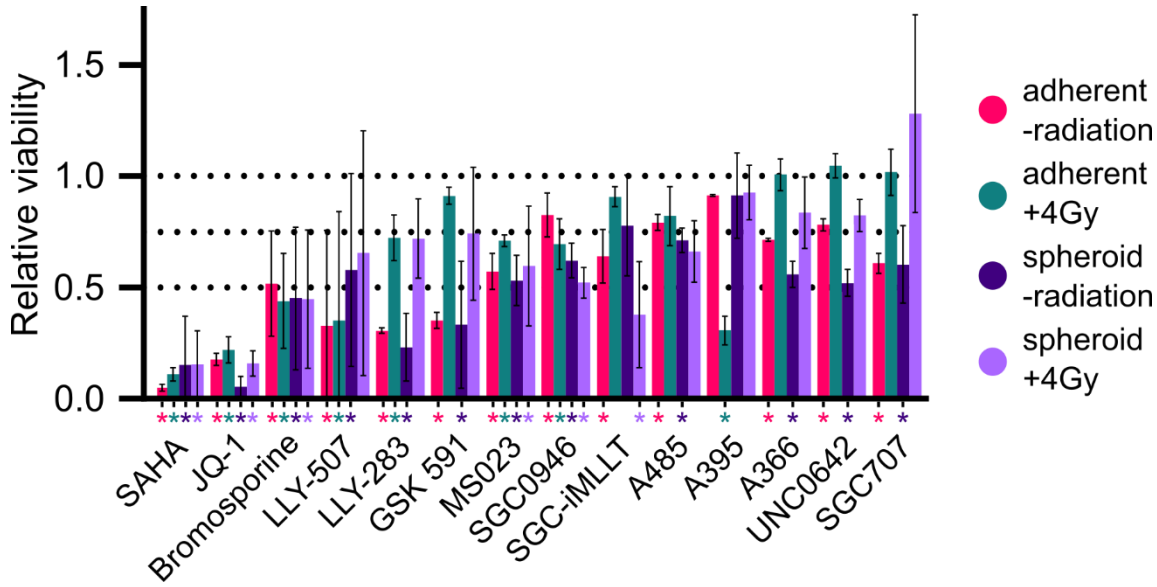

Figure 3.7 - Comparison of hits between screen conditions

*The relative viability of HSJD-DIPG-007 after treatment with probes that significantly reduced more than 25% in at least one of the growth conditions tested (adherent or spheroid and with or without 4 Gy of radiation, by multiple t-tests). Bars show the mean and standard deviation of three independent repeats. Bars marked with * are significant discoveries according to multiple t-tests (treated compared to vehicle, two-stage linear step-up multiple test correction, Q = 1%).*

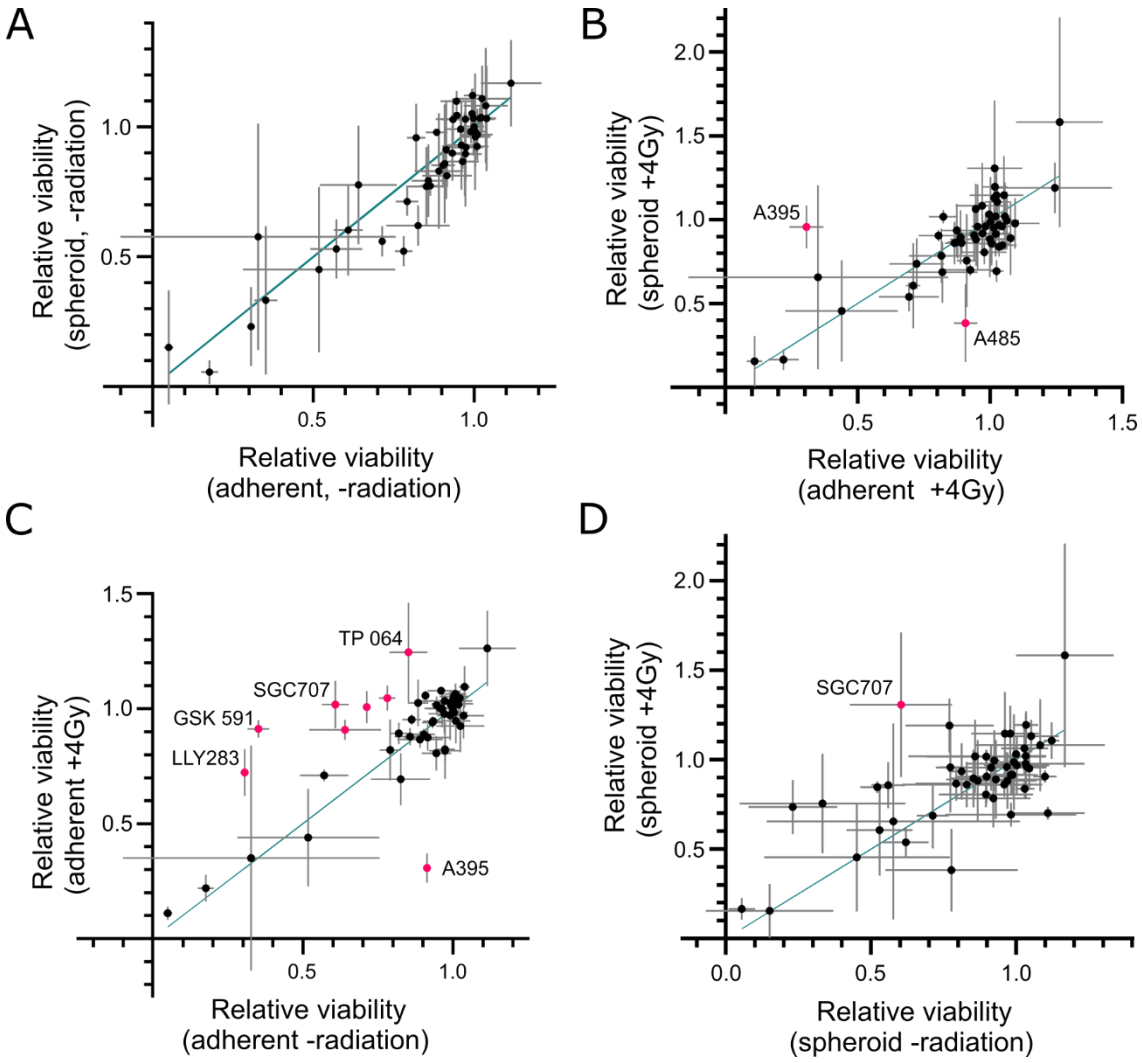

Figure 3.8 - Comparison of viability between different screen conditions highlights probes that are less effective in combination with radiation treatment

Graphs compare the relative viability (mean of 3 independent repeats, with SD) of (A) adherent versus spheroid culture without radiation, (B) adherent versus spheroid culture with radiation, (C) with or without a radiation treatment in adherent culture, or (D) with or without radiation treatment in spheroid culture. Blue line indicates a perfect correlation. Probes that had a significantly different effect in the two conditions (multiple t-tests, FDR approach, q = 1%) are highlighted in pink.

3.2.6. Full growth inhibition curves confirm PRMT5 inhibition as the most significant new treatment affecting viability

A chemical probe screen allows many compounds to be tested rapidly and promising hits to be identified, but is prone to false positive or false negative results because of the relatively low number of technical and independent repeats performed. To overcome such limitations hits were validated with full serial dilutions in HSJD-DIPG-007 and HSJD-DIPG-011 cells to generate growth inhibition curves. As in the full screen, the probes were tested over a 7-day growth period, but were now tested at 8 different concentrations over at least 4 orders of magnitude. The radiation treatment was excluded to streamline the experiment. The experiments were performed using spheroids only, because spheroid culture requires fewer cells and because growth in spheroid or adherent culture did not impact the efficacy of PRMT family probes.

As such validation is more experimentally involved, a subset of high interest probes was selected for further characterisation. All probes targeting PRMT family proteins (LLY-283, GSK591, TP064, MS023, SGC707, MS049) were validated to confirm that the positive hits (LLY-283, GSK591, MS023 and SGC707) and negative compounds (TP064 and MS049) were true findings (**Figure 3.9**, **Figure 3.10**, **Figure 3.12**). SAHA and JQ-1 were not validated, as they were included only as positive controls. LLY-507 and Bromosporine were also excluded as their promiscuity would confound downstream mechanistic investigation. The p300 inhibitor A485 was included as the best specific, non-PRMT hit (**Figure 3.8**). Despite being relatively ineffective in the epigenetic probe screen, the PRC2 inhibitors UNC1999 and A395 were chosen for further analyses (**Figure 3.11**) because of the previously reported efficacy of PRC2 inhibition in DIPG models (Mohammad *et al.*, 2017; Zhang *et al.*, 2017). These 9 probes were validated with three independent growth inhibition experiments.

Although the SGC chemical probes were designed to be highly specific and have detailed inhibition profiles, residual off-target activity could still contribute to the effects observed. For

this reason, the epigenetic probes were each developed with a closely matched negative control compound with a near identical chemical scaffold, but >100-fold less binding potency against the target (henceforth referred to as target-negative controls). As each hit was validated, the same concentrations of the target-negative control for each probe were also tested (except for MS049, for which there was none available). As long as the target-negative control is inactive, this further confirms that hits are effective because of on-target activity only. In all but one effective probes the target-negative control was either completely inactive. The only target-negative probe that was not completely inactive was LLY-284, which was 3 orders less effective than LLY-283 (**Figure 3.9**, **Figure 3.10**, **Figure 3.11**), a result which is in accordance with the published relative activity of LLY-284 against PRMT5 (Bonday *et al.*, 2018). As this data demonstrates that the activity of the epigenetic probes of interest likely is due to on-target activity, these target-negative controls were excluded from subsequent testing.

The growth inhibition curves broadly confirmed the relative effectiveness of each probe in the initial screen (i.e. TP064, MS049, UNC1999 and A395 were largely ineffective, **Figure 3.10, Figure 3.11**), whereas GSK591 and LLY-283 were incredibly potent, with the lowest GI_{50} being 13 nM (95% CI 8-20 nM) for GSK591 treatment of HSJD-DIPG-007 cells (**Figure 3.12**). Demethylation of the PRMT5 target Sm B/B'/N was confirmed by immunoblot (**Figure 3.12**). Again, PRMT5 inhibition was the most effective treatment for these cells and so characterisation of PRMT5 inhibition continued.

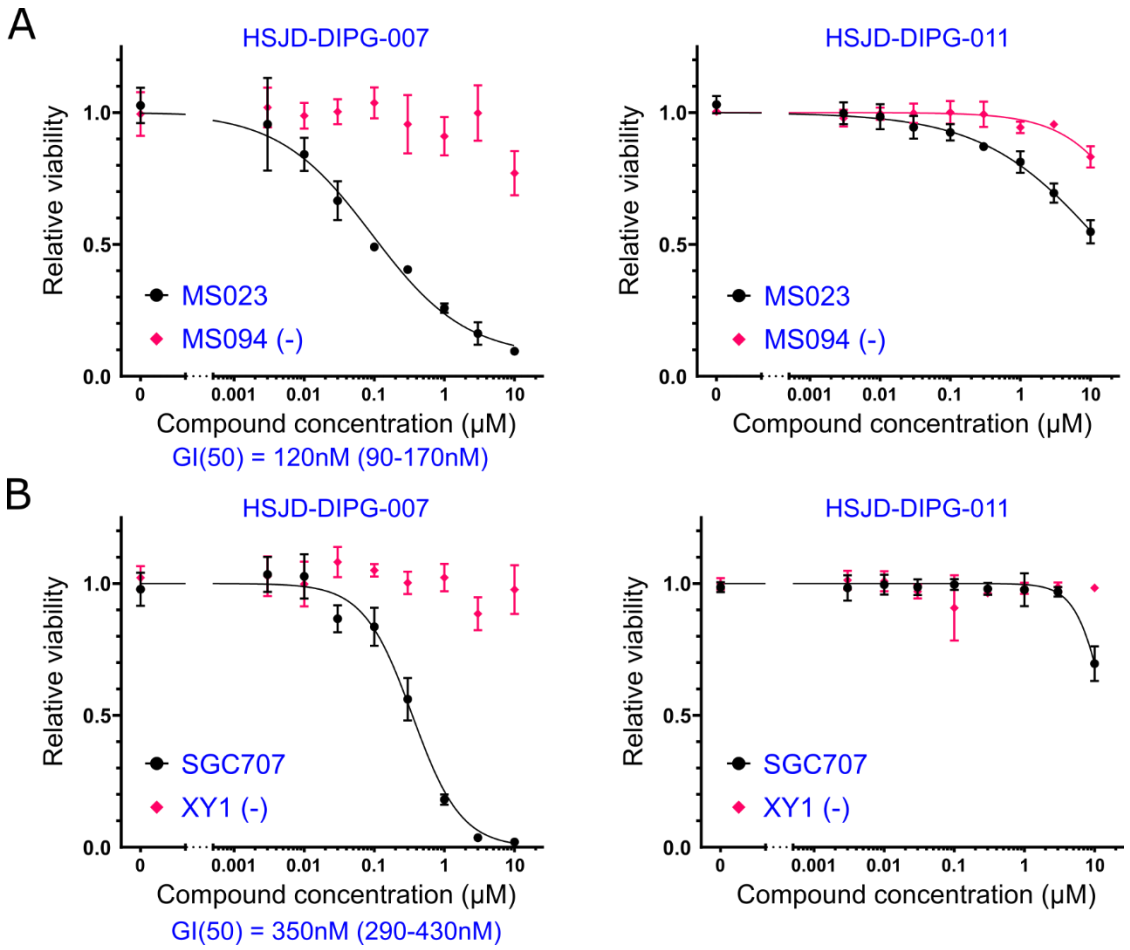

Figure 3.9 - Validation of PRMT family hits from epigenetic probe screen

Graphs showing the viability (relative to a DMSO vehicle control) of HSJD-DIPG-007 (left panels) or HSJD-DIPG-011 (right panels) single spheroids after a 7-day treatment with the type I PRMT inhibitor MS023 and its target-negative control MS094 (A) or the PRMT3 inhibitor SGC707 and its target-negative control XY1 (B). Points are the mean of 3 independent repeats ± SD. Where they could be calculated GI_{50} values are included below each graph. GI_{50} values were calculated by interpolation of the curve generated as described in section 2.4.3 (with Y_{max} additionally constrained to 1).

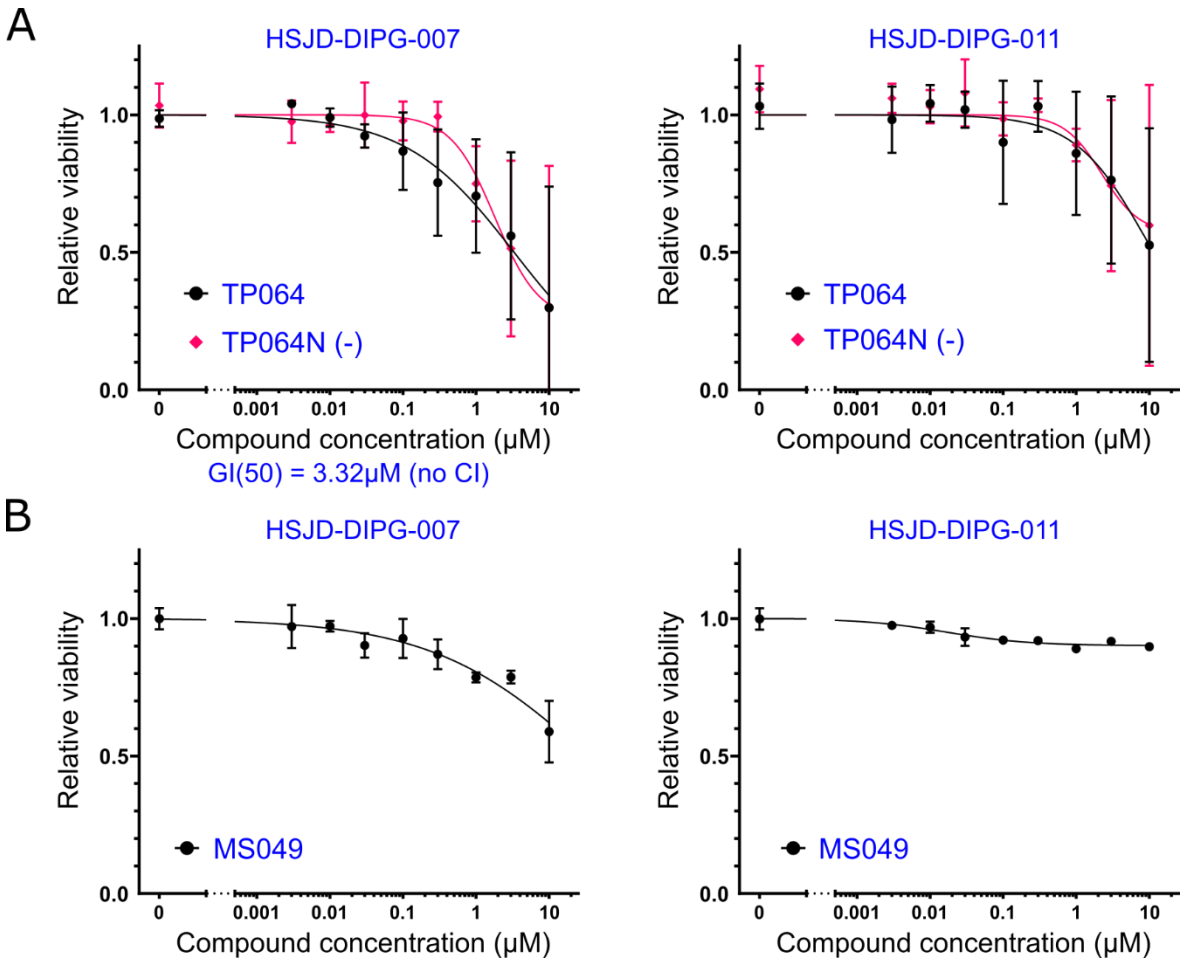

Figure 3.10 - Validation of PRMT probes not identified as hits in initial epigenetic probe screen

Graphs showing the viability (relative to a DMSO vehicle control) of HSJD-DIPG-007 (left panels) or HSJD-DIPG-011 (right panels) single spheroids after a 7-day treatment with the PRMT4 inhibitor TP-064 versus its target-negative control, TP-064N ***(A)*** *or the PRMT4/6 inhibitor MS049* ***(B)****. Points are the mean of 3 independent repeats ± SD. Where they could be calculated* GI_{50} *values are included below each graph.* GI_{50} *values were calculated by interpolation of the curve generated as described in section 2.4.3 (with* Y_{max} *additionally constrained to 1).*

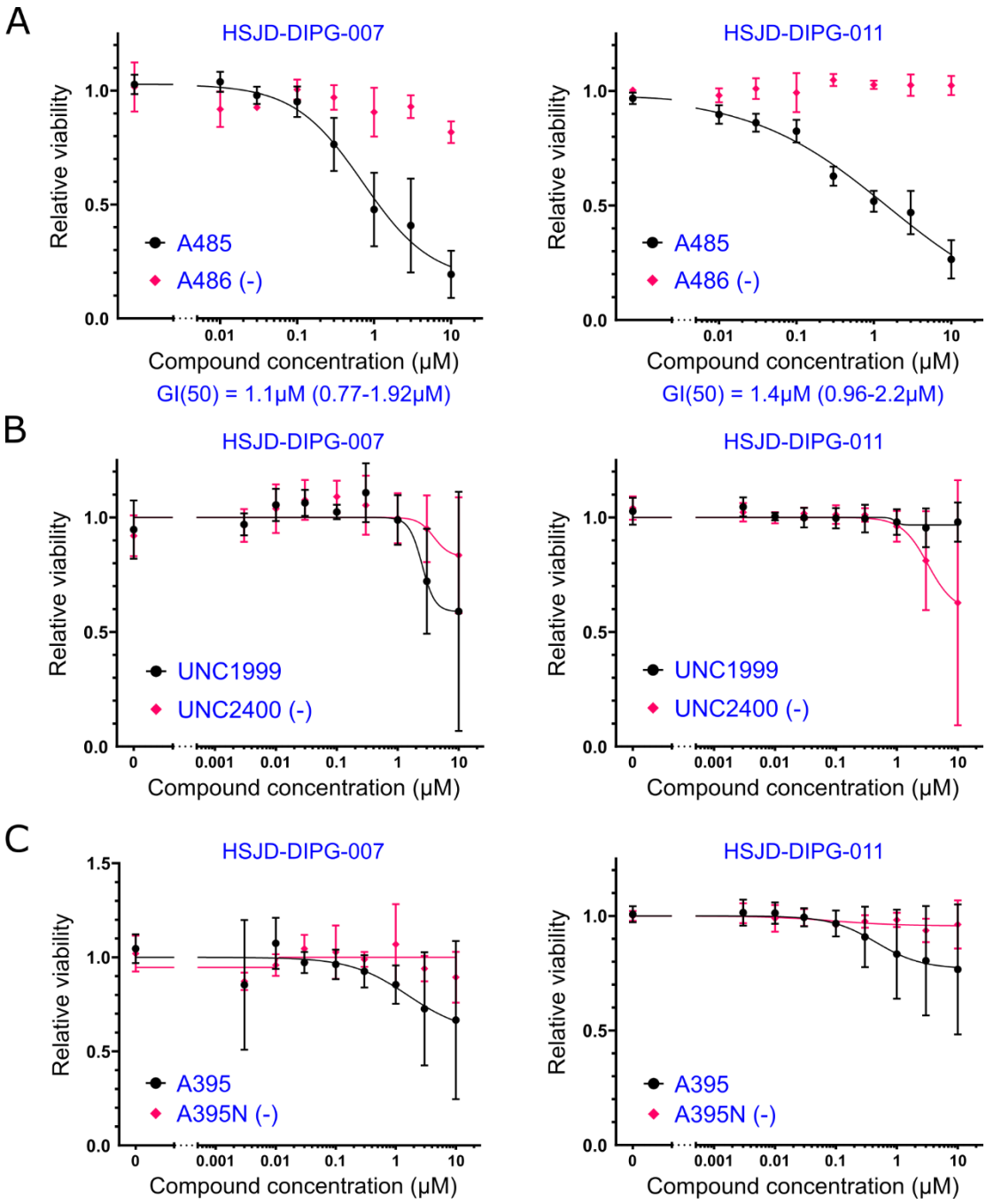

Figure 3.11 - Validation of non-PRMT probes identified in epigenetic probe screen

Graphs showing the viability (relative to a DMSO vehicle control) of HSJD-DIPG-007 (left panels) or HSJD-DIPG-011 (right panels) single spheroids after a 7-day treatment with the p300/CBP inhibitor A485 versus its target-negative control, A486 ***(A)*** *or the EZH1/2 inhibitor UNC1999 versus its target-negative control, UNC2400* ***(B)****, or the EED inhibitor A395 versus its target-negative control A395N* ***(C)****. Points are the mean of 3 independent repeats ± SD. Where they could be calculated GI_{50} values are included below each graph (Using interpolation of the curve generated as described in section 2.4.3).*

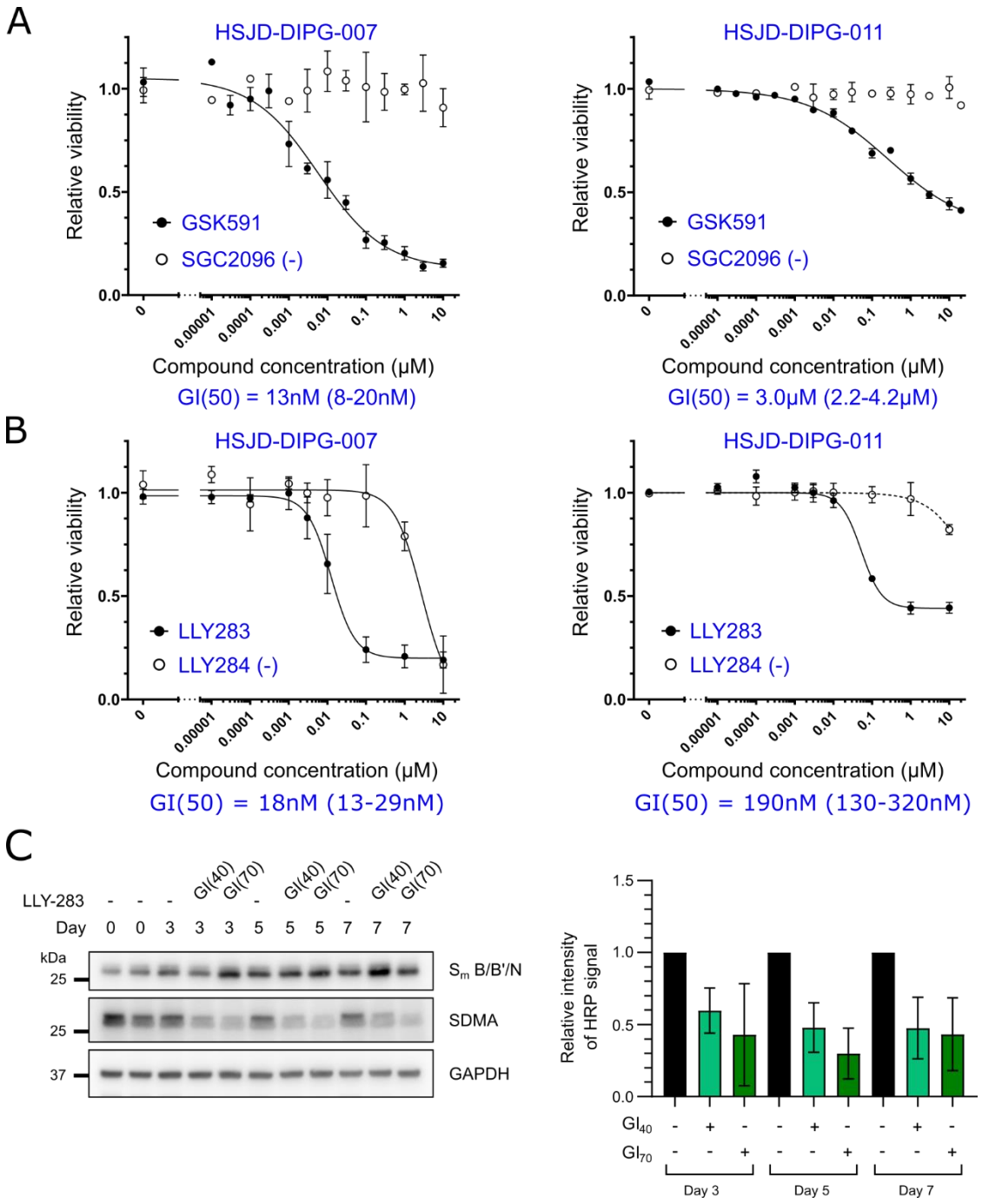

Figure 3.12 – Validation that PRMT5 inhibition potently reduces DIPG cell viability

The viability (relative to a DMSO vehicle control) of HSJD-DIPG-007 or HSJD-DIPG-011 single spheroids after 7 days of treatment with the PRMT5 inhibitor GSK591 and its target negative control (SGC2096) ***(A)****, or the PRMT5 inhibitor LLY-283 and its target negative control (LLY284)* ***(B)****. In panel A each point is the mean of 2-3 independent repeats ± SD, and in panel B points are the mean 3 independent repeats ± SD. All curves were calculated from 3 independent repeats as described in section 2.4.3, and the GI_{50} values (with 95% CI) interpolated from this curve.* ***(C)*** *Left: Representative immunoblot (from 3 independent repeats) showing the demethylation of Sm B/B'/N after treatment with LLY-283. Right: Quantification of band intensity of all 3 independent repeats.*

3.2.7. DIPG cell lines with an ACVR1 mutation are more sensitive to PRMT5 inhibition

Sensitivity to PRMT5 inhibition differed between the HSJD-DIPG-007 and HSJD-DIPG-011 cell lines, so it was of interest to extend these treatments to a larger panel of cell lines to gain a more comprehensive picture of DIPG sensitivity to PRMT5 inhibition. Cell lines SU-DIPG-IV (*ACVR1* G328V, *HIST1H3B* K27M) and SU-DIPG-XXI (*ACVR1* G328W, *HIST1H3B* K27M) were included to contrast the sensitivity of cells with *HIST1H3B* K27M mutations rather than the *H3F3A* K27M present in HSJD-DIPG-007 and HSJD-DIPG-011. Similarly, the glioblastoma cell line HSJD-GBM-002 (*ACVR1* WT, *H3F3A* G34R) was included to test the sensitivity of a cell lines without a histone H3K27M mutation. SU-DIPG-IV and SU-DIPG-XXI also provided additional ACVR1 mutants to compare to the ACVR1 wild-type cell lines SU-DIPG-VI and HSJD-GBM-002. With these additional cell lines, a total of 6 were chosen for further tested with PRMT5 inhibition, including pairings that allowed the comparison of several pertinent DIPG-associated mutations.

The unreliable results of the HSJD-DIPG-011 screen highlighted the need for more careful optimisation of the spheroid seeding densities, as outlined here. Again, U-bottomed 384 well plates were seeded with titrations of each of the cell lines of interest. Previously, selecting the HSJD-DIPG-011 seeding density according to the size of spheroids after 3 days lead to a low signal to noise ratio because it did not account for their slower growth rate versus other cell lines. Here, seeding densities were selected based on the size of spheroids after the full length of the assay (at least 7 days) to ensure all spheres were of an appropriate size when measured. After 8 days of growth the untreated HSJD-DIPG-007 spheroids were 350-400 µm in diameter (**Figure 3.13**), and because this assay was successful this was chosen as the desired spheroid diameter. Accordingly, a seeding density of 2000 cells per well was selected for the cell lines HSJD-GBM-002, SU-DIPG-VI, HSJD-DIPG-011, and SU-DIPG-XXI (**Figure 3.13**).

The panel of cell lines demonstrated a wide range of sensitivities to PRMT5 inhibition that can now be compared to their known mutations. Responses to PRMT5 inhibition ranged from exquisite sensitivity, with HSJD-DIPG-007 having GI_{50} values of just 13 nM (95%CI 3-20 nM) and 18 nM (95% CI of 13-29 nM) for GSK-591 and LLY-283 respectively (**Figure 3.12**a), to HSJD-GBM-002 having only a 10% reduction in viability with exposure to 10 µM of either PRMT5 inhibitor (**Figure 3.14c**). There was, however, some evidence of an intrinsically resistant population demonstrating a 20-25% residual viability following treatment of HSJD-DIPG-007 (**Figure 3.12**). When the GI_{50} value of each cell line was compared to the cell line's mutation status, the 3 most sensitive cell lines were all ACVR1 mutant. (This observation is followed up in Chapter 5). Thus, testing PRMT5 inhibition in a panel of DIPG and glioblastoma cells lines shows that PRMT5 inhibition can potently reduce the viability of multiple ACVR1 mutant cell lines.

Table 3.2 – ACVR1 mutant cells are more sensitive to PRMT5 inhibition

Cell line	Histone mutation	ACVR1 mutation	LLY-283 GI_{50} (µM)	GSK591 GI_{50} (µM)
HSJD-DIPG-007	H3.3 K27M	R206H	0.018	0.013
SU-DIPG-XXI	H3.1 K27M	G328W	0.031	0.057
SU-DIPG-IV	H3.1 K27M	G328V	0.046	0.079
HSJD-DIPG-011	H3.3 K27M	WT	0.191	2.981
HSJD-GBM-002	H3.3 G34R	WT	>10	>10
SU-DIPG-VI	H3.3 K27M	WT	>10	>10

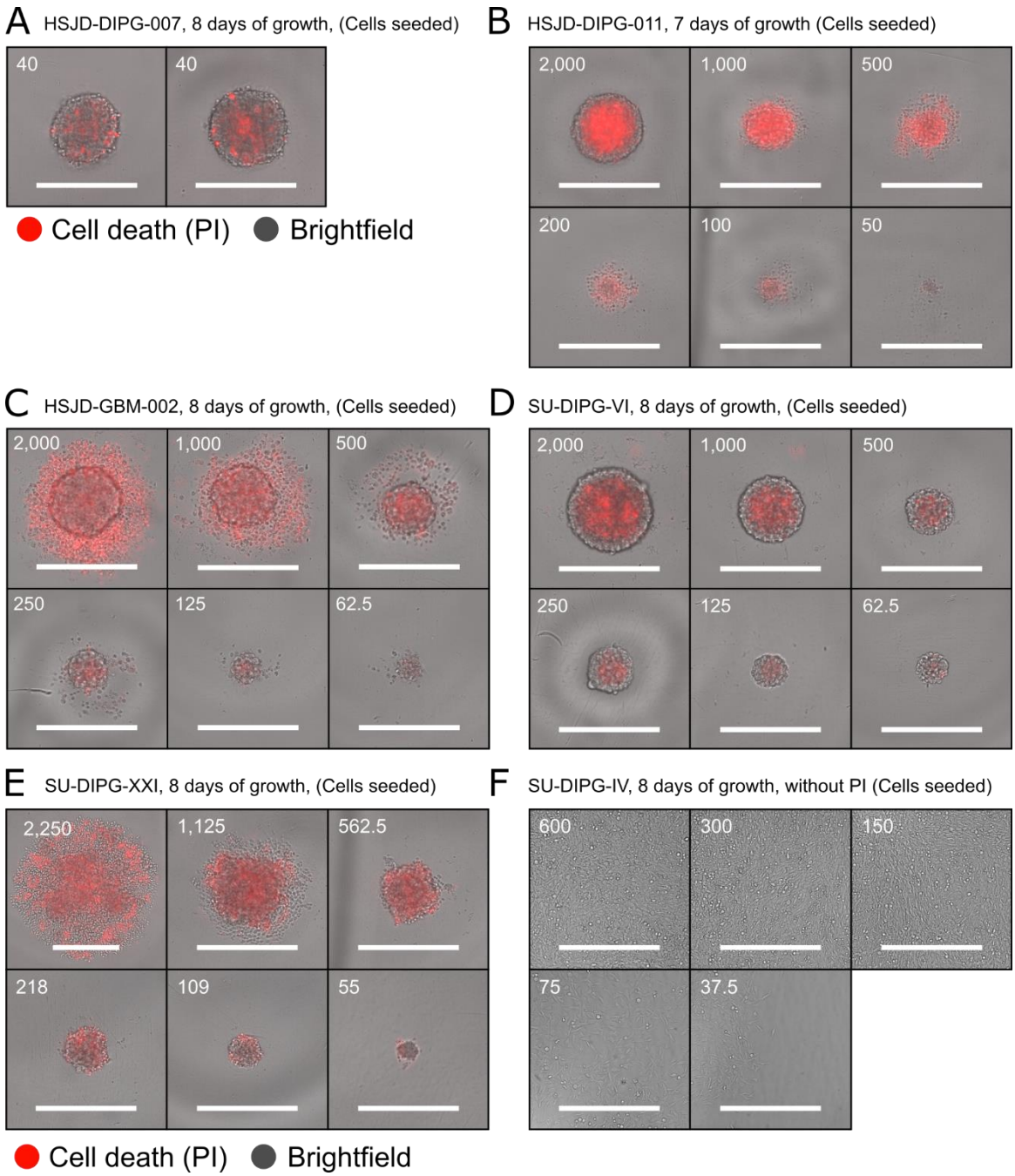

Figure 3.13 – Seeding optimisation for additional cell lines for epigenetic probe screen validation

Merged brightfield and fluorescence (propidium iodide, as a cell death marker) images of HSJD-DIPG-007 (A), HSJD-GBM-002 (B), SU-DIPG-IV (C), SU-DIPG-VI (D), SU-DIPG-IV (E) or SU-DIPG-XXI (F) cells after 7/8 days of growth (as indicated). Images are labelled with the number of cells seeded and scale bars are 500 µm.

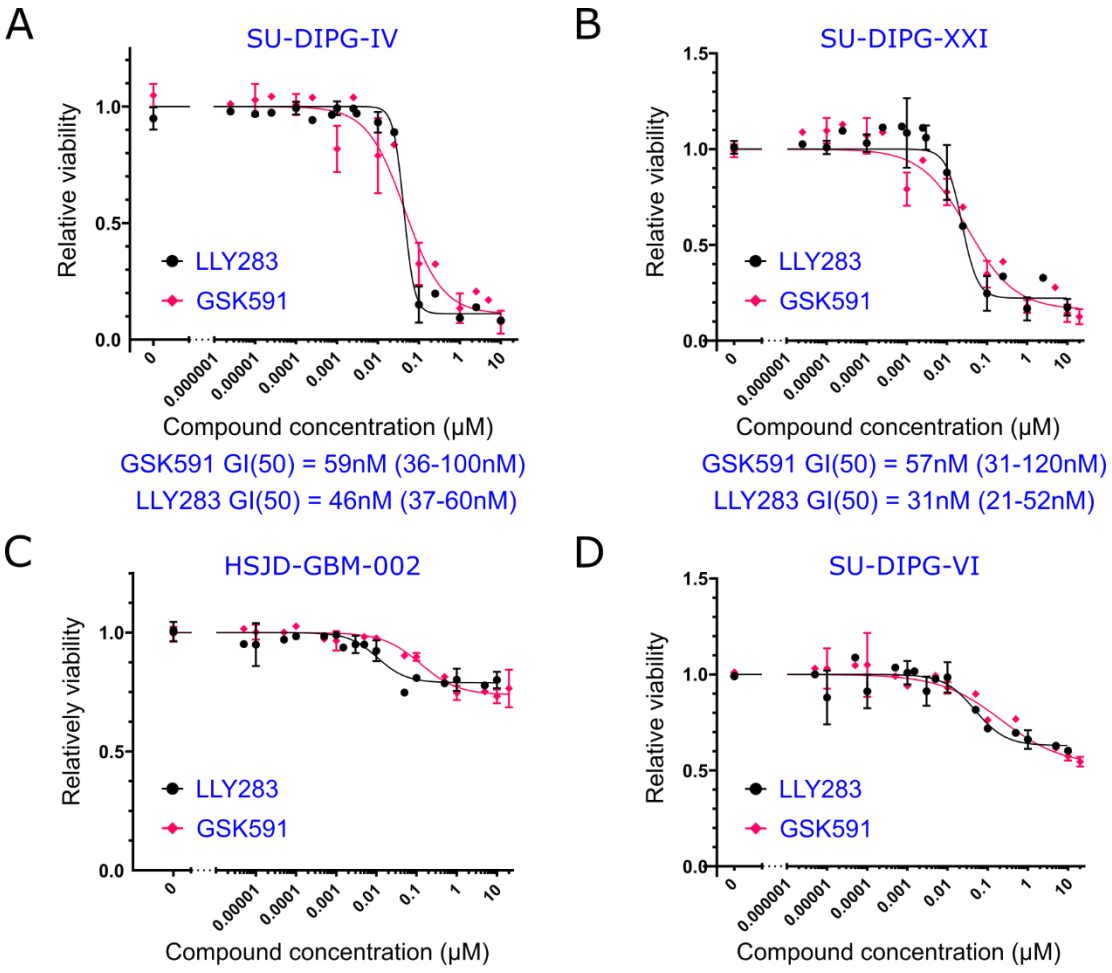

Figure 3.14 - PRMT5 inhibition can reduce the viability of additional ACVR1 mutant DIPG cell lines

*Graphs showing the viability (relative to a DMSO vehicle control) of **(A)** SU-DIPG-IV (ACVR1 G328V), **(B)** SU-DIPG-XXI (ACVRV1 G328W), **(C)** HSJD-GBM-002 (ACVR1 WT), or **(D)** SU-DIPG-VI (ACVR1 WT) single spheroids after 7 days of treatment with the PRMT5 inhibitor LLY-283 (black) or GSK591 (pink). Curves are derived from 3 independent repeats where each data point is the mean 1 or mean ± SD of 2 independent repeats. GI_{50} values (quoted with a 95% CI where calculated) were interpolated from curves generated as described in section 2.4.3.*

3.2.8. PRMT5 inhibition does not induce cell death

A drop in viability could be due to a reduction in proliferation or an increase in cell death (Ucker and Levine, 2018). To measure the level of cell death induced by PRMT5 inhibition PI was included in the growth medium over the course of a 7-day treatment of SU-DIPG-IV cells. Two ALK2 inhibitors (M4K2009 and M4K2163) were included as a positive control as these were previously shown to induce cell death (M4K Pharma, personal communication). M4K2009 and M4K2163 induced a maximum of 2.3-fold increase PI staining at 3 µM and 2.1-fold at 1 µM, respectively, which fell at higher concentrations because cell death became so great that there were fewer cells to stain positively (Figure 3.15). In contrast, PRMT5 inhibition with either GSK591 or LLY-283 did not induce a peak of cell death at any concentration (**Figure 3.15**). This implies that PRMT5 inhibition impairs proliferation rather than induces cell death.

Together these experiments show that the growth of *ACVR1* mutant DIPG cells is highly sensitive to the inhibition of PRMT5. However, the decrease in viability appears to not be associated with cell death.

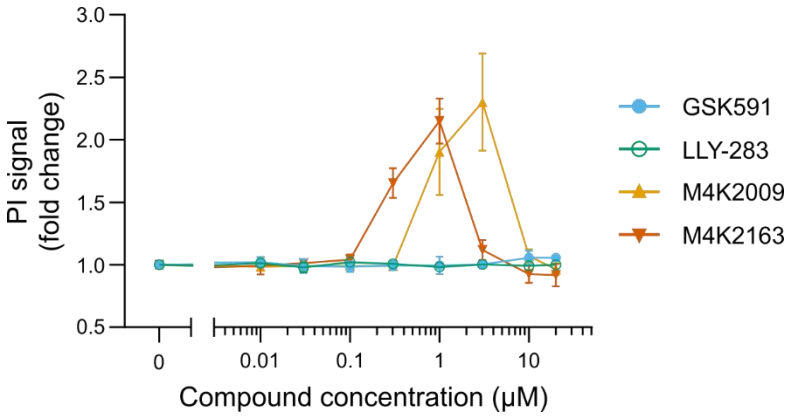

Figure 3.15 - PRMT5 inhibition does not induce cell death

SU-DIPG-IV cells were treated with the indicated concentration of the PRMT5 inhibitors GSK591 or LLY-283, or ALK2 inhibitors M4K2009 or M4K2163 for 7 days in the presence of 1 µg/mL PI. Fluorescence signal was measured with a ClarioSTAR plate reader and normalised to the vehicle control for each compound. Data points represent the mean of 3 independent repeats ± SD.

3.3. Discussion

A non-biased screen of the SGC epigenetic probe set identified 10 probes that significantly reduced HSJD-DIPG-007 viability by more than 25% (relative to a vehicle control). Of the hits, 5 inhibited members of the PRMT family, and the 2 most potent of those inhibited PRMT5 specifically by distinct molecular mechanisms. Full growth inhibition curves were generated for PRMT5 inhibition in a further 4 cell lines which demonstrated a range of sensitivities to PRMT5 inhibition. A glioblastoma cell line (*ACVR1* WT, *H3F3A* G34R) was insensitive to PRMT5 inhibition whereas *ACVR1, H3K27M* cells were exquisitely sensitive to PRMT5 inhibition and all had GI_{50} values under 80 nM for both probes. A similar range in sensitivity to PRMT5 has previously been observed when screening adult glioblastoma cell lines (Sachamitr *et al.*, 2021), suggesting that genetic variance in both diseases contributes to sensitivity to PRMT5 inhibition.

Multiple known differences between cell lines were considered, including their known mutations and whether the cell like was from autopsy or biopsy. Interestingly, the three cell lines most sensitive to PRMT5 inhibition all had mutations in *ACVR1,* although one *ACVR1* WT cell line was also sensitive to LLY-283. Previous publications do suggest that PRMT proteins could directly regulate ACVR1 signalling: PRMT1 can activate BMP signalling by methylating and inactivating the inhibitory protein SMAD6 (Xu *et al.*, 2013) and PRMT5 co-purifies with SMAD2, 3 and 4 (Tabata *et al.*, 2009). However, the observation made here that *ACVR1* mutant cells are more sensitive to PRMT5 inhibition is just a correlation made in a small number of cell lines and is more thoroughly interrogated in Chapter 5.

The epigenetic probe screen was carried out on DIPG cells grown both adherently and as spheroids, to ensure no growth dependent hits were missed. This comparison was necessary because of the multiple cases in which the method by which a cancer cell line is cultured can alter the outcome of a compound screen (Howes *et al.*, 2007; Vinci *et al.*, 2012). In the

experiments without radiation treatment, the results of the adherent and spheroid versions of the screen were well correlated; no probes behaved significantly differently between growth conditions. This could be because laminin is primarily a component of the basement membrane rather than the ECM in the brain parenchyma (Howes *et al.*, 2007; Mentlein, Hattermann and Held-Feindt, 2012; Vinci *et al.*, 2012) and is therefore unlikely to be integral to DIPG function. Alternatively, the DIPG cells in culture may have been surrounded by endogenous ECM in both growth conditions because glioma cells can produce their own ECM (Bourdon *et al.*, 1983; Su *et al.*, 2006; Qi *et al.*, 2019). At least in this case, both growth models equally recapitulate the disease, and beyond the initial screen all experiments were conducted without including laminin.

In contrast, the inclusion of a radiation treatment significantly altered the effect of 8 treatments in adherent culture, and 1 in spheroid culture. This could simply reflect the increased variance and reduced signal to noise ratio in the data when the radiation treatment was included. However, because 4 of 6 PRMT probes were significantly less effective in combination with radiation it is worth considering whether the mechanism by which PRMT inhibition reduces viability is incompatible with radiation treatment. For example, if PRMT5 inhibition arrested or slowed the G1-S cell cycle transition (Cho *et al.*, 2012; Zheng *et al.*, 2013; Banasavadi-Siddegowda *et al.*, 2017), this could protect cells from DNA damage by allowing time for DNA repair. However, if that were the case one might expect that cells from autopsy (i.e. post relapse from radiotherapy) to be less sensitive to PRMT5 inhibition, but this was not the case. The interaction between PRMT5 inhibition and radiation treatment was not pursued further in this study, however, the possibility that PRMT5 inhibitors may be relatively less effective in combination with radiotherapy should be carefully monitored in ongoing clinical trials.

One limitation of small molecule inhibitors is that the effects seen could be due to off-target effects of the probe, but this risk has been mitigated in two ways in this study. Closely matched target-negative control compounds, which do not inhibit the target protein, were tested alongside the active probes and failed to induce a similar reduction in DIPG viability. Additionally, the two PRMT5 probes found to be effective are structurally different and have different inhibitory mechanisms: LLY-283 binds to the S-adenosylmethionine (SAM) cofactor pocket (Bonday *et al.*, 2018), whereas GSK591 binds in the peptide binding groove of PRMT5 (Chan-Penebre *et al.*, 2015). Given inactivity of target-negative controls, and the improbability that two diverse PRMT5 probes would have the same off-target activity, it is very unlikely that the observed phenotype is due to an off-target effect.

Alongside the non-biased set of SGC epigenetic probes, several probes were included to test hypotheses proposed elsewhere, but none produced results as promising as that of the PRMT5 inhibitor. EZH2 inhibition has been tested extensively as a means to kill DIPG cells (Mohammad *et al.*, 2017; Zhang *et al.*, 2017), but appeared ineffective in this screen. Indeed, most published experiments use EZH2 inhibitors at a concentration in excess of 1 µM (Mohammad *et al.*, 2017) or in combination with other inhibitors (Zhang *et al.*, 2017). I hypothesise that in a system where EZH2 activity is already suppressed, that inhibiting it further would be inefficient. Instead, this screen has identified 16 inhibitors that potently reduce DIPG viability at a concentration two orders lower than that of EZH2 inhibitors.

In this chapter, a non-biased screen of small molecule inhibitors of epigenetic mediators of the patient derived DIPG cell line HSJD-DIPG-007 (*ACVR1* R206H, *H3F3A* K27M) identified the PRMT family as necessary for DIPG viability. By comparing the reduction in viability in response to inhibition of each PRMT family member it was found that the two most potent probes both inhibited PRMT5, by distinct molecular mechanisms. PRMT5 inhibition was tested in a total of 5 DIPG cell lines. This demonstrated a range of sensitivity to PRMT5 inhibition, but all *ACVR1*

mutant cell lines were exquisitely sensitive to PRMT5 inhibition even though it did not induce cell death.

However, this project aims not just to find a novel therapeutic target for the treatment of DIPG, but to describe why these cells are sensitive to the inhibition of this target, to help better understand and treat DIPG in future. For this reason, the next stage of the project (Chapter 4) will focus on interrogating what PRMT5 inhibition does to the cell by analysing the transcriptome following PRMT5 inhibition.

Chapter 4. The functional impact of PRMT5 inhibition *in vitro* and *in vivo*

4.1. Background

PRMT5 is a promising therapeutic target for several reasons. In Chapter 3, PRMT5 was identified as necessary for DIPG cell viability from a screen of inhibitors of epigenetic proteins. The overexpression of PRMT5 correlates with tumour grade or progression in a variety of tumour types, including glioma (Cho *et al.*, 2012; Bao *et al.*, 2013; Han *et al.*, 2014; Wu *et al.*, 2017; Gullà *et al.*, 2018; Sachamitr *et al.*, 2021). Thus, a range of PRMT5 small molecule inhibitors have entered phase I or phase II clinical trials (ClinicalTrials.gov identifiers NCT03886831, NCT04676516, NCT03573310, NCT03854227 and NCT04089449). In the brain, PRMT5 is highly expressed in the oligodendroglial lineage (Scaglione *et al.*, 2018) and regulates processes including neural differentiation and developmental myelination (Blanc and Richard, 2017; Scaglione *et al.*, 2018). Therefore, PRMT5 was chosen as the focus for further pre-clinical evaluation.

Post translational modifications are an indispensable mechanism for the dynamic regulation of protein activity. One such protein modification is arginine methylation, which in mammals is mediated by nine protein arginine methyltransferases (PRMTs) (Hwang *et al.*, 2021). These PRMTs are divided into type I (catalyse asymmetrical or mono-methylation), type II PRMTs (symmetrical or mono-methylation) and type III PRMTs (mono-methylation only) (Hwang *et al.*, 2021). As reviewed previously (Mulvaney *et al.*, 2021), the type II PRMT5 symmetrically dimethylates its substrates by catalysing the two-step transfer of methyl groups from two S-adenosyl methionine (SAM) molecules onto an arginine residue (Gary and Clarke, 1998; Stopa, Krebs and Shechter, 2015). This requires the assembly of a methylosome complex that includes a PRMT5:MEP50 hetero-octamer, and variable substrate adaptors that provide substrate

specificity (Sun *et al.*, 2011; Ho *et al.*, 2013). With this mechanism, PRMT5 regulates the activity of countless proteins by direct methylation.

In addition to directly regulating protein activity, PRMT5 regulates protein expression by methylating histones or splicing proteins. Histone methylation is a well characterised mechanism for regulating genes expression by altering DNA accessibility (Whetstine, 2010). PRMT5 represses transcription by dimethylating either histone H4 (H4R3me2s) or H3R8me2s which allows recruitment DNA methyltransferase 3a (DNMT3a) (Zhao *et al.*, 2009) or prevents binding of the SWI/SNF chromatin remodelling complex (Pal *et al.*, 2004) respectively. PRMT5 mediated histone methylation is generally considered to repress transcription, however, by demethylating H3R2, PRMT5 mediated chromatin opening by promoting recruitment of the mixed-lineage leukemia (MLL)-family coactivator complex, which in turn promotes H3K4me3 – a marker of active promoters (Chiang *et al.,* 2017; Migliori *et al.*, 2012). Furthermore, PRMT5 regulates the formation and localisation of the spliceosome complex by methylating its components, for example the S_m family (Meister *et al.*, 2001; Hebert *et al.*, 2002; Hwang *et al.*, 2021). Thus, PRMT5 depletion leads to reduced constitutive and alternative splicing (Bezzi *et al.*, 2013). In the brain, this is of particular relevance, given that the complexity of RNA splicing may differentiate the human brain from that of other species (Barbosa-Morais *et al.*, 2012). As such, by modulating protein expression via chromatin organisation and splicing, and post-translational activity by direct methylation, PRMT5 regulates multiple cellular processes, as outlined below.

PRMT5 promotes progression through the cell cycle, as reviewed in detail by (Raposo and Piller, 2018). PRMT5 promotes the expression of genes including *CDK4/6*, and cyclins D1 and D2 (Wei *et al.*, 2012). Disrupted splicing of cell cycle products following PRMT5 depletion impairs the proliferation of glioblastoma cells (Bezzi *et al.*, 2013; Sachamitr *et al.*, 2021). Furthermore, PRMT5 binds to CDK4 and releases it from CDK inhibitor 2A (CDKN2A) allowing completion of the G1-S transition (Yang *et al.*, 2016). Depending on the cellular context, PRMT5 can either

mediate cell cycle arrest or apoptosis by methylating p53 such that its promoter binding specificity is altered (Jansson *et al.*, 2008). Similarly, in undifferentiated glioblastoma neurospheres, PRMT5 deficiency causes G1 cell cycle arrest, whereas in differentiated glioblastoma cells it triggers apoptosis (Banasavadi-Siddegowda *et al.*, 2017). Thus, depletion of PRMT5 can impair proliferation or trigger proliferation in multiple tumour types (Cho *et al.*, 2012; Bezzi *et al.*, 2013; Rengasamy *et al.*, 2017; Sachamitr *et al.*, 2021).

PRMT5 regulates stemness and the differentiation of multiple tissues including the nervous system as reviewed by (Blanc and Richard, 2017). PRMT5 is necessary for neural stem cell survival and postnatal brain development (Bezzi *et al.*, 2013) and its depletion can eliminate cancer stem cells (Jin *et al.*, 2016). Furthermore, alongside Yamanaka factors PRMT5 can reprogram somatic cells into pluripotent stem cells (Nagamatsu *et al.*, 2011). In contrast, PRMT5 expression is necessary for differentiation of oligodendrocyte precursor cells (OPCs) into mature oligodendrocytes (Huang *et al.*, 2011; Scaglione *et al.*, 2018). Thus, depletion of PRMT5 leads to hypomyelination (Scaglione *et al.*, 2018), which is of particular note because of the coincidence of DIPG diagnosis with a period of developmental myelination (Loveson and Fillmore, 2018). Importantly, FOP patients can suffer from demyelination (Kan *et al.*, 2012), suggesting that ACVR1 could be involved in the same developmental process. H3K27M arrests DIPG cells in an immature OPC-like state (Filbin *et al.*, 2018; Silveira *et al.*, 2019) and promoting differentiation by inhibiting PRMT5 could impair stemness or proliferation of DIPG.

By altering the activity of numerous transcription factors PRMT5 also regulates cellular metabolism in multiple tissues. Master regulator of lipid metabolism, Sterol Regulatory Element Binding Transcription Factor 1a (SREBP1a), is methylated and stabilised by PRMT5 in hepatocytes and adipocytes (Liu *et al.*, 2016; Jia *et al.*, 2020). Similarly, by methylating the nuclear receptor small heterodimer partner (SHP), PRMT5 indirectly inhibits transcription factors that regulate lipid and glucose synthesis in the liver (Kanamaluru *et al.*, 2011). Given that

H3K27M metabolically reprograms DIPG cells (Chung *et al.*, 2020), this is another aspect of DIPG tumorigenesis regulated by PRMT5.

Finally, some have described roles for PRMT5 or arginine methylation in regulation of signalling processes relevant to DIPG specifically:

25% of DIPG patients carry missense mutations in the kinase receptor ACVR1 which render it sensitive to activation an additional ligand – Activin A – thus increasing BMP signalling within DIPG cells (Taylor *et al.*, 2014). PRMT1 can activate BMP signalling by methylating and causing dissociation of the inhibitory SMAD6 from the BMPRII receptor thus allowing activation of the effector SMADs by phosphorylation (Xu *et al.*, 2013). It is worth noting that as PRMT1 mediates asymmetrical methylation, it often opposes the action of PRMT5 (Blanc and Richard, 2017), therefore PRMT5 may inactivate BMP signalling. This is supported by the observation that PRMT5 depletion increases expression of Id2 and Id4 (Huang *et al.*, 2011) which are often expressed downstream of BMP signalling activation (Hollnagel *et al.*, 1999; Katagiri *et al.*, 2002; Kurooka *et al.*, 2012). However, others have reported that PRMT5 localises to the promoter of the inhibitory SMAD7 as part of a repressive complex which maintains low basal levels of SMAD7 (Tabata *et al.*, 2009).

At least 75% of patients carry H3K27M mutations which impair polycomb repressive complex 2 (PRC2) activity and sequester it on the genome (Chan *et al.*, 2013; Lewis *et al.*, 2013) leading to global hypomethylation and aberrant gene expression. Crosstalk between PRMT5 and activity of the catalytic subunit of PRC2, enhancer of zeste homolog 2 (EZH2), has already been reported although their specific relationship seems to be cell type dependent. In leukemia cells PRMT5 opposes EZH2 activity as methylation of histone H3 by PRMT5 impairs subsequent EZH2 methylation (Liu *et al.*, 2020). Whereas, in colorectal cancer cells knockdown of either PRMT5 or EZH2 impairs CDKN2B expression and inhibition of PRMT5 and EZH2 is synergistic suggesting that in colorectal cancer cells EZH2 and PRMT5 act co-operatively to repress transcription (Yang

et al., 2021). Thus, in addition to regulating multiple hallmarks of cancer PRMT5 may directly impact signalling pathways known to be crucial in DIPG.

4.1.1. Experimental overview

To investigate the specific role of PRMT5 in DIPG cells *in vitro*, RNA-sequencing was performed in the presence and absence of PRMT5 inhibition to assess each of these potential mechanisms simultaneously. Classical DESeq2 based transcriptomic analysis was combined with a novel pipeline developed by the company Trajecture, which aims to identify subtle differences in gene expression over time. Differentially expressed gene sets were also compared to curated ChIP-seq databases. The signatures identified from transcriptomic analysis were validated with numerous *in vitro* functional assays.

Given the dismal outlook for DIPG patients, this potential novel therapeutic was rapidly tested in a mouse xenograft model of DIPG by collaboration with Ángel Montero Carcaboso in Barcelona. In his laboratory, mice bearing established HSJD-DIPG-007 tumours were treated with 50 mg/kg LLY-283 (daily, 3 days on, 4 days off) for 4 weeks. Survival, tumour burden, differentiation markers and DIPG cell location were all assessed after treatment.

4.2. Results

4.2.1. Design of RNA-sequencing experiment

To identify which of the key functions of PRMT5 drive DIPG cells, their transcriptomes with or without PRMT5 inhibition were compared. The PRMT5 inhibition sensitive HSJD-DIPG-007 cell line was selected as it can also be xenografted into mice to enable subsequent *in vivo* evaluation (see section 4.2.9) (Vinci *et al.*, 2018; Carvalho *et al.*, 2019). Similarly, LLY-283 was selected over GSK 591, because can penetrate the blood-brain-barrier (BBB) *in vivo* (Sachamitr *et al.*, 2021). Cells were treated with the GI_{40} to avoid killing all inhibitor-sensitive cells and thus

recording the transcriptome of inhibitor-resistant cells rather than changes in response to PRMT5 inhibition.

The experiment was designed as a time course in order to capture both the primary and secondary changes observed following PRMT5 inhibition (Daigle *et al.*, 2011; Vedadi *et al.*, 2011; Bonday *et al.*, 2018). To avoid overgrowth of untreated samples or those from later time points, fewer cells were seeded for longer and/or untreated samples (as outlined in Chapter 2: Methods). This experiment was designed for both classical R based analysis (requiring multiple technical repeats at each time point) and the Trajecture analysis platform (optimised for more time points with fewer technical repeats). Thus, many time points were included (0, 1, 2, 3, 5, 7 and 10 days) and three technical repeats were collected at each time point. However, all three technical repeats were sequenced at day 0 and 5 only, 2 repeats were sequenced at day 7 and 1 technical repeat for days 1, 2, 3, and 10. An experimental overview is illustrated below (**Figure 4.1**).

After each treatment period, total cellular RNA was harvested from cells, purified, and passed to the NDORMS NGS facility for poly(A) enrichment, cDNA library generation, and paired end sequencing (NextSeq 500 platform, Illumina, USA).

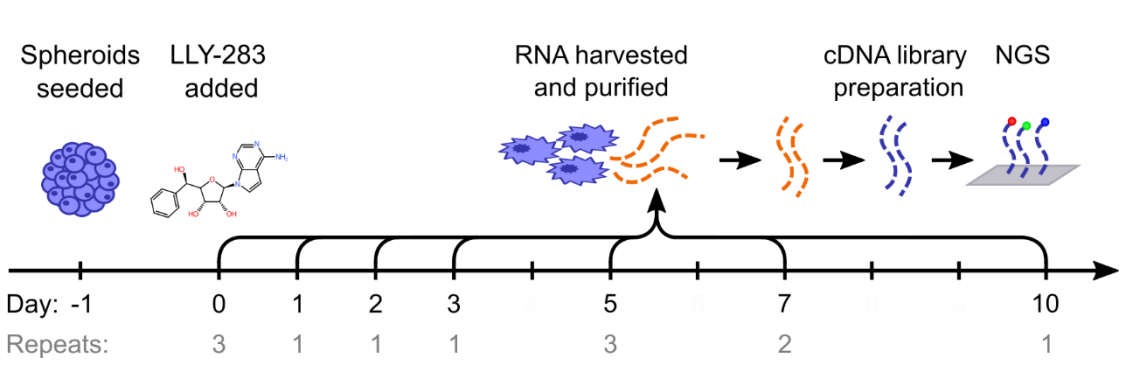

Figure 4.1 - Overview of RNA-sequencing experiment

HSJD-DIPG-007 cells were seeded as spheroids and treated with the LLY-283 GI_{40} the following day. Total cellular RNA was collected after 0, 1, 2, 3, 5, 7 and 10 days of growth in the presence of the LLY-283 GI_{40}. One technical repeat was collected on days 1, 2, 3, and 10; two for day 7 and three for days 0 and 5. Poly(A) enrichment was used to select for mRNA over abundant rRNA prior to cDNA library preparation and paired end sequencing.

4.2.2. Overview of results

Sequencing reads were pseudoaligned to the human reference genome (hg38), and counts tables generated by Adam Cribbs (NDORMS) were then passed to me for differential expression analysis.

Principal component analysis (PCA) is a method for reducing the dimensionality of a complex dataset, to aid its interpretation, by converting it into 'principal components' (PCs) which are uncorrelated linear functions that capture the majority of the variance in the dataset (Jolliffe and Cadima, 2016). PCA here demonstrated good grouping of technical repeats and illustrated the separation of samples according to time along PC1 (which explains 46% of the variance) and segregation according to treatment along PC2 after 3 days of treatment (explaining 9% of the variation) (**Figure 4.2a**). The exceptions to this pattern were the treated and untreated day 10 samples, which did not separate well along PC2. As this was likely due to compromised health of the cells after 10 days without passage, these samples were excluded from subsequent analysis, to avoid confounding the comparison of +/- LLY-283 groups. Repeating the PCA without day 10 samples improved the variance explained by PC1 and 2 to 48% and 10% respectively (**Figure 4.2**b). The top weighted genes of PC1 and PC2 are illustrated in **Figure 4.3**. Unsupervised hierarchical clustering of samples again illustrates the grouping of samples according to time by PC1 and according to treatment by PC2. As PC analysis illustrates that the day 5 samples have the greatest separation according to treatment (and a complete set of technical repeats) they were the focus of subsequent analysis.

The DESeq2 package is routinely used to test for differential expression analysis in -omic datasets (Love, Huber and Anders, 2014). Here, two models were built: one consisting of only of day 5 samples compared according to treatment ('day 5 only') and one including all day 0-7 samples to identify samples that behave differently over time according to treatment ('time course'). The day 5 only model found 4295 ($p.adj < 0.05$) and 3085 ($p.adj < 0.01$) differentially

expressed genes (visualised in **Figure 4.4**). In contrast, the time course model found only 2385 (p.adj < 0.05) and 1566 (p < 0.01) differentially expressed genes. In both datasets, more genes were downregulated that up regulated – 60% in the day 5 only dataset and 61% at day 5 of the time course dataset (p < 0.05 for both) – which aligns with the observation that PRMT5 methylation of histones mainly represses transcription (Pal *et al.*, 2004; Zhao *et al.*, 2009).

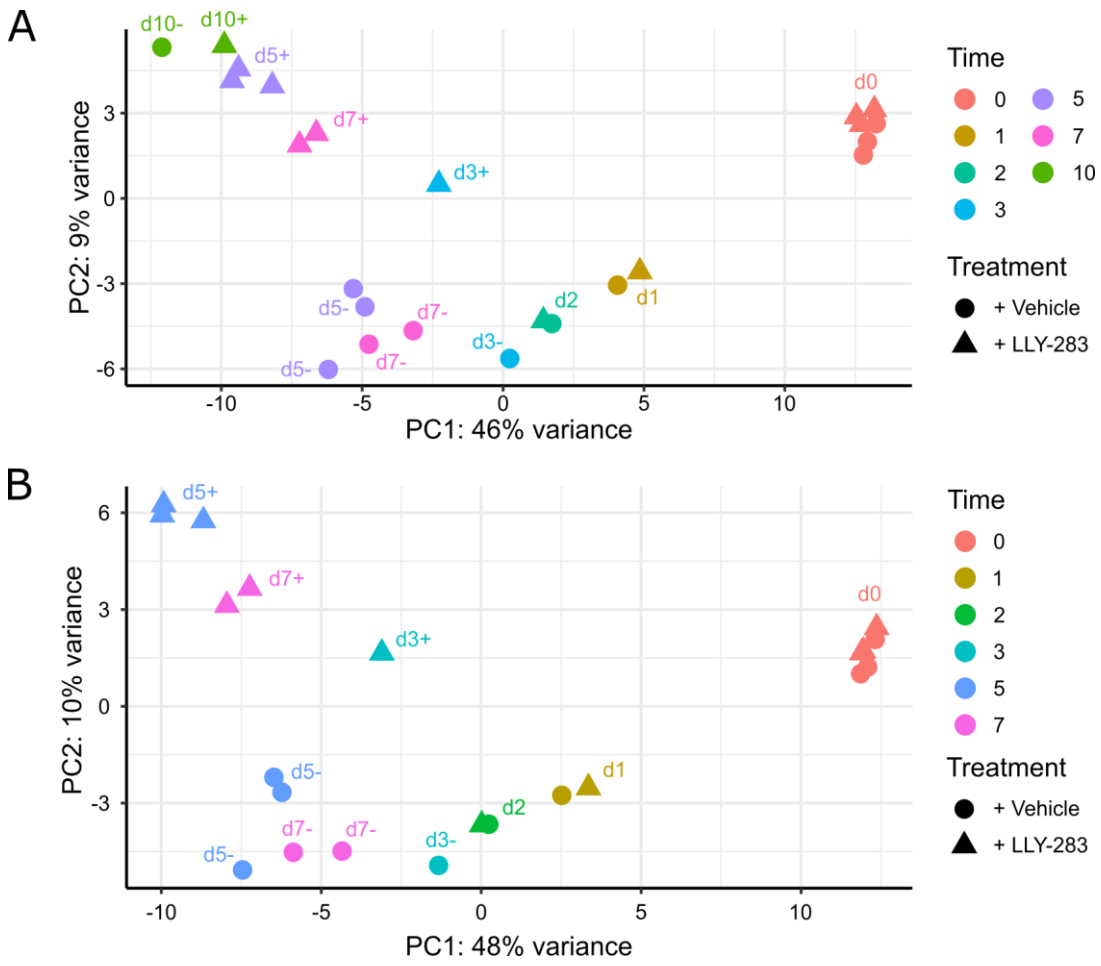

Figure 4.2 - Principal component analysis shows divergence of samples over time

A plot showing the clustering of samples according to the principal components of variation. Gene expression changes over time and diverges after 3 days according to whether they are vehicle or treated samples. Each point represents a technical repeat. Plots include (A) or exclude (B) samples from day 10.

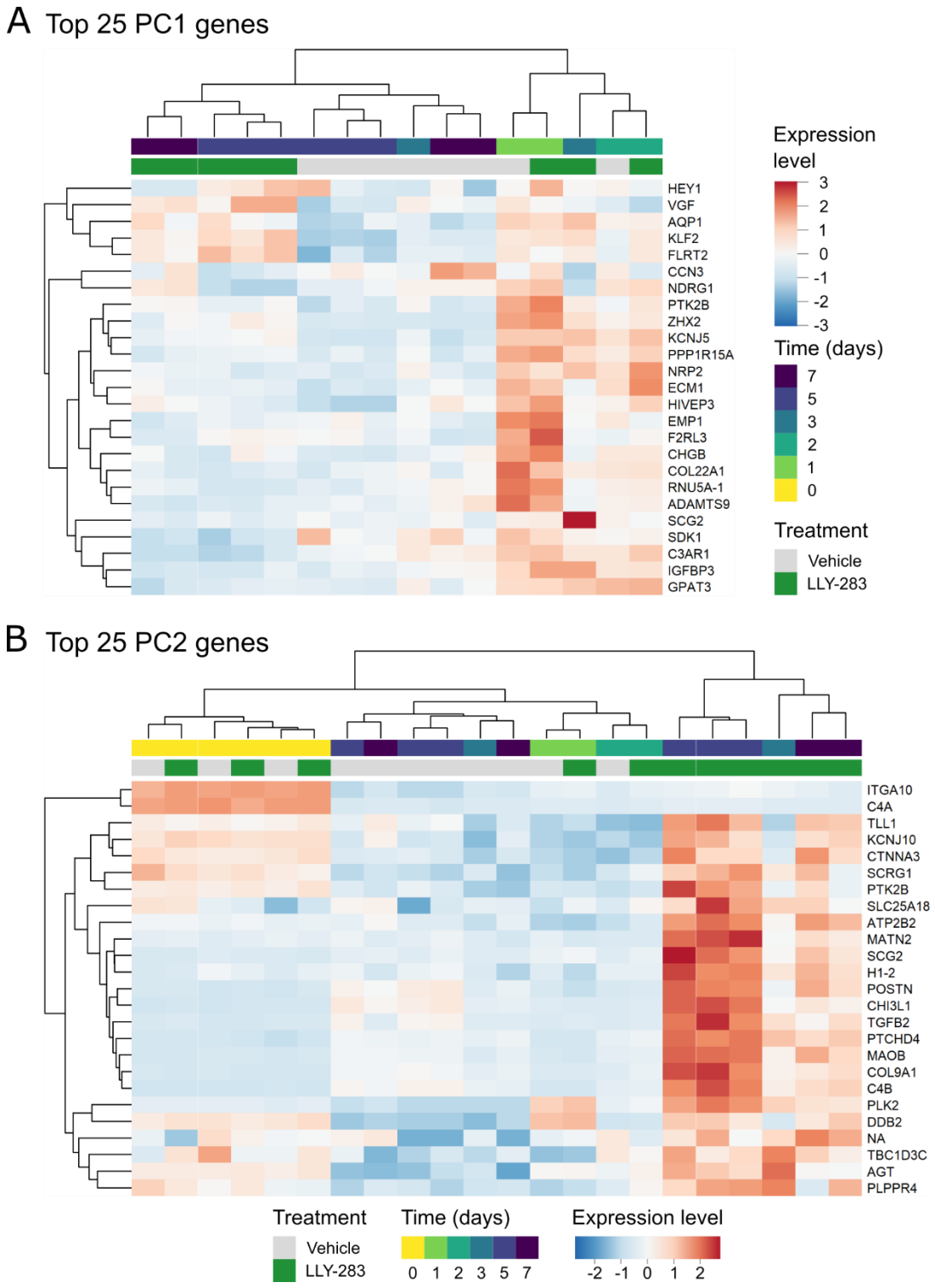

Figure 4.3 - Top genes in Principal Components 1 and 2

Heatmaps of the counts in each sample of the 25 transcripts with the greatest weighting in PC1 (A) and PC2 (B). Samples (columns) and transcripts (rows) have been sorted according to unsupervised hierarchical clustering. Counts were scaled across each row. For PC1, day 0 samples were excluded to facilitate the visualisation of transcript expression across the rest of the time course.

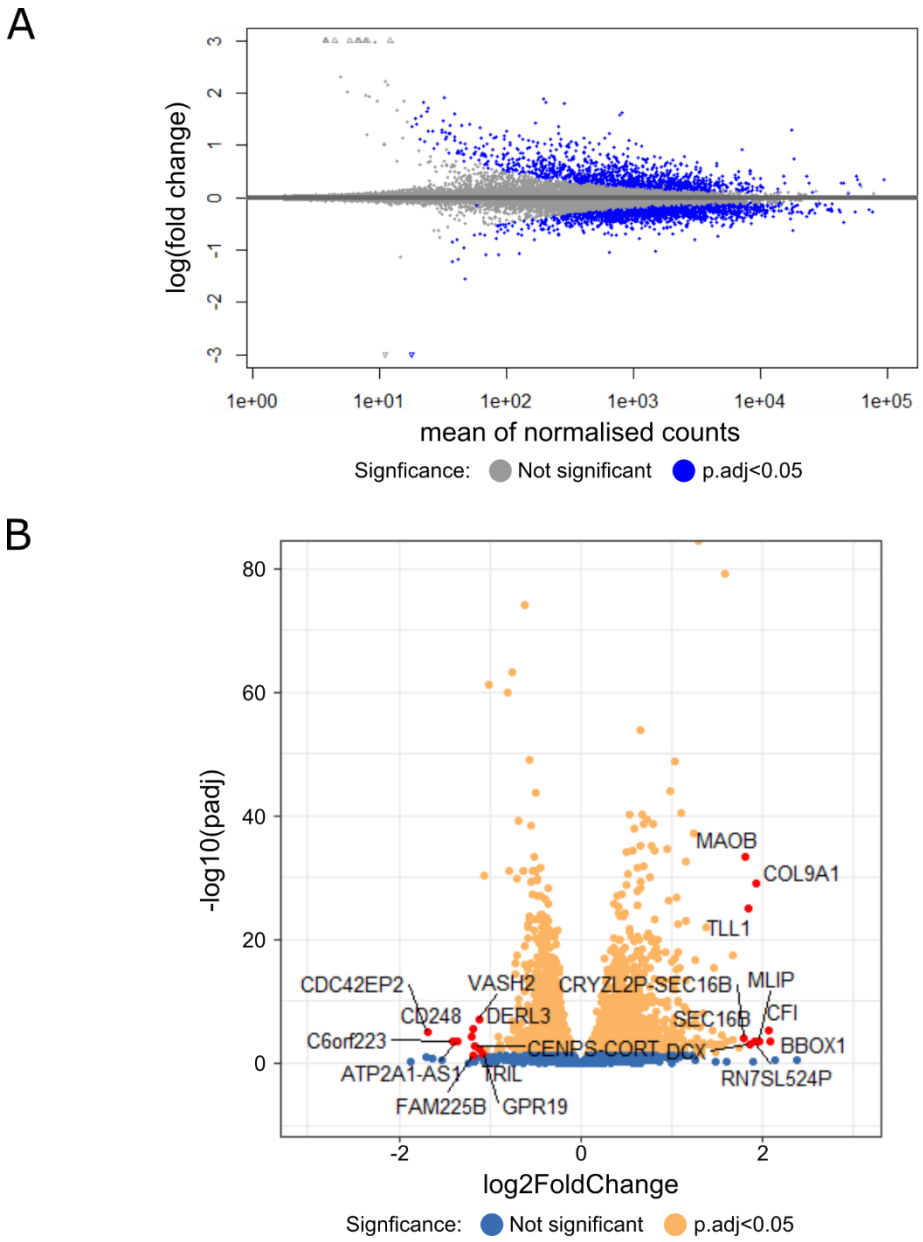

Figure 4.4 - Overview of differential analysis

(A) *A plot of the log(fold change) versus mean normalised counts of each transcript at day 5. Statistically significant changes are highlighted in blue (p.adj < 0.05).* ***(B)*** *A plot of the -log_{10}(p.adj) versus the log_2(fold change) (l2fc) for each transcript on day 5. Non-significantly DE transcripts are shown in blue, statistically significant DE transcripts are highlighted in yellow (p.adj < 0.05), the ten highest fold change (up and down) are highlighted in red and labelled.*

4.2.3. Gene Ontology Analysis identifies an enrichment in genes associated with differentiation and extracellular matrix organisation after PRMT5 inhibition

Gene ontology (GO) enrichment analysis identifies patterns in an entire set of differentially expressed (DE) genes by testing for an enrichment of genes with the same functional annotations (i.e., the same GO terms). GO enrichment analysis was performed on both the day 5 only and time course results sets. Considering first the day 5 only result set, initial GO enrichment analysis with no fold change filter ($p < 0.01$, 3085 genes) identified 1136 enriched GO terms (p value > 0.05, q value > 0.05) with the most significant terms relating mainly to RNA processing or the cell cycle (**Figure 4.6a**). To reduce the number of enriched GO terms to a more manageable number, the gene list was reduced to 727 genes by further filtering to include $\log_2$(fold change) (l2fc) ± 0.5 genes only. This list was enriched for 48 terms (p value > 0.01, q value > 0.01) (**Figure 4.6b**). This analysis of filtered gene lists found that differentially expressed genes were enriched with transcripts associated with GO terms relating to metabolism (such as 'sterol biosynthetic process'), extracellular matrix (ECM) organisation and differentiation (such as 'negative regulation of neuron differentiation'). The differential expression of genes associated with these GO terms is illustrated in **Figure 4.7**.

The same analyses were performed on the time course dataset (1566 DE genes with no l2fc filter and 512 DE genes when filtered to l2fc ± 0.5) found 799 and 35 enriched GO terms respectively (**Figure 4.6**). Similar GO terms were enriched in the day 5 only and time course datasets, although the unfiltered time course DE genes were also enriched for GO terms relating to metabolism (**Figure 4.6a**).

A subset of enriched GO terms was selected for validation by RT-qPCR of the associated DE genes (**Figure 4.8a**). Genes from the GO term 'sterol metabolism' were selected given the prevalence of lipid synthesis terms in the day 5 only and time course analysis, and the previously described role of PRMT5 in cholesterol and lipid synthesis (Liu *et al.*, 2016; Jia *et al.*, 2020; Webb

et al., 2020). Genes from the GO terms 'negative regulation of neural differentiation' and 'gliogenesis' were also selected because of the established role of PRMT5 in neural differentiation (Blanc and Richard, 2017). HSJD-DIPG-007 cells were seeded and treated as in the previous experiment. Here, both the GI_{40} and GI_{70} were included to capture dose dependent changes. The time points were reduced to day 0, 3, 5 and 7 only, and three independent repeats were completed. Two genes were selected from the highest and lowest fold change genes from each enriched GO term, favouring genes associated with multiple terms, and quantified by qPCR. 70% of the observations from transcriptomic analysis were confirmed (**Figure 4.8**).

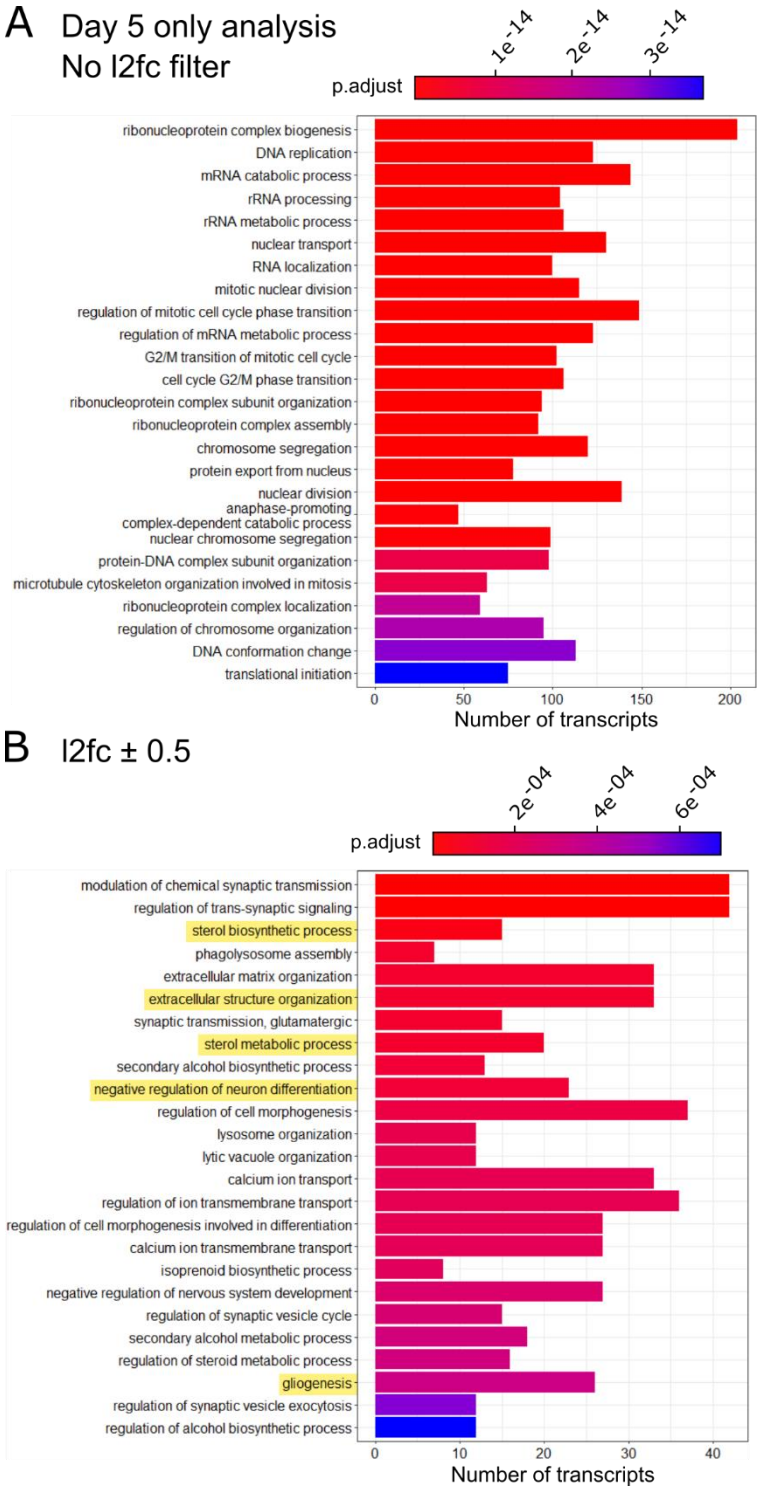

Figure 4.5 – Day 5 only DE genes were enriched for transcripts associated with sterol metabolism, ECM organisation and differentiation

*The top 25 significantly enriched GO terms in the day 5 only dataset with **(A)** no log fold change filter or **(B)** ± 0.5 log fold change filter. Redundant GO terms have been omitted. GO terms followed up in subsequent sections are highlighted in yellow.*

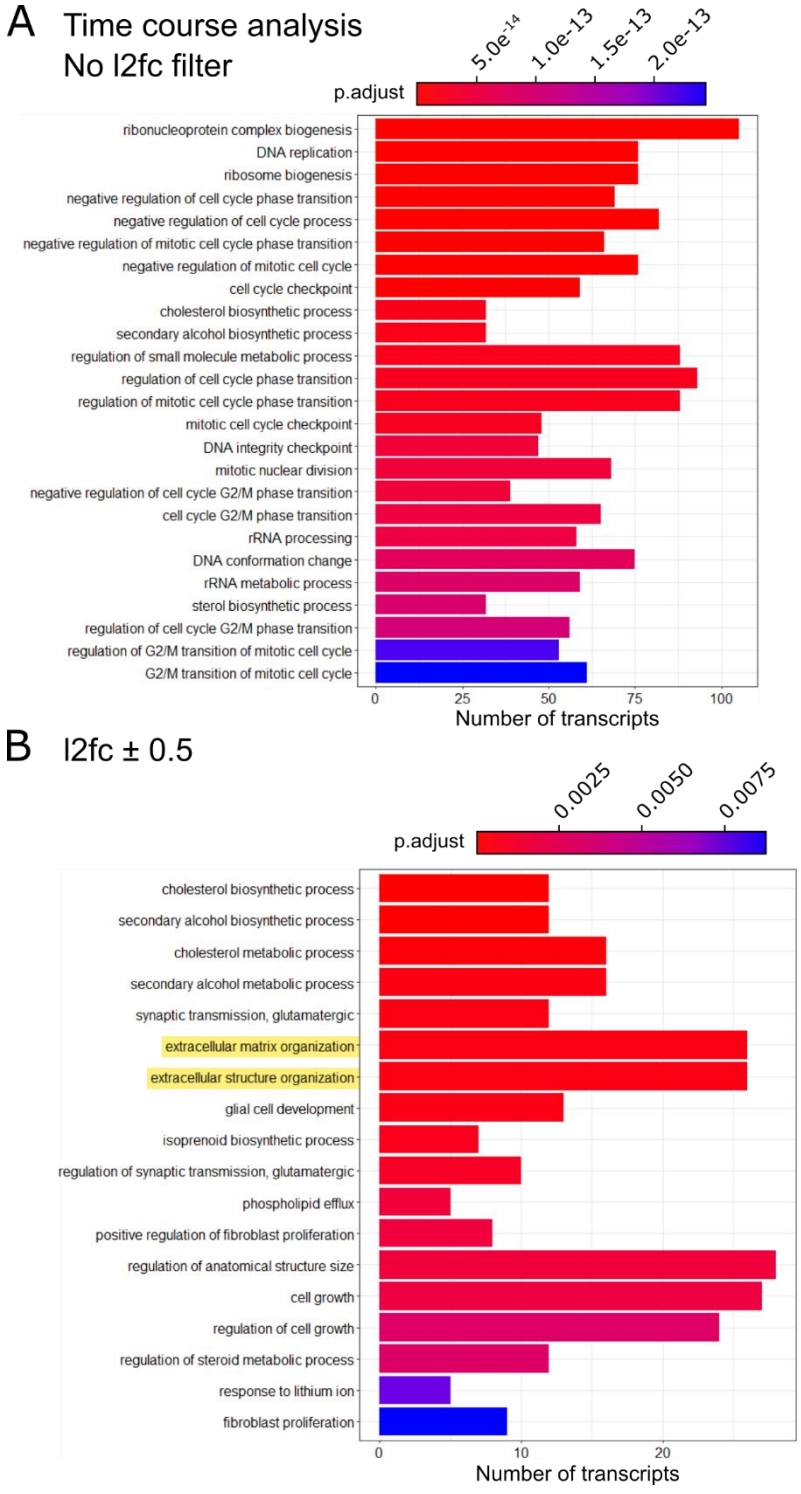

Figure 4.6 – Genes DE over the time course were enriched for transcripts associated with cholesterol metabolism, ECM organisation and differentiation

*The top 25 significantly enriched GO terms in the day 5 only dataset with **(A)** no log fold change filter or **(B)** ± 0.5 log fold change filter. Redundant GO terms have been omitted. GO terms followed up in subsequent sections are highlighted in yellow. The colour of the bars indicates the p.adj value for the enrichment of that term.*

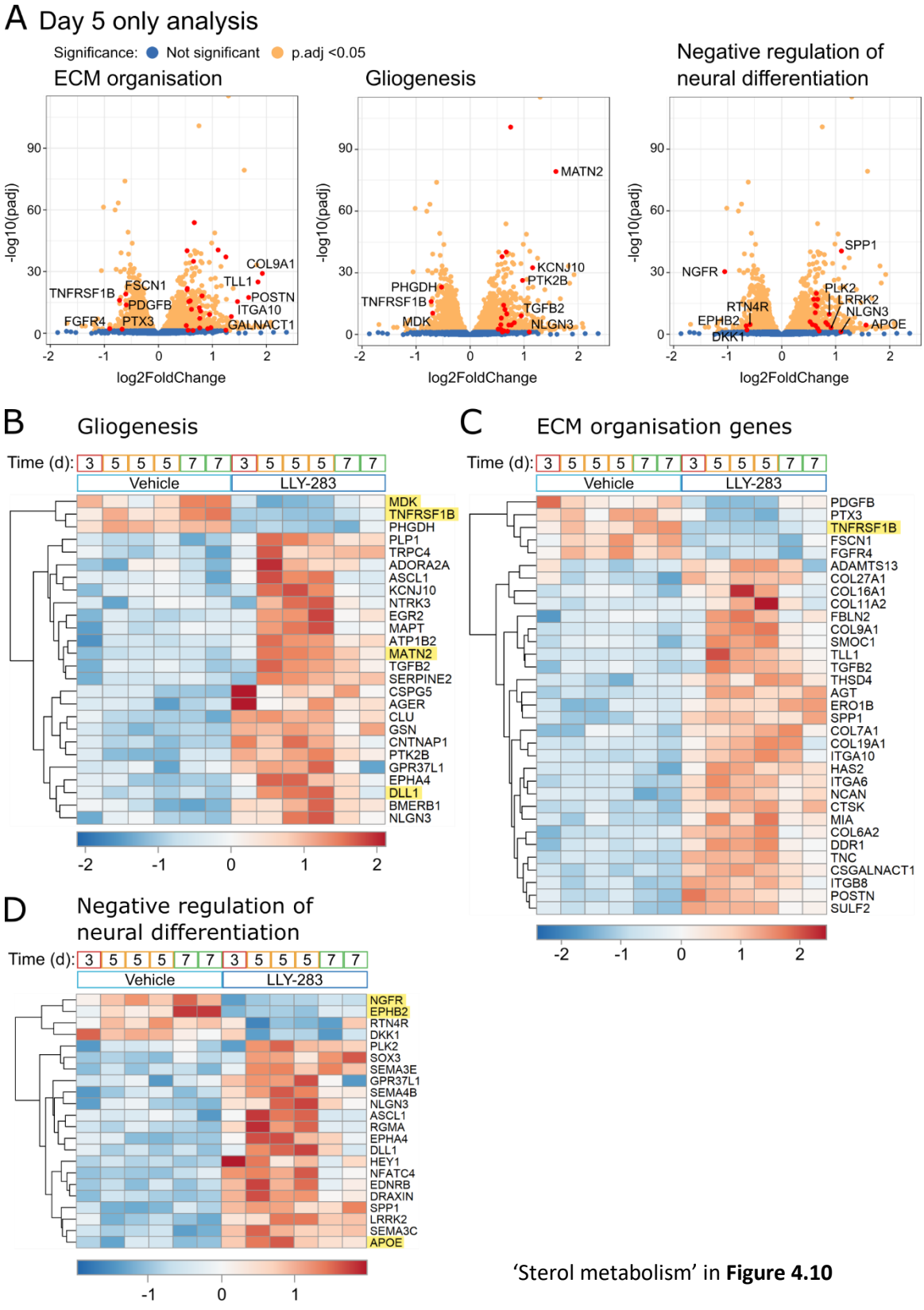

'Sterol metabolism' in **Figure 4.10**

Figure 4.7 - Top fold change genes associated with gene ontology terms of interest

(A) *Volcano plots of differentially expressed genes at day 5 of LLY-283 treatment. Significantly differentially expressed genes (p.adj < 0.05) are highlighted in yellow. Genes associated with the indicated GO term are highlighted in red and the 5 highest log fold change (+/-) are labelled with their gene symbol.* ***(B, C, D)*** *Read counts of transcripts associated with each GO term over days 3-7, scaled across each row. Transcripts have been sorted according to unsupervised hierarchical clustering (illustrated with the black tree). Genes validated by RT-qPCR are highlighted in yellow.*

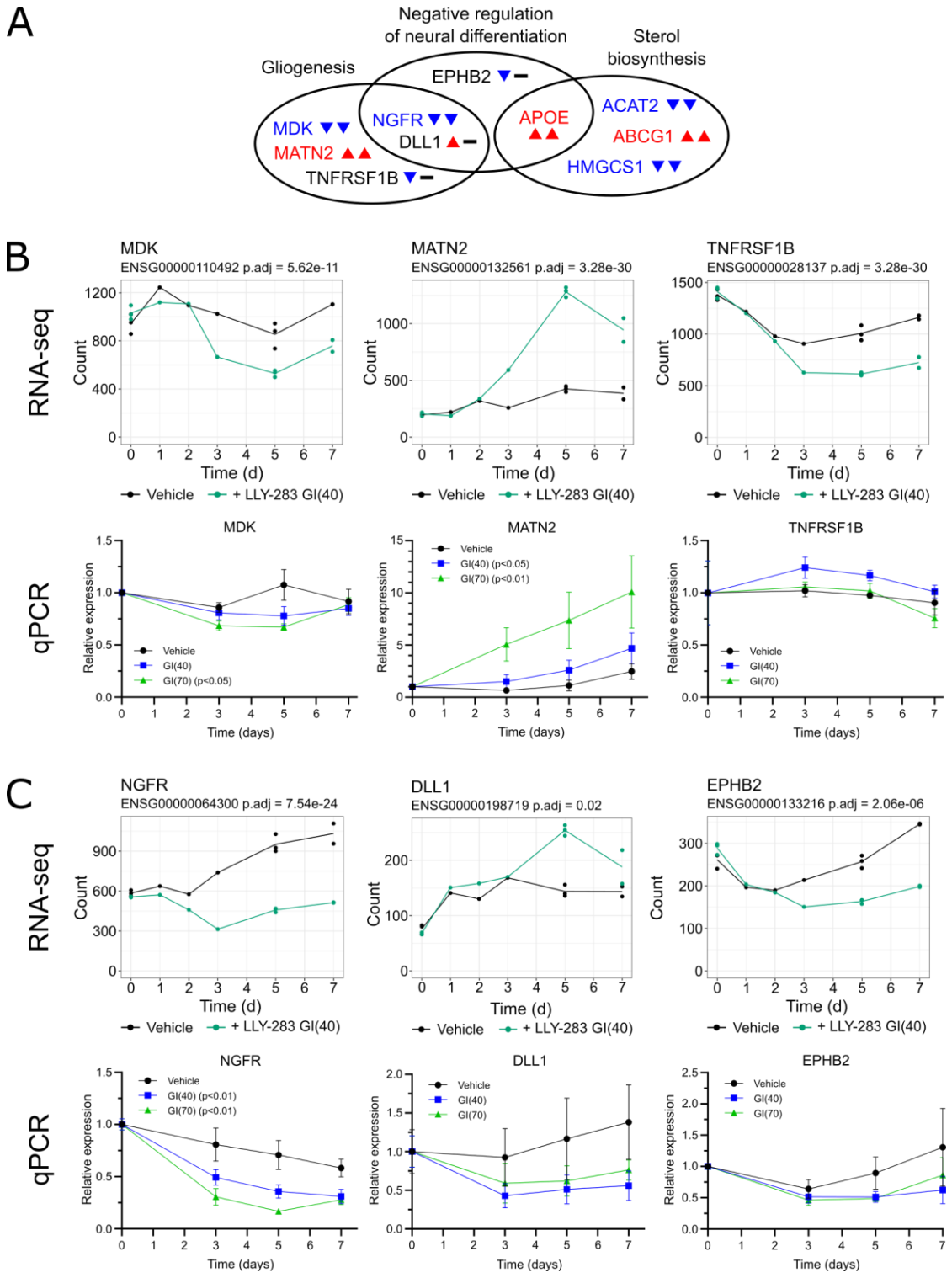

Figure 4.8 continues on P113

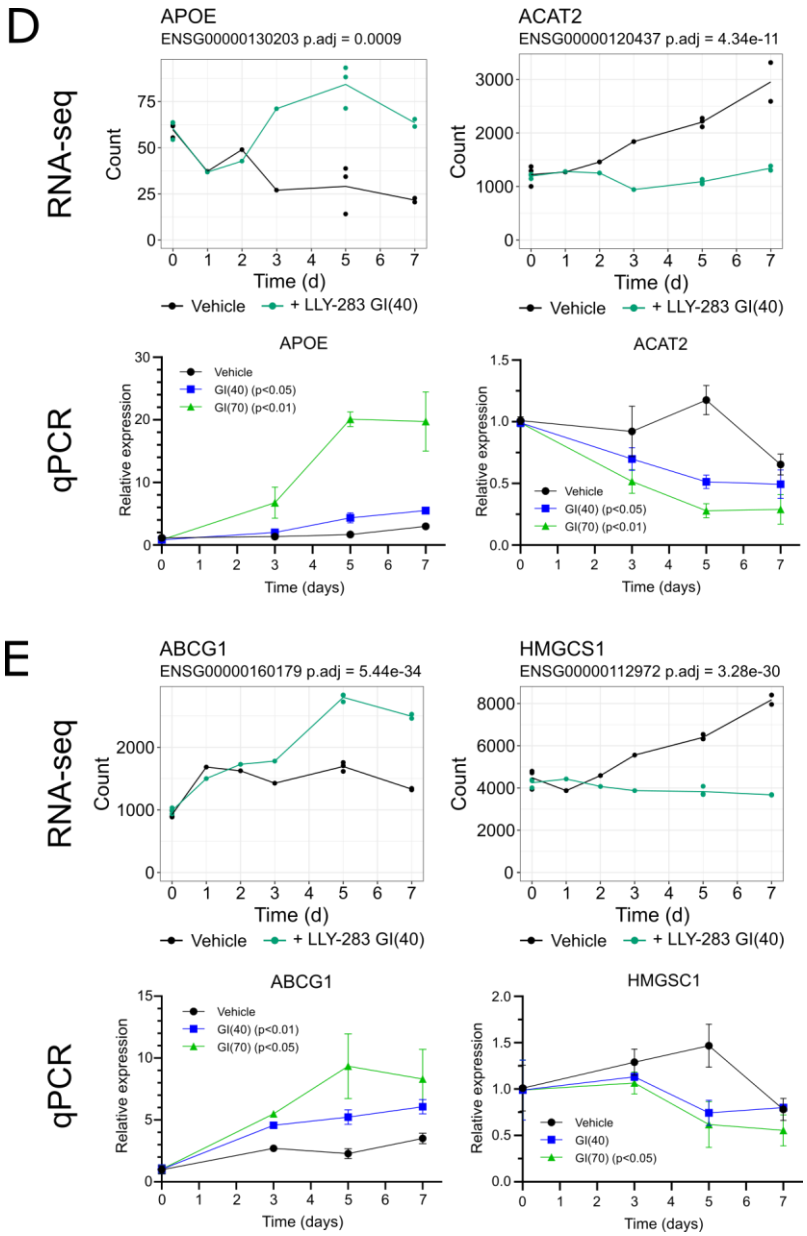

Figure 4.8 - qPCR validation of selected genes from RNA-sequencing

(A) *A summary of the transcripts from each GO term that were validated by RT-qPCR. Each transcript is annotated with the differential change observed with RNA-sequencing (left arrow) and the change observed by RT-qPCR (right arrow).* ***(B-D)*** *(Top rows) Graphs of counts for the same transcripts over time measured by RNA-sequencing, labelled with the p.adj value generated by DESeq2. (Bottom rows) HSJD-DIPG-007 cells were treated with LLY-283 GI_{40} or GI_{70} for 0, 3, 5 or 7 days. Transcripts for MDK, MATN2, TNFRSF1B (B), NGFR, DLL1, EPHB2 (C), APOE, ACAT2 (D), ABCG1 and HMGSC1 (E) were quantified by RT-qPCR. Data points are the mean of 3 independent repeats ± SEM. P values were generated as described in section 2.5.3.*

4.2.4. Trajecture analysis reiterates changes in extracellular matrix proteins

In parallel, read counts tables and sample annotation were passed to Trajecture for analysis in their pipeline. The Trajecture pipeline was designed to assess the behaviour of gene expression across a time course and identify genes which behaved differently over time according to treatment group with more sensitivity than DESeq2.

Visualisation of all transcripts (total read count > 50, l2fc > 1) illustrated that an initial change in the transcriptome took place around day 3, with a return to initial behaviour around day 7-10 (**Figure 4.9a, b**). This was complementary to the classical PCA that showed changes in transcription beginning at day 3 (**Figure 4.2b**). When considering this initial change in the transcriptome, Trajecture identified 354 markers of interest, consisting of 258 annotated transcripts and 96 unassigned novel transcripts (full list in appendix **Table 0.2**).

A comparison of the Trajecture markers to those found by DESeq2 analysis (using the day 5 only, p.adj < 0.05, l2fc > ± 0.5 transcript list) showed that only 64 (26%) were identified in the original DESeq2 analysis (**Figure 4.9d**). Visualisation of the Trajecture markers with the ConsensusPathDB highlighted the large number of genes involved in the cytoskeleton or extracellular matrix including 5 collagen genes, fibronectin (*FN1*), matrilin 2 (*MATN2)*, periostin (*POSTN*) and matrix metalloproteinase 2 (*MMP2*) (**Figure 4.9**). Interestingly, this network included *TGFB2* and linked *COL1A2* to *SMAD3/SMAD4* suggesting that PRMT5 may regulate the ECM and cytoskeleton by methylation of SMAD7 – a regulator of TGF-β signalling (Tabata *et al.*, 2009). The network also linked fibronectin to histone H4 (*HIST2H4A)* which is methylated by PRMT5 (Zhao *et al.*, 2009).

The Trajecture marker list re-iterated that PRMT5 regulated organisation of the ECM and cytoskeleton in DIPG cells and provided hypotheses as to how this regulation occurs, which motivated its prioritisation for further functional investigation.

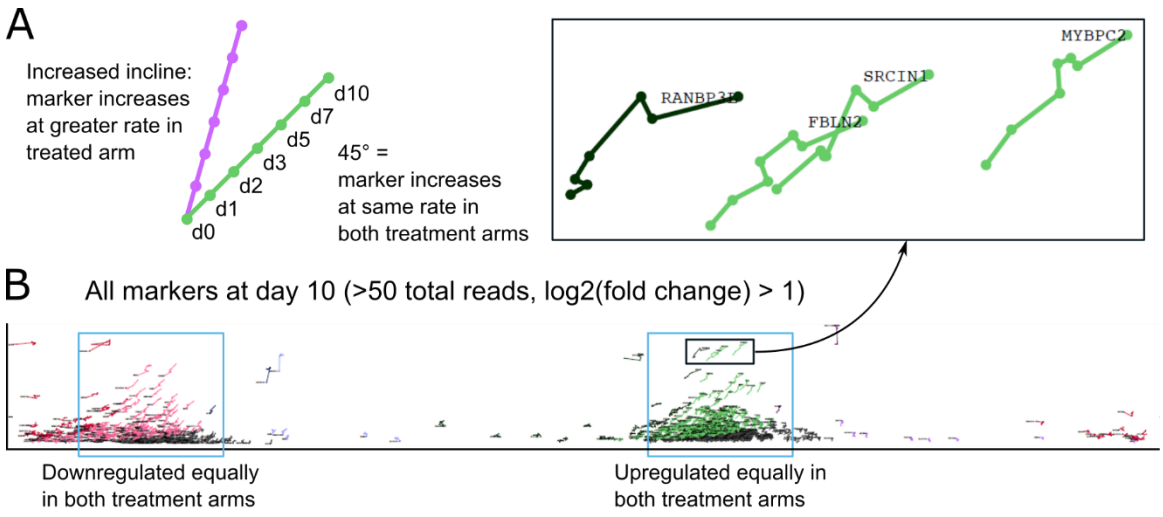
A
Increased incline:
marker increases
at greater rate in
treated arm
d0
d1
d2
d3
d5
d7
d10
45° =
marker increases
at same rate in
both treatment arms
RANBP3P5
FBLN2
SRCIN1
MYBPC2
B
All markers at day 10 (>50 total reads, log2(fold change) > 1)
Downregulated equally
in both treatment arms
Upregulated equally in
both treatment arms

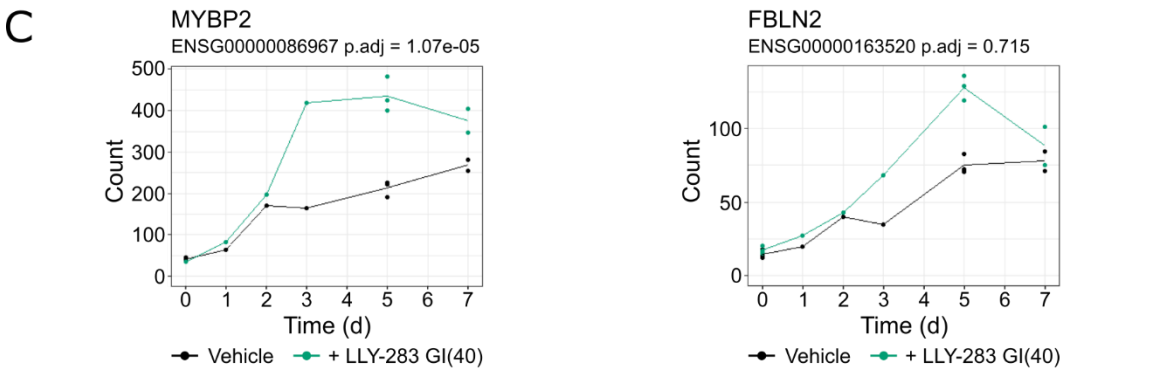
C
MYBP2
ENSG00000086967 p.adj = 1.07e-05
Count
Time (d)
Vehicle
+ LLY-283 GI(40)
FBLN2
ENSG00000163520 p.adj = 0.715
Count
Time (d)
Vehicle
+ LLY-283 GI(40)

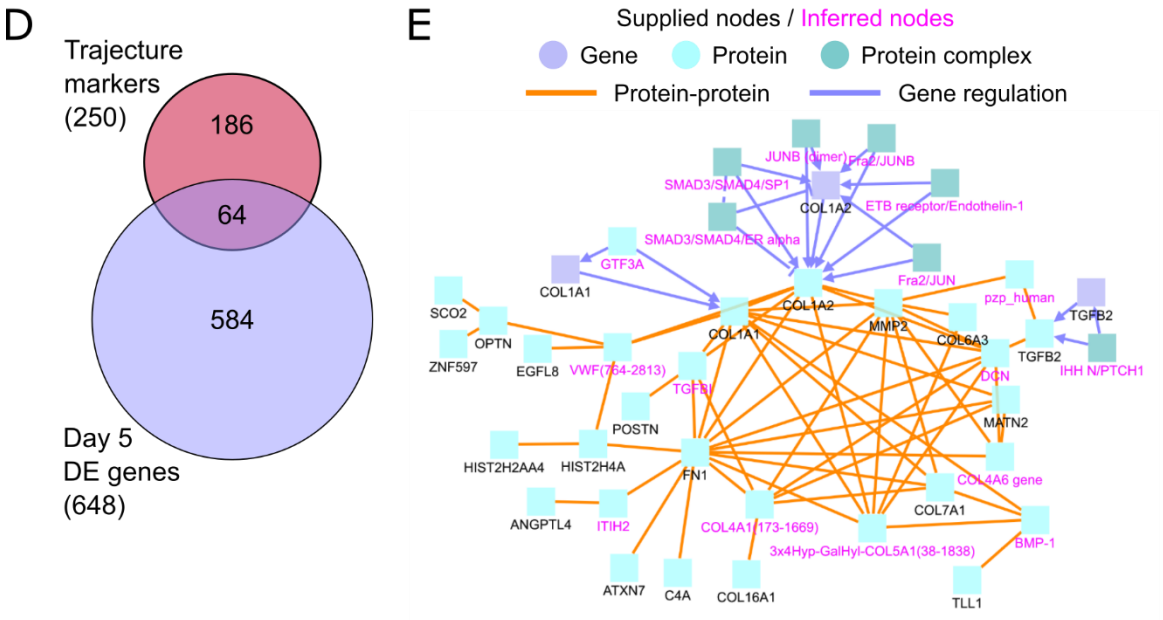
D
Trajecture
markers
(250)
186
64
584
Day 5
DE genes
(648)
E
Supplied nodes / Inferred nodes
Gene
Protein
Protein complex
Protein-protein
Gene regulation
JUNB (dimer)
Fra2/JUNB
SMAD3/SMAD4/SP1
COL1A2
ETB receptor/Endothelin-1
SMAD3/SMAD4/ER alpha
GTF3A
COL1A1
Fra2/JUN
SCO2
OPTN
ZNF597
EGFL8
VWF(764-2813)
COL1A2
COL1A1
MMP2
COL6A3
pzp_human
TGFB2
TGFB2
IHH N/PTCH1
DCN
TGFBI
MATN2
POSTN
HIST2H2AA4
HIST2H4A
FN1
COL4A6 gene
COL7A1
ANGPTL4
ITIH2
COL4A1(173-1669)
3x4Hyp-GalHyl-COL5A1(38-1838)
BMP-1
ATXN7
C4A
COL16A1
TLL1

Figure 4.9 - Trajecture analysis highlights changes in the extracellular matrix

(A) *Left: An illustration of how gene expression is visualised in (B). As gene expression increases in the vehicle arm from one time point to the next, the point moves rightwards on the x axis. As expression increases in the treated arm, the point moves upwards on the y axis. Thus, a marker that increases in expression equally over time in both the vehicle and treated arm results in a 45° incline (green line), but if expression increases to a greater extent in the treated arm, the incline increases (purple line). Right: selected genes from (B) highlighting the change in gene expression in the treatment arm around day 3 observed for many genes.* ***(B)*** *Overview of all markers at day 10, filtered to remove markers with less than 50 total read counts and those with l2fc < 1. Each trace represents the expression of one gene over time and is organised along the x and y axis such that genes are spatially grouped according to specific behaviours. For example, the left pale blue box contains pink traces representing genes for which expression decreased equally in the vehicle and treatment arms over time.* ***(C)*** *Read counts over time of genes from (A).* ***(D)*** *The overlap of markers selected by the Trajecture analysis pipeline and from the classical DESeq2 analysis (day 5 only, p < 0.05, l2fc > +/- 0.5). E) Visualisation of a network of collagen and extracellular matrix associated genes within the Trajecture marker set visualised with ConsensusPathDB-human and a z-score threshold of 40.*

4.2.5. Cholesterol supplementation does not rescue DIPG cells from PRMT5 inhibition

Perturbation of cholesterol synthesis was selected for functional follow up because altered metabolism is a hallmark of cancer (Seyfried and Mukherjee, 2005; Hanahan and Weinberg, 2011). Furthermore, cholesterol biosynthesis has been highlighted as a potential therapeutic target in glioblastoma and DIPG (Ahmad *et al.*, 2019; Phillips *et al.*, 2019). Phillips et al., (2019) found that DIPG cells are vulnerable to inhibition of lanosterol synthase (LSS), but that cell death could be rescued by providing exogenous cholesterol. The transcription of multiple enzymes required for steroid biosynthesis, including lanosterol synthase, were repressed by PRMT5 inhibition (**Figure 4.10a**). If PRMT5 inhibition reduces DIPG viability by impairing cholesterol synthesis, exogenous cholesterol should improve DIPG viability. In HSJD-DIPG-007, supplementation of growth medium with exogenous cholesterol was not sufficient to rescue the drop in viability following PRMT5 inhibition (**Figure 4.10d**). A retrospective positive control was then completed using SU-DIPG-IV instead to completely match Philips *et al.*. Here, the drop in viability following lanosterol synthase inhibition and rescue by cholesterol in SU-DIPG-IV was recapitulated (**Figure 4.10c**). This suggests that in the HSJD-DIPG-007 cell line, a reduction in cholesterol does not underlie the vulnerability to PRMT5 inhibition, but to fully

draw the conclusion that loss of cholesterol synthesis is not the cause of sensitivity to PRMT5 inhibition, additional experiments and independent repeats would need to be completed to confirm that cholesterol supplementation can rescue LSS inhibition in HSJD-DIPG-007 and also to test cholesterol supplementation after PRMT5 inhibition in SU-DIPG-IV.

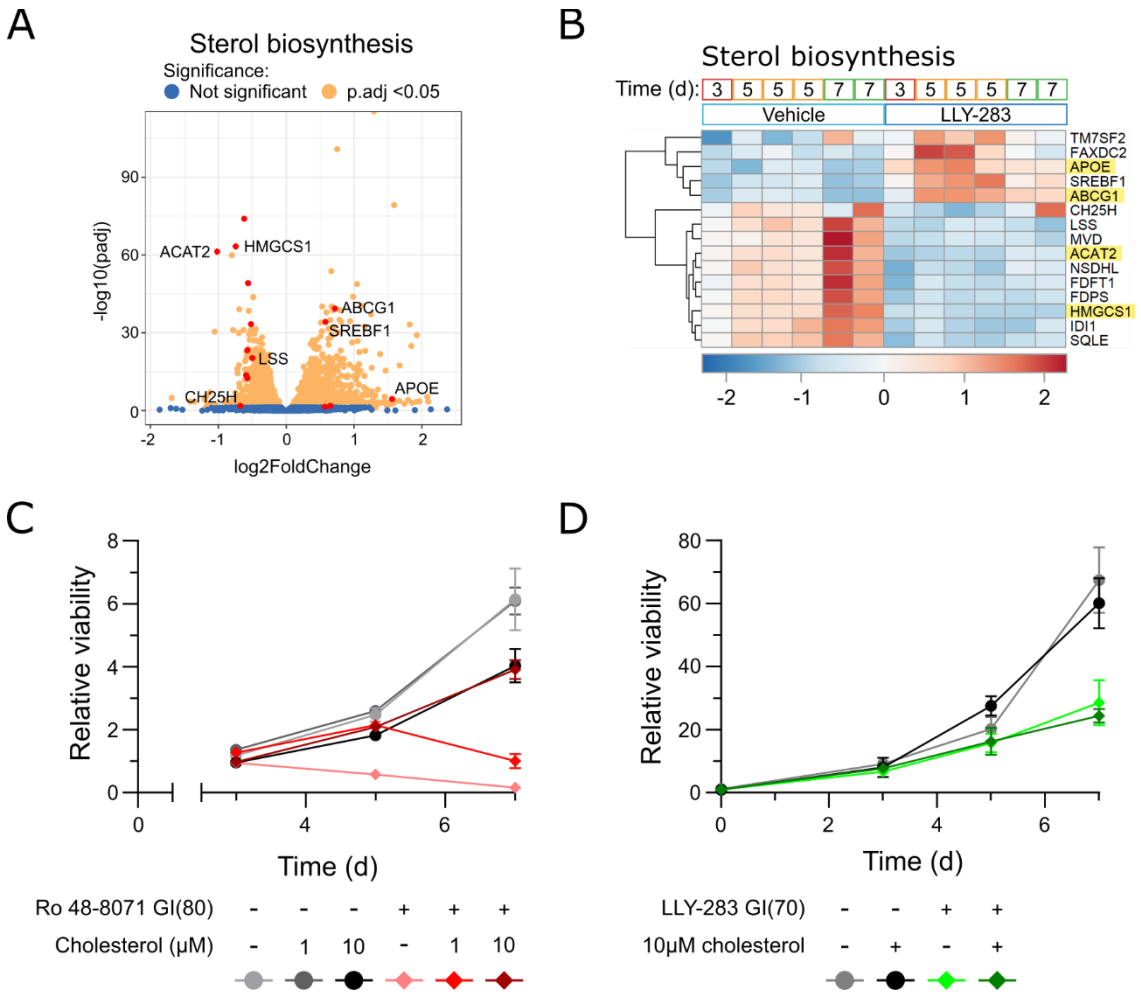

Figure 4.10 - Exogenous cholesterol cannot rescue DIPG cells from PRMT5 inhibition

(A) *Volcano plots of differentially expressed genes at day 5 of LLY-283 treatment. Significantly differentially expressed genes (p.adj < 0.05) are highlighted in yellow. Genes associated with the 'Sterol biosynthesis' GO term are highlighted in red. The 3 highest log fold change (+/-) (and LSS) are labelled with their gene symbol.* ***(B)*** *Read counts of transcripts associated with the 'Sterol biosynthesis' GO term over days 3-7, scaled across each row. Transcripts have been sorted according to unsupervised hierarchical clustering (illustrated with the black tree) to highlight patterns of gene expression. Genes validated by RT-qPCR are highlighted in yellow.* ***(C)*** *24 h after seeding SU-DIPG-IV cells were treated with the LSS inhibitor ± Ro 48-8071 and ± cholesterol. After the indicated time viability was recorded normalised to the viability of the vehicle only, day 3 wells. Data points are the mean of 4 technical repeats ± SD.* ***(D)*** *24 h after seeding HSJD-DIPG-007 cells were treated ± LLY-283 GI_{70} and ± 10 μM cholesterol. After the time indicated viability was recorded and normalised to the viability of vehicle only, day 0 wells. Data points are the mean of 4 technical repeats ± SD.*

4.2.6. PRMT5 inhibition may restore H3K27me3 levels in DIPG cells

PRMT5 often works in concert with other epigenetic or transcription factors (Pal *et al.*, 2004; Zhao *et al.*, 2009) to alter gene expression. A number of tools exist to compare gene lists to ChIP-seq datasets as a way to infer whether collective transcriptional changes could be due to a single factor (Zambelli, Pesole and Pavesi, 2009; Heinz *et al.*, 2010; Auerbach, Chen and Butte, 2013). The Binding Analysis for Regulation of Transcription (BART) 2.0 analysis tool uses the curated set of 8,000 ChIP-seq datasets in the Cistrome Data Browser (Mei *et al.*, 2017) to predict the specific transcription factors and chromatin modulators that regulate a gene set (Ma *et al.*, 2021). The tool is cell type agnostic and uses the union between DNAse I hypersensitive region and H3K27ac ChIP-seq datasets to create a cis-regulatory profile for 918 transcriptional regulators (Wang *et al.*, 2016; Ma *et al.*, 2021). It was selected because of its reported outperformance of other tools in the prediction of the true regulatory factor for gene lists (Wang *et al.*, 2018). The list of DE genes following PRMT5 inhibition (day 5 only, $p < 0.05$, l2fc > +/- 0.5) was supplied to BART. The top 3 factors predicted were STAG1, SMC1A and CTCF (by Wilcoxon Rank Sum test score, with Irwin-Hall p value < 0.05) (**Table 4.1**). PRMT5 binding sites were not significantly enriched (**Table 4.1**), perhaps reflecting that the DE genes at day 5 represent the indirect secondary response to PRMT5 inhibition. Additionally, the RNA-sequencing showed that there was a modest but significant decrease in expression of EZH2, EED and SUZ12 at day 5 (**Figure 4.11a**). Both observations, which imply a change in PRC2 activity, were notable because of the importance of PRC2 dysregulation due to H3K27M mutations in DIPG (Chan *et al.*, 2013; Mohammad *et al.*, 2017).

Table 4.1 - Top 10 factors predicted to regulate day 5 only DE genes

Wilcoxon rank sum test statistic: *Compares the association scores of each factor to those of every factor. A higher value means it's more likely that the factor regulates the input gene list.* ***Z score:*** *The deviation of the factor's Wilcoxon test score from the background model.* ***Max AUC****: the maximum association score of each factor.* ***Relative rank****: average of Wilcoxon p value, Z score and max AUC and divide by total number of factors.*

Factor	Wilcoxon test statistic	Wilcoxon p value	Z score	Max AUC	Relative rank	Rank significance (Irwin-Hall p value)
STAG1	9.864	3.00E-23	2.449	0.769	0.008	2.23E-06
SMC1A	7.723	5.67E-15	2.303	0.782	0.011	6.23E-06
CTCF	29.427	1.23E-190	2.231	0.771	0.012	7.51E-06
SMC3	8.026	5.03E-16	2.238	0.763	0.014	1.15E-05
RAD21	8.804	6.58E-19	2.029	0.786	0.018	2.61E-05
H2AZ	10.019	6.28E-24	2.057	0.736	0.019	3.11E-05
SUZ12	5.464	2.33E-08	1.535	0.84	0.034	1.79E-04
EZH2	7.678	8.07E-15	1.394	0.834	0.04	2.78E-04
JARID2	5.414	3.08E-08	1.299	0.782	0.05	5.74E-04
KDM2B	5.651	7.96E-09	1.007	0.801	0.07	1.55E-03
PRMT5	-1.361	9.13E-01	-1.284	0.47	0.844	9.83E-01

As DIPG cells have impaired but not complete loss of PRC2 activity (Bender *et al.*, 2013; Chan *et al.*, 2013), both a therapeutic inhibition or enhancement of PRC2 activity could reduce the viability of DIPG cells by removing them from the particular epigenetic state that drives their uncontrolled proliferation. PRC2 activity was assessed by collecting cellular protein after 0, 3, 5 and 7 days of PRMT5 inhibition in HSJD-DIPG-007 cells and immunoblotting for the abundance of H3K27me3, the histone mark mediated by EZH2. This showed that H3K27me3 levels increased in cells treated with LLY-283 over time ($p < 0.0001$), in a dose dependent manner (**Figure 4.11b**). This increase in H3K27me3 levels implies that PRMT5 inhibition could restore PRC2 activity in DIPG cells.

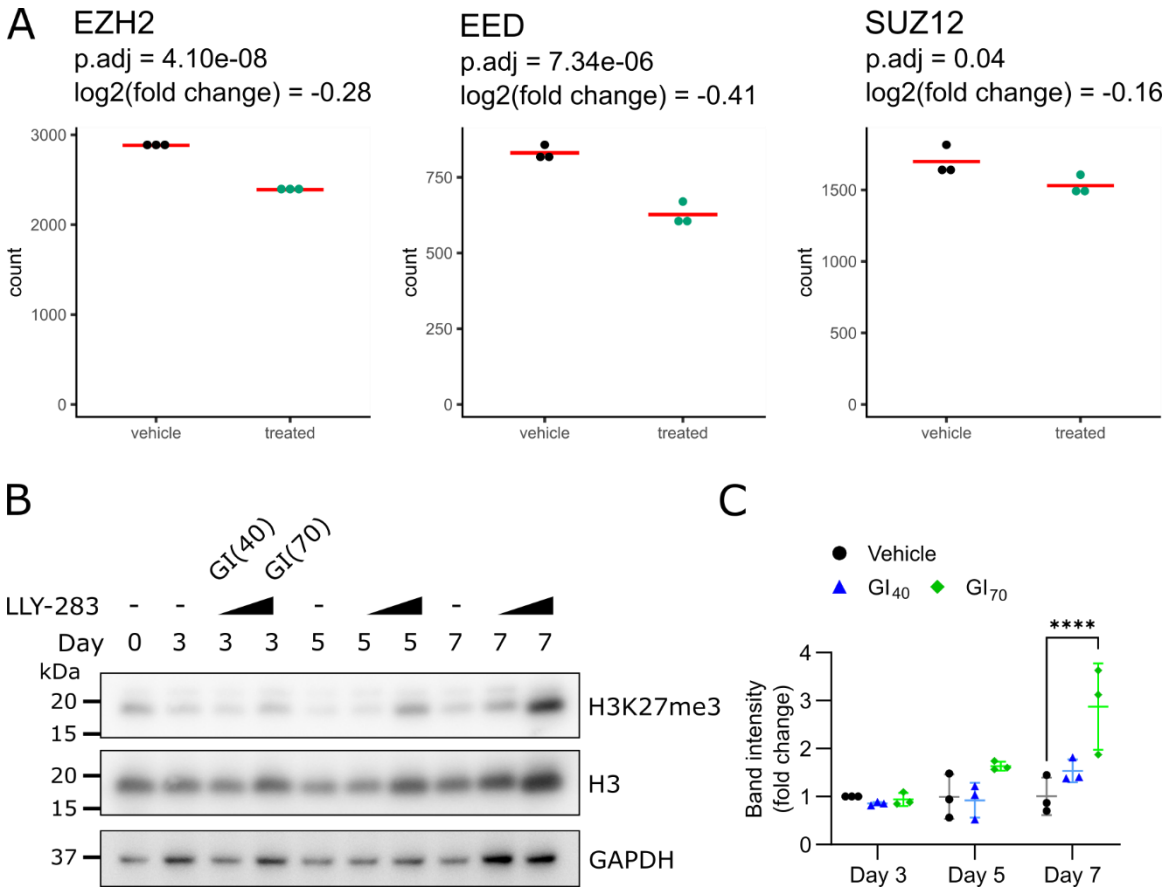

Figure 4.11 - H3K27me3 levels were restored following PRMT5 inhibition

(A) *RNA-sequencing read counts of the PRC2 components EZH2, EED and SUZ12. Each point is one technical repeat and the bar represents the mean counts.* ***(B)*** *HSJD-DIPG-007 cells were seeded into 6-well plates. The following day cells were treated with the LLY-283 GI_{40} or GI_{70}, or a vehicle control. After the indicated treatment period cellular protein was harvested and H3K27me3, H3 and GAPDH levels visualised by immunoblot. Image is representative of 3 independent repeats.* ***(C)*** *Quantification of band intensity of all 3 independent repeats normalised to the intensity of the H3 band, then to the day 3 vehicle. **** = p < 0.0001 by two-way ANOVA with Dunnett's multiple comparisons test*

4.2.7. PRMT5 inhibition reduces the stem-ness of DIPG cells

The role of PRMT5 in differentiation and stemness is well characterised (Nagamatsu *et al.*, 2011; Blanc and Richard, 2017) and therefore GO terms relating to differentiation signature were selected from the transcriptomic findings for follow up. DIPG cells exist in a proliferative OPC-like state with high tumour initiating capacity (Filbin *et al.*, 2018) and therapeutic differentiation could therefore reduce stemness or proliferation.

The described roles of the specific genes that form the 'gliogenesis' and 'negative regulation of neural differentiation' GO terms support this hypothesis. Genes upregulated following PRMT5 inhibition (**Figure 4.7**) are associated with differentiation: Matrilin-2 (*MATN2*) induces differentiation of OPCs to mature oligodendrocytes (Sozmen *et al.*, 2019); Apolipoprotein E (*APOE*) is expressed in differentiated astrocytes and can promote oligodendroglial differentiation (Safina *et al.*, 2016; Zhao *et al.*, 2017); Potassium Inwardly Rectifying Channel Subfamily J Member 10 (*KCJN10*) expression is correlated with cell cycle exit and can arrest glioma growth (Olsen and Sontheimer, 2008).

Whereas repressed genes (**Figure 4.7**)) are associated with stemness: Midkine (*MDK*) is expressed in human embryonic stem cells and promotes their proliferation and self-renewal (Yao *et al.*, 2010); Stimulation of Tumor necrosis factor receptor 2 (*TNFR2*) increases entry of stem-like renal carcinoma cells into the cell cycle (Al-Lamki *et al.*, 2016); Ephrin type-B receptor 2 precursor (*EPHB2*) promotes tumoursphere formation and receptor activation increases expression of stem cell markers (Chen *et al.*, 2015); Nerve growth factor receptor (*NGFR*) is highly expressed in human adult neural stem cells (NSCs) and its knockdown can impair colony formation of melanoma cells (Redmer *et al.*, 2014; Sandberg *et al.*, 2014). Altogether these changes in gene expression suggest that PRMT5 inhibition does promote differentiation and could reduce stem-like behaviour of DIPG cells.

The stem-like behaviour, specifically the colony forming capacity, was experimentally tested by extreme limiting dilution (ELDA) (Hu and Smyth, 2009). An *in vitro* functional assay was selected as stemness or differentiation marker genes can be contentious or difficult to validate (Goldman, 2008) and because it was more experimentally tractable than the 'gold standard' *in vivo* limiting dilution assays (Rycaj and Tang, 2015). An overview of the method is illustrated in **Figure 4.12.** Briefly, dissociated cells are seeded at densities low enough that at least one stem cell will be present in < 100% of wells at a given density and colonies will be

formed from a single 'stem-like' (clonogenic) cell. The fraction of wells in which a colony forms is used to estimate a Poisson distribution that describes the frequency of clonogenic cells, which is then related to the number of cells seeded as a stem cell fraction.

A pilot assay was performed in which 16, 8, 4, 2, 1 or 0.5 HSJD-DIPG-007 cells/well were seeded in 6 wells each in a 96 well plate and colonies quantified after 5 days. Automated analysis of brightfield images was unable to reliably detect colonies (>2 cells) so they were counted manually. Analysis in R found a clonogenic cell fraction of 1 in 2.19 cells (95% CI 1.27-3.78). However, colonies were present in 5/6 wells at 16 cells/well and in all wells at 8 and 4 cells/well and at the lowest cell concentration colonies were still present in 3/6 wells. This saturation at the upper end and high frequency at the lower end limits the information supplied about the frequency of clonogenic cells, therefore seeding densities were reduced in future assays. Furthermore, to facilitate colony detection in future assays, the growth window was increased to 7 days, and live colonies were stained with Calcein AM allowing high contrast fluorescent imaging.

To assay the change in colony forming potential of DIPG cells following PRMT5 inhibition, HSJD-DIPG-007 cells were pre-treated with LLY-283 GI_{70} then reseeded without LLY-283 in limiting dilutions of 9, 6, 4 and so on, in 1.5X serial dilutions to a final density of 0.23 cells/well (**Figure 4.12a**). A pre-treatment was selected to test whether the population which remains after treatment (**Figure 3.13b**) is enriched for stem-like cells (implying that PRMT5 inhibition is unable to kill stem-like cells) and whether any drop in stemness can persist post treatment. The 7-day pre-treatment with LLY-283 decreased the fraction of colony forming cells from 72% to 23% (**Figure 4.12d**). Thus, reduction in viability of DIPG cells following PRMT5 inhibition may be due to a loss of stem-like characteristics. The resulting reduction in proliferation and self-renewal could reduce DIPG metastasis to distant regions of the CNS via the cerebrospinal fluid (Lu, Brown and Daniels, 2020).

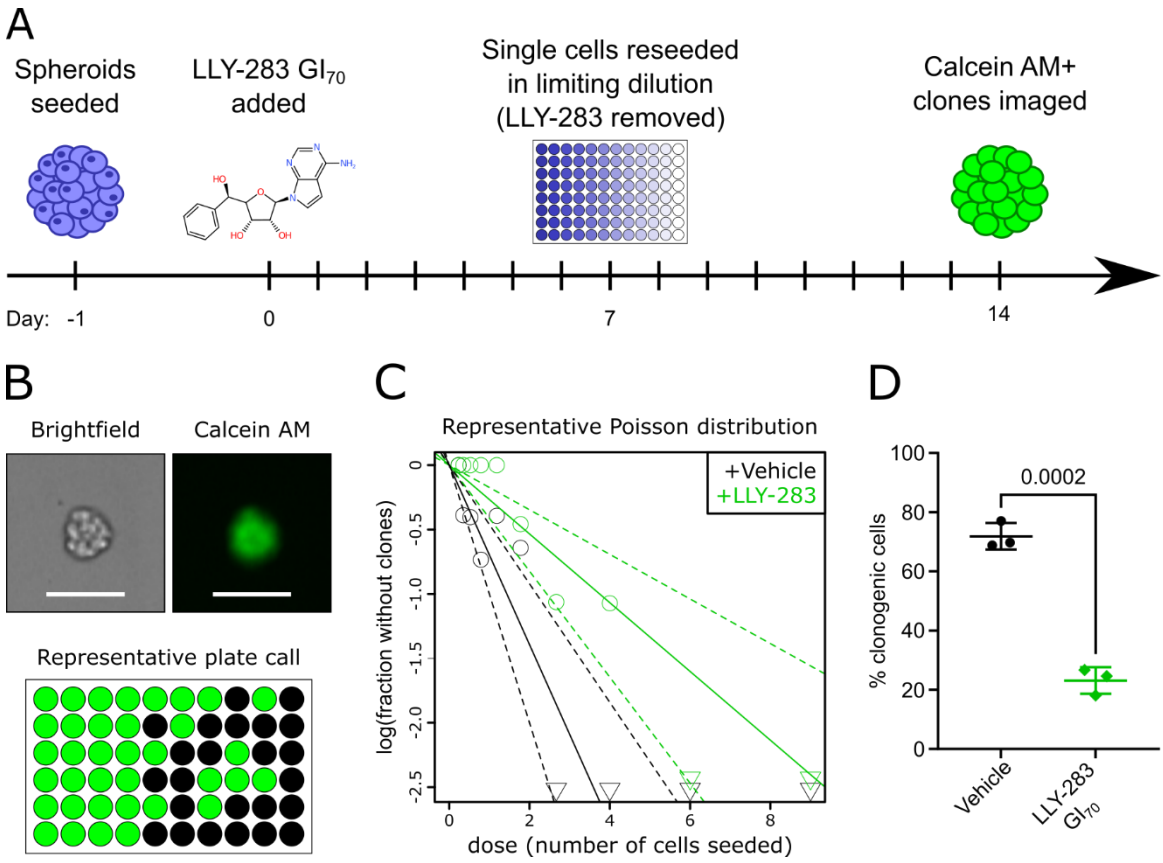

Figure 4.12 - PRMT5 inhibition reduces clonogenicity of DIPG cells in vitro

(A) *HSJD-DIPG-007 cells were seeded as loose spheroids. The following day the LLY-283 GI_{70} was added to the growth medium. After 7 days of growth in the presence of LLY-283 GI_{70} spheroids were split and seeded as single cells in a titration (6 technical repeats per seeding density) which allows derivation of the fraction of clonogenic cells in the population. After 7 days calcein AM was added to the growth medium and viable clones were imaged with the Celigo Image Cytometer.* ***(B)*** *Representative brightfield and fluorescent images of a HSJD-DIPG-007 clone, and overview of calls (green where at least one clone is present) of one 96 well plate.* ***(C)*** *Representative Poisson distribution calculated from one independent limiting dilution assay.* ***(D)*** *The estimated percentage of clonogenic cells in vehicle or LLY-283 treated cells. Points are the estimated stem cell fraction from each independent repeat annotated with mean and SD. Statistical significance (p = 0.0002) was calculated by unpaired t-test.*

4.2.8. PRMT5 inhibition impairs DIPG invasion into Matrigel

The role of PRMT5 in regulation of the ECM or cytoskeleton has not yet been elucidated, but many of the downregulated genes from the 'ECM organisation' GO term (**Figure 4.7**) have roles in cell invasion; Fascin-1 (*FSCN-1),* Fibroblast Growth Factor Receptor 4 (*FGFR4)*, Pentraxin 3 (*PTX3*) and Platelet Derived Growth Factor Beta (*PDGF-B*) mediate invasion in multiple solid tumours, including glioma (Vignjevic *et al.*, 2007; Sugiyama *et al.*, 2010; Sun *et al.*, 2013; Tung *et*

al., 2016; Liu *et al.*, 2018; Louca *et al.*, 2020). The characteristic extensive infiltration of DIPG cells into extrapontine tissues prevents complete surgical resection and contributes the neurological symptoms associated with DIPG (Kluiver *et al.*, 2020). Thus, an *in vitro* assay was developed to assess the invasive behaviour of DIPG cells after PRMT5 inhibition.

A spheroid invasion assay was adapted from a previously published study (Vinci, Box and Eccles, 2015) wherein single spheroids are embedded in Matrigel which induces their invasion outwards in 3 dimensions. A pilot experiment compared the impact of the number of cells initially seeded and the time needed to observe invasion into Matrigel. Spheroids formed from 40 cells (i.e. the density used in previous spheroid viability assays) were compared to those formed from 200 cells (**Figure 4.13**). Larger spheroids were included according to the hypothesis that a larger spheroid would have more pronounced internal nutrient or oxygen gradients (consequent as a necrotic core) that would then promote a greater deal of invasion away from the spheroid centre. Indeed, larger spheroids demonstrated a greater deal of invasion into surrounding Matrigel (**Figure 4.13a, b**). Additionally, half of the spheroids were treated with an ACVR1 inhibitor (LDN-193189), which was included as a positive control to kill the spheroid and thus prevent invasion. The IC_{50} curve for LDN-193189 generated at day 3 had a greater dynamic range than at day 1, because invasion continued over the full 3 days observed (**Figure 4.13a, c**). Thus, for future assays spheroids were generated from 200 cells, and invasion imaged after 3 days post Matrigel addition.

Another optimisation experiment was performed to compare the extent of migration in different concentrations of Matrigel. Reducing the concentration of Matrigel also reduces the degree of invasion (**Figure 4.14**). Perhaps a lower Matrigel concentration means there are fewer chemotactic growth factors to encourage outward invasion. Alternatively, with a lower concentration of ECM proteins there were fewer anchor points for the formation of focal adhesion complexes which stimulate generation of the actin structures necessary for cell

migration (Gkretsi and Stylianopoulos, 2018). Intriguingly, equal concentrations of the ACVR1 inhibitor M4K1139 only killed the spheroids at the highest concentrations of Matrigel (**Figure 4.14**). Although ECM-cell interactions can support cell survival (Stupack and Cheresh, 2002), ACVR1 inhibition can kill spheroids in the absence of Matrigel (Carvalho *et al.*, 2019). Instead, this difference is likely due to incomplete mixing in low Matrigel concentration wells because of a protocol inconsistency: In the higher concentration wells M4K1139 was added directly to the well, whereas at low Matrigel concentrations it was added separately (see section 2.5.6). To avoid this problem, in the subsequent experiment LLY-283 was diluted directly into Matrigel rather than growth medium before addition to the well.

In these initial optimisation experiments the concentration of Matrigel was expressed as a percentage, however this is not recommended because the concentration of Matrigel varies between lots (8-12 mg/mL, averaging to 10 mg/mL)[7]. Considering the concentrations quoted by Corning (USA), the concentrations tested in **Figure 4.14** are non-overlapping, and optimisation should be sufficient for future experiments. For the final assay Matrigel was added to final concentration of 4.65 mg/mL (corresponding approximately to the 50% Matrigel used in the optimisation experiments).

Initially the area of invasion was expressed as the change in area from day 0 to day 3 in Matrigel (**Figure 4.13c, Figure 4.14b**), but over 3 days the cells will divide as well as invade making it difficult to disentangle the contributions of these two processes to the increase in cross-sectional area. Therefore, in the final assay additional controls – spheroids to which no Matrigel was added – were included so the increase in cross-sectional area purely caused by invasion could be measured. For the final assay 'invasion (fold change)' refers to the fold change in area relative to the matched Matrigel free control, rather than a previous time point.

[7] https://www.corning.com/emea/en/products/life-sciences/products/surfaces/matrigel-matrix.html accessed 2021-11-12

To test whether reduction of transcripts associated with tumour cell invasion does translate into a change in invasion of DIPG cells HSJD-DIPG-007 cells were treated *in vitro* with LLY-283 and their invasion into Matrigel measured (**Figure 4.15**). Cells were treated with LLY-283 for a total of 6 days: 3 days prior to Matrigel addition and a further 3 days in Matrigel. The invasion induced by Matrigel caused a 3-fold greater increase in cross-sectional area relative to growth in the absence of extracellular matrix (**Figure 4.15**). Treatment with LLY-283 GI_{50} did not significantly reduce this invasion, but LLY-283 GI_{70} treated spheroids increased in area only 1.5-fold ($p < 0.0001$, one-way ANOVA with Dunnett's multiple comparisons test) (**Figure 4.15b, c**). Altogether these experiments show that PRMT5 inhibition can reduce three clinically important phenotypes: viability, clonogenicity and invasiveness in DIPG cells *in vitro*.

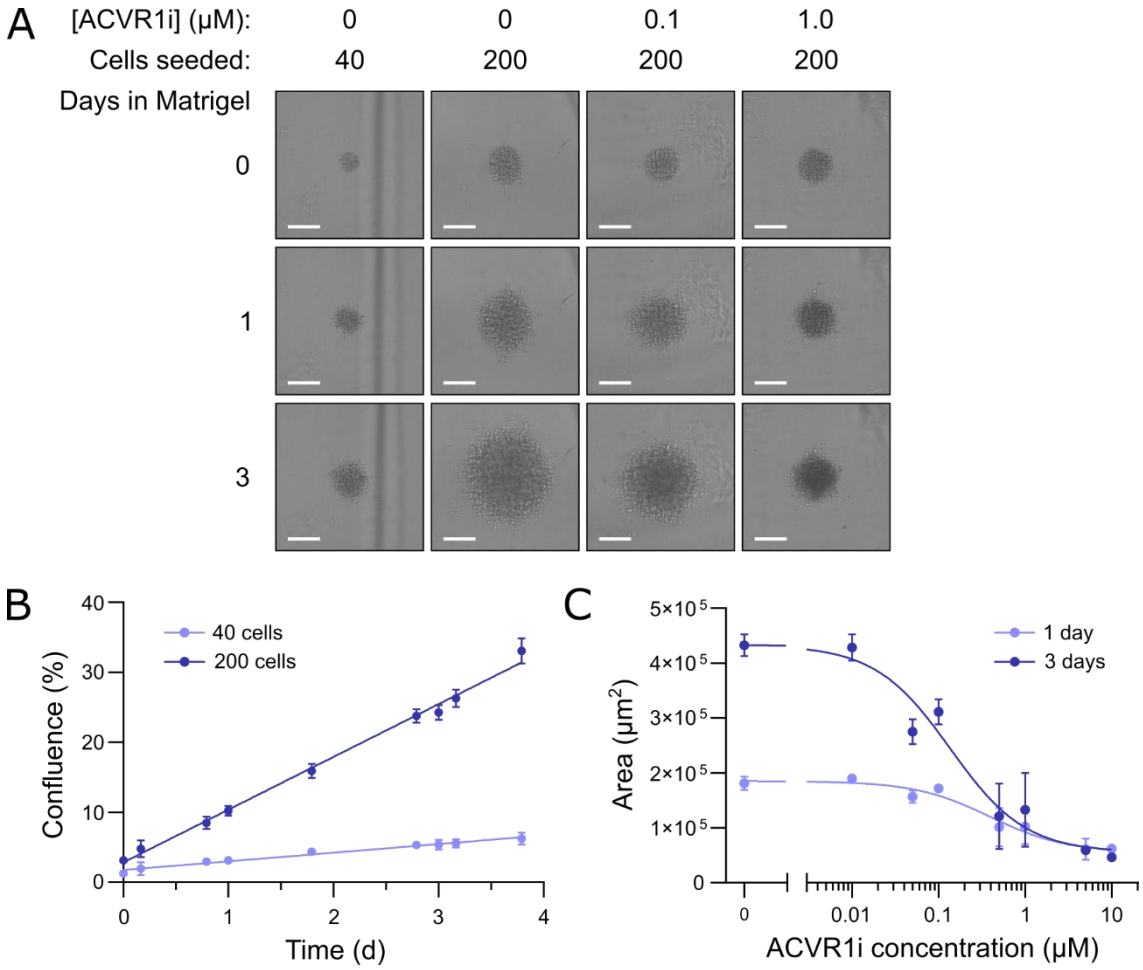

Figure 4.13 - Optimisation of in vitro migration assay

40 or 200 HSJD-DIPG-007 cells were seeded into a U-bottomed ultra-low-attachment 384 well plate. 3 days later Matrigel was added to a final concentration of 50% along with ACVR1 inhibitor LDN-193189 to the final concentrations indicated. Spheres were imaged daily by brightfield. ***(A)*** *Shows representative images. Scale bars are 250 μm.* ***(B)*** *A comparison of quantification of cross-sectional area (expressed as confluence) between spheroids seeded from 40 or 200 cells over time. Points are mean of 3 technical repeats annotated with SD.* ***(C)*** *Comparison of invasion inhibition curves between day 1 and day 3 time points. Points are mean of 3 technical repeats annotated with the SD. Curve was fit with the '[Inhibitor] vs response (three parameters)' GraphPad Prism module.*

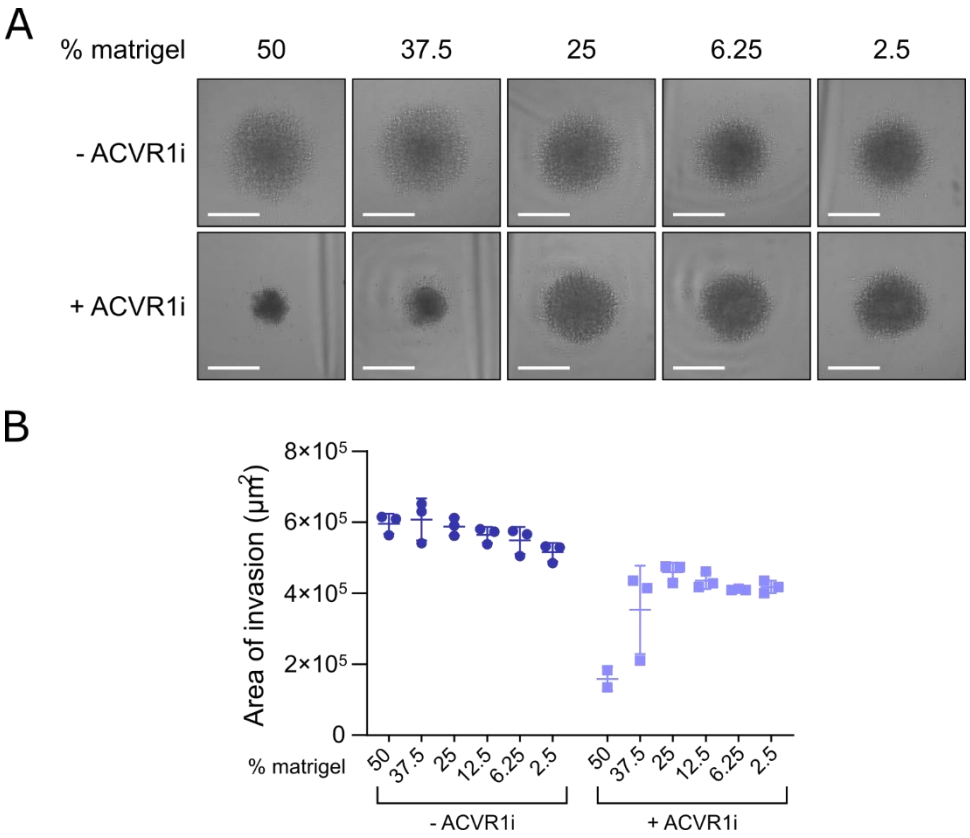

Figure 4.14 - Comparison of Matrigel concentrations

(A) 200 HSJD-DIPG-007 cells were seeded into a U-bottomed ultra-low-attachment 384 well plate. After 3 days Matrigel was added to the final concentrations indicated +/- 1 µM M4K1139 (ACVR1 inhibitor). Invasion into Matrigel was imaged 4 days later by brightfield (representative images shown). Scale bars are 500 µm. (B) Quantification of the degree of invasion into differing concentrations of Matrigel +/- ACVR1 inhibition. Area of invasion refers to the increase in cross sectional area from 0 to 3 days in Matrigel. Points are technical repeats annotated with mean and SD.

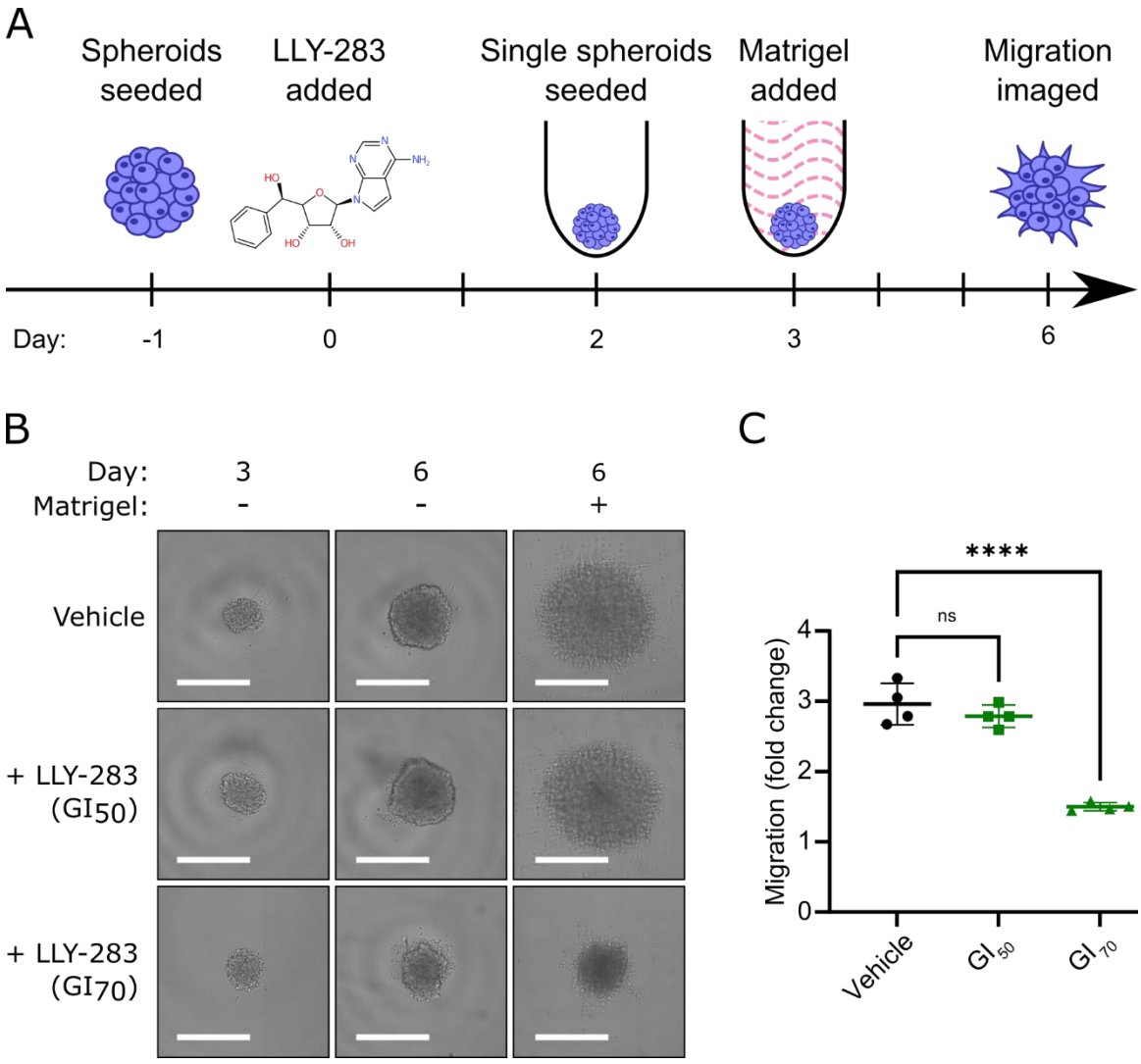

Figure 4.15 - PRMT5 inhibition reduces invasion of DIPG cells intro Matrigel

(A) *200 HSJD-DIPG-007 cells were seeded as loose spheroids and the following day were treated with a vehicle control, the LLY-283 GI_{40} or GI_{70}. After 2 days HSDJ-DIP-007 cells were dissociated, counted and 200 cells were reseeded as single spheroids in medium containing the same concentration of vehicle/LLY-283. The following day half of the spheroids were embedded in 4.65 mg/mL Matrigel (again maintaining vehicle/LLY-283) and the other half remained as controls for undisturbed spheroid growth. Invasion into Matrigel was imaged by brightfield after a further 3 days (6 days total treatment period).* ***(B)*** *Representative images of spheroids before Matrigel addition (day 3) and at 3 days +/- Matrigel addition (day 6) showing characteristic outward invasion of HSJD-DIPG-007 cells. Scale bars are 500 µm.* ***(C)*** *Quantification of HSJD-DIPG-007 invasion into the surrounding Matrigel expressed as the fold change in overhead cross-sectional area compared to the without Matrigel spheroid growth control. **** = $p < 0.0001$ by ordinary one-way ANOVA with Dunnett's multiple comparisons test.*

4.2.9. First test of LLY-283 in a murine xenograft model of DIPG

The dire prognosis and lack of effective targeted therapies for DIPG patients warrants rapid testing of putative therapeutic targets in *in vivo* models. Thus, LLY-283 was passed to Ángel Montero Carcaboso to be tested in previously published orthotopic xenograft model of DIPG (Vinci *et al.*, 2018; Carvalho *et al.*, 2019) with which his group has expertise. Despite GSK591 having a lower GI_{50} *in vitro* against the cell line used in the xenograft model (HSJD-DIPG-007), LLY-283 was selected because it has been confirmed to enter the brain (Sachamitr *et al.*, 2021). Established HSJD-DIPG-007 brainstem xenografts were treated with 50 mg/kg LLY-283 by oral gavage, 3 days on, 4 days off, for 4 weeks (n = 15 per group) (**Figure 4.16a**), which is a dosing strategy previously established from pharmacokinetic and tolerability experiments (Sachamitr et al. 2021). Treatment with LLY-283 caused only a minor weight loss (-4.1% ± 1.7%, unpaired t-test at day 56) compared to the vehicle control (**Figure 4.16b**). LLY-283 treatment did not prolong survival (log rank test, p = 0.238) (**Figure 4.16c**) or reduce tumour burden (p = 0.084, unpaired t-test) (**Figure 4.16d**). This negative result is perhaps not surprising given the aggressive nature of DIPG and expected need for combination therapies to achieve survival improvement, as discussed in later in this chapter.

4.2.10. Systemic administration of LLY-283 caused demethylation in the mouse brainstem

Given negative result *in vivo*, the levels of arginine methylation present in the brainstem were tested to confirm whether target engagement was achieved. Arginine methylation in the brainstem was visualised by immunohistochemical staining of paraffin embedded tissue sections for symmetrical dimethyl arginine (SDMA, the methylation mark created by PRMT5) and histone H4 methylation (H4R3me2s, a specific histone mark created by PRMT5) (Bonday *et al.*, 2018; Scaglione *et al.*, 2018), alongside histone H4 itself as an indication of total protein expression. After the final dose of LLY-283 ('after last dose') the levels of both SDMA and

H4R3me2s were significantly reduced (one way ANOVA with Tukey's multiple comparison test, $p<0.05$), but neither were completely lost (**Figure 4.17a**). Methylation had fully returned, and perhaps even increased, by experimental end point ('endpoint') (**Figure 4.17b**). This confirms at least partial target engagement within the brainstem, although, given no survival benefit was achieved, this may not represent the maximum inhibition that could be achieved with more complete penetration into the brain.

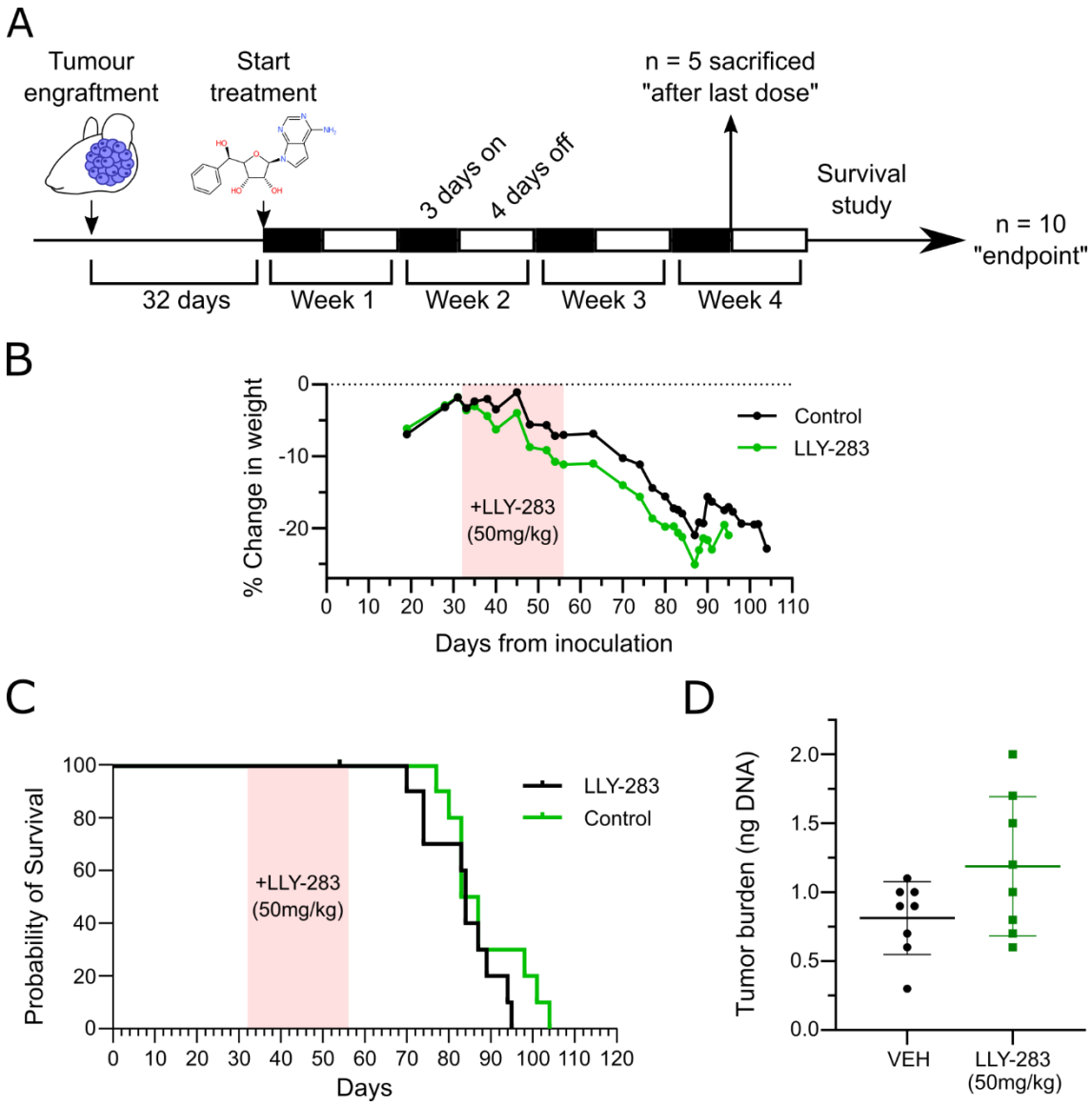

Figure 4.16 - PRMT5 inhibition does not prolong survival of HSJD-DIPG-007 xenografts

(A) *Athymic nude mice were engrafted with HSJD-DIPG-007 cells. Tumours were allowed to initiate for 32 days before vehicle (n = 15) or LLY-283 (n = 15) was administered at 50 mg/kg, 3 days on/4 days off for 4 weeks. After 4 weeks 5 mice from each group were sacrificed, and the remaining were used to measure survival (endpoint criteria: 20% weight loss due to disease).* ***(B)*** *Weight of mice over time, showing toxicity due to treatment.* ***(C)*** *Survival curve of mice after 4 week treatment with vehicle or LLY-283. The treatment period is highlighted in red.* ***(D)*** *Tumour burden as indicated by digital drop PCR for the amount of R206H ACVR1 DNA present in the brains of mice sacrificed just after administration of the final LLY-283 dose.*

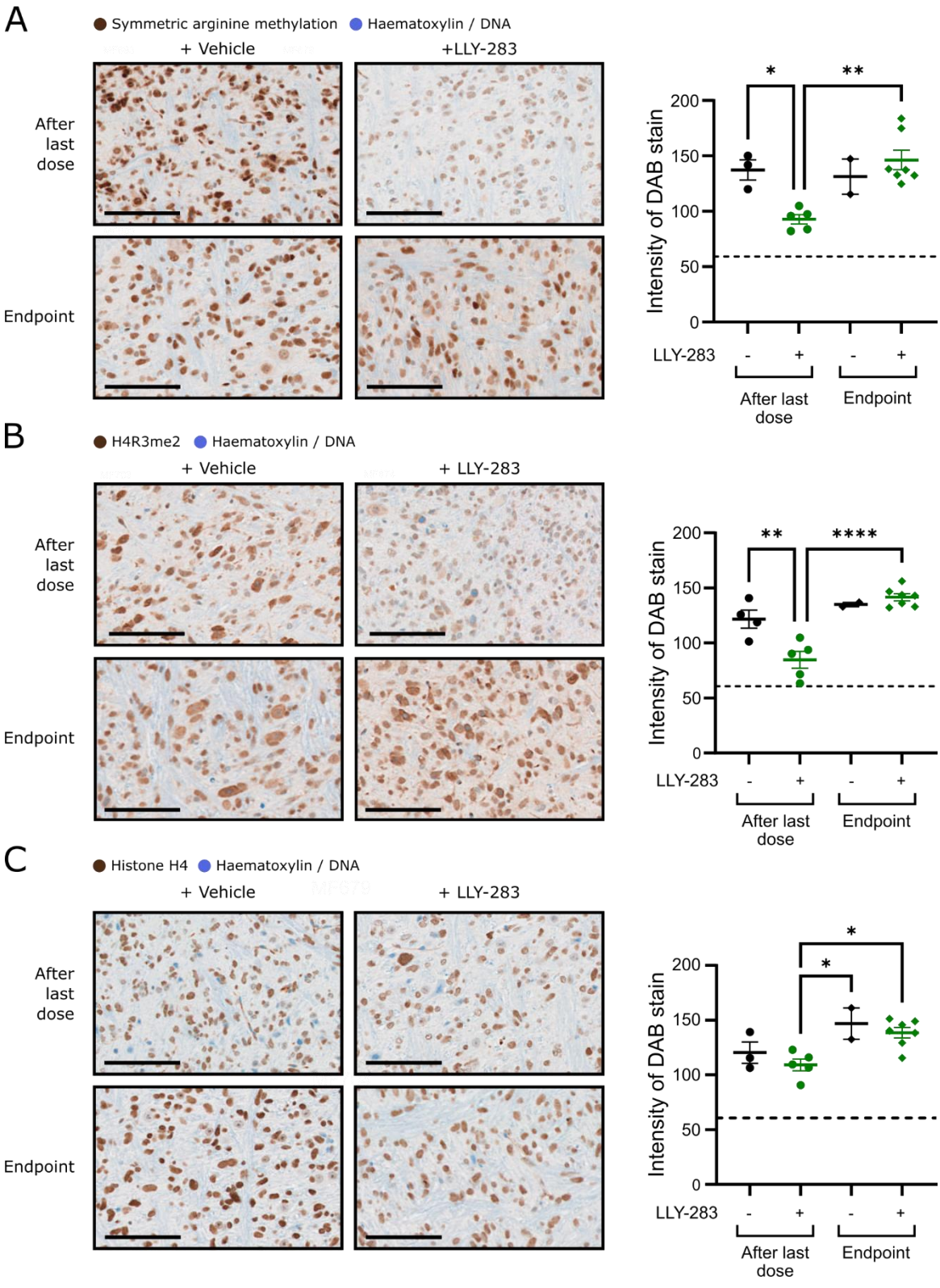
A
Symmetric arginine methylation
Haematoxylin / DNA
+ Vehicle
+LLY-283
After last dose
Endpoint
Intensity of DAB stain
200
150
100
50
0
*
**
LLY-283
-
+
-
+
After last dose
Endpoint
B
H4R3me2
Haematoxylin / DNA
+ Vehicle
+ LLY-283
After last dose
Endpoint
Intensity of DAB stain
200
150
100
50
0
**
****
LLY-283
-
+
-
+
After last dose
Endpoint
C
Histone H4
Haematoxylin / DNA
+ Vehicle
+ LLY-283
After last dose
Endpoint
Intensity of DAB stain
200
150
100
50
0
*
*
LLY-283
-
+
-
+
After last dose
Endpoint

Figure 4.17 - Systemic LLY-283 administration leads to demethylation in the brainstem

Paraffin embedded sections from treated and vehicle mouse brains harvested immediately after the final dose of LLY-283 ('after last dose') or at the experimental end point ('endpoint') were immunohistochemically stained for symmetric dimethyl arginine (SDMA) ***(A)****, symmetric dimethylation of histone H4 arginine (H4R3me2s)* ***(B)*** *or histone H4* ***(C)****. Left, Representative images of immunohistochemical staining. Scale bars are 100 µm. Right, Quantification of staining intensity of SDMA (A), H4R3me2s (B) or H4 (C). Each point represents the median staining intensity of individual cells (SDMA) or nuclei (H4R3me2s/H4) in one field of view of one biological repeat, annotated with mean and SEM. Statistical difference between groups was tested by one way ANOVA with Tukey's multiple comparison test (* $p < 0.05$; ** $p < 0.01$; **** $p < 0.0001$). The dashed line indicates the intensity of staining in the matched IgG isotype control.*

4.2.11. PRMT5 administration does not alter stemness of DIPG cells

To test whether the decrease in stem-like behaviour following PRMT5 inhibition *in vitro* also occurs *in vivo,* the expression of stem cell and differentiation markers in tissue sections was visualised by immunohistochemistry. The markers tested were: GFAP, a major component of the astrocyte cytoskeleton (Pekny and Pekna, 2004); MASH1/Ascl1, a transcription factor expressed in proneural and oligodendrocyte precursor cells that is implicated in the tumorigenesis of DIPG (Nakatani *et al.*, 2013; Fortin *et al.*, 2020); and Olig2, a marker for the oligodendroglial lineage and DIPG cells (Ligon *et al.*, 2004; Sturm *et al.*, 2012). After PRMT5 inhibition GFAP expression (Figure 4.18a), proportion of MASH1 positive cells (Figure 4.18b) and proportions of OLIG2 positive cells (Figure 4.18c) did not significantly change. This small selection of differentiation markers does not change in response to *in vivo* PRMT5 inhibition, although further functional testing could be warranted.

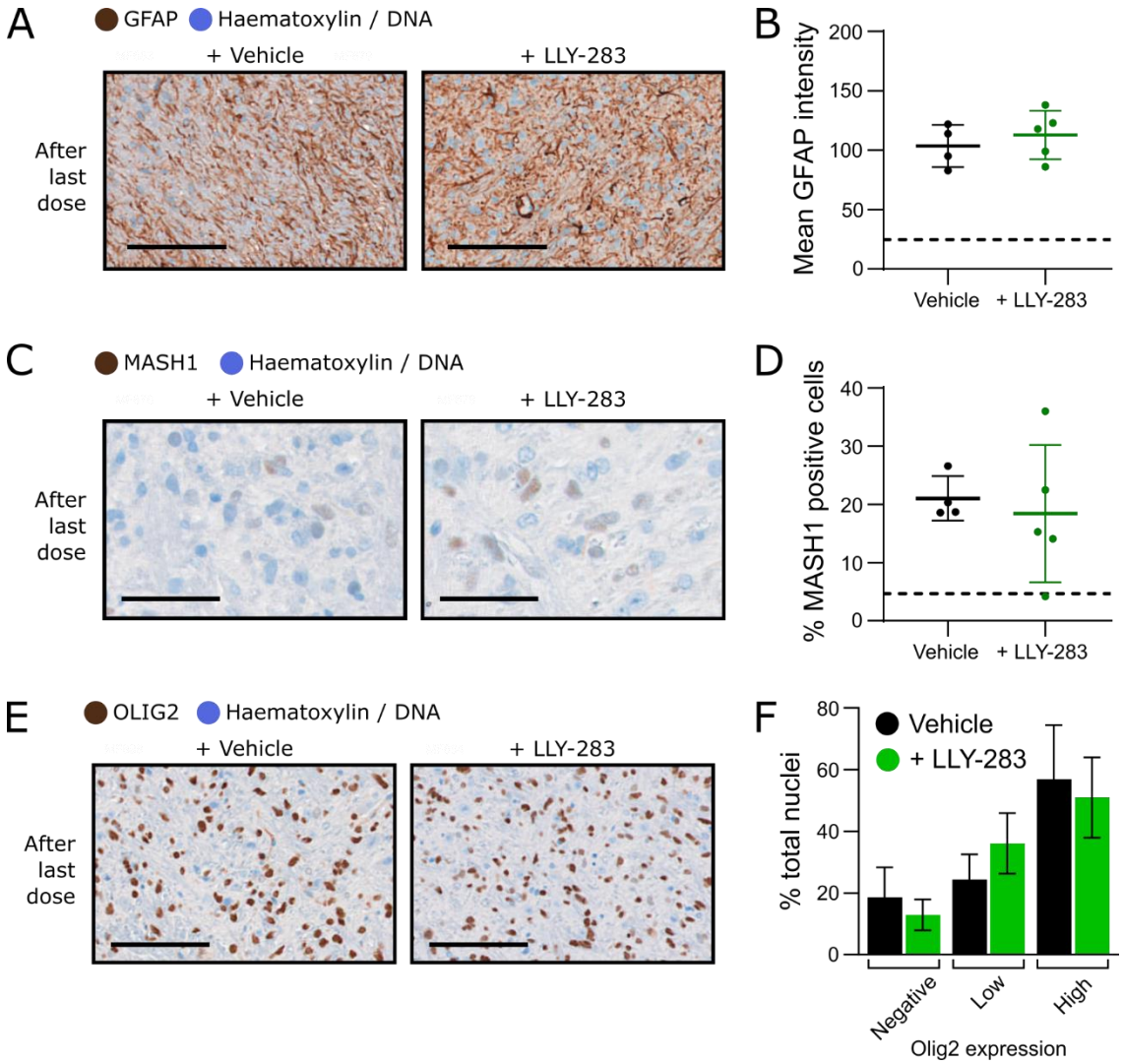

Figure 4.18 - PRMT5 inhibition did not alter differentiation markers in the brainstem

Paraffin embedded sections from treated (50 mg/kg LLY-283) and vehicle mouse brains harvested immediately after the final treatment dose were immunohistochemically stained for differentiation markers. ***(A, C, E)*** *Representative images of GFAP* ***(A)****, MASH1* ***(B)*** *and OLIG2* ***(C)****. Scale bars are 50 µm (A, C), or 100 µm (C).* ***(B)*** *Quantification of the mean intensity of GFAP staining. Each point represents one field of view and is a separate biological repeat. Bars are mean and SD. The dashed line is the mean staining intensity of two biological repeats stained with a matched isotype control.* ***(D)*** *Quantification of the proportion of MASH1 positive cells. Each point represents the proportion of positive nuclei in one field of view and is from a different biological repeat. Bars are mean and SD. The dashed line indicates the mean proportion of positive cells detected in two sections stained with a matched isotype control.* ***(F)*** *Quantification of Olig2 expression. Nuclei were scored as having negative, low, or high Olig2 expression based on their mean intensity. Bars are the mean proportion of negative, low or high nuclei in one field of view each for four (vehicle) or five (+ LLY-283) biological repeats, annotated with SD. 98.5% of cells were scored negative in a matched isotype control (mean of 2 biological repeats).*

4.2.12. PRMT5 inhibition impairs migration of DIPG cells

As further validation of digital droplet (dd)PCR measurements of tumour burden and to assess whether PRMT5 inhibition impairs DIPG cell invasion *in vivo*, the number of DIPG cells in the mouse brainstems was counted. DIPG cells were visualised by immunohistochemically staining the mouse brain for human nuclear antigen (**Figure 4.19**). In accordance with ddPCR quantification of tumour burden, the number of human cells in the brainstem did not significantly change after LLY-283 treatment (unpaired t-test) (**Figure 4.19a**). Interestingly, in LLY-283 treated mice there was a trend towards decreased invasion of DIPG cells into the forebrain ($p = 0.15$, unpaired t-test) (**Figure 4.19b**). The number of cells that had invaded into the forebrain was markedly reduced in 3/5 of the LLY-283 treated mice (1.9-7.9-fold fewer human cells) (**Figure 4.19b**). Although further experiments to systematically sample the brain in 3 dimensions would be desirable, this suggests that PRMT5 inhibition reduced invasion of DIPG out of the brainstem into other anatomical locations.

In this chapter, transcriptomic analysis and *in vitro* assays demonstrated that PRMT5 inhibition by LLY-283 altered expression of metabolic genes, reduced stemness and restored H3K27me3 levels in DIPG cells *in vitro.* LLY-283 was tested in an orthotopic murine xenograft model of DIPG but did not prolong survival with partial target engagement in the brainstem. However, invasive behaviour of DIPG cells was reduced *in vitro* and *in vivo* after PRMT5 inhibition.

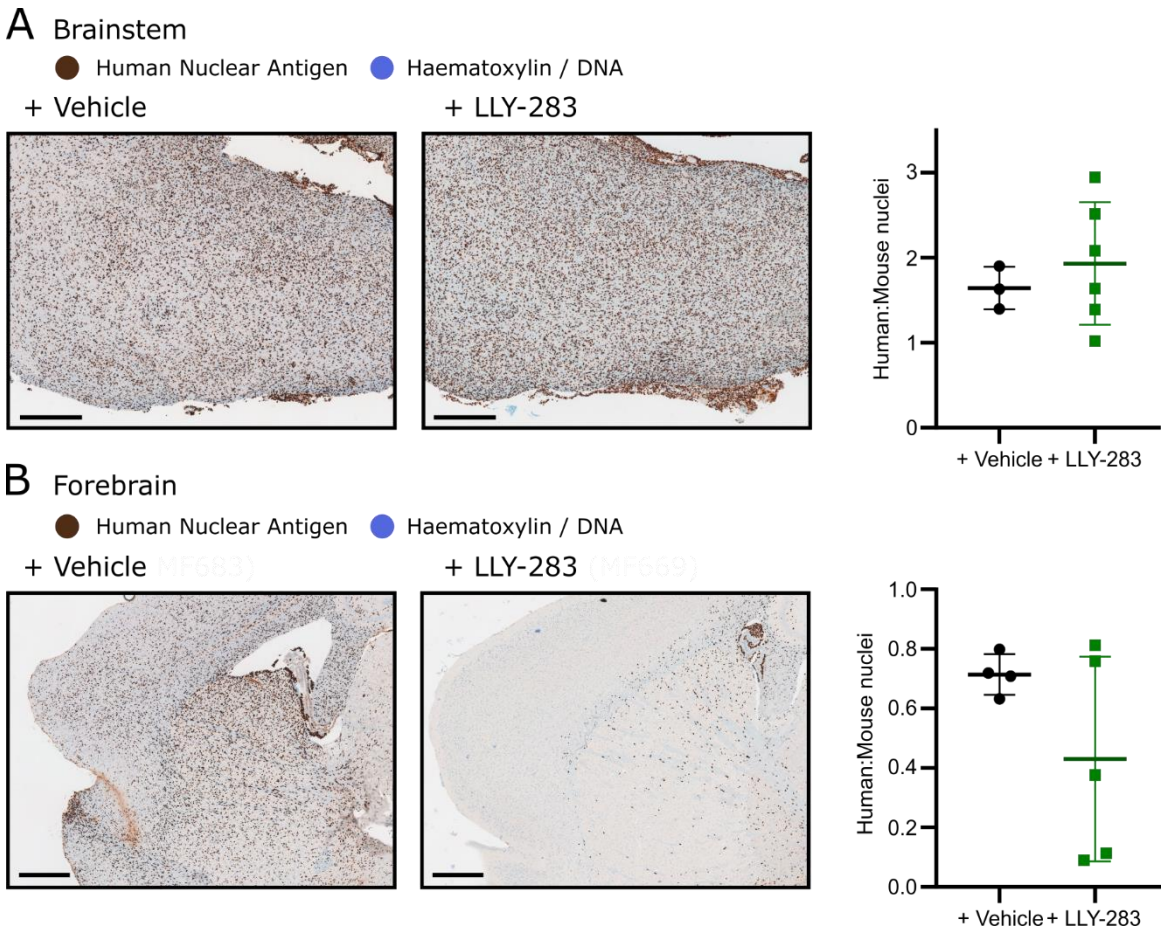

Figure 4.19 - PRMT5 inhibition reduced migration of DIPG cells into the mouse forebrain

*Left, Representative images of the brainstem **(A)** and forebrain **(B)** from mouse brains harvested immediately after the final dose of LLY-283 (50 mg/kg) immunohistochemically stained for human nuclear antigen. Scale bars are 500 µm. Right, Quantification of the proportion of human nuclear antigen positive (human):negative (mouse) nuclei in one field of view. Each point is one biological repeat, annotated with mean and SD.*

4.3. Discussion

In Chapter 3 PRMT5 inhibition was found to potently reduce DIPG viability. PRMT5 regulates many cellular processes (Blanc and Richard, 2017; Hwang *et al.*, 2021) and it was hypothesised that this pleiotropy could make PRMT5 inhibition a good therapeutic strategy as a single agent could potentially impair multiple hallmarks of cancer simultaneously. Here, the aim was to understand more completely how PRMT5 inhibition affects DIPG *in vitro* and *in vivo*.

The potent effect of PRMT5 inhibition *in vitro*, and the poor prognosis for DIPG patients motivated the rapid testing of PRMT5 inhibition *in vivo*. Systemic administration of LLY-283 (50 mg/kg daily, 3 days on, 4 days off, for 4 weeks) did not extend survival in a commonly used orthotopic xenograft model of DIPG (Vinci *et al.*, 2018), despite this model using the same patient derived cell line as was most sensitive to PRMT5 inhibition *in vitro*. This is not surprising given the aggressive nature of DIPG – it is exclusively diagnosed at grade IV and progresses rapidly (Louis *et al.*, 2016; Cooney *et al.*, 2017) – and there are multiple reasons why this initial test may have failed.

A question throughout any attempt to develop cancer therapeutics is whether they induce cell death or simply growth arrest. Induction of cell death is often seen as preferable to growth arrest *in vivo,* as it could lead to tumour regression rather than just halted progression (Ewald *et al.*, 2010). In Chapter 3, PRMT5 inhibition did not induce cell death and in this chapter, GO analysis of unfiltered DE gene lists found enrichment of terms relating to the G2/M cell cycle transition. There is limited evidence that PRMT5 inhibition can induce G2/M cell cycle arrest (Vinet *et al.*, 2019) although PRMT5 is mainly associated with regulation of the G1/S cell cycle transition (Banasavadi-Siddegowda *et al.*, 2018; Raposo and Piller, 2018). Together, these observations suggest that PRMT5 inhibition reduces DIPG viability *in vitro* by arresting cell division rather than inducing cell death. However, in the xenograft model there was no relative

reduction in tumour burden after treatment with LLY-283, implying that cell cycle arrest was also not induced *in vivo.*

Growth arrest may not have occurred because target engagement (i.e. arginine demethylation) in the tumour was incomplete. That is, the brainstem penetration of LLY-283 may have been insufficient to produce a clinical response. LLY-283 was selected over GSK591 as, prior to the study, it had been found to have a CNS penetrance of 0.3 (Cheryl Arrowsmith, personal communication), which was less than ideal but thought to be sufficient to proceed. After completion of the experiment, published data showed that LLY-283 remains in the brain at therapeutic concentrations 24 h after a single dose (Sachamitr *et al.*, 2021), although the concentration likely falls further in the 4 withdrawal days of the dosing strategy. However, these measures do not refer specifically to the brainstem which compounds often penetrate to an even lesser degree than the rest of the brain (Warren, 2018; Zeiadeh, Najjar and Karaman, 2018).

Although LLY-283 can partially penetrate the BBB, it was developed as an experimental chemical probe, not a drug compound and more drug-like PRMT5 inhibitors, such as JNJ64619178 may achieve better penetration of the brainstem (Quinlan and Brennan, 2021). Alternatively, convection enhanced delivery (CED), which circumvents the BBB by delivering a compound directly into the brain under positive pressure, can significantly improve the outcome of treatment in animals models where systemic administration was insufficient (Sasaki *et al.*, 2020). Either of these strategies could improve target engagement in the brainstem or alternatively subcutaneous flank xenografting could test whether PRMT5 inhibition is effective *in vivo* independent of the blood brain barrier.

Interestingly, PRMT5 was also independently identified from another screen of the SGC epigenetic probe set for the treatment of adult glioblastoma, but in this case was effective at extending the survival of an orthotopic forebrain xenograft model (median survival of 37 days

when treated with LLY-283 versus 30 days with the vehicle) (Sachamitr *et al.*, 2021). These contrasting results echo the observation that treatments which work for adult glioma do not work for the treatment of paediatric glioma because of their different genetic drivers (Jones *et al.*, 2017).

Nevertheless, it is interesting to consider the specific mechanisms by which PRMT5 inhibition impairs viability of DIPG cells *in vitro,* where it was potently effective. One of the most overt signatures in the day 5 DE gene list and was repression of sterol synthesis. Metabolism is frequently altered in brain tumours (Seyfried and Mukherjee, 2005; Phillips *et al.*, 2019; Michealraj *et al.*, 2020) and in DIPG H3K27M mutations cause enhanced glycolysis, glutaminolysis and tricarboxylic acid metabolism have previously been observed in DIPG cells as a consequence of H3K27M mutations (Chung *et al.*, 2020). As LSS expression was repressed after PRMT5 inhibition and DIPG cells are reportedly dependent on LSS (Phillips *et al.*, 2019), it was hypothesised that the decreased viability was caused by cholesterol deficiency and therefore could be reversed with exogenous cholesterol. Rescue of LLS inhibition by exogenous cholesterol was successfully recapitulated, but cholesterol could not similarly rescue PRMT5 inhibition. Thus, it seems the dependence of DIPG cells on PRMT5 was not due to cholesterol deficiency specifically.

Without clear confirmation of a role of metabolism in PRMT5 dependent DIPG viability, the study moved on to investigate differential expression of differentiation genes at day 5. The role of PRMT5 is highly context dependent; in NSCs PRMT5 is necessary for survival (Bezzi *et al.*, 2013) but paradoxically in OPCs PRMT5 expression is needed for oligodendrocyte differentiation (Huang *et al.*, 2011). Here, PRMT5 inhibition led to decreased expression of transcripts associated with stemness and a functional decrease in clone forming potential *in vitro*. Thus, in this context PRMT5 seems to behave as it does in NSCs, despite previous reports that DIPG cells have a gene expression profile similar to OPCs (Banasavadi-Siddegowda *et al.*, 2017; Filbin *et al.*,

2018). Perhaps the epigenetic changes caused by H3K27M that prevent glial differentiation (Funato *et al.*, 2014) also bias PRMT5 towards the role it plays in neural stem cells, to promote cell survival rather than differentiation.

Comparison of the differentially expressed genes at day 5 to a curated database of ChIP-seq datasets using the BART tool (Wang *et al.*, 2018) found an enrichment of targets of PRC2 components. Differential PRC2 activity after PRMT5 inhibition was pursued because of the known importance of PRC2 dysregulation in DIPG (Chan *et al.*, 2013; Lewis *et al.*, 2013; Mohammad *et al.*, 2017). There are contrasting theories for the interaction between EZH2 and PRMT5: one which suggests they oppose each other's activity (Liu *et al.*, 2020) and one which suggests they co-operate (Yang *et al.*, 2021). The most likely explanation for these differences is that the role of PRMT5 is highly cell context dependent. The data here suggest that PRMT5 and PRC2 act in opposition as PRMT5 inhibition restored H3K27me3 implying improved PRC2 activity. There are two potential mechanisms by which this could occur:

1. Methylation of histone H3 by PRMT5 was shown to impair subsequent methylation by EZH2 (Liu *et al.*, 2020). Loss of PRMT5 mediated methylation could therefore facilitate methylation by EZH2, despite the inhibitory effect of H3K27M.

2. High levels of intracellular alpha-ketoglutarate enable H3K27 hypomethylation because lysine demethylation requires alpha-ketoglutarate as a co-factor. In this context disruption of its synthesis was therapeutic (Chung *et al.*, 2020). The changes in metabolism after PRMT5 inhibition could have reduced cellular alpha-ketoglutarate and facilitated H3K27 re-methylation.

The observed restoration of PRC2 activity should discourage the combination of PRMT5 inhibition with EZH2 inhibitors.

Enrichment of ECM or cytoskeletal proteins was evident in both the day 5 DE genes and Trajecture marker list. The genes repressed (for example *FSCN-1* or *PTX3*) were associated with cell invasion (Vignjevic *et al.*, 2007; Tung *et al.*, 2016) and implied that PRMT5 inhibition could reduce the invasive behaviour of DIPG cells. Indeed, treatment with LLY-283 did impair invasion of DIPG cells into Matrigel *in vitro*. Furthermore, in 3 out of 5 mice treated with LLY-283 the number of DIPG cells that had infiltrated the forebrain was markedly reduced. Future work could include a more systematic examination of DIPG spread throughout the brain after LLY-283 treatment. PRMT5 inhibition could potentially be used to reduce extrapontine spread and limit symptoms associated with infiltration of other anatomical sites or improve efficacy of focal radiotherapy (Caretti, Bugiani, *et al.*, 2014; Kluiver *et al.*, 2020).

Although PRMT5 inhibition *alone* may be insufficient to slow the progression of DIPG *in vivo,* it has been suggested that DIPG prognosis will only be improved by combination treatment (Aziz-Bose and Monje, 2019). Treatment with a single agent often fails to prolong the survival of mouse models of DIPG and many report only achieving extended survival when targeted agents are combined, for example (Wiese *et al.*, 2016; Miyahara *et al.*, 2017; Meel *et al.*, 2020; Carvalho *et al.*, 2021). Those studies where a single agent was effective often report only a modest survival improvement (Hashizume *et al.*, 2014; Piunti *et al.*, 2017; Zhang *et al.*, 2017; Carvalho *et al.*, 2019). Thus, despite the failure of LLY-283 in this *in vivo* experiment, it would be worth testing LLY-283 in combination with other targeted therapeutics.

Chapter 5. CRISPR/Cas9 mediated correction of disease-causing mutations in patient derived DIPG cells

5.1. Background

25% of Diffuse Intrinsic Pontine Glioma (DIPG) patients carry a heterozygous missense activating ACVR1 mutation (Buczkowicz *et al.*, 2014; Fontebasso *et al.*, 2014; Taylor *et al.*, 2014; Wu *et al.*, 2014), but the role of this mutation in the development and maintenance of DIPG remains unclear.

Many ACVR1 knockout and knock-in experiments have been performed in FOP and developmental models (Dudas *et al.*, 2004; Rajagopal *et al.*, 2008; Chakkalakal *et al.*, 2012; Wang *et al.*, 2019; Hu *et al.*, 2021; Ramachandran *et al.*, 2021) but not in DIPG. Genetically engineered induced pluripotent stem cell (iPSC) DIPG models include histone H3 K27M, but not *ACVR1* mutations (Haag *et al.*, 2021). shRNA knockdown of *ACVR1* in HSJD-DIPG-007 DIPG cells (expressing ACVR1 R206H) showed that these cells were genetically dependent on ACVR1, but did not differentiate between the mutant and wild-type alleles (Carvalho *et al.*, 2019). Thus far, few tools exist for the study of ACVR1 mutations specifically in DIPG cells.

In this chapter, the aim was to interrogate the role of ACVR1 mutations on the DIPG cell by correcting the genomic *ACVR1* sequence to that of the wild-type gene using the CRISPR/Cas9 genome editing system. Patient-derived cell lines are invaluable for the study of DIPG, because they recapitulate the complex suite of genetic alterations found in primary tumours. However, it is difficult to infer the consequence of any specific mutation by comparing different cell lines with wild-type or mutant *ACVR1*, as each line would have a complex unmatched mutational background. This problem is compounded by the relatively small number of patient-derived cell lines available. By contrast, the removal or introduction of *ACVR1* mutations by CRISPR/Cas

genome engineering would generate genetically matched pairs (or sets) of patient-derived DIPG cell lines allowing more controlled experiments to be performed.

Most existing studies of *ACVR1* mutations in DIPG have focused on ACVR1 R206H, likely because of its high frequency in FOP patients, despite codon 328 being the most frequently mutated in DIPG (Han, Jain and Resnick, 2018; Carvalho *et al.*, 2019). Independent study of *ACVR1* G328V is warranted because this mutation has been noted to have a higher kinase activity, support greater oligodendrocyte differentiation, partition more often with H3.1 mutations and grant a better prognosis than *ACVR1* R206H (Carvalho *et al.*, 2019; Cao *et al.*, 2020). Thus, correction of the G328V mutation in SU-DIPG-IV cells was selected for this project.

The clustered regularly interspaced short palindromic repeats (CRISPR)/CRISPR associated nuclease (Cas) system was discovered as an adaptive immune system within prokaryotes (Horvath and Barrangou, 2010) and was rapidly repurposed into an arguably revolutionary genome engineering tool (Ran *et al.*, 2013). When used for genome engineering, the Cas endonuclease complexes with a single piece of guide RNA (sgRNA). The sgRNA is composed of a scaffold section which binds to the Cas endonuclease, and a variable 20 nt sequence which then targets the Cas to cut specific sections of DNA. The double strand breaks (DSBs) introduced can be repaired by two mechanisms: by non-homologous end joining (NHEJ) which leads to the introduction of small insertion or deletion mutations (indels) which can lead to the knockout of a protein by introduction of a stop codon or nonsense mediated decay; or by homology directed repair (HDR) where the other endogenous DNA strand (or an exogenous DNA template) is used to re-synthesise a section of the genome which can be used introduce custom mutations, or knock-in larger sections of DNA.

5.1.1. Experimental overview

For this study, the *S. pyogenes* (Sp)Cas9 nuclease was introduced alongside an sgRNA targeted to the *ACVR1* c.983G>T (G328V) locus as a ribonucleoprotein (RNP) complex.

Concurrently, a DNA template corresponding to the wild-type sequence was introduced (in addition to the wild-type allele already present in the cell) to encourage repair by HDR to the wild-type sequence rather than NHEJ or HDR with the mutant sequence. Following correction of the *ACVR1* G328V to the wild-type sequence the proliferation, clone forming capacity and protein secretion profile of each cell line was characterised. The sensitivity of these matched DIPG cell lines to ACVR1 and PRMT5 inhibition was assessed to confirm or refute the previous observation that sensitivity to inhibition of either protein correlated with *ACVR1* mutation status.

5.2. Results

5.2.1. Optimisation of electroporation conditions

Delivery of the CRISPR system into cells by electroporation of ribonucleoprotein complexes was selected because of the high on-target editing efficiency generally achieved (Kim *et al.*, 2014; Lattanzi *et al.*, 2019). However, unlike plasmid based delivery, a marker gene cannot be included to assess transfection efficiency. Instead, the efficiency of RNP delivery must be assessed by transfection with either a fluorescent protein or fluorescently tagged RNA (Seki and Rutz, 2018; Xu *et al.*, 2018; Leoni *et al.*, 2021).

To optimise the electroporation of RNP complexes into SU-DIPG-IV cells, Alexa Fluor 488 (AF488) fluorescent secondary antibodies were used as a surrogate for Cas9 in sgRNA/AF488 RNP complexes, as previously described (Xu *et al.*, 2018). 24 different combinations of pulse voltage, duration and frequency were tested and 24 h later flow cytometry was used to record the proportion of live cells, as determined with forward and side scatter (FSC and SSC), and the intensity of AF488 fluorescence measured (**Figure 5.1**). A small proportion of cells became AF488 positive without electroporation when AF488 was present suggesting the antibody was binding the outer surface of the cells (**Figure 5.1b**). Therefore, this was subtracted as background when quantifying the proportion of AF488 positive cells in the test settings. In the

initial gating strategy, all but one setting tested produced over 80% AF488 positive cells so an 'hyperpositive' gate was added to quantify cells with a higher fluorescence intensity, indicating more protein entry to the cell. The most effective electroporation setting, where 92.6% of live cells were AF488 'hyperpositive', was a single 20 ms pulse at 1700 V (**Figure 5.1d**). This setting also induced the most cell death suggesting that a harsher electroporation also allowed entry of more RNP complexes. Thus, all subsequent electroporation reactions were performed with a single 20 ms pulse at 1700 V.

Table 5.1 - Efficiency of electroporation settings

The 3 most effective settings are highlighted in green. The 3 settings that produced the most cell death are highlighted in orange.

Pulse voltage (V)	**Pulse length (ms)**	**Number of pulses**	**% live cells**	**AF488+ cells (% of live, -background)**	**AF488 hyper-positive cells (% of live)**	**AF488 hyper-positive cells (% of total)**
-electroporation, -AF488			83.6	0	0.33	27.6
-electroporation, +AF488			81.3	(1.44)	0	0
+ electroporation, -AF488			84.8	0	0	0
1300	30	1				
1400	20	1	82.9	97.86	19.7	16.3
1500	20	1	81.7	98.26	44.2	36.1
1600	20	1	81.5	98.26	68.7	56.0
1700	20	1	77.8	98.26	92.6	72.0
1100	30	1	84.2	91.76	6.58	5.5
1200	30	1	84.9	91.36	7.67	6.5
1300	30	1	83.6	98.16	52.2	43.6
1400	30	1	83.4	97.86	19.7	16.4
1000	40	1	84.9	86.66	6.87	5.8
1100	40	1	84.3	97.66	21.1	17.8
1200	40	1	82.7	98.26	57.1	47.2
1100	20	2	84.5	90.96	6.55	5.5
1200	20	2	84.3	97.96	24.6	20.7
1300	20	2	82.1	98.16	58.2	47.8
1400	20	2	75.8	98.06	85.1	64.5
850	30	2	85.4	35.26	1.38	1.2
950	30	2	84.5	82.26	5.17	4.4
1050	30	2	84.5	97.96	27	22.8
1150	30	2	82.7	98.26	71.4	59.0
1300	10	3	84.3	94.76	5.93	5.00
1400	10	3	82.6	97.86	18.9	15.6
1500	10	3	83.6	98.26	35.9	30.0
1600	10	3	80.4	98.26	62.6	50.3

A

No electroporation, no AlexaFluor488

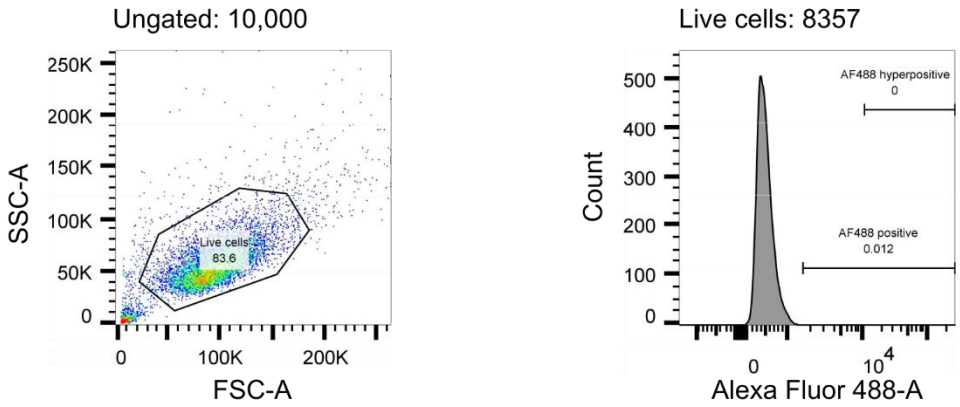

B

No electroporation, +AlexaFluor488

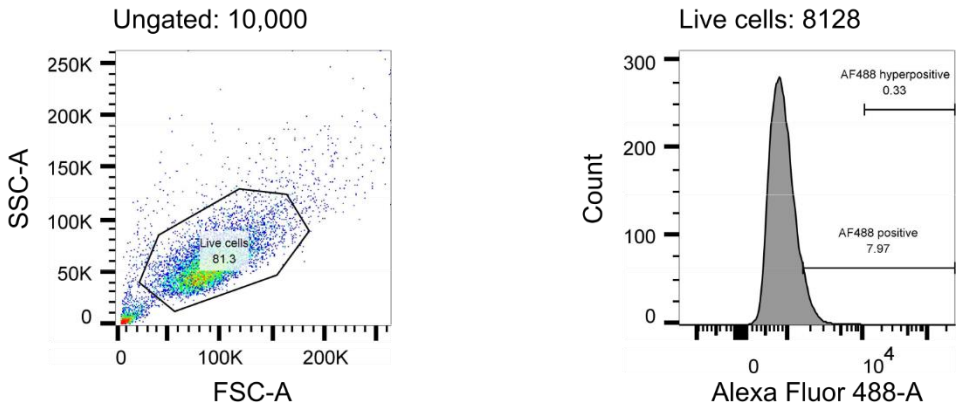

C

+ Electroporation, no AlexaFluor488

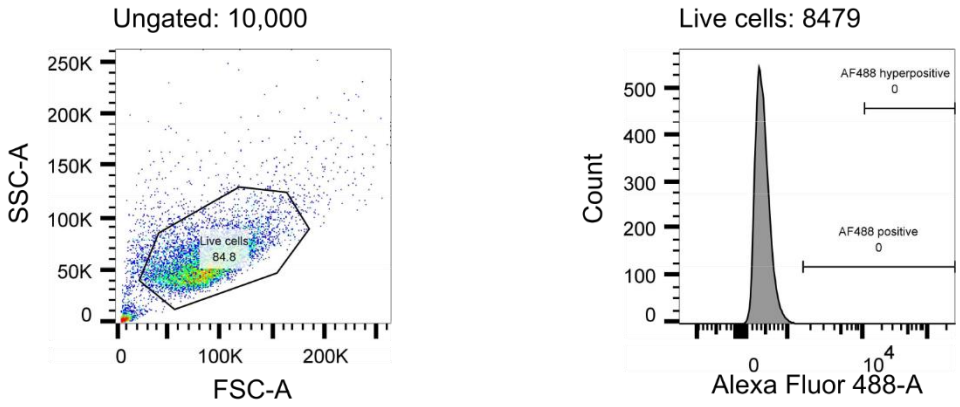

D

+ Electroporation (1x 1700V 20ms), +AlexaFluor488

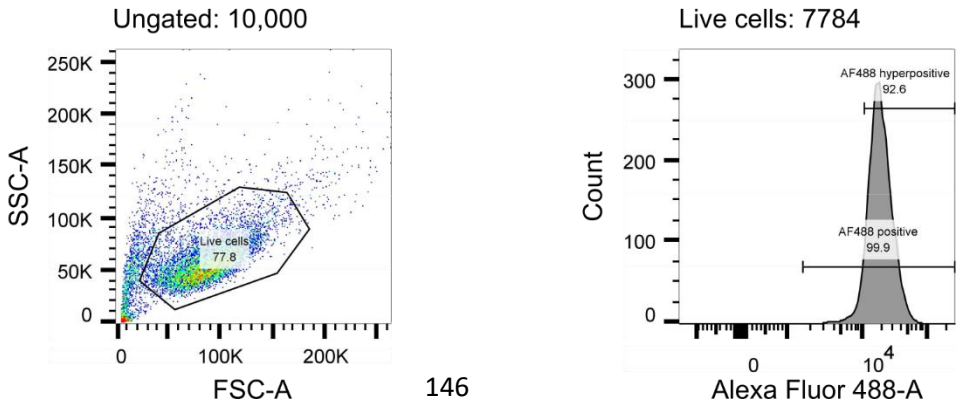

Figure 5.1 - Optimisation of electroporation of RNP complexes into SU-DIPG-IV cells

24 combinations of pulse voltage, duration and frequency were tested for their ability to transfect sgRNA/AF488 RNP complexes into SU-DIPG-IV cells. ***Left:*** *Live cells were identified using side scatter (SSC-A) and forward scatter (FSC-A).* ***Right:*** *AlexaFluor448 fluorescent intensity was gated into positive and hyperpositive cells. Results for the* ***(A)*** *no electroporation/no AF488,* ***(B)*** *no electroporation/+AF488,* ***(C)*** *+electroporation/-AF488 controls and* ***(D)*** *the most effective electroporation settings are illustrated.*

5.2.2. Design of sgRNAs set

Despite countless algorithms designed to predict successful sgRNA target sequences, no individual sgRNA can be guaranteed to successfully mediate genomic cutting (Doench *et al.*, 2014). Therefore, it is recommended to test multiple sgRNA sequences for their genome cutting efficiency (Hanna and Doench, 2020). To mitigate the idiosyncrasies of any one design algorithm, two different sgRNA design tools were used to predict target sequences. The CRISPOR (Concordet and Haeussler, 2018) and Broad Institute GPP/CRISPick (Doench et al., 2014; Sanson et al., 2018) were provided with the genomic sequence 100 nt on either side of the c.983G>T mutation. Each tool predicted 15 sgRNA target sequences and the top 5 from each were mapped onto the genome and compared (**Figure 5.2**). Only those which cut <30nt from c.983G>T were considered, as outside of this range the efficiency for the introduction of edits by HDR is dramatically reduced (Yang et al., 2013). Thus, 6 sgRNA target sequences within the 30 nt range were identified, only 1 of which was predicted by both design tools (**Table 5.2**).

Alongside these sgRNAs targeting the G328V locus, a negative control must be included to differentiate between changes due to the specific targeting of G328V and the experimental procedure itself. For CRISPR experiments, the negative or 'non-targeting' control is generally an sgRNA with a sequence not found in the target genome (Doench *et al.*, 2016). Here, a previously validated sgRNA that targets the enhanced green fluorescent protein (EGFP) gene was used (**Table 5.2**) (Shalem *et al.*, 2014), as this gene is not present in the human genome. Henceforth, this is referred to as the 'EGFP' control.

Table 5.2 - sgRNA sequences

Name	Algorithm	Orientation	Target sequence (without PAM)	Selected?
CL1/BL3	CRISPOR/ CRISPick	antisense	CTATGGACAGCACTATTCGA	N (outside of range)
CL2	CRISPOR	antisense	CTTTAAATCTCGATGGGCAA	Y
CL3/BL2	CRISPOR	antisense	ATGTGCAAGACCACTAGCTA	Y
CL4	CRISPOR	sense	ATAGTGCTGTCCATAGCTAG	N (outside of range)
CL5	CRISPOR	antisense	AAATCTCGATGGGCAATGGC	Y
BL1	CRISPick	antisense	GGCAATGGCTGGTTTCACTT	Y
BL4	CRISPick	antisense	GGGCAATGGCTGGTTTCACT	Y
BL5	CRISPick	antisense	TTTGCTCTTTAAATCTCGAT	Y
EGFP	(Shalem *et al.*, 2014)	n/a	GAAGTTCGAGGGCGACACCC	Y

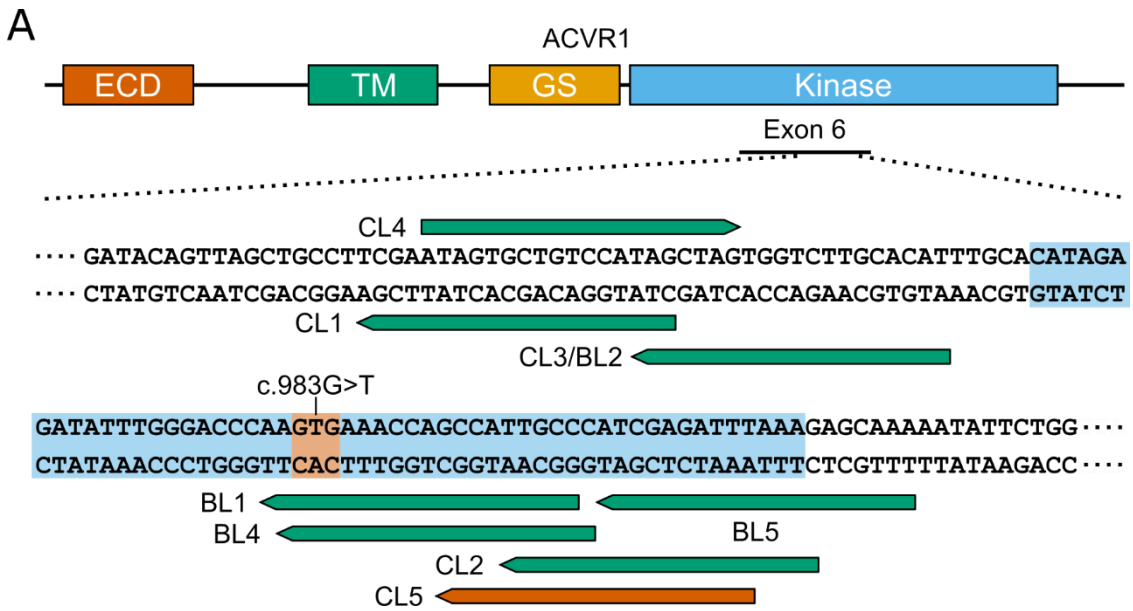

Figure 5.2 - map of sgRNAs relative to the G328V mutation

A map of ACVR1 showing the region of the kinase domain surrounding the G328V (c.983G>T) mutation annotated with the locations of the sgRNA sequences generated by the CRISPOR and CRISPick algorithms. ECD = extracellular domain, TM = transmembrane domain, GS = GS loop. The 30bp region on either side of c.983G>T (in which the Cas9 cut should be made) is highlighted in blue.

5.2.3. Selection of sgRNA by indel generation

Once designed, the set of sgRNAs must be tested for their ability to mediate Cas9 genomic cutting. If an sgRNA does mediate genomic DSBs by Cas9, the most frequent outcome is the introduction indel mutations due to NHEJ (Ran *et al.*, 2013; Okamoto *et al.*, 2019). To test

for the introduction of indels by these sgRNAs, RNP complexes were made with each sgRNA and transfected into the cells using the optimised electroporation settings. Mixed populations were allowed to grow until confluent and then DNA harvested for Sanger sequencing. Only RNPs made with the sgRNA CL5 introduced indels (**Figure 5.3**). Tracking of Indels by Decomposition (TIDE) analysis of the sequencing trace estimated that 47.7% of the reads included indels mutations (**Figure 5.4b**), and that 62% of the indels were insertion of a single adenine (**Figure 5.4c**). Thus, sequencing of mixed populations to quantify indels has allowed the selection of an efficient sgRNA, CL5, for future CRISPR experiments.

SU-DIPG-IV (no electroporation)

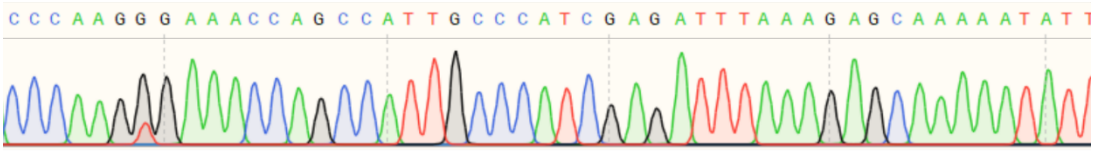

EGFP control sgRNA

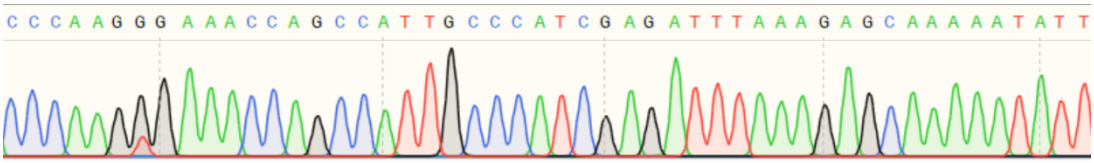

BL1

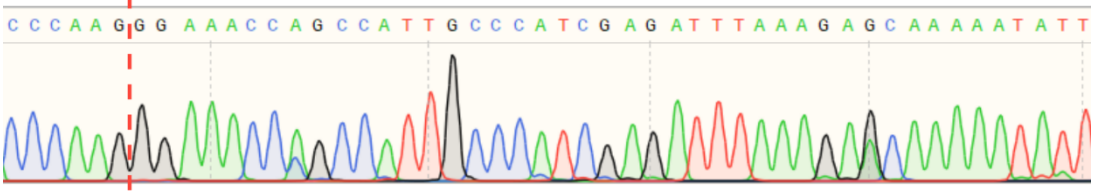

BL4

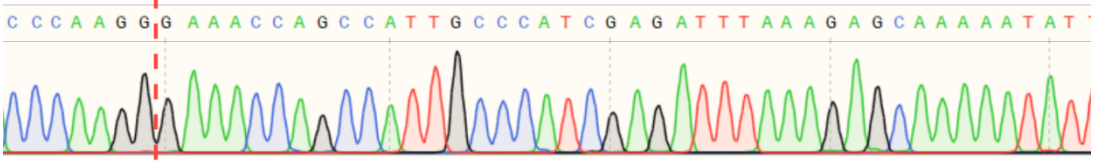

BL5

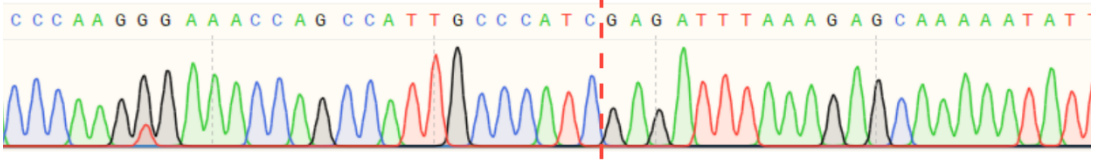

CL2

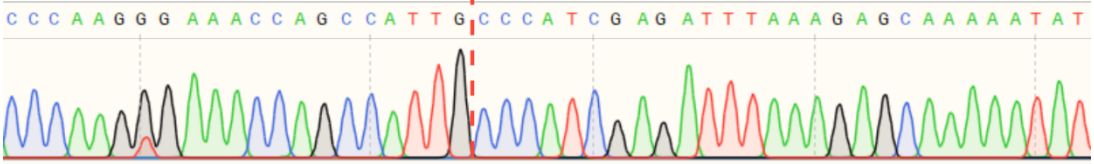

CL3

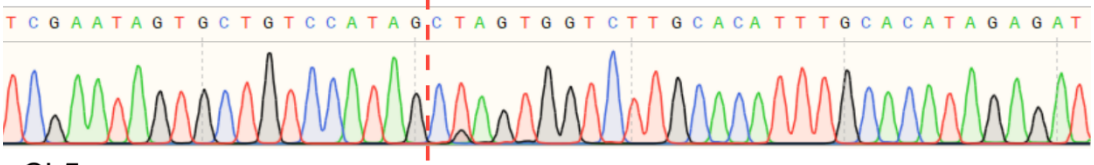

CL5

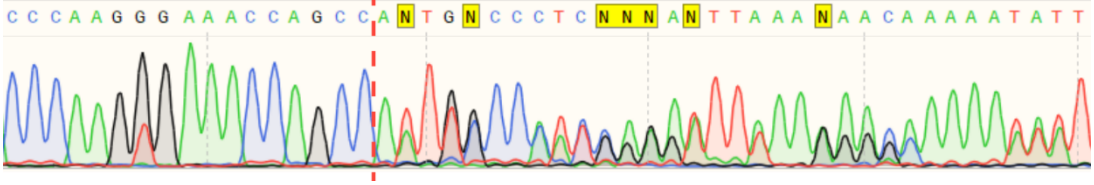

Figure 5.3 - sgRNA CL5 introduces indel mutations to the SU-DIPG-IV genome

500,000 SU-DIPG-IV cells were transfected with RNP complexes consisting of Cas9 and the indicated sgRNA by electroporation. Cells were seeded as mixed population and allowed to grow to confluence, when DNA was harvested and Sanger sequenced. Predicted cut site marked with a dashed red line. Only transfection with CL5:Cas9 RNPs introduced indels.

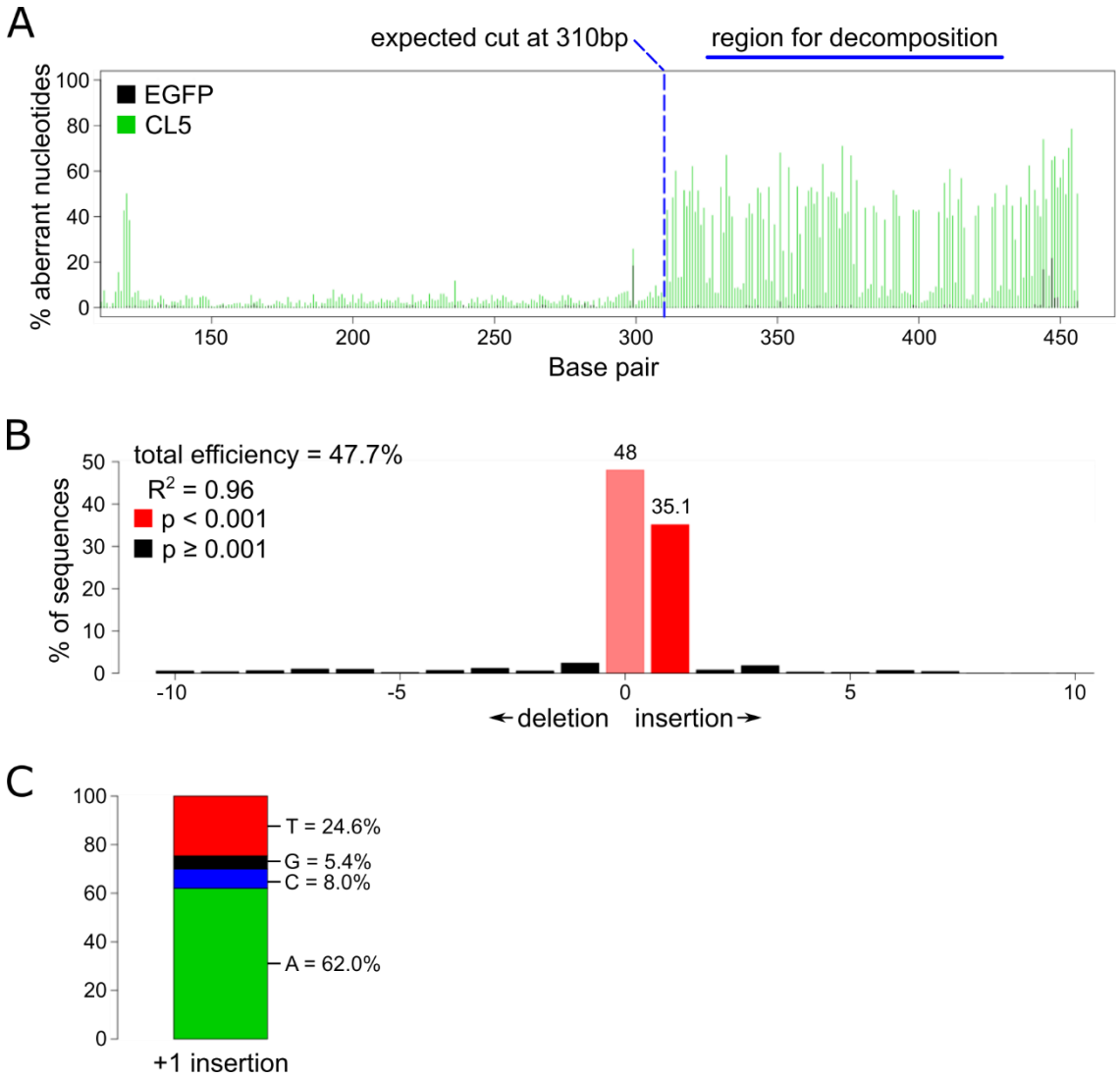

Figure 5.4 - TIDE analysis of CL5 treated mixed population ACVR1 sequence

The frequency of indels in the CL5 sample were quantified by comparison to the EGFP control treated cells by the TIDE algorithm. ***A,*** *A graph of the percentage of aberrant nucleotides recorded at each position. The low percentage of aberrant nucleotides across the EGFP control sequence indicates good sequence quality. The increase in aberrant nucleotides past the break site in the CL5 trace is indicative of the indels present.* ***B,*** *A graph of the spectrum of indels which best explains the sequence trace provided to the TIDE algorithm. R^2 value indicates the goodness of fit of this model. The colour of each bar indicates the statistical significance of the detection of each indel.* ***C,*** *An estimate of the base composition of the +1 insertion. All plots were generated using the online TIDE analysis tool (http://shinyapps.datacurators.nl/tide/ accessed 2021.09.13).*

5.2.4. Design of HDR repair template set

Once an sgRNA had been selected, the HDR repair template could be designed around the expected cut site. When a section of DNA containing the desired genome edit is transfected alongside the CRISPR system, the repair of the DSB introduced by Cas9 by HDR using this as the repair template will thus integrate the designed DNA sequence into the genome (Ran *et al.*, 2013). In this experimental system, the desired repair template – the wild-type allele – was conveniently already present in the cell because the mutation is heterozygous. Nevertheless, an exogenous repair template was included with the hope of biasing the system towards repairing DSBs with the wild-type rather than the G328V sequence.

This HDR repair template was designed by supplying the sequence of CL5 to the Horizon Discovery Edit-R HDR Donor Designer (*https://Horizondiscovery.Com/En/Ordering-and-Calculation-Tools/Edit-r-Hdr-Donor-Designer-Oligo*, accessed 2020.08.09). The repair template was designed to be complementary to the target sequence, with homology arms of 30 nt each according to a previously optimised repair template design strategy (Okamoto *et al.*, 2019). As it was based on the wild-type genome, the suggested repair template already included the desired c.983G edit. It is recommended to include a silent mutation that destroys the protospacer adjacent motif (PAM) sequence, as this prevents repeated cutting and editing of the same site (Okamoto *et al.*, 2019). However, in this location the final base of the codon 331 corresponded the 'N' of the PAM making silent mutations impossible. Instead, a silent c.993C>T mutation at the neighbouring 5' base was introduced, to reduce the complementarity of the sgRNA to the site, and as genomic marker for HDR using this template. The final repair template is illustrated below (**Figure 5.5**).

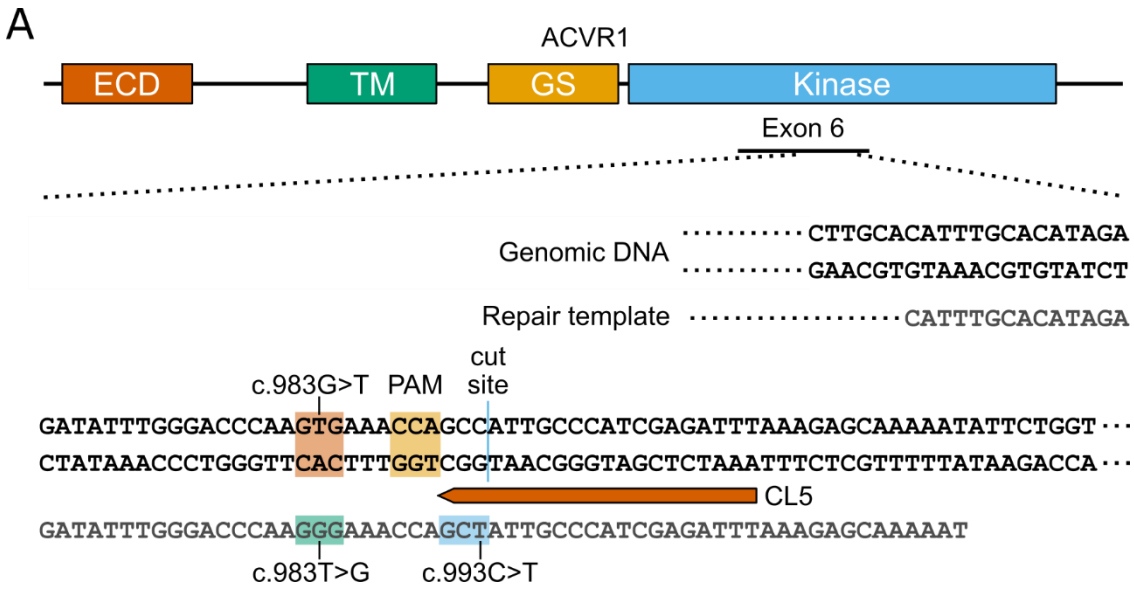

Figure 5.5 - design of HDR template

A map of ACVR1 showing the region of the kinase domain surrounding the G328V (c.983G>T) mutation annotated with the location of the selected sgRNA CL5, the associated PAM site and the single stranded repair template, itself annotated with the corrective c.983T>G mutation, and the silent c.993C>T mutation that it will introduce. ECD = extracellular domain, TM = transmembrane domain, GS = GS loop.

5.2.5. Results of final screen

With all components of the CRISPR/Cas9 experiment optimised the genomic editing was started (overview in ***Figure 5.6***). SU-DIPG-IV (*ACVR1* c.993C>T) cells were transfected with either CL5:Cas9 or EGFP:Cas9 RNP complexes using the optimised electroporation procedure. As the HDR rate in DIPG cells was unknown, cells were seeded into two separate populations post transfection, and one was treated with a small molecule HDR enhancer (IDT, USA). As the HDR enhancer can reduce cell viability, initially only cells from the untreated population were seeded for single cell cloning. Cells from both mixed populations were collected for Sanger sequencing revealing that, although both populations contained the expected indels, only the population treated with the HDR enhancer had 1.11% reads corresponding to thymine at base c.993, indicating the introduction of the silent mutation included in the ssDNA repair template (***Figure 5.6***b). As only the population treated with HDR enhancer had evidence of HDR instead of NHEJ

mediated repair, cells from this mixed population were seeded out as single cell clones, and only clones from this population were collected.

A total of 62 clones from this single cell cloning effort were successfully expanded from a 96 well to 6 well culture and sequenced. Of 62 clones sequenced, 49 (79%) had any edit and 2 clones (3%) had the desired reversion of c.983T>G, with no unwanted indel mutations (**Figure 5.6c**). Sequence traces from these two clones are shown in **Figure 5.7**. Corrected clone 1G6 does not have the silent c.993G>T mutation included in the HDR repair template indicating that HDR was performed using the already present wild-type allele as a repair template. Corrected clone 2H3 had both the target c.983T>G and silent c.993G>T mutations, indicating repair by HDR from the provided ssDNA template. Thus, using the latest methods for efficient CRISPR delivery, 2 successfully edited clones were generated from less than 100 unselected single cell clones.

During the initial collection of the two edited *ACVR1* wild-type clones, differences between the two could already be observed. Clone 1G6 had a morphology similar to the parental cell line, whereas 2H3 was more inclined to spheroid-like growth (**Figure 5.7**b). This novel spheroid character in 2H3 was observed in many single cell clones and could happen spontaneously when SU-DIPG-IV was expanded as single cell clones. Clone 1G6 was picked from the 96 well plate 22 days after seeding, and clone 2H3 29 days after seeding, suggesting a greater growth defect in 2H3 than in 1G6. Unfortunately, the growth defect of 2H3 was so great that it could not be expanded or maintained in culture sufficiently for further validation or characterisation. Thus, 1G6 was the focus of characterisation for the rest of this chapter.

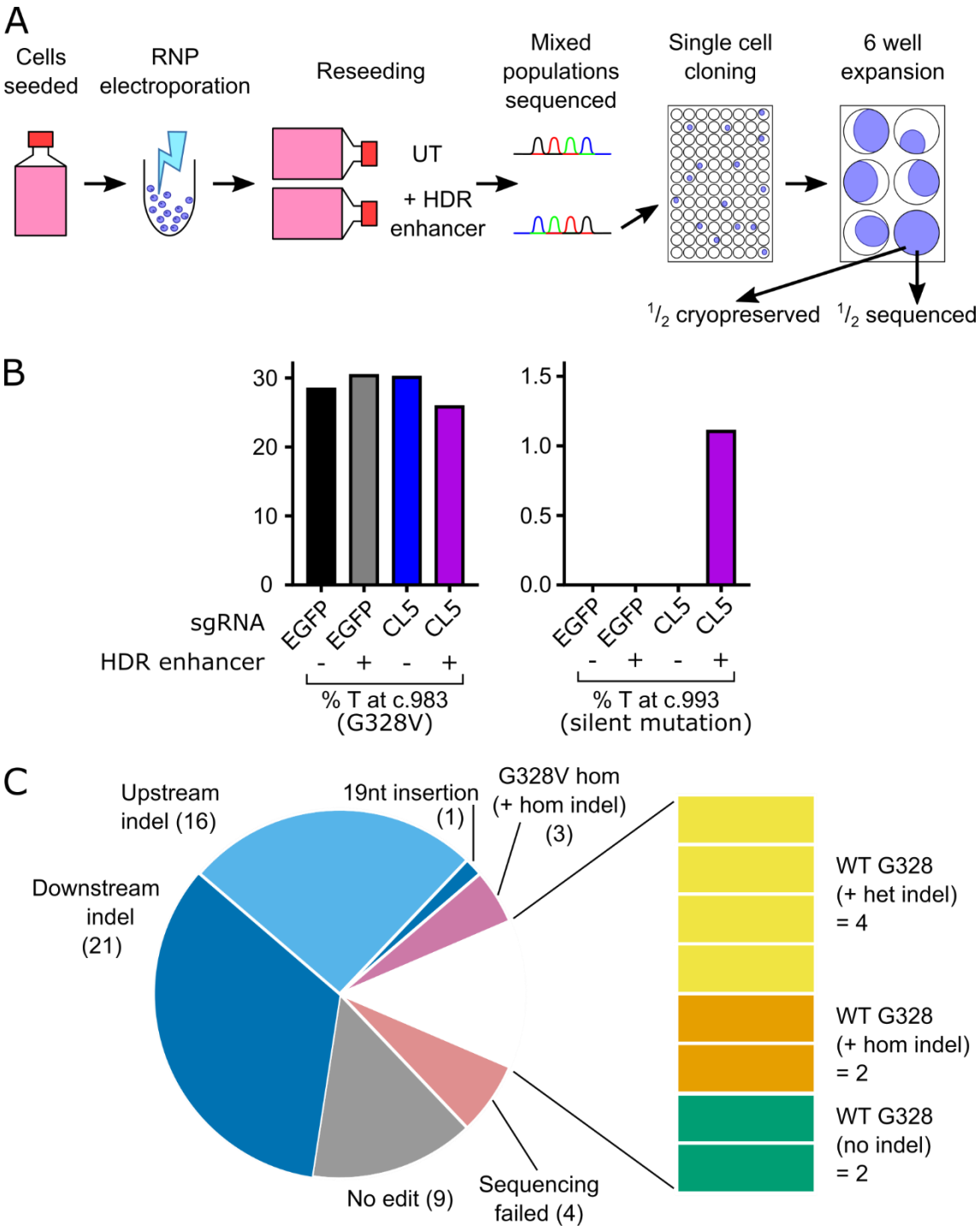
A
Cells seeded
RNP electroporation
Reseeding
UT
+ HDR enhancer
Mixed populations sequenced
Single cell cloning
6 well expansion
1/2 cryopreserved
1/2 sequenced
B
30
20
10
0
1.5
1.0
0.5
0.0
sgRNA
EGFP EGFP CL5 CL5
HDR enhancer
- + - +
% T at c.983 (G328V)
% T at c.993 (silent mutation)
C
Upstream indel (16)
19nt insertion (1)
G328V hom (+ hom indel) (3)
Downstream indel (21)
No edit (9)
Sequencing failed (4)
WT G328 (+ het indel) = 4
WT G328 (+ hom indel) = 2
WT G328 (no indel) = 2

Figure 5.6 - Summary of single cell cloning following CRISPR/Cas9

A) *Overview of the final procedure for CRISPR/Cas9 editing of SU-DIPG-IV cells. Briefly, cells were electroporated and reseeded as mixed populations +/- a small molecule HDR enhancer. These mixed populations were sequenced, and the HDR enhancer treated population was selected for single cell cloning in 96 well plates. Clones were expanded to 6 well from which cells were harvested for sequencing of ACVR1 exon 6 and cryopreservation.* ***B)*** *Results of sequencing of CRISPR/Cas9 mixed populations. No notable change in the proportion of thymine bases at c.983 was observed, but only the population treated with the CL5 sgRNA and HDR enhancer had 1.1% thymine reads at c.993, indicating the introduction of the silent mutation within the supplied HDR repair template.* ***C)*** *Results of sequencing single cell clones from the CL5 + HDR enhancer population. A total of 62 clones were sequenced, of which 49 clones (79%) were edited in some way, and 2 clones (3%) had the desired correction of G328V to the wild-type glycine.*

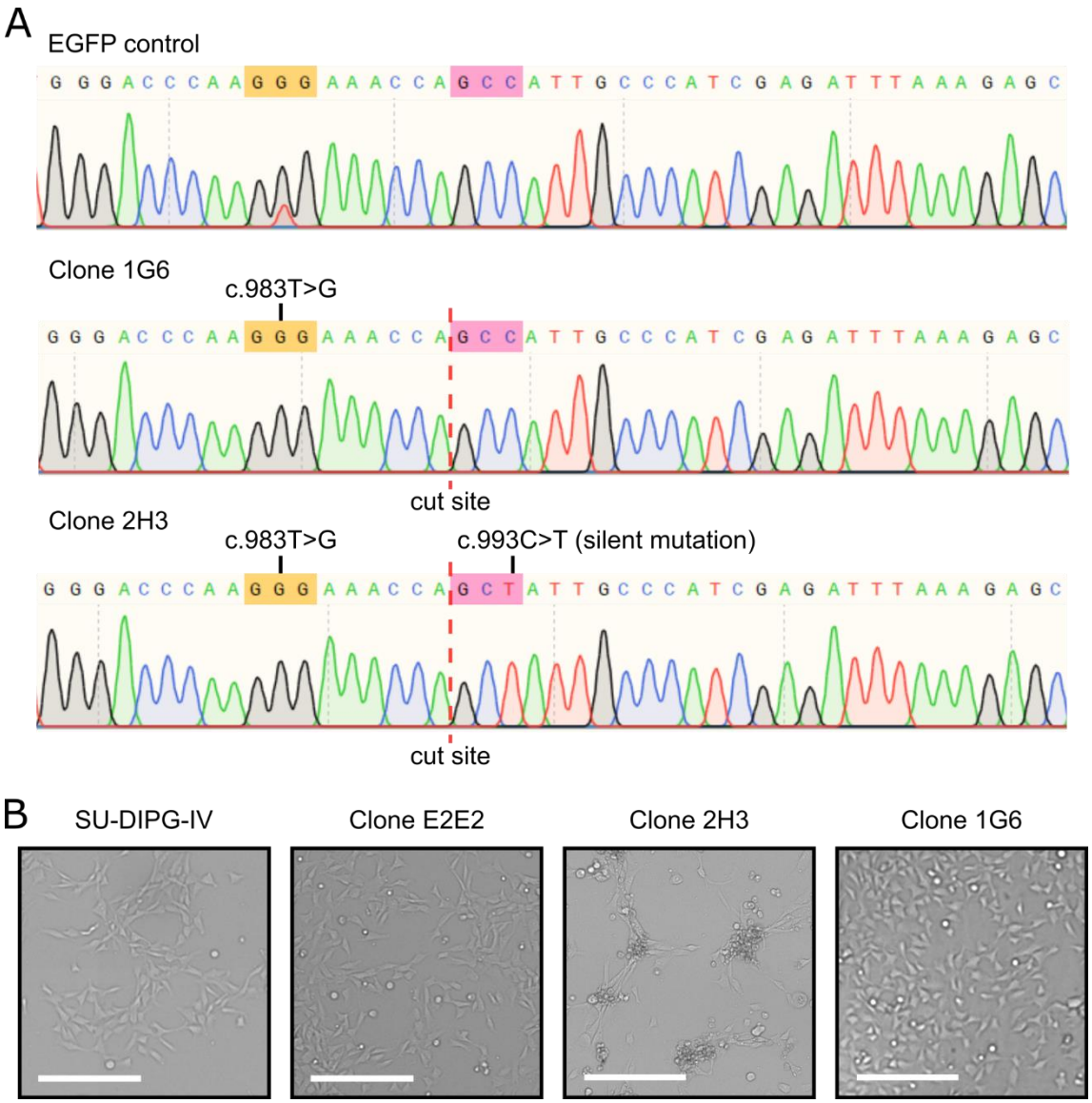

Figure 5.7 – Sequences traces and morphology of successfully edited clones

(A) *The sequencing traces of an EGFP clone (E2E2) (top), the edited clones 1G6 (middle) and 2H3 (bottom). The original heterozygous c.983G>T mutation can be seen in the EGFP clone only. The successful c.983T>G reversion can be seen in clones 1G6 and 2H3. The silent c.993C>T mutation included in the HDR repair template can be seen in clone 2H3. Codon 328 is highlighted in orange. Codon 331 is highlighted in pink.* ***(B)*** *Brightfield images of parental SU-DIPG-IV, EGFP control clone E2E2 and edited clones 2H3 and 1G6 highlighting their morphologies. Scale bars are 250 µm.*

5.2.6. Selection of EGFP control clone

Alongside collection of the successfully edited clones, EGFP targeting negative control sgRNA treated clones were collected from single cell cloning. The process of single cell cloning is the step most likely to lead to collection of cell lines with phenotypes differing from the parental

cell line. Simply using the first EGFP clone to grow to confluence would bias this control towards being fast growing, therefore multiple EGFP clones were collected over time and their growth rates compared to the parental cell line by tracking confluence over time. The clone E2E2 had a growth rate closest to that of the parental SU-DIPG-IV cell line (**Figure 5.8**), and thus was chosen to be the EGFP control cell line in future experiments.

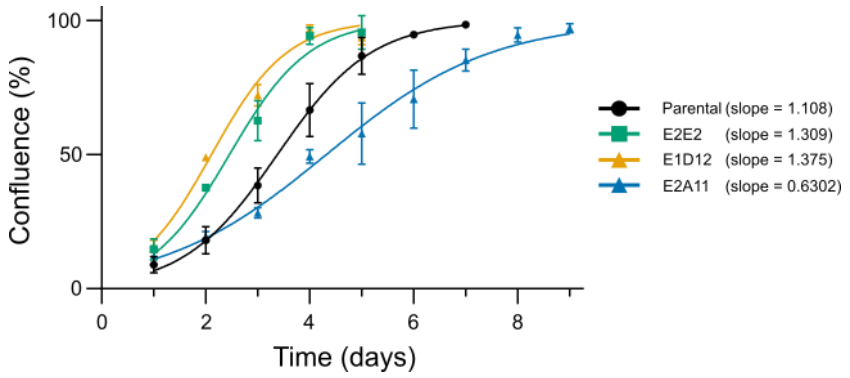

Figure 5.8 - Comparison of growth rates of EGFP control clones

SU-DIPG-IV cells and various EGFP clones were seeded in 24-well plates and their confluence tracked over time using brightfield imaging. E2E2, the EGFP clone with the growth rate most similar to the parental line was selected as the EGFP control for further experiments. Points are the mean of 3 technical repeats, bars are SD. Slope was calculated by non-linear regression (assuming logistic growth, Y_{max} = 100).

5.2.7. Off-target sequencing of clones

One of the main concerns when performing CRISPR/Cas9 is other genomic loci with sequences similar to the target locus will also be cut by Cas9 (known as off-target activity) (Y *et al.*, 2013). Off-target activity is already reduced by RNP rather than plasmid delivery of CRISPR/Cas9, as active Cas9 is present in the cell at a lower concentration and shorter period (Liang *et al.*, 2015). Even with this reduced risk, off-target mutagenesis was assessed as follows: Alongside the predicted target sequences, the CRISPOR sgRNA design algorithm produced a list of potential off-target sequences (**Table 5.3**). The top 5 intron or exon sequences were selected for validation by Sanger sequencing, as these are the most likely to have a functional effect if edited. In 4/5 off-target regions sequenced there were no differences between the reference,

parental, EGFP control or 1G6 sequences (**Figure 5.9**). Relative to the reference sequence (ENSG00000107779) the parental *BMPR1A* sequence had an apparent heterozygous SNP (G>C, Gly>Arg) upstream of the predicted off-target site (**Figure 5.9**). The EGFP control and *ACVR1* wild-type 1G6 had sequences matching the reference (**Figure 5.9**). It is improbable that the parental SNP was corrected with an independent C>G edit in both the E2E2 and 1G6 clones, therefore it is likely an artefact due to a high background of cytosine reads in this sequencing reaction (**Figure 0.3**). In summary, no concerning off-target editing was found and 1G6 was considered suitable for further experimental studies.

Table 5.3 – The top 15 predicted off-target sites for sgRNA CL5

*Off-target sites selected for sequencing are highlighted in green. * Correspond to mismatches from the sgRNA target sequence.*

Locus description	Off Target Sequence	Mismatches from CL5 (*)
intergenic: RP11-545H22.1-AC006552.1	AAAGCACAATAGGCAATGGCAGG	...*.*.*..*.....
intergenic: Y_RNA-RNF150	AATTCAAGATGGACAATGGCAGG	..*..**.....*.....
intergenic: RN7SKP229-ZNF648	GAATCCTGATGGCCAATGGCAGG	*....**.....*.....
exon: BMPR1APS1	AGGTCTCGATGAGCAATTGCGGG	.**.....*.....*..
exon: BMPR1A	AGGTCTCGATGAGCAATTGCGGG	.**.....*.....*..
exon: BMPR1APS2	AGGTCTCGATGAGCAATTGCGGG	.**.....*.....*..
exon: ACVR1C	ATGTCTCGATGAGCAATAGCAGG	.**.....*.....*..
intergenic: MBL2-Y_RNA	CTTTCTCTATGGGCAATGGCAGG	***....*.....
intergenic: RP11-84H6.1-RNA5SP173	TCATCTCAATGGGAAATGGCAGG	**.....*.....*.....
intergenic: RP11-324C10.1-NLGN1	AATTCTCCCTAGGCAATGGCAGG	..*....**.*.....
intergenic: RP11-666E17.1-EIF3LP1	AAATCTCCAAGGACAATGCCAGG	.....*.*..*.....*.
intergenic: FOXB1-MESTP2	AAAACTAGAAGGGCAATGTCAGG	...*..*..*.....*.
intron: ZNF534	AAATTTAGCTGGGTAATGGCAGG	....*.*.*....*.....
intron: EPHA3	AAATCTCAATGCAAAATGGCAGG	.....*...***.....
exon: ACVR1B	AAGTCTCGATGAGCAATTCCAGG	..*.....*.....**.

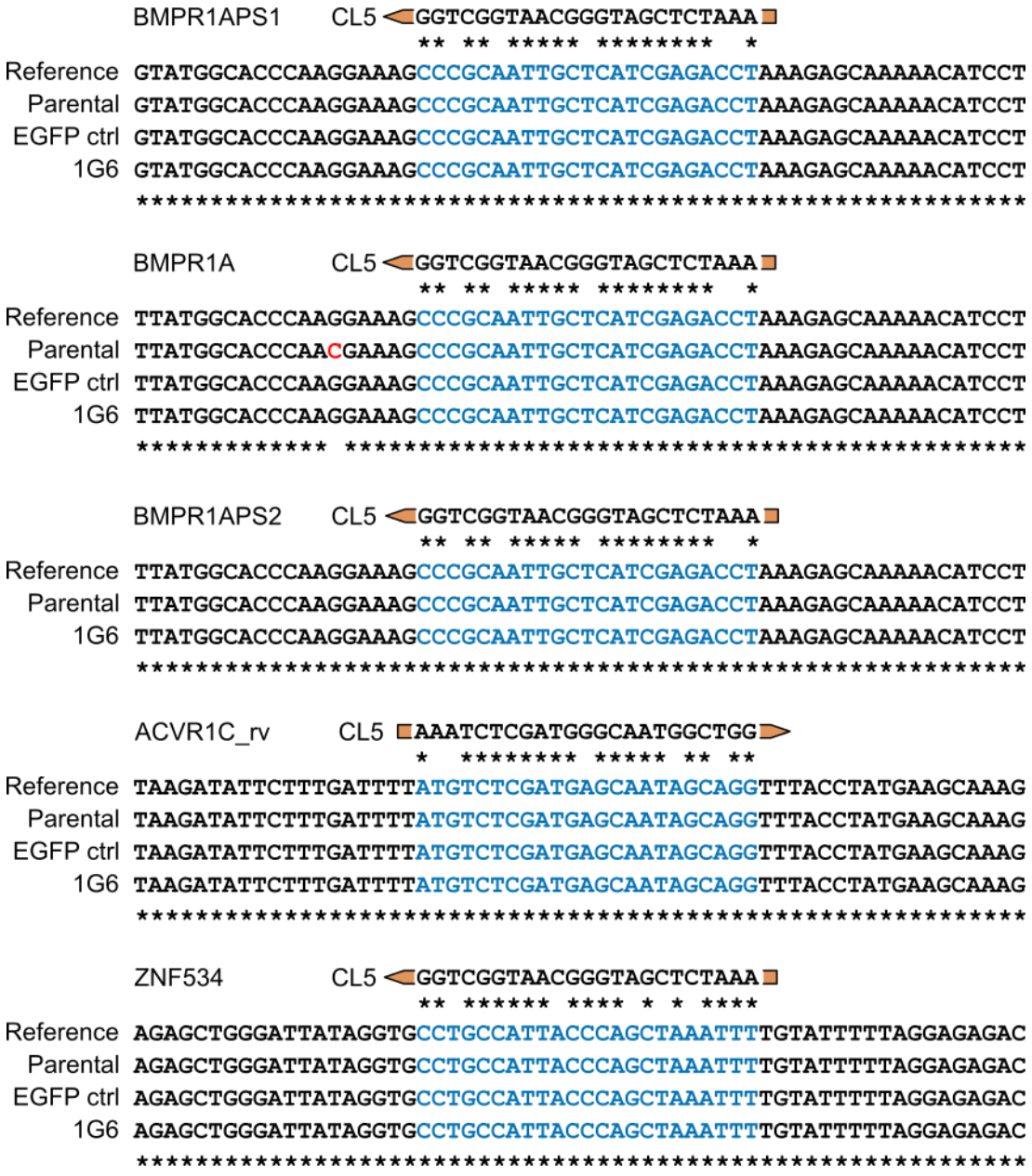

Figure 5.9 - Sequencing of predicted off-target sequences

Aligned sequence results for the predicted off-target sites in BMPR1APS1, BMPR1A, BMPR1APS2, ACVR1C and ZNF534 in the parental SU-DIPG-IV, control EGFP and edited 1G6 cell lines. The alignment is annotated underneath with an asterisk where it aligns perfectly or left blank where there is an SNP (also highlighted in red). The predicted off-target region is highlighted in blue, with bases matching or complementary to the sgRNA CL5 annotated with an asterisk.

5.2.8. Functional validation of clones by ligand stimulation

Following genomic validation of the clone 1G6, functional validation was warranted to confirm the expected concomitant loss of activin A neofunction (i.e., ACVR1-mediated phosphorylation of SMAD1/5/8 following cell stimulation by Activin A). This was tested by treating the parental, EGFP control line and 1G6 with a vehicle control, 50 ng/mL BMP-7 or 50 ng/mL Activin A and testing phosphorylation of SMAD1/5/8 by immunoblot (**Figure 5.10**). This confirmed the expected normal signalling induced by BMP-7 and abnormal signalling induced by Activin A in the parental and EGFP cell lines, but that the signalling in response to Activin A was absent in the edited 1G6 line (**Figure 5.10**). In future, comparison of signalling in clone 1G6 to that of another *ACVR1* wild-type cell line would be desirable. Thus, as expected the edited *ACVR1* WT 1G6 clone no longer exhibited the gain of functioning signalling that is characteristic of *ACVR1* mutant cells.

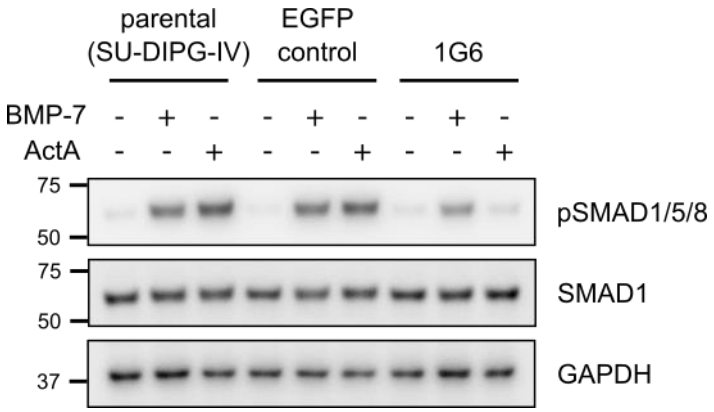

Figure 5.10 - Validation of loss of Activin A signalling via ACVR1/SMAD1/5/8 in the CRISPR edited 1G6 cell line

Parental SU-DIPG-IV, control EGFP and edited 1G6 cell line were stimulated with 50 ng/mL of BMP-7 or activin A (ActA) for 1 h before protein was harvested and the levels of phosphor-SMAD1/5/8 (indicating activation of signalling via ACVR1) was imaged by immunoblotting. As expected Activin A induced phosphorylation of SMAD1/5/8 in the G328V ACVR1 parental and EGFP control cell lines, but the aberrant signalling was lost in 1G6 where the G328V mutations has been corrected to the WILD-TYPE sequence. The blot pictured is representative of three independent repeats.

5.2.9. *ACVR1* wild-type 1G6 cells grow more slowly than G328V SU-DIPG-IV cells

To assess the contribution of the *ACVR1 G328V* mutation to the proliferation of SU-DIPG-IV cells, the growth rates of each cell line were compared. Each cell line was seeded into 96-well plates and the confluence tracked over time (**Figure 5.11**). A logistic growth curve was fit to the mean values from 3 independent repeats. The rate constant or slope (k) calculated for clone 1G6 (k = 0.75) was less than that calculated for SU-DIPG-IV (k = 1.24) or clone E2E2 (k = 1.11) and are statistically different (sum-of-squares F test, $p < 0.0001$). Thus, removal of G328V from *ACVR1* introduced a growth defect to the DIPG cells.

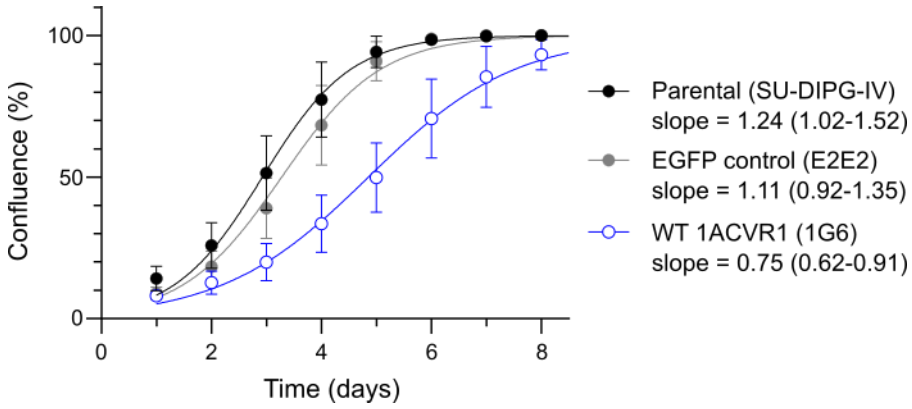

Figure 5.11 - ACVR1 wild-type DIPG cells proliferate more slowly than ACVR1 G328V DIPG cells

Parental (SU-DIPG-IV), EGFP control (E2E2) and edited ACVR1 wild-type (1G6) cells were seeded and their confluence measured over time using brightfield microscopy. Points are the mean of 3 independent repeats, bars are SEM. Slope (quoted with 95% CIs) was calculated my non-linear regression (assuming logistic growth, $Y_{max} = 100$, Y_0 equal for all cell lines).

5.2.10. Correction of *ACVR1 G328V* removes a PRMT5 inhibition resistant population

An important translational question is whether *ACVR1* mutation status alters the sensitivity of DIPG cells to inhibition of specific proteins. Here, PRMT5 and ACVR1 inhibition were tested because of the observed PRMT5 inhibitor sensitivity in Chapter 3 (section 3.2.7) and because of similar published data on ACVR1 inhibitors in DIPG cells (Carvalho *et al.*, 2019).

The parental, EGFP control and edited *ACVR1* wild-type cell lines were treated for 7 days with a range of concentrations of both the GSK591 and LLY-283 PRMT5 inhibitors, before

viability was measured with the CTG viability assay. The values calculated were of the same order as those calculated in Chapter 3 (**Table 3.2**), for example here SU-DIPG-IV cells treated with LLY-283 showed GI_{50} = 71 nM, compared to 46 nM calculated previously. Correction of the G328V mutation to wild-type did not significantly change the GI_{50} of either compound (**Figure 5.12a, b**). However, at high concentrations of LLY-283 or GSK591 viability was reduced to a lower level in *ACVR1* wild-type 1G6 cells (**Figure 5.12a, b**). This resulted in a significantly lower Y_{min} value after LLY-283 treatment and a significantly lower GI_{80} value for GSK591 treatment of 1G6 cells (**Table 5.4**). Therefore, correction of *ACVR1* G328V to the wild-type sequences appears to remove a PRMT5 inhibition resistant subpopulation.

Table 5.4 - Y_{min} and GI_{80} of paired CRISPR cell lines after PRMT5 inhibition

Cell line	**Y_{min} (95% CI)**	**GI_{80} (95% CI)**
Parental (SU-DIPG-IV)	171 nM (146 - 196 nM)	5.5 µM (2.6 µM - >20 µM)
EGFP control (E2E2)	185 nM (163 - 207 nM)	9.2 µM (4.5 µM - >20 µM)
ACVR1 wild-type (1G6)	63 nM (46 - 81 nM)	1.2 µM (0.86 - 1.6 µM)

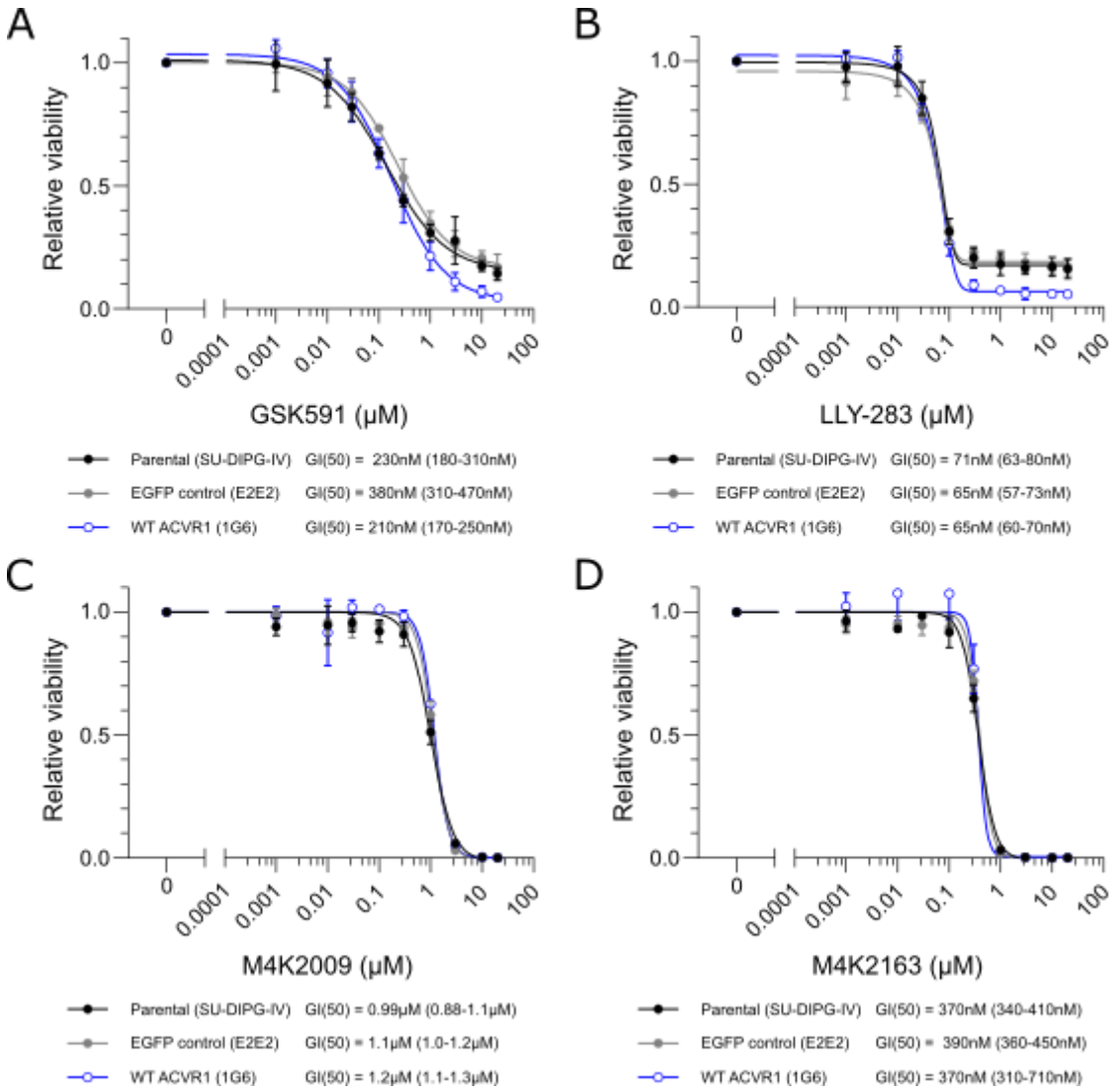

Figure 5.12 - ACVR1 mutation status of DIPG cells does not affect sensitivity to PRMT5 or ACVR1 inhibition

Parental (SU-DIPG-IV), EGFP control or edited wild-type DIPG cells were treated with the indicated concentration of the PRMT5 inhibitors GSK591 ***(A)****, LLY-283* ***(B)*** *or the ACVR1 inhibitors M4K2009* ***(C)*** *or M4K2163* ***(D)*** *for 7 days, then their viability measured with the CTG assay. Points are the mean of 3 independent repeats, bars are SD. GI_{50} values (with 95% CI in brackets) were generated as described in section 2.4.3 with no Y_{max} constraint.*

5.2.11. *ACVR1* wild-type 1G6 cells are less clonogenic than *ACVR1* G328V SU-DIPG-IV cells

Treatment resistant cancer cells are often stem-like (Zhou *et al.*, 2021) and *ACVR1* mutations are known to impair differentiation of DIPG cells (Fortin *et al.*, 2020). Therefore, it was hypothesised that the loss of a PRMT5 inhibition resistant subpopulation represented a loss

in stem-like cells. The clone forming potential of parental *ACVR1* G328V cells was compared to that of *ACVR1 wild-type* 1G6 cells. Parental, EGFP control and edited *ACVR1* wild-type cells were seeded in a titration of densities, and the frequency at which clones had formed was measured after 7 days. The estimated percentage of clonogenic cells was not significantly different in the parental and EGFP control cell lines (60% and 49%, respectively), but the percentage of clonogenic cells was reduced to 23% in the *ACVR1* wild-type 1G6 line ($p < 0.05$, 95% CI of each Poisson distribution).

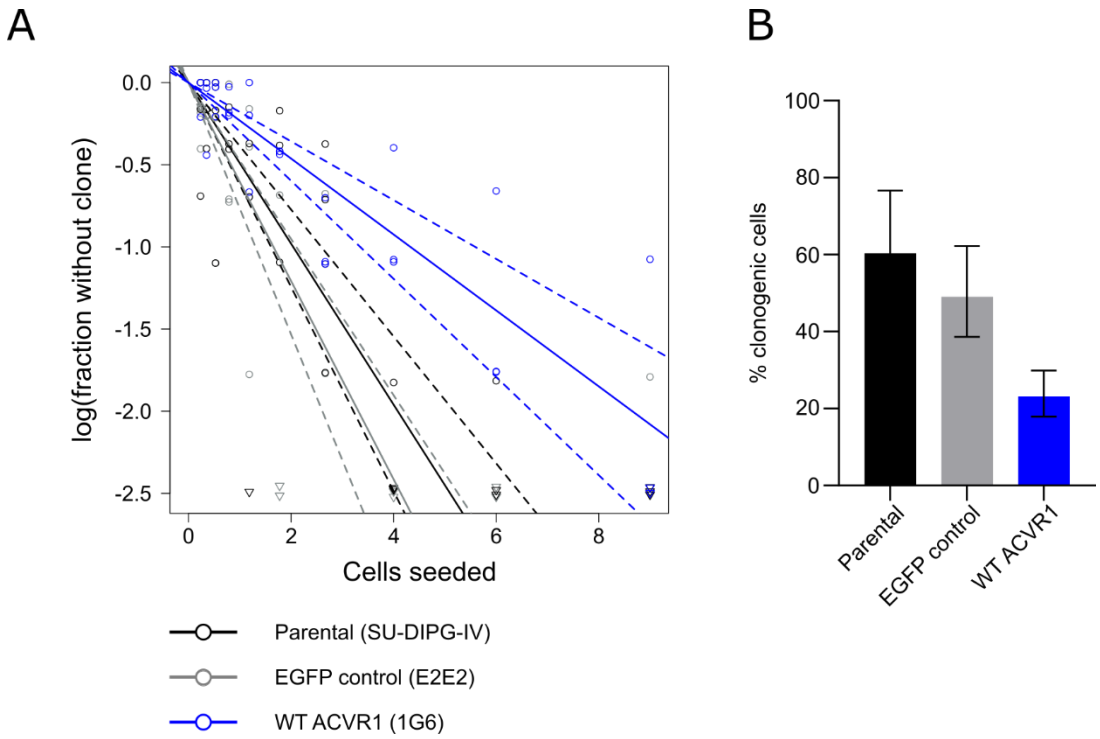

Figure 5.13 - The ACVR1 wild-type DIPG line (1G6) has a lower proportion of clonogenic cells than ACVR1 G328V SU-DIPG-IV cells

Left, *The Poisson distributions calculated for each cell line. Points are the log(fraction without a clone) for each independent repeat, dashed lines are 95% CI for the estimated Poisson distribution.* ***Right,*** *The percentage of clonogenic cells estimated by each Poisson distribution (bars are 95% CIs).*

5.2.12. Correction of the G328V mutation promotes secretion of proteins associated with Stat3 signalling and astrocyte activation

As the clonogenic potential fell after correction of the *ACVR1* G328V mutation the secretion of a range of proteins was measured to characterise markers of the differentiation or signalling state of the cells. Growth medium that had been conditioned by each cell line for 72 h was collected and the relative abundance of secreted proteins measured with a Proteome Profiler Human XL Cytokine Array Kit. The correction of *ACVR1* G328V triggered a 2-fold or greater increase in the signal of 6 proteins (MCP-1, GDF-15, IL-6, VEGF, IGFBP-3, IL-8) relative to the parental and EGFP control, with no comparable reductions in protein secretion (**Figure 5.14**). The greatest fold change was a 10.7-fold increase in the MCP-1 signal in *ACVR1* wild-type cells relative to the parental control (**Figure 5.14**). MCP-1 expression is associated with inflammation, astrocyte activation and differentiation, Stat3 and NF-κB signalling (Barna *et al.*, 1994; Vrotsos, Kolattukudy and Sugaya, 2009; Chen *et al.*, 2014; Yoshimura, 2017). Secretion of GDF-15, IL-6, VEGF, IGFBP-3 and IL-8 are all associated with astrocyte activation (Loeffler *et al.*, 2005; Shah *et al.*, 2012; Watanabe *et al.*, 2015; Chen *et al.*, 2016; Malik *et al.*, 2020). IL-6, IL-8 and VEGF either induce or are induced by Stat3 signalling (Loeffler *et al.*, 2005; Iglesia *et al.*, 2008; Chen *et al.*, 2014).

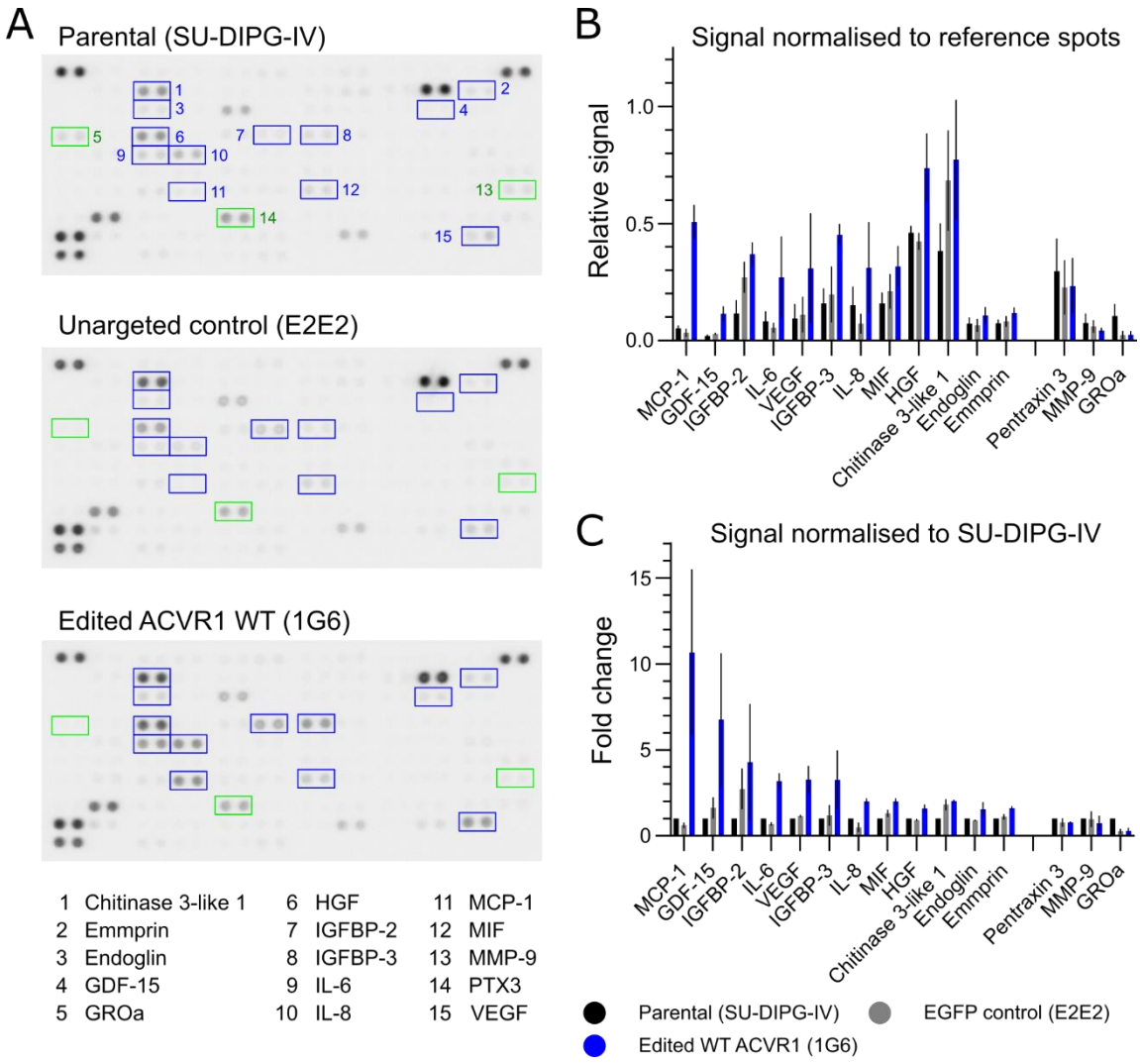

Figure 5.14 - Correction of G328V ACVR1 mutation triggered the secretion of additional proteins

(A) *Conditioned growth medium (72h) was collected from parental (SU-DIPG-IV), EGFP control (E2E2) and edited ACVR1 wild-type (1G6) cells and the protein composition tested with the Proteome Profiler Human XL Cytokine Array Kit. Differentially secreted proteins are highlighted with blue (increased in 1G6) or green (decreased in 1G6). Signal was quantified and normalised first to the reference spots on the upper and lower left corners of each array* ***(B)****, then to the signal in the SU-DIPG-IV line* ***(C)****. Bars are the mean of 3 independent repeats, bars are SD.*

5.3. Discussion

In this chapter, the CRISPR/Cas9 system was used to correct the disease causing G328V *ACVR1* mutation to the wild-type sequence in the patient derived SU-DIPG-IV cell line. By applying the latest methods, namely delivery of the sgRNA/Cas9 as RNP complexes, only 62 single celled clones had to be isolated and sequenced to generate 2 clones with the desired edit. Furthermore, sequencing of predicted sites of potential off-target editing confirmed that RNP delivery of CRISPR/Cas9 did not support off-target editing (Liang *et al.*, 2017). It was unfortunate that one of these clones could not be used experimentally – ideally experiments would be performed with multiple edited clones to account for the variation introduced by single cell cloning.

To assess the contribution of the G328V mutation to the ongoing growth of these DIPG cells, the growth rates of the parental, control and edited cell lines were compared, and impaired proliferation was observed in the edited clone 1G6. This growth defect was less dramatic than that observed in following shRNA knockdown of R206H *ACVR1* by Carvalho et al. in 2019, which could be due to one of the following:

1. The need to maintain a stable cell line selected against the most severe growth defects. For instance, the clone 2H3 could not be used for experiments, because it failed to grow.
2. The G328V mutation has a lesser effect on DIPG growth than R206H. This may reflect the worse prognosis for patients with R206H compared to G328V (Carvalho *et al.*, 2019).
3. The shRNA was not selective for R206H. By knocking down both the mutant and wild-type alleles simultaneously, the previous experiment over-estimated the role of ACVR1 in DIPG cell growth.

In Chapter 3, I observed that *ACVR1* wild-type DIPG cells lines were less sensitive to PRMT5 inhibition than *ACVR1* mutant cells. It would therefore be expected that the drug sensitivity of the SU-DIPG-IV cell line would be diminished upon correction of the *ACVR1* G328V mutant back to wild-type. However, the GI_{50} in response to the PRMT5 inhibitors LLY-283 and GSK591 was unchanged by this gene editing. Thus, it seems that a strict correlation between mutant *ACVR1* and sensitivity to PRMT5 inhibition is not supported, and that an as yet unknown genetic difference is likely to cause this variation. Notably, the most sensitive cell lines were also derived from autopsy material and the radiotherapy that these cells likely received could have expanded the spectrum of mutations they contain.

Of note, at the highest LLY-283 or GSK591 doses, the apparent viability of the edited *ACVR1* wild-type cells fell below that of the parental and control (EGFP) edited SU-DIPG-IV cells. The reduced viability at high concentrations of LLY-283 in *ACVR1* wild-type cells, rather than a shift of the entire growth inhibition curve could suggest the loss of a specific subpopulation or change in baseline ATP consumption. It has previously been proposed that a developmental hierarchy within DIPG tumours contributes to their intratumoural heterogeneity (Filbin *et al.*, 2018), that *ACVR1* mutations arrest glial cell differentiation (Fortin *et al.*, 2020), and that ACVR1 regulates proliferation and cell cycle exit (Rajagopal *et al.*, 2008; Sorkin *et al.*, 2017). Therefore, the correction of G328V could promote differentiation of the DIPG cells and render this population more susceptible to cell cycle arrest by PRMT5 inhibition. This hypothesis is supported by the reduction in clonogenicity also observed in clone 1G6.

In addition to the observed growth defect, the edited *ACVR1* wild-type 1G6 clone was less clonogenic than the parental SU-DIPG-IV. The 49-60% clonogenic cells recorded for the EGFP control and parental cell lines is consistent with previous findings that ~50-100% of DIPG cells are proliferative oligodendrocyte precursor like cells (Filbin *et al.*, 2018). The loss of clonogenicity and increase in expression of proteins associated with astrocyte differentiation or

activation is in line with previous work showing that *ACVR1* G328V arrests glial cell differentiation (Fortin *et al.*, 2020).

Similar to the observation in Chapter 3 that *ACVR1* wild-type DIPG cells were more resistant to PRMT5 inhibition, it was previously reported that *ACVR1* wild-type cells were more resistant to ACVR1 inhibition (Carvalho *et al.*, 2019). Again, strikingly this correlation was not recapitulated in this genetically edited experimental model. Thus, the cell death induced by these inhibitors may reflect that wild-type *ACVR1* is a necessary in addition to mutant *ACVR1* for DIPG cell survival or is induced by currently unknown off-target activity of these *ACVR1* inhibitors.

Interestingly, correction of *ACVR1* G328V induced the secretion of multiple additional proteins, from which potential phenotypic changes can be inferred. After correction of *ACVR1* G328V, secretion of IL-6, IL-8 and VEGF increased. These cytokines are associated with activation of Stat3 and NF-κB signalling (Loeffler *et al.*, 2005; Iglesia *et al.*, 2008; Chen *et al.*, 2014). Furthermore, MCP-1 and GDF-15 expression is regulated Specificity protein 1 (Sp1), which directly interacts with STAT3 (Loeffler *et al.*, 2005; Huang and Xie, 2012; Yoshimura, 2017; Segherlou *et al.*, 2021). However, increased activation of STAT3 or NF-κB signalling would be need to be confirmed directly before drawing conclusions, especially because this observation would contradict the findings of other experimental models: *ACVR1* mutant DIPG cells have higher Stat3 activation than matched normal tissue (Hoeman *et al.*, 2019); *ACVR1* R206H overexpression leads to increased Stat3 activation (Hoeman *et al.*, 2019); In FOP patients *ACVR1* mutations enhance NF-κB signalling (Barruet *et al.*, 2016; Matsuo *et al.*, 2021).

It should be noted that these signalling changes inferred by protein secretion happened in the absence of ligand stimulation and further differences in ligand response could exist between the matched cell lines.

This matched pair of cell lines is already an invaluable experimental tool, but could be improved by the continued generation of additional edited cell lines. Firstly, restoration of G328V into the *ACVR1* gene would be a robust positive control to further confirm that changes are due to this genomic change. Furthermore, introduction of different *ACVR1* mutations, such as R206H, into this cell line could allow detailed comparison of the effect of different *ACVR1* mutations on DIPG cells. This would be especially interesting given the differences in kinase activity, prognosis and co-segregation with H3.3 or H3.1 K27M between G328V and R206H (Carvalho *et al.*, 2019; Cao *et al.*, 2020). This genomic editing could be repeated for the other disease-causing mutations, or in other cell lines in order to interrogate each mutation in turn, with increasing robustness.

Chapter 6. Discussion

With a dismal median overall survival of 9-11 months (Cooney *et al.*, 2017) – a prognosis which has not improved in 30 years (Gallitto *et al.*, 2019) – DIPG remains an area of striking unmet clinical need. For this reason, this DPhil project aimed to identify and characterise a novel epigenetic target for potential DIPG therapy and to assess the importance of understudied *ACVR1* mutations in DIPG maintenance.

In Chapter 3, the PRMT family proteins were identified as novel therapeutic targets by screening of a comprehensive range of epigenetic regulators using a chemical probe set released by the SGC. The two most effective PRMT family probes both targeted PRMT5 for inhibition by distinct molecular mechanisms raising confidence that their effect is on-target. This is the first publication to highlight PRMT5 as a potential therapeutic target within DIPG. Previously PRMT5 has only been investigated in the context of adult glioma and neuroblastoma (Park *et al.,* 2015; Sachamitr *et al.,* 2021). In comparison, other pre-clinical candidates, such as EZH2 inhibitors (Mohammad *et al.*, 2017; Zhang *et al.*, 2017), appeared relatively inactive against cell viability. Full growth inhibition curves generated for both PRMT5 inhibitors, LLY-283 and GSK591, in 5 patient-derived DIPG cell lines generated GI_{50} values ranging from 13 nM to >10 µM, with the three most sensitive cell lines being *ACVR1* mutant. Therefore, the role of *ACVR1* in PRMT5 inhibition sensitivity was interrogated using genomic engineering in Chapter 5.

The variation in sensitivity to PRMT5 inhibition suggests that genetic or epigenetic variation between DIPG patients could influence their sensitivity to treatment with PRMT5 inhibitors. Similar variation in sensitivity to PRMT5 inhibition was also observed when adult glioblastoma cells were treated with LLY-283 (Sachamitr *et al.*, 2021). This could necessitate stratification of DIPG patients according to their genetic or epigenetic markers during clinical testing. Stratification of DIPG patients is not ideal because the already small number of DIPG patients limits the clinical testing of any new treatment (Veldhuijzen van Zanten *et al.*, 2017)

and a minority of patients undergo biopsy (Freeman and Farmer, 1998), however it may be necessary in order to statistically detect improved survival. In clinical trials DIPG patients are typically stratified only according to histone mutational status (for example, NCT03416530) or not at all, despite demonstrating differential responses to treatments tested (for example Chi *et al.*, 2019; Hall *et al.,* 2019; Majzner *et al.*, 2022). Thus, the potential need to stratify patients according to *ACVR1* mutational status was interrogated in Chapter 5.

In Chapter 4, PRMT5 inhibition was evaluated pre-clinically *in vitro* and *in vivo.* In collaboration with Ángel Montero Carcaboso, LLY-283 was tested in an orthotopic PDX model of DIPG (Vinci *et al.*, 2018; Carvalho *et al.*, 2019), but did not improve survival or reduce tumour burden in this preliminary experiment. This is not surprising for the initial test of a therapeutic compound against DIPG, because of its rapid progression and aggressive phenotype (Langmoen *et al.*, 1991; Caretti, Bugiani, *et al.*, 2014; Louis *et al.*, 2016; Cooney *et al.*, 2017), and there are simple reasons that the results may have been inconclusive:

LLY-283 was selected for *in vivo* testing because it had a brain to plasma ratio of 0.3 (Cheryl Arrowsmith, personal communication). This was thought to be sufficient for *in vivo* efficacy, but only partial target engagement was observed by IHC in the brainstem, suggesting that LLY-283 may not have reached a therapeutic concentration in the brainstem. This could be further exacerbated during the 4 off days in the dosing strategy. LLY-283 was later shown to enter the whole brain at therapeutic doses in a glioma xenograft model (Sachamitr *et al.*, 2021), however, drugs often penetrate the brainstem to a lesser extent than that of other brain regions (Warren, 2018; Zeiadeh, Najjar and Karaman, 2018). Detailed characterisation of the penetrance of LLY-283 throughout the brain may therefore be pertinent. Additional tests using convection enhanced delivery or subcutaneous xenografts would either bypass or disregard the blood-brainstem-barrier and could assess whether insufficient brainstem penetration prevented LLY-283 from prolonging survival.

Finally, it is possible that the PDX model does not faithfully represent DIPG. Translation of efficacy from mouse studies into human clinical trials is notoriously poor (Huszthy *et al.*, 2012; Seyhan, 2019), suggesting that most current mouse models do not represent human disease. Relative to humans, mice have different genomes and develop different tumours in response to the same oncogenes (Seyhan, 2019). That is, although *in vitro* models are simpler than *in vivo* models, *in vivo* models are not necessarily more faithful.

Although LLY-283 did not prolong the survival of PDX mice, it did reduce the invasion of DIPG cells into the forebrains of 3 out of 5 mice treated. PRMT5 inhibition could therefore be used clinically to reduce symptoms associated with extrapontine infiltration or improve the outcome of focal radiotherapy by limiting the tumour to the pons (Caretti, Bugiani, *et al.*, 2014; Kluiver *et al.*, 2020). However, as the pons regulates vital processes including breathing (Moini, Koenitzer and LoGalbo, 2021), the ultimate aim is still a therapeutic response within the pons.

A local response may only be achieved by combining PRMT5 inhibition with another targeted therapeutic, as single targeted inhibitors are often unable to prolong survival in DIPG mouse models (Wiese *et al.*, 2016; Miyahara *et al.*, 2017; Aziz-Bose and Monje, 2019; Meel *et al.*, 2020; Carvalho *et al.*, 2021). For example, LLY-283 could be combined with inhibitors of CDK4/6, mTOR, ACVR1 or VEGF which have all demonstrated efficacy in DIPG PDX models (Asby *et al.*, 2018; Carvalho *et al.*, 2019, 2021; Otani *et al.*, 2021). However, the restoration of PRC2 activity by PRMT5 inhibition could render it incompatible with EZH2 inhibitors. In short, there remains much potential for the pre-clinical development of this novel therapeutic target.

Nevertheless, it was interesting to consider the mechanisms by which PRMT5 impact DIPG cells *in vitro,* where the potency was high. RNA-sequencing of the DIPG transcriptome after low dose LLY-283 treatment identified multiple PRMT5 dependent processes in these cells. RNA-sequencing and an *in vitro* limiting dilution assay showed that the fraction of clonogenic cells was reduced. Given the lack of cell death after PRMT5 inhibition it's likely the observed

drop in stemness is due to cell cycle arrest, and it would be worth confirming this with flow cytometric cell cycle analysis in future. In parallel, DE genes were enriched for PRC2 targets and restoration of H3K27me3 after PRMT5 inhibition *in vitro* suggested increased PRC2 activity after PRMT5 inhibition. In fact, the drop in stemness could be as a result of increased PRC2 activity because H3K27M itself impairs differentiation (Silveira *et al.*, 2019; Wiese *et al.*, 2020). By reducing stemness, PRMT5 inhibition could slow DIPG progression by the same mechanism as H3K27M knockdown does (Silveira *et al.*, 2019). The mechanism by which PRMT5 influences EZH2 activity in H3K27M cells would be an important focus for future study. For example, ChIP-seq could identify whether PRMT5 inhibition influences the genomic location of EZH2 or H3K27me3 and whether this correlates with a loss of PRMT5 mediated histone methylation or the gene expression changes already observed.

Chapter 5 used CRISPR/Cas9 genome engineering to correct *ACVR1* G328V to the wild-type sequence in a patient derived DIPG cell line and hence characterise the role of *ACVR1* in DIPG maintenance and therapeutic sensitivity. Most notably, the isogenic edited *ACVR1* wild-type cell line was not less sensitive to PRMT5 inhibition than the *ACVR1* mutant parental line, which refuted the positive correlation between *ACVR1* mutations and sensitivity to PRMT5 inhibition that was observed in Chapter 3. By removing the confounding effect of background mutations, the matched pair of cell lines demonstrated that a different genetic factor must underlie the range of sensitivities to PRMT5 inhibition. In future, a genome-wide CRISPR screen could be used to systematically identify the causative genetic variant, which could greatly improve future clinical testing of PRMT5 inhibition. Furthermore, this issue highlights the need for more studies that aim to improve the stratification of DIPG patients in clinical trials, alongside development of therapeutics themselves.

The growth defect in the *ACVR1* wild-type 1G6 cell line was also less pronounced than that produced by shRNA knockdown of R206H and wild-type ACVR1 (Carvalho *et al.*, 2019). By

retaining the wild-type allele in this experiment the effect of the mutant allele specifically was quantified here. The only partial impairment of tumour maintenance after removal of the *ACVR1* G328V mutation in this study raises the question as to whether *ACVR1* is more important for DIPG initiation than maintenance. If *ACVR1* were only necessary in the early stages of tumour development, this would emphasise the need for longitudinal study of DIPG or development of early detection methods. However, both of these goals remain challenging as brainstem biopsy cannot be performed repeatedly and DIPG cannot easily be imaged with MRI, although detection of tumour DNA in the CSF is now being developed (Azad *et al.,* 2020; Kossatz *et al.,* 2017).

These differing results and conclusions highlight the value of closely controlled experimental models such as these isogenic cell lines. Future work could interrogate differences in gene expression downstream of BMP or activin A stimulation to characterise the differential gene expression profile induced by stimulation of mutant *ACVR1.* Alternatively, genome editing could be expanded into DIPG cell lines that can be xenografted into mice and could allow the assessment of whether *ACVR1* plays a greater role in DIPG initiation than maintenance. Given the variation in sensitivity to PRMT5 remains unexplained, a genome-wide CRISPR screen could identify what genetic factors underpinned the variation in sensitivity to PRMT5 or ACVR1 inhibition, and would greatly aid stratification of future clinical trials testing PRMT5 inhibition. In addition to providing an experimental tool for future study of G328V *ACVR1,* this chapter provides a framework for rapid generation of further bespoke DIPG cell lines.

In summary this project identified the PRMT family as putative therapeutic targets in DIPG and began the characterisation of PRMT5 inhibition specifically. The initial test of the PRMT5 inhibitor LLY-283 in PDX mice had mixed results, however there are clear next steps to its pre-clinical development. In parallel, an isogenic pair of DIPG cells lines was generated, providing a useful experimental tool for the study of ACVR1 in DIPG. Importantly, isogenic cell

lines will avoid the drawing of inaccurate conclusions from improperly controlled panels of patient-derived cell lines. Here isogenic DIPG cells demonstrated that mutant *ACVR1* contributed to the rapid proliferation, stemness and potentially the therapeutic resistance of DIPG cells. Development of therapeutic strategies for DIPG remains incredibly challenging and this work provides a putative therapeutic target as well as experimental tools for its ongoing study.

References

'5X SDS-loading buffer' (2006) *Cold Spring Harbor Protocols*, 2006(6), p. pdb.rec10700. doi: 10.1101/pdb.rec10700.

Ackloo, S., Brown, P. J. and Müller, S. (2017) 'Chemical probes targeting epigenetic proteins: Applications beyond oncology', *Epigenetics*, 12(5), pp. 378–400. doi: 10.1080/15592294.2017.1279371.

Agnew, C. *et al.* (2021) 'Structural basis for ALK2/BMPR2 receptor complex signaling through kinase domain oligomerization', *Nature Communications*, 12(1), p. 4950. doi: 10.1038/s41467-021-25248-5.

Ahmad, F. *et al.* (2019) 'Cholesterol Metabolism: A Potential Therapeutic Target in Glioblastoma', *Cancers*, 11(2), p. 146. doi: 10.3390/cancers11020146.

Al-Lamki, R. S. *et al.* (2016) 'Tumor necrosis factor receptor 2-signaling in CD133-expressing cells in renal clear cell carcinoma.', *Oncotarget*, 7(17), pp. 1–14. doi: 10.18632/oncotarget.8125.

Aldape, K. *et al.* (2019) 'Challenges to curing primary brain tumours', *Nature Reviews Clinical Oncology*, 16(8), pp. 509–520. doi: 10.1038/s41571-019-0177-5.

Arganda-Carreras, I. *et al.* (2017) 'Trainable Weka Segmentation: a machine learning tool for microscopy pixel classification', *Bioinformatics*, 33(15), pp. 2424–2426. doi: 10.1093/BIOINFORMATICS/BTX180.

Asby, D. *et al.* (2018) 'Combined use of CDK4/6 and mTOR inhibitors induce synergistic growth arrest of diffuse intrinsic pontine glioma cells via mutual downregulation of mTORC1 activity', *Cancer Management and Research*, Volume 10, pp. 3483–3500. doi: 10.2147/CMAR.S167095.

Ashton, T. M. *et al.* (2016) 'The anti-malarial atovaquone increases radiosensitivity by alleviating tumour hypoxia', *Nature Communications*, 7(1), pp. 1–13. doi: 10.1038/ncomms12308.

Auerbach, R., Chen, B. and Butte, A. (2013) 'Relating genes to function: identifying enriched transcription factors using the ENCODE ChIP-Seq significance tool', *Bioinformatics (Oxford, England)*, 29(15), pp. 1922–1924. doi: 10.1093/BIOINFORMATICS/BTT316.

Azad, T. D. *et al.* (2020) 'Liquid biopsy for pediatric diffuse midline glioma: a review of circulating tumor DNA and cerebrospinal fluid tumor DNA', *Neurosurgical Focus*, *48*(1), E9. https://doi.org/10.3171/2019.9.FOCUS19699

Aziz-Bose, R. and Monje, M. (2019) 'Diffuse intrinsic pontine glioma: molecular landscape and emerging therapeutic targets', *Current opinion in oncology*, 31(6), p. 522. doi: 10.1097/CCO.0000000000000577.

Banasavadi-Siddegowda, Y. K. *et al.* (2017) 'PRMT5–PTEN molecular pathway regulates senescence and self-renewal of primary glioblastoma neurosphere cells', *Oncogene*, 36(2), pp. 263–274. doi: 10.1038/onc.2016.199.

Banasavadi-Siddegowda, Y. K. *et al.* (2018) 'PRMT5 as a druggable target for glioblastoma therapy', *Neuro-Oncology*, 20(6), pp. 753–763. doi: 10.1093/neuonc/nox206.

Banks, W. A. (2009) 'Characteristics of compounds that cross the blood-brain barrier',

BMC Neurology, *9*(SUPPL. 1), 1–5. https://doi.org/10.1186/1471-2377-9-S1-S3/FIGURES/1

Bao, X. *et al.* (2013) 'Overexpression of PRMT5 Promotes Tumor Cell Growth and Is Associated with Poor Disease Prognosis in Epithelial Ovarian Cancer', *Journal of Histochemistry and Cytochemistry*, 61(3), p. 206. doi: 10.1369/0022155413475452.

Barbosa-Morais, N. L. *et al.* (2012) 'The Evolutionary Landscape of Alternative Splicing in Vertebrate Species', *Science*, 338(6114), pp. 1587–1593. doi: 10.1126/science.1230612.

Barna, B. *et al.* (1994) 'Regulation of monocyte chemoattractant protein-1 expression in adult human non-neoplastic astrocytes is sensitive to tumor necrosis factor (TNF) or antibody to the 55-kDa TNF receptor', *Journal of neuroimmunology*, 50(1), pp. 101–107. doi: 10.1016/0165-5728(94)90220-8.

Barnett, K. K. *et al.* (2021) 'Abstract 49: Brain penetrant HDAC inhibitor RG2833 induces DIPG cell death and synergizes with lomustine', in *Experimental and Molecular Therapeutics*. American Association for Cancer Research, pp. 49–49. doi: 10.1158/1538-7445.AM2021-49.

Barruet, E. *et al.* (2016) 'The ACVR1 R206H mutation found in fibrodysplasia ossificans progressiva increases human induced pluripotent stem cell-derived endothelial cell formation and collagen production through BMP-mediated SMAD1/5/8 signaling.', *Stem cell research & therapy*, 7(1), p. 115. doi: 10.1186/s13287-016-0372-6.

Barton, K. L. *et al.* (2013) 'PD-0332991, a CDK4/6 Inhibitor, Significantly Prolongs Survival in a Genetically Engineered Mouse Model of Brainstem Glioma', *PLoS ONE*. Edited by M. M. Alonso, 8(10), p. e77639. doi: 10.1371/journal.pone.0077639.

Becher, O. J. *et al.* (2010) 'Preclinical Evaluation of Radiation and Perifosine in a Genetically and Histologically Accurate Model of Brainstem Glioma', *Cancer Research*, 70(6), pp. 2548–2557. doi: 10.1158/0008-5472.CAN-09-2503.

Bender, S. *et al.* (2013) 'Reduced H3K27me3 and DNA Hypomethylation Are Major Drivers of Gene Expression in K27M Mutant Pediatric High-Grade Gliomas', *Cancer Cell*, 24(5), pp. 660–672. doi: 10.1016/j.ccr.2013.10.006.

Benjamini, Y. and Hochberg, Y. (1995) 'Controlling the False Discovery Rate: A Practical and Powerful Approach to Multiple Testing', *Journal of the Royal Statistical Society: Series B (Methodological)*, 57(1), pp. 289–300. doi: 10.1111/j.2517-6161.1995.tb02031.x.

Benjamini, Y., Krieger, A. M. and Yekutieli, D. (2006) 'Adaptive linear step-up procedures that control the false discovery rate', *Biometrika*, 93(3), pp. 491–507. Available at: https://doi.org/10.1093/biomet/93.3.491.

Bernier-Chastagner, V. *et al.* (2005) 'Topotecan as a radiosensitizer in the treatment of children with malignant diffuse brainstem gliomas', *Cancer*, 104(12), pp. 2792–2797. doi: 10.1002/cncr.21534.

Bezzi, M. *et al.* (2013) 'Regulation of constitutive and alternative splicing by PRMT5 reveals a role for Mdm4 pre-mRNA in sensing defects in the spliceosomal machinery', *Genes & Development*, 27(17), pp. 1903–1916. doi: 10.1101/gad.219899.113.

Billings, P. C. *et al.* (2008) 'Dysregulated BMP Signaling and Enhanced Osteogenic Differentiation of Connective Tissue Progenitor Cells From Patients With Fibrodysplasia Ossificans Progressiva (FOP)', *Journal of Bone and Mineral Research*, 23(3), pp. 305–313. doi: 10.1359/jbmr.071030.

Blanc, R. S. and Richard, S. (2017) 'Arginine Methylation: The Coming of Age', *Molecular Cell*, 65(1), pp. 8–24. doi: 10.1016/j.molcel.2016.11.003.

Bonday, Z. Q. *et al.* (2018) 'LLY-283, a Potent and Selective Inhibitor of Arginine Methyltransferase 5, PRMT5, with Antitumor Activity', *ACS Medicinal Chemistry Letters*, 9(7), pp. 612–617. doi: 10.1021/acsmedchemlett.8b00014.

Bouffet, E. *et al.* (2000) 'Radiotherapy followed by high dose busulfan and thiotepa', *Cancer*, 88(3), pp. 685–692. doi: 10.1002/(SICI)1097-0142(20000201)88:3<685::AID-CNCR27>3.0.CO;2-K.

Bourdon, M. *et al.* (1983) 'Human glioma-mesenchymal extracellular matrix antigen defined by monoclonal antibody', *Cancer Research*, 43(6), pp. 2796–2805.

Bradley, K. A. *et al.* (2013) 'Motexafin-Gadolinium and Involved Field Radiation Therapy for Intrinsic Pontine Glioma of Childhood: A Children's Oncology Group Phase 2 Study', *International Journal of Radiation Oncology*Biology*Physics*, 85(1), pp. e55–e60. doi: 10.1016/j.ijrobp.2012.09.004.

Bray, N. L. *et al.* (2016) 'Near-optimal probabilistic RNA-seq quantification', *Nature Biotechnology 2016 34:5*, 34(5), pp. 525–527. doi: 10.1038/nbt.3519.

Bressan, R. B. *et al.* (2021) 'Regional identity of human neural stem cells determines oncogenic responses to histone H3.3 mutants', *Cell Stem Cell*, 28(5), pp. 877-893.e9. doi: 10.1016/j.stem.2021.01.016.

Brinkman, E. K. *et al.* (2014) 'Easy quantitative assessment of genome editing by sequence trace decomposition', *Nucleic Acids Research*, 42(22), pp. e168–e168. doi: 10.1093/NAR/GKU936.

Bruinsmann, F. A. *et al.* (2019) 'Nasal Drug Delivery of Anticancer Drugs for the Treatment of Glioblastoma: Preclinical and Clinical Trials', Molecules, 24(23). https://doi.org/10.3390/MOLECULES24234312

Buczkowicz, P. *et al.* (2014) 'Genomic analysis of diffuse intrinsic pontine gliomas identifies three molecular subgroups and recurrent activating ACVR1 mutations', *Nature Genetics*, 46(5), pp. 451–456. doi: 10.1038/ng.2936.

Cancer Research UK (2021) *Children's cancers mortality statistics*. Available at: https://www.cancerresearchuk.org/health-professional/cancer-statistics/childrens-cancers/mortality (Accessed: 10 August 2021).

Cao, R. *et al.* (2002) 'Role of histone H3 lysine 27 methylation in polycomb-group silencing', *Science*, *298*(5595), 1039–1043. https://doi.org/10.1126/SCIENCE.1076997/SUPPL_FILE/CAOR1076997.SUP.PDF

Cao, H. *et al.* (2020) 'Differential kinase activity of ACVR1 G328V and R206H mutations with implications to possible TβRI cross-talk in diffuse intrinsic pontine glioma', *Scientific Reports 2020 10:1*, 10(1), pp. 1–12. doi: 10.1038/s41598-020-63061-0.

Caretti, V. *et al.* (2013) 'Implementation of a multi-institutional diffuse intrinsic pontine glioma autopsy protocol and characterization of a primary cell culture', *Neuropathology and Applied Neurobiology*, 39(4), pp. 426–436. doi: 10.1111/j.1365-2990.2012.01294.x.

Caretti, V., Sewing, A. C. P., *et al.* (2014) 'Human pontine glioma cells can induce murine tumors', *Acta Neuropathologica*, 127(6), pp. 897–909. doi: 10.1007/s00401-014-1272-4.

Caretti, V., Bugiani, M., *et al.* (2014) 'Subventricular spread of diffuse intrinsic pontine glioma', *Acta Neuropathologica*, 128(4), pp. 605–607. doi: 10.1007/s00401-014-1307-x.

Carvalho, D. M. *et al.* (2019) 'ALK2 inhibitors display beneficial effects in preclinical models of ACVR1 mutant diffuse intrinsic pontine glioma', *Communications Biology 2019 2:1*, 2(1), pp. 1–10. doi: 10.1038/s42003-019-0420-8.

Carvalho, D. M. *et al.* (2021) 'Repurposing vandetanib plus everolimus for the treatment of ACVR1-mutant diffuse intrinsic pontine glioma', *Cancer Discovery*, p. candisc.1201.2020. doi: 10.1158/2159-8290.CD-20-1201.

Chakkalakal, S. *et al.* (2012) 'An Acvr1 R206H knock-in mouse has fibrodysplasia ossificans progressiva', *Journal of bone and mineral research : the official journal of the American Society for Bone and Mineral Research*, 27(8), pp. 1746–1756. doi: 10.1002/JBMR.1637.

Chan-Penebre, E. *et al.* (2015) 'A selective inhibitor of PRMT5 with in vivo and in vitro potency in MCL models', *Nature Chemical Biology*, 11(6), pp. 432–437. doi: 10.1038/nchembio.1810.

Chan, K. M. *et al.* (2013) 'The histone H3.3K27M mutation in pediatric glioma reprograms H3K27 methylation and gene expression', *Genes and Development*, 27(9), pp. 985–990. doi: 10.1101/gad.217778.113.

Chen, P. *et al.* (2015) 'EphB2 activation is required for ependymoma development as well as inhibits differentiation and promotes proliferation of the transformed cell', *Scientific Reports*, 5(1), p. 9248. doi: 10.1038/srep09248.

Chen, W. *et al.* (2014) 'The CCL2/CCR2 axis enhances IL-6-induced epithelial-mesenchymal transition by cooperatively activating STAT3-Twist signaling', *Tumor Biology 2014 36:2*, 36(2), pp. 973–981. doi: 10.1007/S13277-014-2717-Z.

Chen, W. *et al.* (2016) 'Human astrocytes secrete IL-6 to promote glioma migration and invasion through upregulation of cytomembrane MMP14', *Oncotarget*, 7(38), pp. 62425–62438. doi: 10.18632/ONCOTARGET.11515.

Chi, A. S. *et al.* (2019) ' Pediatric and adult H3 K27M-mutant diffuse midline glioma treated with the selective DRD2 antagonist ONC201', *Journal of Neuro-Oncology*, *145*(1), 97–105. https://doi.org/10.1007/S11060-019-03271-3

Chiang, K. *et al.* (2017) 'PRMT5 Is a Critical Regulator of Breast Cancer Stem Cell Function via Histone Methylation and FOXP1 Expression', *Cell Reports*, 21(12), pp. 3498–3513. doi: 10.1016/j.celrep.2017.11.096.

Cho, E.-C. *et al.* (2012) 'Arginine methylation controls growth regulation by E2F-1', *The EMBO Journal*, 31(7), pp. 1785–1797. doi: 10.1038/emboj.2012.17.

Chu, Z. *et al.* (2015) 'PRMT5 enhances generation of induced pluripotent stem cells from dairy goat embryonic fibroblasts via down-regulation of p53', *Cell proliferation*, 48(1), pp. 29–38. doi: 10.1111/CPR.12150.

Chung, C. *et al.* (2020) 'Integrated Metabolic and Epigenomic Reprograming by H3K27M Mutations in Diffuse Intrinsic Pontine Gliomas', *Cancer Cell*, 0(0). doi: 10.1016/j.ccell.2020.07.008.

Ciechomska, I. A. *et al.* (2016) 'BIX01294, an inhibitor of histone methyltransferase, induces autophagy-dependent differentiation of glioma stem-like cells', *Scientific Reports*, 6(1),

pp. 1–15. doi: 10.1038/srep38723.

Cohen, K. J. *et al.* (2011) 'Temozolomide in the treatment of children with newly diagnosed diffuse intrinsic pontine gliomas: a report from the Children's Oncology Group', *Neuro-Oncology*, 13(4), pp. 410–416. doi: 10.1093/neuonc/noq205.

Cohen, K. J., Jabado, N. and Grill, J. (2017) 'Diffuse intrinsic pontine gliomas—current management and new biologic insights. Is there a glimmer of hope?', *Neuro-Oncology*, 19(8), p. 1025. doi: 10.1093/NEUONC/NOX021.

Concordet, J.-P. and Haeussler, M. (2018) 'CRISPOR: intuitive guide selection for CRISPR/Cas9 genome editing experiments and screens', *Nucleic Acids Research*, 46(W1), pp. W242–W245. doi: 10.1093/NAR/GKY354.

Conroy, S. *et al.* (2000) 'Drug trials in children: problems and the way forward', *British Journal of Clinical Pharmacology*, 49(2), pp. 93–97. doi: 10.1046/j.1365-2125.2000.00125.x.

Cooney, T. *et al.* (2017) 'Contemporary survival endpoints: an International Diffuse Intrinsic Pontine Glioma Registry study', *Neuro-Oncology*, 19(9), p. 1279. doi: 10.1093/NEUONC/NOX107.

Cordero, F. J. *et al.* (2017) 'Histone H3.3K27M Represses p16 to Accelerate Gliomagenesis in a Murine Model of DIPG', *Molecular Cancer Research*, 15(9), pp. 1243–1254. doi: 10.1158/1541-7786.MCR-16-0389.

Daigle, S. R. *et al.* (2011) 'Selective killing of mixed lineage leukemia cells by a potent small-molecule DOT1L inhibitor.', *Cancer cell*, 20(1), pp. 53–65. doi: 10.1016/j.ccr.2011.06.009.

Deland, K. *et al.* (2021) 'Tumor genotype dictates radiosensitization after Atm deletion in primary brainstem glioma models', *The Journal of Clinical Investigation*, 131(1). doi: 10.1172/JCI142158.

DeWire, M. *et al.* (2020) 'A phase I/II study of ribociclib following radiation therapy in children with newly diagnosed diffuse intrinsic pontine glioma (DIPG)', *Journal of Neuro-Oncology*, *149*(3), 511–522. https://doi.org/10.1007/S11060-020-03641-2

Doench, J. G. *et al.* (2014) 'Rational design of highly active sgRNAs for CRISPR-Cas9–mediated gene inactivation', *Nature Biotechnology*, 32(12), pp. 1262–1267. doi: 10.1038/nbt.3026.

Doench, J. G. *et al.* (2016) 'Optimized sgRNA design to maximize activity and minimize off-target effects of CRISPR-Cas9', *Nature Biotechnology 2015 34:2*, 34(2), pp. 184–191. doi: 10.1038/nbt.3437.

Donahue, B. *et al.* (1998) 'Patterns of recurrence in brain stem gliomas: Evidence for craniospinal dissemination', *International Journal of Radiation Oncology*Biology*Physics*, 40(3), pp. 677–680. doi: 10.1016/S0360-3016(97)00846-8.

Dong, X. (2018) 'Current Strategies for Brain Drug Delivery', *Theranostics*, 8(6), p. 1481. doi: 10.7150/THNO.21254.

Dudas, M. *et al.* (2004) 'Craniofacial defects in mice lacking BMP type I receptor Alk2 in neural crest cells', *Mechanisms of development*, 121(2), pp. 173–182. doi: 10.1016/J.MOD.2003.12.003.

Dunkel, I. *et al.* (1998) 'High dose chemotherapy with autologous bone marrow rescue for children with diffuse pontine brain stem tumors', *Journal of Neuro-Oncology*, 37, pp. 67–73. doi:

https://doi.org/10.1023/A:1005874508975.

Ensan, D. *et al.* (2020) 'Targeting ALK2: An Open Science Approach to Developing Therapeutics for the Treatment of Diffuse Intrinsic Pontine Glioma', *Journal of Medicinal Chemistry*, 63(9), pp. 4978–4996. doi: 10.1021/acs.jmedchem.0c00395.

Ewald, J. A. *et al.* (2010) 'Therapy-Induced Senescence in Cancer', *JNCI: Journal of the National Cancer Institute*, 102(20), pp. 1536–1546. doi: 10.1093/jnci/djq364.

Fauquette, W. *et al.* (2012) 'Radiation-induced blood–brain barrier damages: An in vitro study', *Brain Research*, 1433, pp. 114–126. doi: 10.1016/j.brainres.2011.11.022.

Filbin, M. G. *et al.* (2018) 'Developmental and oncogenic programs in H3K27M gliomas dissected by single-cell RNA-seq.', *Science (New York, N.Y.)*, 360(6386), pp. 331–335. doi: 10.1126/science.aao4750.

Fontebasso, A. M. *et al.* (2014) 'Recurrent somatic mutations in ACVR1 in pediatric midline high-grade astrocytoma', *Nature Genetics*, 46(5), pp. 462–466. doi: 10.1038/ng.2950.

Fortin, J. *et al.* (2020) 'Mutant ACVR1 Arrests Glial Cell Differentiation to Drive Tumorigenesis in Pediatric Gliomas', *Cancer Cell*, 37(3), pp. 308-323.e12. doi: 10.1016/j.ccell.2020.02.002.

Freeman, C. R. and Farmer, J.-P. (1998) 'Pediatric brain stem gliomas: A review', *International Journal of Radiation Oncology*Biology*Physics*, 40(2), pp. 265–271. doi: 10.1016/S0360-3016(97)00572-5.

Fukuda, T. *et al.* (2009) 'Constitutively Activated ALK2 and Increased SMAD1/5 Cooperatively Induce Bone Morphogenetic Protein Signaling in Fibrodysplasia Ossificans Progressiva', *Journal of Biological Chemistry*, 284(11), pp. 7149–7156. doi: 10.1074/jbc.M801681200.

Funato, K. *et al.* (2014) 'Use of human embryonic stem cells to model pediatric gliomas with H3.3K27M histone mutation', *Science*, 346(6216), pp. 1529–1533. doi: 10.1126/science.1253799.

Gallitto, M. *et al.* (2019) 'Role of Radiation Therapy in the Management of Diffuse Intrinsic Pontine Glioma: A Systematic Review', *Advances in Radiation Oncology*, 4(3), pp. 520–531. doi: 10.1016/j.adro.2019.03.009.

Gary, J. D. and Clarke, S. (1998) 'RNA and Protein Interactions Modulated by Protein Arginine Methylation', in, pp. 65–131. doi: 10.1016/S0079-6603(08)60825-9.

Gilmore, A. C. *et al.* (2021) 'An in vitro tumorigenesis model based on live-cell-generated oxygen and nutrient gradients', *Communications Biology*, 4(1), p. 477. doi: 10.1038/s42003-021-01954-0.

Gkretsi, V. and Stylianopoulos, T. (2018) 'Cell Adhesion and Matrix Stiffness: Coordinating Cancer Cell Invasion and Metastasis', *Frontiers in Oncology*, 8. doi: 10.3389/fonc.2018.00145.

Gleeson, M. P. *et al.* (2011) 'Probing the links between in vitro potency, ADMET and physicochemical parameters', *Nature Reviews Drug Discovery 2011 10:3*, 10(3), pp. 197–208. doi: 10.1038/nrd3367.

Goldman, B. (2008) 'Magic marker myths', *Nature Reports Stem Cells*. doi: 10.1038/stemcells.2008.26.

Grasso, C. S. *et al.* (2015) 'Functionally defined therapeutic targets in diffuse intrinsic pontine glioma', *Nature Medicine*, 21(6), pp. 555–559. doi: 10.1038/nm.3855.

Gullà, A. *et al.* (2018) 'Protein arginine methyltransferase 5 has prognostic relevance and is a druggable target in multiple myeloma', *Leukemia*, 32(4), pp. 996–1002. doi: 10.1038/LEU.2017.334.

Gupta, N. *et al.* (2018) 'Prospective feasibility and safety assessment of surgical biopsy for patients with newly diagnosed diffuse intrinsic pontine glioma', *Neuro-Oncology*, 20(11), pp. 1547–1555. doi: 10.1093/neuonc/noy070.

Gururangan, S. *et al.* (2006) 'Incidence and patterns of neuraxis metastases in children with diffuse pontine glioma★', *Journal of Neuro-Oncology*, 77(2), pp. 207–212. doi: 10.1007/s11060-005-9029-5.

Haag, D. *et al.* (2021) 'H3.3-K27M drives neural stem cell-specific gliomagenesis in a human iPSC-derived model', *Cancer Cell*, 39(3), pp. 407-422.e13. doi: 10.1016/J.CCELL.2021.01.005.

Hall, M. D. (2019) ' First clinical experience with DRD2/3 antagonist ONC201 in H3 K27M–mutant pediatric diffuse intrinsic pontine glioma: a case report', *Journal of Neurosurgery: Pediatrics*, *23*(6), 719–725. https://doi.org/10.3171/2019.2.PEDS18480

Hamard, P. *et al.* (2018) 'PRMT5 Regulates DNA Repair by Controlling the Alternative Splicing of Histone-Modifying Enzymes', *Cell reports*, 24(10), pp. 2643–2657. doi: 10.1016/J.CELREP.2018.08.002.

Han, H. J., Jain, P. and Resnick, A. C. (2018) 'Shared ACVR1 mutations in FOP and DIPG: Opportunities and challenges in extending biological and clinical implications across rare diseases', *Bone*, 109, pp. 91–100. doi: 10.1016/j.bone.2017.08.001.

Han, X. *et al.* (2014) 'Expression of PRMT5 correlates with malignant grade in gliomas and plays a pivotal role in tumor growth in vitro.', *Journal of neuro-oncology*, 118(1), pp. 61–72. doi: 10.1007/s11060-014-1419-0.

Hanahan, D. and Weinberg, R. A. (2011) 'Hallmarks of Cancer: The Next Generation', *Cell*, 144(5), pp. 646–674. doi: 10.1016/j.cell.2011.02.013.

Hanna, R. E. and Doench, J. G. (2020) 'Design and analysis of CRISPR–Cas experiments', *Nature Biotechnology*, 38(7), pp. 813–823. doi: 10.1038/s41587-020-0490-7.

Harlow, E. and Lane, D. (2006) 'Immunoblotting: antigen detection using chemiluminescence.', *CSH protocols*, 2006(1), p. pdb.prot4271. doi: 10.1101/pdb.prot4271.

Harutyunyan, A. S. *et al.* (2019) 'H3K27M induces defective chromatin spread of PRC2-mediated repressive H3K27me2/me3 and is essential for glioma tumorigenesis', *Nature Communications*, 10(1), p. 1262. doi: 10.1038/s41467-019-09140-x.

Hashizume, R. *et al.* (2014) 'Pharmacologic inhibition of histone demethylation as a therapy for pediatric brainstem glioma', *Nature Medicine*, 20(12), pp. 1394–1396. doi: 10.1038/nm.3716.

Hata, A. *et al.* (1998) *Smad6 inhibits BMP/Smad1 signaling by specifically competing with the Smad4 tumor suppressor*. Available at: www.genesdev.org (Accessed: 25 August 2018).

Hatsell, S. J. *et al.* (2015) 'ACVR1R206H receptor mutation causes fibrodysplasia ossificans progressiva by imparting responsiveness to activin A.', *Science translational medicine*, 7(303), p.

303ra137. doi: 10.1126/scitranslmed.aac4358.

Haupt, J., Xu, M. and Shore, E. M. (2018) 'Variable signaling activity by FOP ACVR1 mutations', *Bone*, 109, pp. 232–240. doi: 10.1016/j.bone.2017.10.027.

Hebert, M. D. *et al.* (2002) 'Coilin Methylation Regulates Nuclear Body Formation', *Developmental Cell*, 3(3), pp. 329–337. doi: 10.1016/S1534-5807(02)00222-8.

Heinz, S. *et al.* (2010) 'Simple combinations of lineage-determining transcription factors prime cis-regulatory elements required for macrophage and B cell identities', *Molecular cell*, 38(4), pp. 576–589. doi: 10.1016/J.MOLCEL.2010.05.004.

Hennika, T. *et al.* (2017) 'Pre-Clinical Study of Panobinostat in Xenograft and Genetically Engineered Murine Diffuse Intrinsic Pontine Glioma Models', *PLOS ONE*. Edited by M. G. Castro, 12(1), p. e0169485. doi: 10.1371/journal.pone.0169485.

Hino, K. *et al.* (2015) 'Neofunction of ACVR1 in fibrodysplasia ossificans progressiva', *Proceedings of the National Academy of Sciences*, 112(50), pp. 15438–15443. doi: 10.1073/pnas.1510540112.

Ho, M.-C. *et al.* (2013) 'Structure of the Arginine Methyltransferase PRMT5-MEP50 Reveals a Mechanism for Substrate Specificity', *PLoS ONE*. Edited by S. Cotterill, 8(2), p. e57008. doi: 10.1371/journal.pone.0057008.

Hoeman, C. M. *et al.* (2019) 'ACVR1 R206H cooperates with H3.1K27M in promoting diffuse intrinsic pontine glioma pathogenesis', *Nature Communications*, 10(1), p. 1023. doi: 10.1038/s41467-019-08823-9.

Hoffman, L. M. *et al.* (2018) 'Clinical, Radiologic, Pathologic, and Molecular Characteristics of Long-Term Survivors of Diffuse Intrinsic Pontine Glioma (DIPG): A Collaborative Report From the International and European Society for Pediatric Oncology DIPG Registries', *Journal of Clinical Oncology*, 36(19), p. 1963. doi: 10.1200/JCO.2017.75.9308.

Hollnagel, A. *et al.* (1999) 'Id Genes Are Direct Targets of Bone Morphogenetic Protein Induction in Embryonic Stem Cells', *Journal of Biological Chemistry*, 274(28), pp. 19838–19845. doi: 10.1074/jbc.274.28.19838.

Horvath, P. and Barrangou, R. (2010) 'CRISPR/Cas, the immune system of bacteria and archaea.', *Science (New York, N.Y.)*, 327(5962), pp. 167–70. doi: 10.1126/science.1179555.

Howes, A. L. *et al.* (2007) 'The phosphatidylinositol 3-kinase inhibitor, PX-866, is a potent inhibitor of cancer cell motility and growth in three-dimensional cultures', *Molecular Cancer Therapeutics*, 6(9), pp. 2505–2514. doi: 10.1158/1535-7163.MCT-06-0698.

https://horizondiscovery.com/en/ordering-and-calculation-tools/edit-r-hdr-donor-designer-oligo (no date). Available at: https://horizondiscovery.com/en/ordering-and-calculation-tools/edit-r-hdr-donor-designer-oligo (Accessed: 9 August 2020).

Hu, Y. *et al.* (2021) 'Acvr1 deletion in osteoblasts impaired mandibular bone mass through compromised osteoblast differentiation and enhanced sRANKL-induced osteoclastogenesis', *Journal of cellular physiology*, 236(6), pp. 4580–4591. doi: 10.1002/JCP.30183.

Hu, Y. and Smyth, G. K. (2009) 'ELDA: Extreme limiting dilution analysis for comparing depleted and enriched populations in stem cell and other assays', *Journal of Immunological Methods*, 347(1–2), pp. 70–78. doi: 10.1016/J.JIM.2009.06.008.

Huang, C. and Xie, K. (2012) 'Crosstalk of Sp1 and Stat3 signaling in pancreatic cancer

pathogenesis', *Cytokine & Growth Factor Reviews*, 23(1–2), pp. 25–35. doi: 10.1016/j.cytogfr.2012.01.003.

Huang, J. *et al.* (2010) 'G9a and Glp methylate lysine 373 in the tumor suppressor p53', *Journal of Biological Chemistry*, 285(13), pp. 9636–9641. doi: 10.1074/jbc.M109.062588.

Huang, J. *et al.* (2011) 'Type II arginine methyltransferase PRMT5 regulates gene expression of inhibitors of differentiation/DNA binding Id2 and Id4 during glial cell differentiation.', *The Journal of biological chemistry*, 286(52), pp. 44424–32. doi: 10.1074/jbc.M111.277046.

Huse, M. *et al.* (1999) 'Crystal Structure of the Cytoplasmic Domain of the Type I TGF β Receptor in Complex with FKBP12', *Cell*, 96(3), pp. 425–436. doi: 10.1016/S0092-8674(00)80555-3.

Huse, M. *et al.* (2001) 'The TGFβ Receptor Activation Process', *Molecular Cell*, 8(3), pp. 671–682. doi: 10.1016/S1097-2765(01)00332-X.

Huszthy, P. C. *et al.* (2012) 'In vivo models of primary brain tumors: pitfalls and perspectives', *Neuro-Oncology*, 14(8), pp. 979–993. doi: 10.1093/neuonc/nos135.

Hwang, J. W. *et al.* (2021) 'Protein arginine methyltransferases: promising targets for cancer therapy', *Experimental & Molecular Medicine 2021 53:5*, 53(5), pp. 788–808. doi: 10.1038/s12276-021-00613-y.

Iglesia, N. de la *et al.* (2008) 'Deregulation of a STAT3–Interleukin 8 Signaling Pathway Promotes Human Glioblastoma Cell Proliferation and Invasiveness', *The Journal of Neuroscience*, 28(23), p. 5870. doi: 10.1523/JNEUROSCI.5385-07.2008.

Izquierdo, E. *et al.* (2022) 'DIPG Harbors Alterations Targetable by MEK Inhibitors, with Acquired Resistance Mechanisms Overcome by Combinatorial Inhibition', *Cancer Discovery*, *12*(3), 712–729. https://doi.org/10.1158/2159-8290.CD-20-0930

Jain, S. U. *et al.* (2020) 'H3 K27M and EZHIP Impede H3K27-Methylation Spreading by Inhibiting Allosterically Stimulated PRC2', *Molecular Cell*, 80(4), pp. 726-735.e7. doi: 10.1016/j.molcel.2020.09.028.

Jansen, M. H. *et al.* (2015) 'Survival prediction model of children with diffuse intrinsic pontine glioma based on clinical and radiological criteria', *Neuro-Oncology*, 17(1), pp. 160–166. doi: 10.1093/NEUONC/NOU104.

Jansen, M. H. A. *et al.* (2012) 'Diffuse intrinsic pontine gliomas: A systematic update on clinical trials and biology', *Cancer Treatment Reviews*, 38(1), pp. 27–35. doi: 10.1016/J.CTRV.2011.06.007.

Jansson, M. *et al.* (2008) 'Arginine methylation regulates the p53 response', *Nature Cell Biology*, 10(12), pp. 1431–1439. doi: 10.1038/ncb1802.

Jia, Z. *et al.* (2020) 'Protein Arginine Methyltransferase PRMT5 Regulates Fatty Acid Metabolism and Lipid Droplet Biogenesis in White Adipose Tissues', *Advanced Science*, 7(23), p. 2002602. doi: 10.1002/advs.202002602.

Jin, Y. *et al.* (2016) 'Targeting methyltransferase PRMT5 eliminates leukemia stem cells in chronic myelogenous leukemia', *The Journal of Clinical Investigation*, 126(10), pp. 3961–3980. doi: 10.1172/JCI85239.

Johung, T. and Monje, M. (2016) 'Diffuse Intrinsic Pontine Glioma: New

Pathophysiological Insights and Emerging Therapeutic Targets', *Current Neuropharmacology*, 15(1), pp. 88–97. doi: 10.2174/1570159X14666160509123229.

Jolliffe, I. T. and Cadima, J. (2016) 'Principal component analysis: a review and recent developments', *Philosophical Transactions of the Royal Society A: Mathematical, Physical and Engineering Sciences*, 374(2065), p. 20150202. doi: 10.1098/rsta.2015.0202.

Jones, C. *et al.* (2017) 'Pediatric high-grade glioma: biologically and clinically in need of new thinking', *Neuro-Oncology*, 19(2), pp. 153–161. doi: 10.1093/NEUONC/NOW101.

Justin, N. *et al.* (2016) 'Structural basis of oncogenic histone H3K27M inhibition of human polycomb repressive comlex 2', *Nature Communications*, 7(1), p. 11316. doi: 10.1038/ncomms11316.

Kan, L. *et al.* (2012) 'CNS demyelination in fibrodysplasia ossificans progressiva', *Journal of Neurology*, 259(12), pp. 2644–2655. doi: 10.1007/s00415-012-6563-x.

Kanamaluru, D. *et al.* (2011) 'Arginine Methylation by PRMT5 at a Naturally Occurring Mutation Site Is Critical for Liver Metabolic Regulation by Small Heterodimer Partner', *Molecular and Cellular Biology*, 31(7), pp. 1540–1550. doi: 10.1128/MCB.01212-10.

Kaplan, F. S. *et al.* (2009) 'Classic and atypical fibrodysplasia ossificans progressiva (FOP) phenotypes are caused by mutations in the bone morphogenetic protein (BMP) type I receptor ACVR1', *Human Mutation*, 30(3), pp. 379–390. doi: 10.1002/humu.20868.

Katagi, H. *et al.* (2019) 'Radiosensitization by Histone H3 Demethylase Inhibition in Diffuse Intrinsic Pontine Glioma', *Clinical cancer research : an official journal of the American Association for Cancer Research*, 25(18), p. 5572. doi: 10.1158/1078-0432.CCR-18-3890.

Katagiri, T. *et al.* (2002) 'Identification of a BMP-responsive element in Id1 , the gene for inhibition of myogenesis', *Genes to Cells*, 7(9), pp. 949–960. doi: 10.1046/j.1365-2443.2002.00573.x.

Khuong-Quang, D. A. *et al.* (2012) 'K27M mutation in histone H3.3 defines clinically and biologically distinct subgroups of pediatric diffuse intrinsic pontine gliomas', *Acta Neuropathologica*, 124(3), pp. 439–447. doi: 10.1007/s00401-012-0998-0.

Kossatz, S. *et al* (2017) 'Biomarker-based PET imaging of diffuse intrinsic pontine glioma in mouse models', *Cancer Research*, *77*(8), 2112–2123. https://doi.org/10.1158/0008-5472.CAN-16-2850/652721/AM/BIOMARKER-BASED-PET-IMAGING-OF-DIFFUSE-INTRINSIC

Kim, S. *et al.* (2014) 'Highly efficient RNA-guided genome editing in human cells via delivery of purified Cas9 ribonucleoproteins', *Genome Research*, 24(6), p. 1012. doi: 10.1101/GR.171322.113.

Kimlin, L. C., Casagrande, G. and Virador, V. M. (2013) 'In vitro three-dimensional (3D) models in cancer research: An update', *Molecular Carcinogenesis*, 52(3), pp. 167–182. doi: 10.1002/mc.21844.

Kluiver, T. A. *et al.* (2020) 'Invaders Exposed: Understanding and Targeting Tumor Cell Invasion in Diffuse Intrinsic Pontine Glioma', *Frontiers in Oncology*. Frontiers Media S.A. doi: 10.3389/fonc.2020.00092.

Knapp, S. and Sundström, M. (2014) 'Recently targeted kinases and their inhibitors—the path to clinical trials', *Current Opinion in Pharmacology*, 17, pp. 58–63. doi: 10.1016/j.coph.2014.07.015.

Kreisl, T. N. *et al.* (2012) 'A phase I/II trial of vandetanib for patients with recurrent malignant glioma', *Neuro-Oncology*, 14(12), pp. 1519–1526. doi: 10.1093/neuonc/nos265.

Kurooka, H. *et al.* (2012) 'BMP signaling is responsible for serum-induced Id2 expression', *Biochemical and Biophysical Research Communications*, 420(2), pp. 281–287. doi: 10.1016/j.bbrc.2012.02.150.

Langmoen, I. A. *et al.* (1991) 'Management of pediatric pontine gliomas', *Child's Nervous System*, 7(1), pp. 13–15. doi: 10.1007/BF00263825.

Lasko, L. M. *et al.* (2017) 'Discovery of a selective catalytic p300/CBP inhibitor that targets lineage-specific tumours', *Nature*, 550(7674), p. 128. doi: 10.1038/nature24028.

Lassaletta, A. *et al.* (2018) 'Reirradiation in patients with diffuse intrinsic pontine gliomas: The Canadian experience', *Pediatric Blood & Cancer*, 65(6), p. e26988. doi: 10.1002/pbc.26988.

Lassman, L. P. and Arjona, V. E. (1967) 'PONTINE GLIOMAS OF CHILDHOOD', *The Lancet*, 289(7496), pp. 913–915. doi: 10.1016/S0140-6736(67)91485-7.

Lattanzi, A. *et al.* (2019) 'Optimization of CRISPR/Cas9 Delivery to Human Hematopoietic Stem and Progenitor Cells for Therapeutic Genomic Rearrangements', *Molecular Therapy*, 27(1), pp. 137–150. doi: 10.1016/J.YMTHE.2018.10.008.

Leoni, C. *et al.* (2021) 'An optimized workflow for CRISPR-Cas9 deletion of surface and intracellular factors in primary human T lymphocytes', *PLOS ONE*, 16(2), p. e0247232. doi: 10.1371/JOURNAL.PONE.0247232.

Levkovitz, Y. *et al.* (2005) 'Differential Induction of Apoptosis by Antidepressants in Glioma and Neuroblastoma Cell Lines: Evidence for p-c-Jun, Cytochrome c, and Caspase-3 Involvement', *Journal of Molecular Neuroscience*, 27(1), pp. 029–042. doi: 10.1385/jmn:27:1:029.

Lewis, P. W. *et al.* (2013) 'Inhibition of PRC2 activity by a gain-of-function H3 mutation found in pediatric glioblastoma', *Science*, 340(6134), pp. 857–861. doi: 10.1126/science.1232245.

Liang, X. *et al.* (2015) 'Rapid and highly efficient mammalian cell engineering via Cas9 protein transfection', *Journal of Biotechnology*, 208, pp. 44–53. doi: 10.1016/J.JBIOTEC.2015.04.024.

Liang, Z. *et al.* (2017) 'Efficient DNA-free genome editing of bread wheat using CRISPR/Cas9 ribonucleoprotein complexes', *Nature communications*, 8. doi: 10.1038/NCOMMS14261.

Ligon, K. *et al.* (2004) 'The oligodendroglial lineage marker OLIG2 is universally expressed in diffuse gliomas', *Journal of neuropathology and experimental neurology*, 63(5), pp. 499–509. doi: 10.1093/JNEN/63.5.499.

Lin, G. L. and Monje, M. (2017) 'A Protocol for Rapid Post-mortem Cell Culture of Diffuse Intrinsic Pontine Glioma (DIPG)', *Journal of Visualized Experiments*, (121). doi: 10.3791/55360.

Litovchick, L. (2018) 'Immunoblotting: Transfer of Proteins from Gels to Membranes.', *Cold Spring Harbor protocols*, 2018(10), p. pdb.prot098442. doi: 10.1101/pdb.prot098442.

Liu, F. *et al.* (2020) 'PRMT5-mediated histone arginine methylation antagonizes transcriptional repression by polycomb complex PRC2', *Nucleic Acids Research*, 48(6), p. 2956. doi: 10.1093/NAR/GKAA065.

Liu, L. *et al.* (2016) 'Arginine Methylation of SREBP1a via PRMT5 Promotes De Novo Lipogenesis and Tumor Growth', *Cancer Research*, 76(5), pp. 1260–1272. doi: 10.1158/0008-5472.CAN-15-1766.

Liu, Q. *et al.* (2018) 'SPOCD1 promotes the proliferation and metastasis of glioma cells by up-regulating PTX3', *American Journal of Cancer Research*, 8(4), pp. 624–635. Available at: /pmc/articles/PMC5934553/%0A/pmc/articles/PMC5934553/?report=abstract%0Ahttps://www.ncbi.nlm.nih.gov/pmc/articles/PMC5934553/.

Loeffler, S. *et al.* (2005) 'Interleukin-6 induces transcriptional activation of vascular endothelial growth factor (VEGF) in astrocytes in vivo and regulates VEGF promoter activity in glioblastoma cells via direct interaction between STAT3 and Sp1', *International Journal of Cancer*, 115(2), pp. 202–213. doi: 10.1002/IJC.20871.

Lotfi Shahreza, M., Ghadiri, N. and Green, J. R. (2020) 'A computational drug repositioning method applied to rare diseases: Adrenocortical carcinoma', *Scientific Reports 2020 10:1*, 10(1), pp. 1–7. doi: 10.1038/s41598-020-65658-x.

Louca, M. *et al.* (2020) 'ILK silencing inhibits migration and invasion of more invasive glioblastoma cells by downregulating ROCK1 and Fascin-1', *Molecular and Cellular Biochemistry 2020 471:1*, 471(1), p. 6. doi: 10.1007/S11010-020-03774-Y.

Louis, D. N. *et al.* (2016) 'The 2016 World Health Organization Classification of Tumors of the Central Nervous System: a summary', *Acta Neuropathologica*, 131(6), pp. 803–820. doi: 10.1007/s00401-016-1545-1.

Love, M. I., Huber, W. and Anders, S. (2014) 'Moderated estimation of fold change and dispersion for RNA-seq data with DESeq2', *Genome Biology*, 15(12), p. 550. doi: 10.1186/s13059-014-0550-8.

Loveson, K. and Fillmore, H. (2018) 'Intersection of Brain Development and Paediatric Diffuse Midline Gliomas: Potential Role of Microenvironment in Tumour Growth', *Brain Sciences*, 8(11), p. 200. doi: 10.3390/brainsci8110200.

Lu, V. M., Brown, D. A. and Daniels, D. J. (2020) 'Rare Diffuse Intrinsic Pontine Glioma Metastasis Throughout the Brain and Spine', *World Neurosurgery*, 140, pp. 301–302. doi: 10.1016/j.wneu.2020.05.205.

Ma, W. *et al.* (2021) 'BARTweb: a web server for transcriptional regulator association analysis', *NAR Genomics and Bioinformatics*, 3(2). doi: 10.1093/nargab/lqab022.

Mackay, A. *et al.* (2017) 'Integrated Molecular Meta-Analysis of 1,000 Pediatric High-Grade and Diffuse Intrinsic Pontine Glioma', *Cancer Cell*, 0(0), pp. 1–18. doi: 10.1016/j.ccell.2017.08.017.

Majzner, R. G., *et al.* (2022) ' GD2-CAR T cell therapy for H3K27M-mutated diffuse midline gliomas', *Nature 2022*, 1–10. https://doi.org/10.1038/s41586-022-04489-4

Malik, V. A. *et al.* (2020) 'GDF15 promotes simultaneous astrocyte remodeling and tight junction strengthening at the blood–brain barrier', *Journal of Neuroscience Research*, 98(7), pp. 1433–1456. doi: 10.1002/JNR.24611.

Mandell, L. R. *et al.* (1999) 'There is no role for hyperfractionated radiotherapy in the management of children with newly diagnosed diffuse intrinsic brainstem tumors: results of a pediatric oncology group phase III trial comparing conventional vs. hyperfractionated radiotherapy', *International Journal of Radiation Oncology*Biology*Physics*, 43(5), pp. 959–964.

doi: 10.1016/S0360-3016(98)00501-X.

Margueron, R. *et al.* (2009) 'Role of the polycomb protein EED in the propagation of repressive histone marks', *Nature*, 461(7265), pp. 762–767. doi: 10.1038/nature08398.

Margueron, R. and Reinberg, D. (2011) 'The Polycomb complex PRC2 and its mark in life', *Nature*, 469(7330), pp. 343–349. doi: 10.1038/nature09784.

Marin-Valencia, I. *et al.* (2012) 'Analysis of Tumor Metabolism Reveals Mitochondrial Glucose Oxidation in Genetically Diverse Human Glioblastomas in the Mouse Brain In Vivo', *Cell Metabolism*, 15(6), pp. 827–837. doi: 10.1016/j.cmet.2012.05.001.

Matsuo, K. *et al.* (2021) 'ACVR1 R206H extends inflammatory responses in human induced pluripotent stem cell-derived macrophages', *Bone*, 153. doi: 10.1016/J.BONE.2021.116129.

McCabe, M. T. *et al.* (2012) 'EZH2 inhibition as a therapeutic strategy for lymphoma with EZH2-activating mutations', *Nature*, 492(7427), pp. 108–112. doi: 10.1038/nature11606.

Meel, M. H. *et al.* (2020) 'Combined Therapy of AXL and HDAC Inhibition Reverses Mesenchymal Transition in Diffuse Intrinsic Pontine Glioma', *Clinical Cancer Research*, 26(13), pp. 3319–3332. doi: 10.1158/1078-0432.CCR-19-3538.

Mei, S. *et al.* (2017) 'Cistrome Data Browser: a data portal for ChIP-Seq and chromatin accessibility data in human and mouse', *Nucleic Acids Research*, 45(D1), pp. D658–D662. doi: 10.1093/nar/gkw983.

Meister, G. *et al.* (2001) 'Methylation of Sm proteins by a complex containing PRMT5 and the putative U snRNP assembly factor pICln', *Current Biology*, 11(24), pp. 1990–1994. doi: 10.1016/S0960-9822(01)00592-9.

Mentlein, R., Hattermann, K. and Held-Feindt, J. (2012) 'Lost in disruption: role of proteases in glioma invasion and progression', *Biochimica et biophysica acta*, 1825(2), pp. 178–185. doi: 10.1016/J.BBCAN.2011.12.001.

Michalski, A. *et al.* (2010) 'The addition of high-dose tamoxifen to standard radiotherapy does not improve the survival of patients with diffuse intrinsic pontine glioma', *Journal of Neuro-Oncology*, 100(1), pp. 81–88. doi: 10.1007/s11060-010-0141-9.

Michealraj, K. A. *et al.* (2020) 'Metabolic Regulation of the Epigenome Drives Lethal Infantile Ependymoma', *Cell*, 181(6), pp. 1329-1345.e24. doi: 10.1016/j.cell.2020.04.047.

Migliori, V. *et al.* (2012) 'Symmetric dimethylation of H3R2 is a newly identified histone mark that supports euchromatin maintenance', *Nature Structural & Molecular Biology*, *19*(2), 136–145. https://doi.org/10.1038/NSMB.2209

Milde, T. *et al.* (2011) 'A novel human high-risk ependymoma stem cell model reveals the differentiation-inducing potential of the histone deacetylase inhibitor Vorinostat', *Acta Neuropathologica*, 122(5), pp. 637–650. doi: 10.1007/s00401-011-0866-3.

Misuraca, K. L., Cordero, F. J. and Becher, O. J. (2015) 'Pre-Clinical Models of Diffuse Intrinsic Pontine Glioma', *Frontiers in Oncology*, 5. doi: 10.3389/fonc.2015.00172.

Mita, M. M. and Mita, A. C. (2020) 'Bromodomain inhibitors a decade later: a promise unfulfilled?', *British Journal of Cancer*, 123(12), pp. 1713–1714. doi: 10.1038/s41416-020-01079-x.

Miyahara, H. *et al.* (2017) 'The dual mTOR kinase inhibitor TAK228 inhibits tumorigenicity and enhances radiosensitization in diffuse intrinsic pontine glioma', *Cancer Letters*, 400, pp. 110–116. doi: 10.1016/j.canlet.2017.04.019.

Miyazawa, K. and Miyazono, K. (2017) 'Regulation of TGF-β Family Signaling by Inhibitory Smads.', *Cold Spring Harbor perspectives in biology*, 9(3), p. a022095. doi: 10.1101/cshperspect.a022095.

Mohammad, F. *et al.* (2017) 'EZH2 is a potential therapeutic target for H3K27M-mutant pediatric gliomas', *Nature Medicine*, 23(4), pp. 483–492. doi: 10.1038/nm.4293.

Moini, J., Koenitzer, J. and LoGalbo, A. (2021) 'Brain structures and functions', in *Global Emergency of Mental Disorders*. Elsevier, pp. 3–30. doi: 10.1016/B978-0-323-85837-3.00023-6.

Monje, M. *et al.* (2011) 'Hedgehog-responsive candidate cell of origin for diffuse intrinsic pontine glioma.', *Proceedings of the National Academy of Sciences of the United States of America*, 108(11), pp. 4453–8. doi: 10.1073/pnas.1101657108.

Mueller, S. *et al.* (2014) 'Targeting Wee1 for the treatment of pediatric high-grade gliomas', *Neuro-Oncology*, 16(3), pp. 352–360. doi: 10.1093/neuonc/not220.

Mueller, T. D. and Nickel, J. (2012) 'Promiscuity and specificity in BMP receptor activation', *FEBS Letters*, 586(14), pp. 1846–1859. doi: 10.1016/j.febslet.2012.02.043.

Muir, A., Danai, L. V. and Vander Heiden, M. G. (2018) 'Microenvironmental regulation of cancer cell metabolism: implications for experimental design and translational studies', *Disease Models & Mechanisms*, 11(8). doi: 10.1242/dmm.035758.

Mulvaney, K. M. *et al.* (2021) 'Molecular basis for substrate recruitment to the PRMT5 methylosome', *Molecular Cell*, 81(17), pp. 3481-3495.e7. doi: 10.1016/j.molcel.2021.07.019.

Nagamatsu, G. *et al.* (2011) 'A Germ Cell-specific Gene, Prmt5, Works in Somatic Cell Reprogramming', *The Journal of Biological Chemistry*, 286(12), p. 10641. doi: 10.1074/JBC.M110.216390.

Nakatani, H. *et al.* (2013) 'Ascl1/Mash1 Promotes Brain Oligodendrogenesis during Myelination and Remyelination', *The Journal of Neuroscience*, 33(23), p. 9752. doi: 10.1523/JNEUROSCI.0805-13.2013.

Narayan, R. S. *et al.* (2018) 'Identification of MEK162 as a Radiosensitizer for the Treatment of Glioblastoma', *Molecular Cancer Therapeutics*, 17(2), pp. 347–354. doi: 10.1158/1535-7163.MCT-17-0480.

Nikbakht, H. *et al.* (2016) 'Spatial and temporal homogeneity of driver mutations in diffuse intrinsic pontine glioma', *Nature Communications*, 7(1), p. 11185. doi: 10.1038/ncomms11185.

Okamoto, S. *et al.* (2019) 'Highly efficient genome editing for single-base substitutions using optimized ssODNs with Cas9-RNPs', *Scientific Reports 2019 9:1*, 9(1), pp. 1–11. doi: 10.1038/s41598-019-41121-4.

Olsen, M. L. and Sontheimer, H. (2008) 'Functional implications for Kir4.1 channels in glial biology: from K + buffering to cell differentiation', *Journal of Neurochemistry*, 107(3), pp. 589–601. doi: 10.1111/j.1471-4159.2008.05615.x.

Olsen, O. E. *et al.* (2015) 'Activin A inhibits BMP-signaling by binding ACVR2A and ACVR2B', *Cell Communication and Signaling*, 13(1), p. 27. doi: 10.1186/s12964-015-0104-z.

Otani, Y. *et al.* (2021) 'Inhibiting protein phosphatase 2A increases the antitumor effect of protein arginine methyltransferase 5 inhibition in models of glioblastoma', *Neuro-Oncology*, 23(9), pp. 1481–1493. doi: 10.1093/neuonc/noab014.

Pal, S. *et al.* (2004) 'Human SWI/SNF-Associated PRMT5 Methylates Histone H3 Arginine 8 and Negatively Regulates Expression of ST7 and NM23 Tumor Suppressor Genes', *Molecular and Cellular Biology*, 24(21), pp. 9630–9645. doi: 10.1128/MCB.24.21.9630-9645.2004.

Pal, S. *et al.* (2018) 'Dual HDAC and PI3K Inhibition Abrogates NFκB- and FOXM1-Mediated DNA Damage Response to Radiosensitize Pediatric High-Grade Gliomas', *Cancer Research*, 78(14), pp. 4007–4021. doi: 10.1158/0008-5472.CAN-17-3691.

Pan, Y., Bartneck, M. and Jahnen-Dechent, W. (2012) 'Cytotoxicity of Gold Nanoparticles', in, pp. 225–242. doi: 10.1016/B978-0-12-391858-1.00012-5.

Park, J. H. *et al.* (2015) 'Protein arginine methyltransferase 5 is a key regulator of the MYCN oncoprotein in neuroblastoma cells', *Molecular Oncology*, *9*(3), 617. https://doi.org/10.1016/J.MOLONC.2014.10.015

Paugh, B. S. *et al.* (2011) 'Genome-wide analyses identify recurrent amplifications of receptor tyrosine kinases and cell-cycle regulatory genes in diffuse intrinsic pontine glioma.', *Journal of clinical oncology : official journal of the American Society of Clinical Oncology*, 29(30), pp. 3999–4006. doi: 10.1200/JCO.2011.35.5677.

Pekny, M. and Pekna, M. (2004) 'Astrocyte intermediate filaments in CNS pathologies and regeneration', *The Journal of pathology*, 204(4), pp. 428–437. doi: 10.1002/PATH.1645.

Perla, A. *et al.* (2020) 'Histone Deacetylase Inhibitors in Pediatric Brain Cancers: Biological Activities and Therapeutic Potential', *Frontiers in Cell and Developmental Biology*, 0, p. 546. doi: 10.3389/FCELL.2020.00546.

Phillips, R. E. *et al.* (2019) 'Target identification reveals lanosterol synthase as a vulnerability in glioma', *Proceedings of the National Academy of Sciences of the United States of America*, 116(16), pp. 7957–7962. doi: 10.1073/pnas.1820989116.

Piunti, A. *et al.* (2017) 'Therapeutic targeting of polycomb and BET bromodomain proteins in diffuse intrinsic pontine gliomas', *Nature Medicine*, 23(4), pp. 493–500. doi: 10.1038/nm.4296.

Pollack, B. P., Sapkota, B. and Cartee, T. V. (2011) 'Epidermal Growth Factor Receptor Inhibition Augments the Expression of MHC Class I and II Genes', *Clinical Cancer Research*, 17(13), pp. 4400–4413. doi: 10.1158/1078-0432.CCR-10-3283.

Qi, J. *et al.* (2019) 'Tenascin-C expression contributes to pediatric brainstem glioma tumor phenotype and represents a novel biomarker of disease', *Acta Neuropathologica Communications 2019 7:1*, 7(1), pp. 1–19. doi: 10.1186/S40478-019-0727-1.

Quinlan, R. B. A. and Brennan, P. E. (2021) 'Chemogenomics for drug discovery: clinical molecules from open access chemical probes', *RSC Chemical Biology*, 2(3), pp. 759–795. doi: 10.1039/D1CB00016K.

Rajagopal, R. *et al.* (2008) 'Functions of the Type 1 BMP Receptor Acvr1 (Alk2) in Lens Development: Cell Proliferation, Terminal Differentiation, and Survival', *Investigative Ophthalmology & Visual Science*, 49(11), pp. 4953–4960. doi: 10.1167/IOVS.08-2217.

Ramachandran, A. *et al.* (2021) ' Pathogenic ACVR1 R206H activation by Activin A-induced

receptor clustering and autophosphorylation ', *The EMBO Journal*. doi: 10.15252/embj.2020106317.

Ran, F. A. *et al.* (2013) 'Genome engineering using the CRISPR-Cas9 system.', *Nature protocols*, 8(11), pp. 2281–308. doi: 10.1038/nprot.2013.143.

Raposo, A. E. and Piller, S. C. (2018) 'Protein arginine methylation: an emerging regulator of the cell cycle', *Cell Division*, 13(1), p. 3. doi: 10.1186/s13008-018-0036-2.

Redmer, T. *et al.* (2014) 'The Nerve Growth Factor Receptor CD271 Is Crucial to Maintain Tumorigenicity and Stem-Like Properties of Melanoma Cells', *PLoS ONE*. Edited by M. Chen, 9(5), p. e92596. doi: 10.1371/journal.pone.0092596.

Rengasamy, M. *et al.* (2017) 'The PRMT5/WDR77 complex regulates alternative splicing through ZNF326 in breast cancer', *Nucleic Acids Research*, 45(19), pp. 11106–11120. doi: 10.1093/nar/gkx727.

Riccardi, C. and Nicoletti, I. (2006) 'Analysis of apoptosis by propidium iodide staining and flow cytometry', *Nature Protocols*, 1(3), pp. 1458–1461. doi: 10.1038/nprot.2006.238.

Robison, N. J. and Kieran, M. W. (2014) 'Diffuse intrinsic pontine glioma: A reassessment', *Journal of Neuro-Oncology*, 119(1), pp. 7–15. doi: 10.1007/S11060-014-1448-8/TABLES/1.

Rodgers, L. *et al.* (2016) 'HG-36PLASMA AND CEREBROSPINAL FLUID (CSF) PHARMACOKINETICS OF PANOBINOSTAT FOLLOWING ORAL ADMINISTRATION TO NONHUMAN PRIMATES', *Neuro-Oncology*, 18(suppl 3), p. iii55.3-iii55. doi: 10.1093/neuonc/now073.33.

Roujeau, T. *et al.* (2007) 'Stereotactic biopsy of diffuse pontine lesions in children', *Journal of Neurosurgery: Pediatrics*, 107(1), pp. 1–4. doi: 10.3171/PED-07/07/001.

Rycaj, K. and Tang, D. G. (2015) 'Cell-of-Origin of Cancer versus Cancer Stem Cells: Assays and Interpretations', *Cancer Research*, 75(19), pp. 4003–4011. doi: 10.1158/0008-5472.CAN-15-0798.

Sachamitr, P. *et al.* (2021) 'PRMT5 inhibition disrupts splicing and stemness in glioblastoma', *Nature Communications 2021 12:1*, 12(1), pp. 1–17. doi: 10.1038/s41467-021-21204-5.

Safina, D. *et al.* (2016) 'Low-density lipoprotein receptor-related protein 1 is a novel modulator of radial glia stem cell proliferation, survival, and differentiation', *Glia*, 64(8), pp. 1363–1380. doi: 10.1002/glia.23009.

Sandberg, C. J. *et al.* (2014) 'Transcriptional Profiling of Adult Neural Stem-Like Cells from the Human Brain', *PLoS ONE*. Edited by F. Szele, 9(12), p. e114739. doi: 10.1371/journal.pone.0114739.

Sanson, K. R. *et al.* (2018) 'Optimized libraries for CRISPR-Cas9 genetic screens with multiple modalities', *Nature Communications 2018 9:1*, 9(1), pp. 1–15. doi: 10.1038/s41467-018-07901-8.

Saratsis, A. M. *et al.* (2014) 'Comparative multidimensional molecular analyses of pediatric diffuse intrinsic pontine glioma reveals distinct molecular subtypes', *Acta Neuropathologica*, 127(6), pp. 881–895. doi: 10.1007/s00401-013-1218-2.Comparative.

Sasaki, T. *et al.* (2020) 'Convection-Enhanced Delivery of Enhancer of Zeste Homolog-2 (EZH2) Inhibitor for the Treatment of Diffuse Intrinsic Pontine Glioma', *Neurosurgery*, 87(6), pp. E680–E688. doi: 10.1093/NEUROS/NYAA301.

Scaglione, A. *et al.* (2018) 'PRMT5-mediated regulation of developmental myelination', *Nature Communications*, 9(1), p. 2840. doi: 10.1038/s41467-018-04863-9.

Scheer, S. *et al.* (2019) 'A chemical biology toolbox to study protein methyltransferases and epigenetic signaling', *Nature communications*, 10(1). doi: 10.1038/S41467-018-07905-4.

Schwartzentruber, J. *et al.* (2012) 'Driver mutations in histone H3.3 and chromatin remodelling genes in paediatric glioblastoma', *Nature*, 482(7384), pp. 226–231. doi: 10.1038/nature10833.

Segherlou, Z. H. *et al.* (2021) 'GDF-15: Diagnostic, prognostic, and therapeutic significance in glioblastoma multiforme', *Journal of Cellular Physiology*, 236(8), pp. 5564–5581. doi: 10.1002/JCP.30289.

Seki, A. and Rutz, S. (2018) 'Optimized RNP transfection for highly efficient CRISPR/Cas9-mediated gene knockout in primary T cells', *Journal of Experimental Medicine*, 215(3), pp. 985–997. doi: 10.1084/JEM.20171626.

Seliger, C. *et al.* (2019) 'Use of metformin and survival of patients with high-grade glioma', *International Journal of Cancer*, 144(2), pp. 273–280. doi: 10.1002/ijc.31783.

Seyfried, T. N. and Mukherjee, P. (2005) 'Targeting energy metabolism in brain cancer: review and hypothesis', *Nutrition & Metabolism*, 2(1), p. 30. doi: 10.1186/1743-7075-2-30.

Seyhan, A. A. (2019) 'Lost in translation: the valley of death across preclinical and clinical divide – identification of problems and overcoming obstacles', *Translational Medicine Communications*, 4(1), p. 18. doi: 10.1186/s41231-019-0050-7.

Shah, A. *et al.* (2012) 'Involvement of metabotropic glutamate receptor 5, AKT/PI3K Signaling and NF-κB pathway in methamphetamine-mediated increase in IL-6 and IL-8 expression in astrocytes', *Journal of Neuroinflammation*, 9, p. 52. doi: 10.1186/1742-2094-9-52.

Shalem, O. *et al.* (2014) 'Genome-Scale CRISPR-Cas9 Knockout Screening in Human Cells', *Science (New York, N.Y.)*, 343(6166), p. 84. doi: 10.1126/SCIENCE.1247005.

Shen, Q. *et al.* (2009) 'The fibrodysplasia ossificans progressiva R206H ACVR1 mutation activates BMP-independent chondrogenesis and zebrafish embryo ventralization.', *The Journal of clinical investigation*, 119(11), pp. 3462–72. doi: 10.1172/JCI37412.

Silveira, A. B. *et al.* (2019) 'H3.3 K27M depletion increases differentiation and extends latency of diffuse intrinsic pontine glioma growth in vivo', *Acta Neuropathologica*, 137(4), pp. 637–655. doi: 10.1007/s00401-019-01975-4.

Song, G. A. *et al.* (2010) 'Molecular consequences of the ACVR1R206H mutation of fibrodysplasia ossificans progressiva', *Journal of Biological Chemistry*, 285(29), pp. 22542–22553. doi: 10.1074/jbc.M109.094557.

Sorkin, M. *et al.* (2017) 'Hair follicle specific ACVR1/ALK2 critically affects skin morphogenesis and attenuates wound healing', *Wound Repair and Regeneration*, 25(3), pp. 521–525. doi: 10.1111/WRR.12549.

Sozmen, E. G. *et al.* (2019) 'White Matter Stroke Induces a Unique Oligo-Astrocyte Niche That Inhibits Recovery', *The Journal of Neuroscience*, 39(47), pp. 9343–9359. doi: 10.1523/JNEUROSCI.0103-19.2019.

Spandidos, A. *et al.* (2010) 'PrimerBank: a resource of human and mouse PCR primer pairs for gene expression detection and quantification', *Nucleic Acids Research*, 38(suppl_1), pp.

D792–D799. doi: 10.1093/nar/gkp1005.

Srikanthan, D. *et al.* (2021) 'Diffuse intrinsic pontine glioma: current insights and future directions', *Chinese Neurosurgical Journal*, 7(1), p. 6. doi: 10.1186/s41016-020-00218-w.

Stopa, N., Krebs, J. E. and Shechter, D. (2015) 'The PRMT5 arginine methyltransferase: many roles in development, cancer and beyond', *Cellular and Molecular Life Sciences*, 72(11), pp. 2041–2059. doi: 10.1007/s00018-015-1847-9.

Structural Genomics Consortium (no date) *LLY-507 | SGC*. Available at: https://www.thesgc.org/chemical-probes/LLY-507 (Accessed: 28 September 2021).

Stupack, D. G. and Cheresh, D. A. (2002) 'Get a ligand, get a life: integrins, signaling and cell survival', *Journal of Cell Science*, 115(19), pp. 3729–3738. doi: 10.1242/jcs.00071.

Sturm, D. *et al.* (2012) 'Hotspot Mutations in H3F3A and IDH1 Define Distinct Epigenetic and Biological Subgroups of Glioblastoma', *Cancer Cell*, 22(4), pp. 425–437. doi: 10.1016/J.CCR.2012.08.024.

Su, G. *et al.* (2006) 'Glypican-1 is frequently overexpressed in human gliomas and enhances FGF-2 signaling in glioma cells', *The American journal of pathology*, 168(6), pp. 2014–2026. doi: 10.2353/AJPATH.2006.050800.

Sugiyama, N. *et al.* (2010) 'Fibroblast Growth Factor Receptor 4 Regulates Tumor Invasion by Coupling Fibroblast Growth Factor Signaling to Extracellular Matrix Degradation', *Cancer Research2*, 70(20), pp. 7851–7861. Available at: https://cancerres.aacrjournals.org/content/70/20/7851%0Ahttps://cancerres.aacrjournals.org/content/70/20/7851.abstract.

Sun, L. *et al.* (2011) 'Structural insights into protein arginine symmetric dimethylation by PRMT5', *Proceedings of the National Academy of Sciences*, 108(51), pp. 20538–20543. doi: 10.1073/pnas.1106946108.

Sun, X. *et al.* (2013) 'PDGF-BB-induced MT1-MMP expression regulates proliferation and invasion of mesenchymal stem cells in 3-dimensional collagen via MEK/ERK1/2 and PI3K/AKT signaling', *Cellular Signalling*, 25(5), pp. 1279–1287. doi: 10.1016/J.CELLSIG.2013.01.029.

Tabata, T. *et al.* (2009) 'Ski co-repressor complexes maintain the basal repressed state of the TGF-β target gene, SMAD7 , via HDAC3 and PRMT5', *Genes to Cells*, 14(1), pp. 17–28. doi: 10.1111/j.1365-2443.2008.01246.x.

Taylor, I. C. *et al.* (2015) 'Disrupting NOTCH Slows Diffuse Intrinsic Pontine Glioma Growth, Enhances Radiation Sensitivity, and Shows Combinatorial Efficacy With Bromodomain Inhibition', *Journal of Neuropathology and Experimental Neurology*, 74(8), pp. 778–790. doi: 10.1097/NEN.0000000000000216.

Taylor, K. R. *et al.* (2014) 'Recurrent activating ACVR1 mutations in diffuse intrinsic pontine glioma', *Nature Genetics*, 46(5), pp. 457–461. doi: 10.1038/ng.2925.

The Brain Tumour Charity (n.d.) 'Diffuse midline glioma brain tumour research.' Available at: https://www.thebraintumourcharity.org/brain-tumour-diagnosis-treatment/types-brain-tumour-children/dipg-diffuse-intrinsic-pontine-glioma/dipg-research/ (Accessed: 1 March 2022)

Truffaux, N. *et al.* (2015) 'Preclinical evaluation of dasatinib alone and in combination with cabozantinib for the treatment of diffuse intrinsic pontine glioma', *Neuro-Oncology*, 17(7), pp. 953–964. doi: 10.1093/neuonc/nou330.

Tung, J.-N. *et al.* (2016) 'Inhibition of pentraxin 3 in glioma cells impairs proliferation and invasion in vitro and in vivo', *Journal of Neuro-Oncology 2016 129:2*, 129(2), pp. 201–209. doi: 10.1007/S11060-016-2168-Z.

Ucker, D. S. and Levine, J. S. (2018) 'Exploitation of Apoptotic Regulation in Cancer', *Frontiers in Immunology*, 0(FEB), p. 241. doi: 10.3389/FIMMU.2018.00241.

Valer, J. A. *et al.* (2019) 'ACVR1 Function in Health and Disease', *Cells*, 8(11). doi: 10.3390/CELLS8111366.

Vedadi, M. *et al.* (2011) 'A chemical probe selectively inhibits G9a and GLP methyltransferase activity in cells', *Nature Chemical Biology 2011 7:8*, 7(8), pp. 566–574. doi: 10.1038/nchembio.599.

Veldhuijzen van Zanten, S. E. M. *et al.* (2017) 'Development of the SIOPE DIPG network, registry and imaging repository: a collaborative effort to optimize research into a rare and lethal disease', *Journal of Neuro-Oncology*, 132(2), pp. 255–266. doi: 10.1007/s11060-016-2363-y.

Vignjevic, D. *et al.* (2007) 'Fascin, a Novel Target of β-Catenin-TCF Signaling, Is Expressed at the Invasive Front of Human Colon Cancer', *Cancer Research*, 67(14), pp. 6844–6853. doi: 10.1158/0008-5472.CAN-07-0929.

Vinci, M. *et al.* (2012) 'Advances in establishment and analysis of three-dimensional tumor spheroid-based functional assays for target validation and drug evaluation', *BMC Biology*, 10(1), p. 29. doi: 10.1186/1741-7007-10-29.

Vinci, M. *et al.* (2018) 'Functional diversity and cooperativity between subclonal populations of pediatric glioblastoma and diffuse intrinsic pontine glioma cells', *Nature Medicine*, 24(8), pp. 1204–1215. doi: 10.1038/s41591-018-0086-7.

Vinci, M., Box, C. and Eccles, S. A. (2015) 'Three-dimensional (3D) tumor spheroid invasion assay', *Journal of Visualized Experiments*, 2015(99), pp. 1–9. doi: 10.3791/52686.

Vinet, M. *et al.* (2019) 'Protein arginine methyltransferase 5: A novel therapeutic target for triple-negative breast cancers', *Cancer Medicine*, 8(5), p. 2414. doi: 10.1002/CAM4.2114.

Vitanza, N. A. and Monje, M. (2019) 'Diffuse Intrinsic Pontine Glioma: From Diagnosis to Next-Generation Clinical Trials', *Current treatment options in neurology*, 21(8). doi: 10.1007/S11940-019-0577-Y.

Vrotsos, E. G., Kolattukudy, P. E. and Sugaya, K. (2009) 'MCP-1 involvement in glial differentiation of neuroprogenitor cells through APP signaling', *Brain Research Bulletin*, 79(2), pp. 97–103. doi: 10.1016/J.BRAINRESBULL.2009.01.004.

Walter, A. W. *et al.* (1998) 'Carboplatin and etoposide with hyperfractionated radiotherapy in children with newly diagnosed diffuse pontine gliomas: A phase I/II study', *Medical and Pediatric Oncology*, 30(1), pp. 28–33. doi: 10.1002/(SICI)1096-911X(199801)30:1<28::AID-MPO9>3.0.CO;2-2.

Wang, S. *et al.* (2016) 'Modeling cis -regulation with a compendium of genome-wide histone H3K27ac profiles', *Genome Research*, 26(10), pp. 1417–1429. doi: 10.1101/gr.201574.115.

Wang, Y. *et al.* (2019) 'ACVR1-knockout promotes osteogenic differentiation by activating the Wnt signaling pathway in mice', *Journal of Cellular Biochemistry*, 120(5), pp. 8185–8194. doi: 10.1002/JCB.28100.

Wang, Z. *et al.* (2018) 'BART: a transcription factor prediction tool with query gene sets or epigenomic profiles', *Bioinformatics*, 34(16), pp. 2867–2869. doi: 10.1093/BIOINFORMATICS/BTY194.

Warren, K. E. (2018) 'Beyond the Blood:Brain Barrier: The Importance of Central Nervous System (CNS) Pharmacokinetics for the Treatment of CNS Tumors, Including Diffuse Intrinsic Pontine Glioma', *Frontiers in Oncology*, 8. doi: 10.3389/fonc.2018.00239.

Watanabe, K. *et al.* (2015) 'The participation of insulin-like growth factor-binding protein 3 released by astrocytes in the pathology of Alzheimer's disease', *Molecular Brain 2015 8:1*, 8(1), pp. 1–14. doi: 10.1186/S13041-015-0174-2.

Webb, L. *et al.* (2020) 'Protein arginine methyltransferase 5 promotes cholesterol biosynthesis-mediated Th17 responses and autoimmunity', *The Journal of clinical investigation*, 130(4), pp. 1683–1698. doi: 10.1172/JCI131254.

Wei, T. Y. W. *et al.* (2012) 'Protein arginine methyltransferase 5 is a potential oncoprotein that upregulates G1 cyclins/cyclin-dependent kinases and the phosphoinositide 3-kinase/AKT signaling cascade', *Cancer Science*, 103(9), pp. 1640–1650. doi: 10.1111/j.1349-7006.2012.02367.x.

Whetstine, J. R. (2010) 'Histone Methylation: Chemically Inert but Chromatin Dynamic', in *Handbook of Cell Signaling*. Elsevier, pp. 2389–2397. doi: 10.1016/B978-0-12-374145-5.00287-4.

Wiese, M. *et al.* (2016) 'No Significant Cytotoxic Effect of the EZH2 Inhibitor Tazemetostat (EPZ-6438) on Pediatric Glioma Cells with Wildtype Histone 3 or Mutated Histone 3.3', *Klinische Padiatrie*, 228(3), pp. 113–117. doi: 10.1055/S-0042-105292.

Wiese, M. *et al.* (2020) 'Combined treatment with CBP and BET inhibitors reverses inadvertent activation of detrimental super enhancer programs in DIPG cells', *Cell Death & Disease*, 11(8), p. 673. doi: 10.1038/s41419-020-02800-7.

Wong, J. F. *et al.* (2019) 'Fostering open collaboration in drug development for paediatric brain tumours', *Biochemical Society Transactions*, 47(5), pp. 1471–1479. doi: 10.1042/BST20190315.

Wrana, J. L. *et al.* (1994) 'Mechanism of activation of the TGF-β receptor', *Nature*, 370(6488), pp. 341–347. doi: 10.1038/370341a0.

Wu, G. *et al.* (2012) 'Somatic histone H3 alterations in pediatric diffuse intrinsic pontine gliomas and non-brainstem glioblastomas', *Nature Genetics*, 44(3), pp. 251–253. doi: 10.1038/ng.1102.

Wu, G. *et al.* (2014) 'The genomic landscape of diffuse intrinsic pontine glioma and pediatric non-brainstem high-grade glioma', *Nature Genetics*, 46(5), pp. 444–450. doi: 10.1038/ng.2938.

Wu, Q. *et al.* (2019) 'A chemical toolbox for the study of bromodomains and epigenetic signaling', *Nature Communications 2019 10:1*, 10(1), pp. 1–14. doi: 10.1038/s41467-019-09672-2.

Wu, T. *et al.* (2021) 'clusterProfiler 4.0: A universal enrichment tool for interpreting omics data', *The Innovation*, 2(3), p. 100141. doi: 10.1016/j.xinn.2021.100141.

Wu, Y. *et al.* (2017) 'Elevated expression of protein arginine methyltransferase 5 predicts the poor prognosis of breast cancer', *Tumour biology : the journal of the International Society*

for Oncodevelopmental Biology and Medicine, 39(4). doi: 10.1177/1010428317695917.

Xu, J. *et al.* (2013) 'Arginine methylation initiates BMP-induced Smad signaling', *Molecular Cell*, 51(1), pp. 5–19. doi: 10.1016/j.molcel.2013.05.004.

Xu, X. *et al.* (2018) 'Efficient homology-directed gene editing by CRISPR/Cas9 in human stem and primary cells using tube electroporation', *Scientific Reports 2018 8:1*, 8(1), pp. 1–11. doi: 10.1038/s41598-018-30227-w.

Y, F. *et al.* (2013) 'High-frequency off-target mutagenesis induced by CRISPR-Cas nucleases in human cells', *Nature biotechnology*, 31(9), pp. 822–826. doi: 10.1038/NBT.2623.

Yang, H. *et al.* (2016) 'PRMT5 competitively binds to CDK4 to promote G1-S transition upon glucose induction in hepatocellular carcinoma', *Oncotarget*, 7(44), pp. 72131–72147. doi: 10.18632/oncotarget.12351.

Yang, L. *et al.* (2013) 'Optimization of scarless human stem cell genome editing', *Nucleic Acids Research*, 41(19), pp. 9049–9061. doi: 10.1093/NAR/GKT555.

Yang, L. *et al.* (2021) 'PRMT5 functionally associates with EZH2 to promote colorectal cancer progression through epigenetically repressing CDKN2B expression', *Theranostics*, 11(8), pp. 3742–3759. doi: 10.7150/thno.53023.

Yao, X. *et al.* (2010) 'Promotion of self-renewal of embryonic stem cells by midkine', *Acta Pharmacologica Sinica*, 31(5), pp. 629–637. doi: 10.1038/aps.2010.39.

Ye, J. *et al.* (2012) 'Primer-BLAST: A tool to design target-specific primers for polymerase chain reaction', *BMC Bioinformatics*, 13(1), p. 134. doi: 10.1186/1471-2105-13-134.

Yoshimura, T. (2017) 'The production of monocyte chemoattractant protein-1 (MCP-1)/CCL2 in tumor microenvironments', *Cytokine*, 98, pp. 71–78. doi: 10.1016/J.CYTO.2017.02.001.

Yu, W. *et al.* (2012) 'Catalytic site remodelling of the DOT1L methyltransferase by selective inhibitors', *Nature Communications 2012 3:1*, 3(1), pp. 1–12. doi: 10.1038/ncomms2304.

Zaghloul, M. S. *et al.* (2014) 'Hypofractionated conformal radiotherapy for pediatric diffuse intrinsic pontine glioma (DIPG): a randomized controlled trial', *Radiotherapy and oncology : journal of the European Society for Therapeutic Radiology and Oncology*, 111(1), pp. 35–40. doi: 10.1016/J.RADONC.2014.01.013.

Zambelli, F., Pesole, G. and Pavesi, G. (2009) 'Pscan: finding over-represented transcription factor binding site motifs in sequences from co-regulated or co-expressed genes', *Nucleic Acids Research*, 37(Web Server issue), p. W247. doi: 10.1093/NAR/GKP464.

Zeiadeh, I., Najjar, A. and Karaman, R. (2018) 'Strategies for Enhancing the Permeation of CNS-Active Drugs through the Blood-Brain Barrier: A Review', *Molecules*, 23(6), p. 1289. doi: 10.3390/molecules23061289.

Zhang, Y. *et al.* (2017) 'Combination of EZH2 inhibitor and BET inhibitor for treatment of diffuse intrinsic pontine glioma', *Cell and Bioscience*, 7(1). doi: 10.1186/s13578-017-0184-0.

Zhao, B. and Pritchard, J. R. (2016) 'Inherited Disease Genetics Improves the Identification of Cancer-Associated Genes', *PLOS Genetics*. Edited by G. M. Cooper, 12(6), p. e1006081. doi: 10.1371/journal.pgen.1006081.

Zhao, J. *et al.* (2017) 'APOE ε4/ε4 diminishes neurotrophic function of human iPSC-derived astrocytes', *Human Molecular Genetics*, 26(14), pp. 2690–2700. doi: 10.1093/hmg/ddx155.

Zhao, Q. *et al.* (2009) 'PRMT5-mediated methylation of histone H4R3 recruits DNMT3A, coupling histone and DNA methylation in gene silencing', *Nature Structural & Molecular Biology*, 16(3), pp. 304–311. doi: 10.1038/nsmb.1568.

Zheng, S. *et al.* (2013) 'Arginine methylation-dependent reader-writer interplay governs growth control by E2F-1', *Molecular cell*, 52(1), pp. 37–51. doi: 10.1016/J.MOLCEL.2013.08.039.

Zhou, H.-M. *et al.* (2021) 'Targeting cancer stem cells for reversing therapy resistance: mechanism, signaling, and prospective agents', *Signal Transduction and Targeted Therapy*, 6(1), p. 62. doi: 10.1038/s41392-020-00430-1.

Appendices

Table 0.1 - Reduction of HSJD-DIPG-011 in response to the probes in Table 3.1

Probe	Class	Target	Relative viability reduction	SD	q value
SGC-iMLLT	YEATS domain	MLLT1/3	-0.03	0.17	>0.99
SGC707	Methyltransferase	PRMT3	-0.01	0.22	>0.99
MS023	Methyltransferase	PRMT type I	0.02	0.36	>0.99
MS049	Methyltransferase	PRMT4/6	0.10	0.20	0.85
TP 064	Methyltransferase	PRMT4	0.12	0.27	0.85
A366	Methyltransferase	G9a/GLP	0.17	0.31	0.79
A485	Histone acetyltransferase	p300/CBP	0.18	0.52	0.79
SAHA	Histone deacetylase	Broad spectrum	0.23	0.52	0.74
UNC0642	Methyltransferase	G9a/GLP	0.30	0.61	0.42
SGC0946	Methyltransferase	DOT1L	0.38	0.59	0.24
Bromosporine	Bromodomain	Broad spectrum	0.39	0.53	0.24
LLY-283	Methyltransferase	PRMT5	0.40	0.43	0.24
LLY-507	Methyltransferase	SMYD2 (non-specific)	0.45	0.70	0.18
A395	PRC2 complex	EED	0.60	0.27	0.04
OF1	Bromodomain	BRPF1/2/3	0.61	0.25	0.04
JQ-1	Bromodomain	BET family	0.62	0.51	0.04
GSK 591	Methyltransferase	PRMT5	0.64	0.15	0.04

Figure 0.1 - Screening of epigenetic probes in HSJD-DIPG-011 cells

A) *The viability of HSJD-DIPG-011 (relative to a vehicle control) after treatment with 1 µM* of the indicated probe for 7 days in adherent culture, without radiation. Data points are the mean of 3 technical repeats from each independent repeat, annotated with the mean ± SD. PRMT inhibitors are highlighted with a red triangle.* ***B)*** *The viability of HSJD-DIPG-011 (relative to a vehicle control) after treatment with 1 µM* of the indicated probe for 7 days in the indicated growth conditions. Bars are the SD of 3 independent repeats of each indicated growth condition. PRMT inhibitors are highlighted with a red triangle. *Probe YT26870 was added at 0.5 µM.*

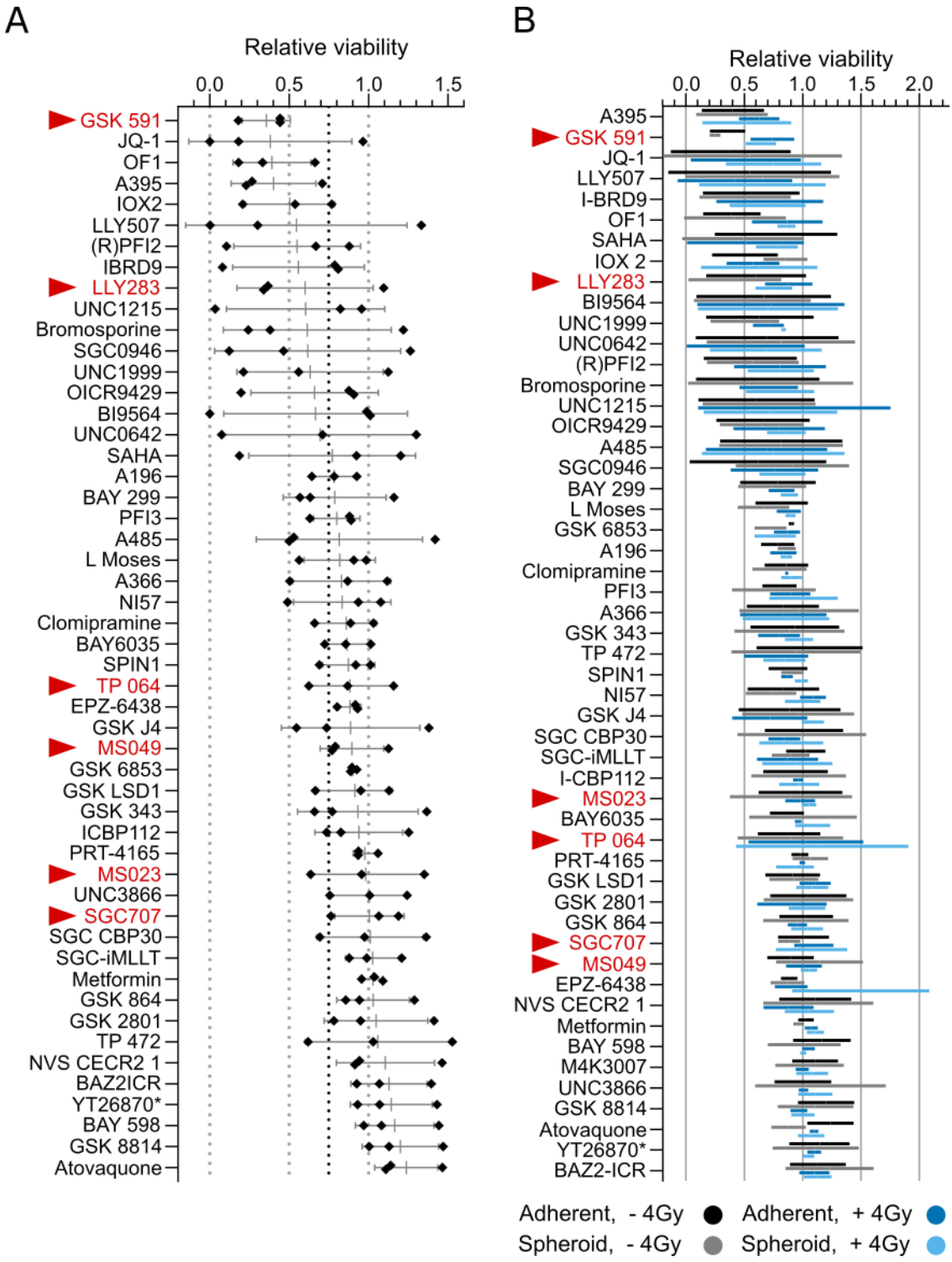

Figure legend on previous page.

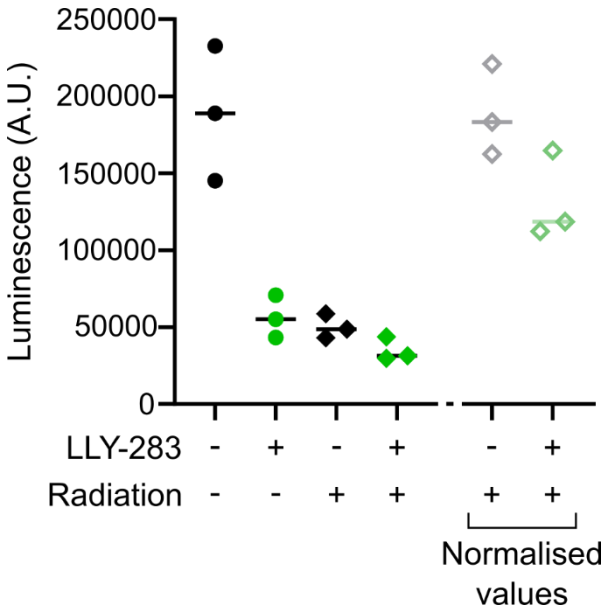

Figure 0.2 – Raw luminescence data for adherent HSJD-DIPG-007 treated with 1 µM LLY-283

The raw luminescence (A.U.), corresponding to viability, recorded after HSJD-DIPG-007 cells were treated with 1 µM LLY-283 (when grown adherently) +/- 4 Gy radiation. Each point is the average of three technical repeats, and groups are annotated with the mean. The right hand side of the graph depicts how the radiation treated samples would appear once normalised to the vehicle control as they were in Figure 3.5 and Figure 3.6. This highlights that, although the relative effectiveness of LLY-283 is reduced in radiation treated samples, the absolute viability is still decreased relative to samples treated with only LLY-283.

Table 0.2 - Markers identified by Trajecture pipeline

MALAT1	MIR100HG	MT-TS2	ZNF501	HMOX1	MAN1B1-DT	CDC42EP5
FP236383.4	RPE65	RIMS1	AC024075.2	NPIPA8	AC011497.2	OPTN
FP671120.6	ATF5	LINC01002	ANGPTL4	TMED7-TICAM2	AP000892.3	AP000295.1
FP236383.5	ISY1-RAB43	AC093668.3	IL3RA	CDH12P2	AL442003.1	WHAMMP2
AD000090.1	CACNA1E	SGK1	POLR2J2	PTRH1	PCSK5	MT-TT
RBM38	AL139300.1	PRRT2	PPAN-P2RY11	TTLL7	FAM229A	RYR3
DAZ2	SLC25A25-AS1	FN1	FAM27C	CYSLTR1	CDH12P3	AC068831.4
ZBED6	NSUN5P2	RNA5-8SN3	MDP1	BTD	CDH12P1	TRIM52-AS1
SLC2A3	RANBP3L	PLCB4	AC009120.2	AC139495.3	AL353622.1	Z83843.1
AC245060.5	AL035412.1	FUOM	SOX9-AS1	PPIAP22	TRIM7	RGPD8
SCN1A	THSD8	ATXN7	OR4F17	GLMP	AL591379.1	IKBKGP1
OLMALINC	AC139256.1	LTB4R	DOK3	AL049840.2	CASC19	AC090984.1
POSTN	AC068448.1	CTNNA3	PLA2G5	IQSEC2	AC084018.2	ZNF547
RAB43	CBR3-AS1	AC114546.3	SRP9P1	FMN1	CIRBP-AS1	APOE
GLIPR1	FAM95B1	AC138866.2	CSPG5	BLOC1S5-TXNDC5	AC010761.1	COL16A1
PTCHD1	AL392172.1	DNLZ	LINC01001	AL109811.2	AC005332.5	MMP2
AC011603.2	COL1A1	AC016026.1	HSP90AA6P	HMGB1P1	GOLGA8A	SLC6A16
AC006064.6	DNAAF4	CYP27B1	RAC1P2	AC007998.4	SNRPEP2	STX16-NPEPL1
SAMD4A	SEMA4B	PCDHGC3	SPTB	LINC01670	AC008764.4	CCDC144A
ABAT	SMOX	AP002360.1	ZDHHC22	ZNF709	SMG1P4	SNRPGP10
ZNF436	AC005329.1	AC073896.1	SLC35E4	AC005253.1	ENO3	TRIM46
DNM3OS	LINC02577	CFAP54	AL138881.1	ELF3-AS1	ACBD7	AC093909.6
MATN2	PLPPR4	AGER	ZNF597	COL1A2	AC110285.2	OR14J1
JMJD4	IFI30	EGFL8	RN7SK	AL928970.1	AC108449.2	AC012368.1
NPAS3	PHLDA3	ARHGAP11B	AC008443.1	AC118553.2	LAG3	NPIPA3
PNRC1	NCKAP5	HIST2H4B	AC055811.4	HIST2H4A	CBSL	CRYZL2P-SEC16B
KCNQ1OT1	FSBP	AC245060.6	AL022238.4	ADAM32	RALGPS1	SATL1
TRPM8	OVCA2	CR381653.2	CD101	AC008581.2	AC008957.3	CNTF
U2AF1	NOX5	CNTNAP3B	ENSG00000266086	PRR34-AS1	COMTD1	FLG
KDELR3	RBPMS2	MBNL2	SAPCD1	CCDC180	AP000866.6	AC018521.5
PCGF6	NOVA2	GLYCTK	NPIPA2	DNAH1	BCL2L15	ZKSCAN2-DT
GPRIN1	GP1BB	CSGALNACT1	AC087741.1	TPTEP2	AP001273.1	OR2M3
AC087473.1	LINC02503	PWAR5	AC037459.2	AC138811.2	AC006557.6	GBP1
AC015813.1	MAOB	POC1B-GALNT4	AC020978.5	AC009404.1	C20orf204	LINC00937
TMEM45A	AC116366.3	AC005832.4	RPS4XP22	CRYAB	AC026464.6	MRPL45P2
SLC7A11	TRIM16L	CBWD6	VLDLR	GPT	C2orf80	ZNF20
AC116533.1	SMIM11A	VPS33B	AC019069.1	SULT1B1	SOSTDC1	INE1
SMIM11B	AGAP9	AC005000.1	ADAMTS10	AC104581.4	KYNU	AC107375.1
FKBP11	EIF4EP2	RNLS	EREG	ZNF559-ZNF177	AL135999.1	BCL2L2-PABPN1
LINC00504	GPR22	ANKRD10-IT1	Z83844.3	MYLK4	COMMD3-BMI1	TMEM110-MUSTN1
CU633906.1	ZNF225	COL7A1	TMX2P1	USP32P2	LINC00624	OR2W3
GSAP	AL121845.3	SCO2	AC092902.4	PLSCR4	LINC00638	AL136295.5
AC092683.1	MIR34AHG	AC073957.3	SPDYE6	SIM2	AL138478.1	COL6A3
SEC31B	AC011511.4	ZNF596	ASIC3	NUDT4B	BEND3P3	SH3BP5-AS1
C4A	AC011448.1	ZNF320	KDM7A	AL034417.4	AC009133.2	AL669831.5
ELMOD1	AL158801.5	SCART1	RPL17-C18orf32	BMS1P4	LYPD1	AP000542.2
BTN3A2	TLL1	CCDC26	HERC2P8	NTRK3	SULT1A4	DLG3
ABHD11	MISP3	FAM174A	RIC3	AC009090.6	NT5M	AL358334.2
HIST2H2AA4	TGFB2	AL353150.1	TMEM91	ANKRD23	AL928654.4	TPTEP1
F3	TSPY26P	ANKDD1A	FDXACB1	GNRHR2	AL358472.6	AC023509.1

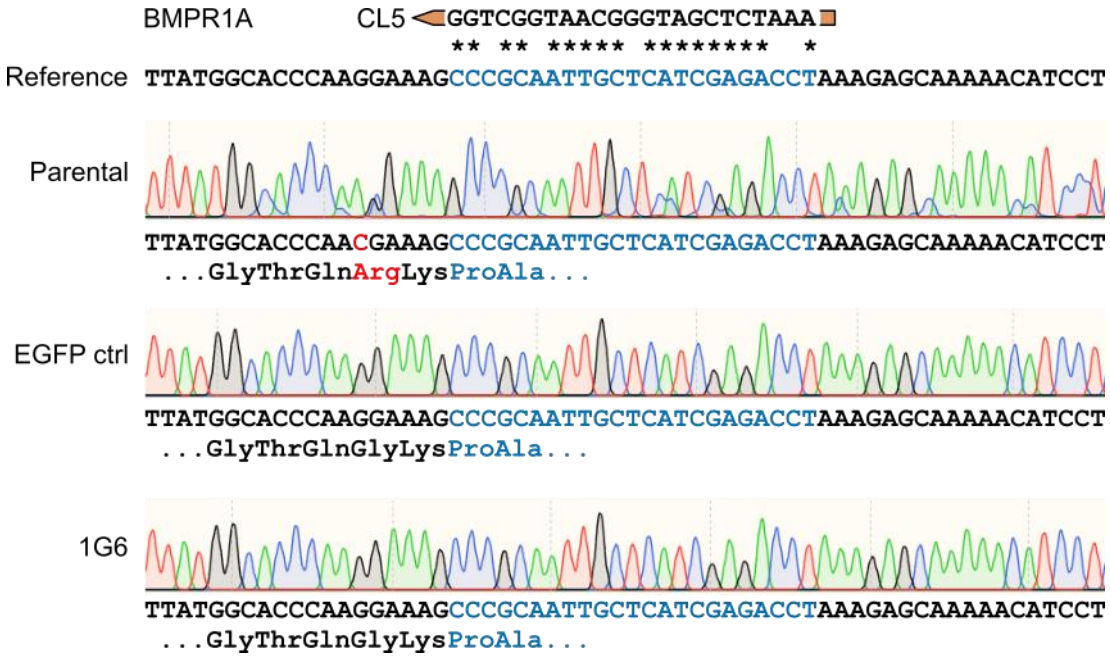

Figure 0.3 - Sequencing of predicted off-target site in BMPR1A

Aligned sequencing traces for the predicted off-target site in BMPR1A in the parental SU-DIPG-IV, control EGFP and edited 1G6 cell lines. Each trace is annotated with the corresponding nucleotides sequence and a region of codons are annotated with the translated amino acid sequence. The predicted off-target region is highlighted in blue, and the SNP and missense mutations in the parental line is highlighted in red.